CFD analysis of the heat transfer from a self-launch sailplane radiator

JP Le Roux

orcid.org/0000-0002-6494-5076

Dissertation submitted in fulfilment of the requirements for the degree *Master of Engineering in Mechanical Engineering* at the North-West University

Supervisor: Dr JJ Bosman

Co-supervisor: Dr JH Kruger

Graduation ceremony: May 2019

Student number: 22143785

Abstract

A self-launch sailplane is an aircraft equipped with a retractable engine/propeller combination which can take-off on its own power. The engine can also be used to extend flights if necessary. The engine-driven propeller is mounted on a pylon and can be deployed from the engine bay as needed.

A new self-launch system is being developed to be incorporated into a high performance sailplane. The radiator plays an integral role to ensure that the engine is adequately cooled. Due to limited space in high performance sailplanes, the components of the self-launch system are located in close proximity to one another. The influence of the different components on the heat transfer capabilities of the radiator needed to be determined. Experimental tests, as well as CFD (Computational Fluid Dynamics) heat transfer and airflow analyses were required to understand how these components influence the heat transfer of the radiator.

Experimental tests were completed on a grounded test bench to characterise the radiator of the self-launch system, and to determine if the engine could be sufficiently cooled by the radiator. The experiments confirmed that the radiator could not deliver satisfactorily cooling to the engine. Propeller static thrust, and radiator pressure drop experiments were also performed to acquire the necessary data for validation and setup of the simplified CFD simulation.

A CFD analysis was performed to investigate the various phenomena of the self-launch system and to acquire a better comprehension of the system. A computationally efficient CFD simulation of the self-launch system was created to assist in making improving alterations to the heat transfer capabilities of the system. The radiator was simulated as a porous medium, and the propeller as a blade element momentum virtual disk. These simplified methods helped to reduce the computational power needed for the CFD simulation.

The CFD simulation revealed that the pylon directed airflow away from the radiator, reducing the airflow travelling through the radiator. A radiator scoop and a pylon fairing were added to the CFD simulation, in an attempt to increase the airflow through the radiator. Both the radiator scoop and the pylon fairing increased the airflow through the radiator by an impressive 25% and 19% respectively. Additionally, the radiator scoop was designed to be uncomplicated, quick and economical to manufacture. It was therefore chosen as the superior concept to be used to reduce the engine temperatures in the final experiments.

The experiments were repeated with the radiator scoop installed in order to determine the improvements made in the heat exchanged by the radiator. It was found that the engine could reach its maximum speed of 6000 rpm without overheating. Without the scoop installed, the system overheated at 5100 rpm. The scoop forced enough air through the radiator to ensure that the engine was adequately cooled when run at full throttle.

All the study's objectives were met and it proved that CFD can be an effective tool to analyse the airflow and heat transfer of a sailplane self-launch system. The study also showed that the CFD simulation can be used to improve systems with complex flow phenomena.

Keywords:
Computational Fluid Dynamics, Heat transfer, Aerodynamics, Sailplane, Radiator, Propeller

Acknowledgement

I would like to thank the following people for their assistance during this study:

- Dr. Johan Bosman, for all the advice and help he provided, and giving me the opportunity to do this study.
- Dr. Jan-Hendrik Kruger, for his valuable support and encouragement, and for sharing his CFD knowledge.
- My wife, Aimee, for her continuous support and encouragement throughout the study.

And lastly the Lord Almighty, for giving me strength to complete the study.

Table of content

LIST OF FIGURES

Tables

NOMENCLATURE

Uppercase Roman Letters:

A	Area	m^2
L	Length	m
U	Velocity	m/s
P	Power	W
Q	Torque	Nm
T	Thrust	N

Lowercase Roman Letters:

c	Chord Length	m
p	Pressure	N/m^2
h	Heat Transfer Coefficient	W/(m²•K)
k	Thermal Conductivity of The Material	W·m⁻¹·K⁻¹
q	Heat Transfer	kW
v	Velocity	m/s

Greek Letters:

α	Angle of Attack	$^{\circ}$ $(degrees)$
ϕ	Inclination	° $(degrees)$
ε	Turbulent Dissipation Rate	
η	Efficiency	
θ	Helix Angle	° $(degrees)$
ρ	Density	kg/m^3
ω	Angular Speed	rad/s
ϕ	Inclination	° $(degrees)$

Subscripted Characters:

c_p	Specific Heat	kJ/kg. ^oC
c_l	2D Section Lift Coefficient	
c_d	2D Section Drag Coefficient	
$\dot{m}$	Mass Flow	kg/s
P_i	Inertial Resistance Coefficient	kg/m^4
P_v	Viscous Resistance Coefficients	kg/m^3s
$\dot{Q}_{\text{conv}}$	Heat Transfer Rate Convection	kW
$\dot{Q}_{\text{cond}}$	Heat Transfer Rate Conduction	kW
T_S	Temperature of The Surface	^{o}C
T_∞	Temperature of The Far Field Fluid	^{o}C

Abbreviations:

BE	Blade Element Method
BEM	Blade Element Momentum Method
BEMD	Blade Element / Momentum Disc Method
CAD	Computer Aided Drawings
CFD	Computational Fluid Dynamics
DNS	Direct Numerical Simulation
LES	Large Eddy Simulations
NACA	National Advisory Committee For Aeronautics
RANS	Reynolds-Averaged Navier-Stokes
rpm	Rotation Per Minute
SLS	Self-Launch System
SST	Menter's Shear Stress Transport
UAG	Global Heat Transfer Coefficient
UAL	Local Heat Transfer Coefficient

Other:

k - ε	K-Epsilon
k - ω	K-Omega
γ − Reθ	Gamma Retheta
ΔP	Pressure Differnce
$\dot{m}$	Mass Flow Rate

1. INTRODUCTION

1.1 Background

A sailplane is a light-weight aircraft designed primarily for unpowered flight. It gains height by utilising thermals and thereafter glides to the desired location. Sailplanes are most commonly used in the sport of gliding and for some military applications.

Sailplane manufacturers are in a continuous drive to deliver versatile and high performance sailplanes. Several sailplane manufacturers offer an optional engine with a retractable propeller. This self-launch system enables the sailplane to take off without any assistance as opposed to the conventional way of using a winch or a tow-plane.

The self-launch systems are designed to be retractable to restore the aerodynamic shape of the sailplane. Therefore, after the sailplane has reached the desired height —using the assistance of the engine— the self-launch system is retracted.

The self-launch system also helps to avoid land-outs and make cross-country flights more practical. This makes gliding more accessible and is, therefore, becoming increasingly popular among the gliding community. Figure 1 shows an example of a sailplane equipped with a self-launch system.

Figure 1: Example of a retractable self-launching sailplane (HPH, 2018)

To be competitive in the sailplane industry, one needs to shorten the development cycle of a sailplane. Virtual computational methods like CFD significantly help to reduce the number of

experiments needed to design a sailplane. By reducing the number of experiments needed, the design cost of the sailplane can be reduced.

1.2 Components and Kinematics of a Self-Launch System

A self-launch system consists of many interdependent components. Failure of one of these components can result in the failure of the whole self-launch system (Greenwell, 2004). The high interdependence between the components makes it challenging to make alterations to a self-launch system. Figure 2 shows the main components of a self-launch system.

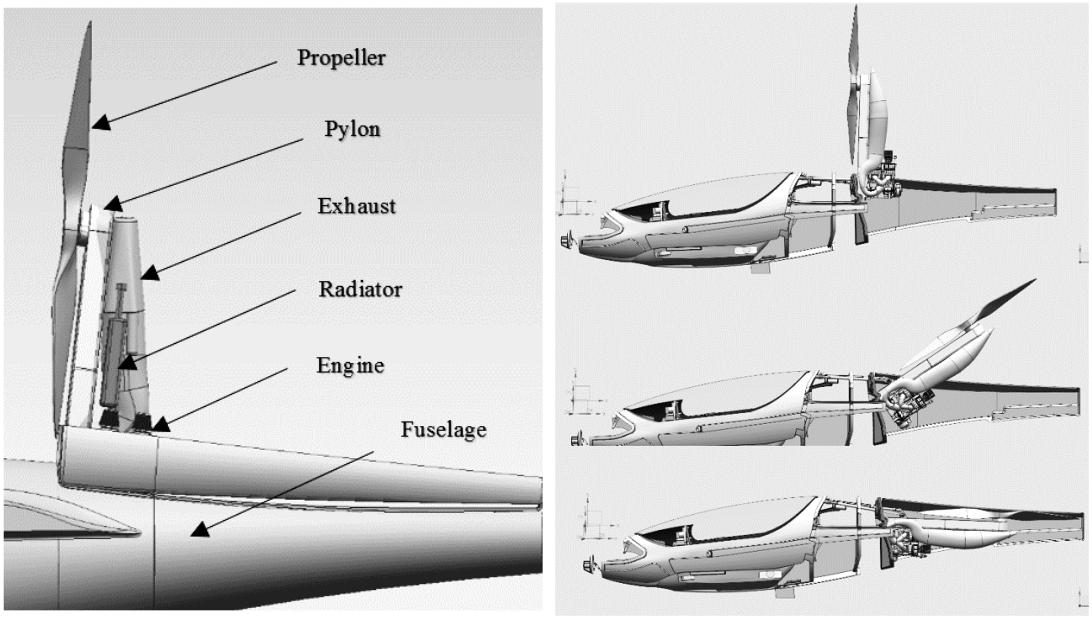

Figure 2: Components of a self-launch system (left). Deployment of the self-launch system (right)

The self-launch system is mounted in the fuselage, behind the cockpit. A linear actuator is used to pull the self-launch system out of the fuselage, as seen in Figure 2. The engine bay doors open and close automatically as the self-launch system extracts or retract. The propeller is driven by a two-stroke engine and connected to the engine by a pulley and belt system.

1.3 Self-Launch Flight Techniques

There are three main types of powered flight techniques used by self-launching sailplanes (Greenwell, 2004). The first technique uses a steady-state cruise, where the pilot is cruising

using the engine for the complete duration of the flight. This technique delivers a limited range as self-launching sailplanes have small fuel tanks due to space constraints.

The second technique involves the sawtooth flight technique, as displayed in Figure 3. This technique of climb consists of using the engine to gain altitude, and then gliding with the engine retracted until a thermal or low altitude is reached. When a low altitude is reached, the self-launch system is started again. This is a very efficient way of flying, and greater distances can be covered using this technique (Sachs *et al.*, 2010).

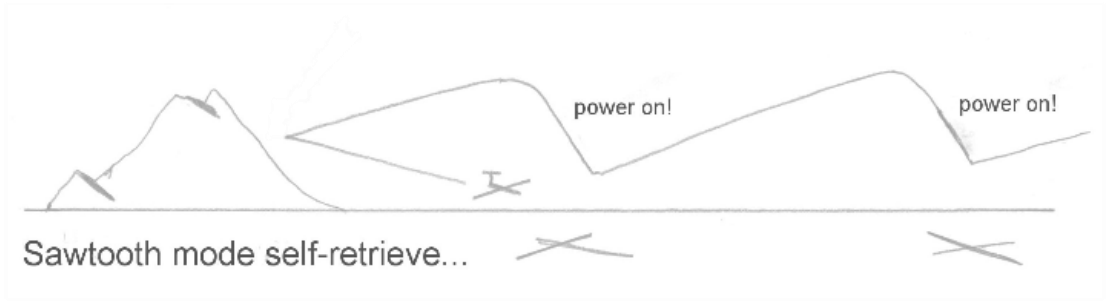

Figure 3: Sawtooth powered flight technique (Greenwell, 2004)

The last type of powered flight techniques consists of only using the self-launch system to avoid land outs where the pilot relies on thermals of lift to glide to the desired location. All three of these techniques require the engine to be operated at high rpm which creates a great deal of heat which needs to be transferred to the environment by the radiator.

A safe height to attempt to start a self-launch system can be difficult to determine. It depends on many factors such as the glide ratio, sink rate, engine reliability, pilot experience, weather conditions and geographical locations. According to Greenwell (2004), a safe height to deploy a self-launch system is at an altitude of 1500 ft. This altitude gives one enough time to act if the engine does not start the first time and to try a few engine restarts. The “windmill” technique is an alternative option to attempt to star the engine. However, a high altitude is needed. This technique consists of performing a nose dive, where the increased airspeed rotates the propeller fast enough to start the engine. When taking off and using a self-launch system, one has to be aware of the conditions. The density altitude and the temperature will have a noticeable effect on the engine performance.

1.4 Effects of Using a Self-Launch System on a Sailplane

When incorporating a self-launch system into a sailplane design, one has to consider the effects it will have on the sailplane. These effects must be taken into account when making changes to the existing self-launch system. The most prominent of these effects are discussed below.

When the self-launch system is deployed, it breaks the streamlined shape of the sailplane and as a result, increases the drag of the sailplane considerably. The increased drag created by the system leads to an increased sink rate of the sailplane. When the engine of the self-launch system fails to start in an emergency deployment, it can become dangerous for the pilot when at low altitude. A DG-1000T self-launch sailplane's sink rate almost increases twofold —from 0.65 m/s to 1.1 m/s— at a speed of 90 km/h, when the self-launcher system is deployed with the propeller not running (Flugzeugbau, 2017). A self-launch system must therefore not be regarded as a life insurance that will give you the needed thrust to gain lift, as engine failures or user errors do occur (Greenwell, 2004).

The position of the propeller from the self-launch systems affects the pitch attitude of the sailplane, as seen in Figure 4. This occurs because of the height difference (moment arm) between the propeller thrust line and the longitudinal axis of the sailplane (Transportation, 2015). The interrupted air behind the propeller also decreases elevator effectiveness.

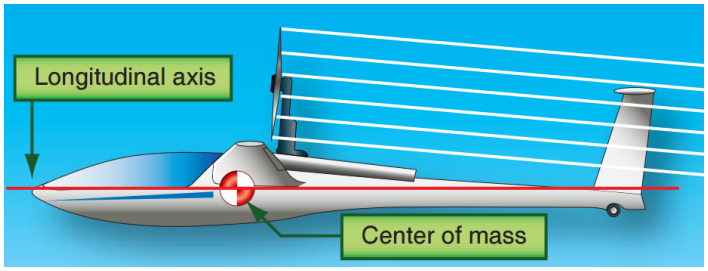

Figure 4: Propeller effect on sailplane pitch attitude (Greenwell, 2004)

The centre of gravity of the aircraft affects the longitudinal static stability of the aircraft. An aircraft is statically longitudinally stable when it tends to return to its trimmed angle of attack, without pilot input, after a disturbance in pitch (Greenwell, 2004). For the sailplane to be stable, one has to ensure that the centre of gravity is in front of the centre of lift. This creates a nose-down force which is balanced out by the horizontal tail, as seen in Figure 5.

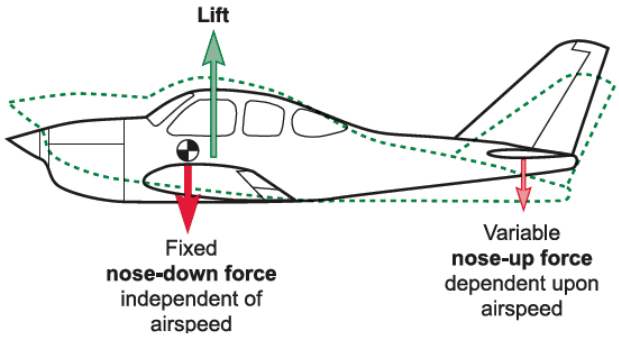

Figure 5: Centre of gravity influence (U.S. Department of Transportation, 2013)

When the self-launch system is incorporated into the fuselage, its added weight shifts the centre of gravity to the rear. By keeping the distance between the centre of gravity and the self-launch system to a minimum, the centre of gravity will not shift too much. If the centre of gravity shifts too far to the rear, the centre of lift and centre of gravity will be too close to each other making the sailplane unsteady (Figure 6). This will make it difficult to recover from a stall or a spin because of insufficient elevator authority (U.S. Department of Transportation, 2013)

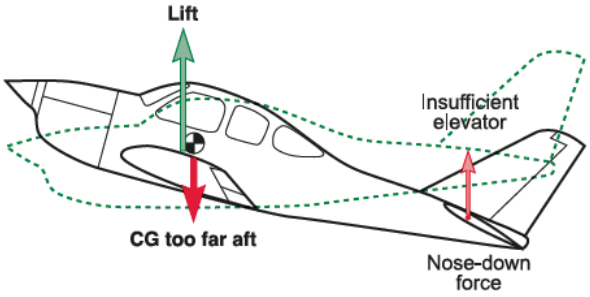

Figure 6: Placment of center of gravity too far aft (U.S. Department of Transportation, 2013)

1.5 Safety

The sport of gliding is fascinating - flying an airplane without an engine - but it can also be a dangerous sport. According to a survey done by the Auxiliary-powered Sailplane Association, where 47 self-launching sailplane pilots participated in, includes the following the following incidents occurred (ASA, 1998):

- 15 extraction/retraction failure of the self-launch system
- 13 engine power loss or engine failure
- 13 unsuccessful engine starts in the air
- 15 windmill engine starts
- 23 landings with the engine out and not running

As seen in the incidents above, the probability of encountering a problem when using a self-launch system does exist. A failed engine start may occur due to faults in the spark plugs, carburettor, starter, low battery voltage, ignition system or wiring. Therefore one must not become too dependent on the self-launch system. It should always be deployed at a safe altitude, and the pilot should be aware of when to abort trying to start the engine.

To ensure the safety of the pilot and airworthiness of an airplane, several airworthiness code came to existence. For this particular sailplane with a self-launch system incorporated, the sailplane must adhere to the European Aviation Safety Agency CS-22 airworthiness code. This code applies to sailplanes and powered sailplanes where the weights of the sailplanes are 750 kg or less, has no or only a single engine and a maximum of two occupants (EASA, 2009).

1.6 Problem Definition

A new self-launch system is being developed to be incorporated into a high-performance sailplane. During a self-launch take-off, or in the event of avoiding a land-out, the pilot must be able to rely on the engine to gain altitude for safety reasons. A substantial amount of heat is generated when the engine is running at high rpm.

The radiator plays a vital role in the self-launch system to ensure that adequate cooling of the engine is obtained. The heat transfer capabilities of the radiator needs to be established, to ensure that the radiator could sufficiently cool the engine. The space in the engine bay of the high performance sailplane is very limited. Due to space constraints, the components of the self-launch system are located in close proximity to one another. The influence of the different components on the heat transfer capabilities of the radiator need to be determined. Examples of these phenomena include; the effect of the disturbance created by the propeller in the flow-field of the radiator, the location of the radiator relative to the pylon and propeller, and the wake created by the pylon in front of the radiator.

An in depth airflow and heat transfer analysis was needed to determine the aforementioned effects on the heat transfer capabilities of the radiator. To analyse the complex 3D flow effects, tool such as CFD codes are required for visualisation and calculation purposes. Finding an effective layout for the self-launch system, by blindly making numerous alterations to the system requires an excessive amount of experiments to determine the influence of the design changes. This process is expensive and time-consuming and does not guarantee a safe nor optimal solution.

1.7 Goal and Objectives of the Study

The goal of this study is to analyse and improve the heat transfer of a self-launch sailplane radiator using a validated CFD-based airflow and heat transfer analysis. The objectives of this study include the following:

- To determine the heat transfer of the radiator used in the self-launch system, both experimentally and by means of numerical simulation.
- To develop a computationally efficient CFD simulation which can assist in making design decisions
- To validate CFD results with experimental data obtained from a ground test rig
- To use CFD to analyse the influence of the heat exchange capabilities of the radiator, pertaining to the following parameters:
    - The wake of the propeller
    - The position of the radiator
    - The airflow through the radiator
- To ensure that adequate cooling of the engine is obtained

1.8 Thesis Layout

Here follows a short description of the chapters included in this study:

1. **Introduction**: The first section contains background information concerning this study, as well as addressing the needs of the study.
2. **Literature Study**: In section two, the related research regarding this study has been explored.
3. **Experimental Tests**: All the experimental test setups are presented, and the results are discussed.
4. **CFD Validation and Analysis**: Section four concern the validation and analysis of the CFD simulation.
5. **Radiator Heat Exchanger Improvements**: In section five, different concepts to improve the cooling capacity of the radiator are explored.
6. **Conclusion**: A conclusion is made concerning the objectives of the study as well as recommendations for further work.

2. LITERATURE STUDY

The literature survey mainly focuses on research concerning the modelling of heat exchangers using CFD. In addition, the fundamental principles concerning heat exchangers, propellers, aerodynamics and CFD are also briefly discussed.

2.1 Heat Exchangers

Heat exchangers are used in almost all engineering applications, ranging from internal combustion engines to power stations. To understand how to characterise a radiator, one needs to understand the basic principles of a heat exchanger.

2.1.1 Basic Principles of a Heat Exchanger

A heat exchanger works by separating two fluids at different temperatures, with the aid of a solid wall. As a result of the difference in the temperature of the fluids, heat exchange will take place (Bergman *et al.*, 2011). The three most common configurations of heat exchangers are concentric, shell-and-tube and cross flow. The cross flow configuration is most commonly used in the aircraft and automotive industry, due to its high effectiveness (Figure 7).

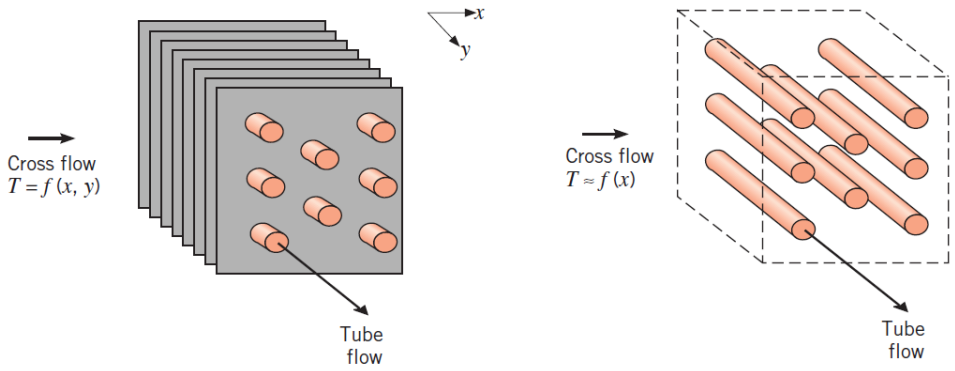

Figure 7: Cross flow heat exchangers (Bergman *et al.*, 2011)

The heat transfer capabilities of a heat exchanger can be improved by utilising fins. The fins increase the effective surface area of the radiator, thus increasing its heat transfer capabilities. Compact heat exchangers utilise a large number of fins to increase the surface area per unit volume, thus, resulting in a dense array of fins surrounding the tubes of the radiator.

When considering to add fins to a radiator, one should take into account the conduction resistance added by the fines, as well as the rise in pressure drop over the radiator (Bergman *et al.*, 2011). By evaluating the effectiveness of the fins, one can make an informed decision whether or not fins should be added to the radiator.

The cooling system used on the self-launch system consists of a compact air-to-liquid heat exchanger. The coolant is circulated through the system using a centrifugal pump. The coolant in the engine block absorbs the heat discharged by the engine. The hot coolant flows through the radiator and heat is transferred to the air. The cold coolant exits the radiator and cools the engine as it enters the engine block. The radiator used in the self-launch system has a double pass flow configuration and uses high density louvre fins between the coolant tubes (Figure 8).

Figure 8: Double pass radiator used in the self-launch system.

2.1.2 Heat Transfer

Heat transfer can be described as a process where thermal energy travels from one point to another due to the difference in temperatures (Bergman *et al.*, 2011). There are three different types of heat transfer, namely convection, conduction and thermal radiation

Convection takes place when a temperature difference exists between a surface and a moving fluid. Fluid motion is needed for convection to take place, as only conduction will take place when the fluid is static. Newton's law of cooling defines convection in equation 1.

$$\dot{Q}_{conv} = hA_S(T_S - T_\infty) \quad \ldots 1$$

Where $\dot{Q}_{\mathrm{conv}}$ is the heat transfer rate, h the heat transfer coefficient, A_S the surface area, T_S the temperature of the surface and T_∞ is the temperature of the fluid far away from the surface.

Conduction can take place in a solid or fluid that is in a stationary state where a temperature difference is present. Fourier's law describes conduction in equation 2

$$\dot{Q}_{cond} = kA\frac{dT}{dx} \quad \text{...2}$$

Where $\dot{Q}_{cond}$ is heat transfer rate, k the thermal conductivity of the material, A is the area of the body and $\frac{dT}{dx}$ is the gradient of the temperature.

Lastly, thermal radiation takes place between any two surfaces that have a difference in temperature (Bergman *et al.*, 2011). Electromagnetic waves transfer the heat between the surfaces and can take place in a vacuum.

In a radiator, heat transfer mainly takes place through convection and conduction. Convection takes place between the airflow and the radiator finned tubes, and also between the tubes and moving water within the radiator. Conduction takes place through the metal of the finned tubes of the radiator.

An understanding of how energy is transferred between a heat exchanger and a system, is provided by the first and second laws of thermodynamics.

The first law of thermodynamics states that the total energy of a system will remain constant (Borgnakke & Sonntag, 2010). Changes in the amount of energy of the system can only take place if energy crosses the boundaries of the system. These changes in energy can take place when work is done by or on the system, as well as when heat transfer takes place through the boundaries.

The second law of thermodynamics can be expressed in several ways. The Kelvin-Plack statement states; it is impossible to build a device that operates in a thermodynamic cycle, and is capable of converting all the heat from a high-temperature body into work (Bergman *et al.*, 2011). An amount of the heat must be exhausted into the low-temperature body (such as a heat exchanger) a certain rate (Figure 9).

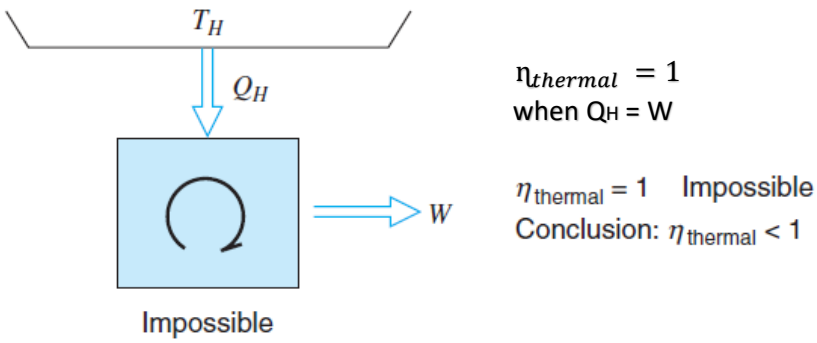

Figure 9: Second law of thermodynamics (Bergman *et al.*, 2011)

To determine the heat transfer capabilities of a heat exchanger, one must be able to calculate the amount of heat transferred by the heat exchanger. A number of parameters need to be measured in order to determine the heat transferred by the heat exchanger. The parameters include:

- Coolant mass flow
- Inlet and outlet coolant temperatures
- Air mass flow
- Inlet and outlet air temperatures

2.1.3 Modelling Heat Exchangers in CFD

The geometry of a heat exchanger can contain intricate details which require a highly detailed mesh, consisting of a large number of cells. To reduce the computational power required, the geometry can be modelled as a simplified porous block region with empirical coefficients that describe the viscous and inertial flow characteristics. By measuring the pressure drop across the radiator at different velocities, one can obtain these coefficients by fitting a quadratic regression curve over the data (CD-Adapco, 2018). The porous inertial resistance as well as the viscous resistance is then represented by the coefficients a and b in equation 3

$$\Delta P = aU^2 + b\mathrm{U} \quad \text{... (3)}$$

Where ΔP is the pressure drop over the radiator, U the velocity of the air, a the porous resistance coefficient and b the viscious porous resistance coefficient .

Star CCM+ has a number of different types of interfaces that can be used to model the transport of phenomena between regions in the numerical domain. One of these interfaces is a heat exchanger interface that models heat transfer between a hot and cold fluid (CD-Adapco, 2018). The heat exchanger interface can consist of a single or dual stream configuration. In the single stream configurations, only one fluid is modelled and the second stream is assumed to be at a

uniform temperature. The dual system configuration explicitly models both steams and creates a heat transfer interface between the two overlapping regions (Figure 10).

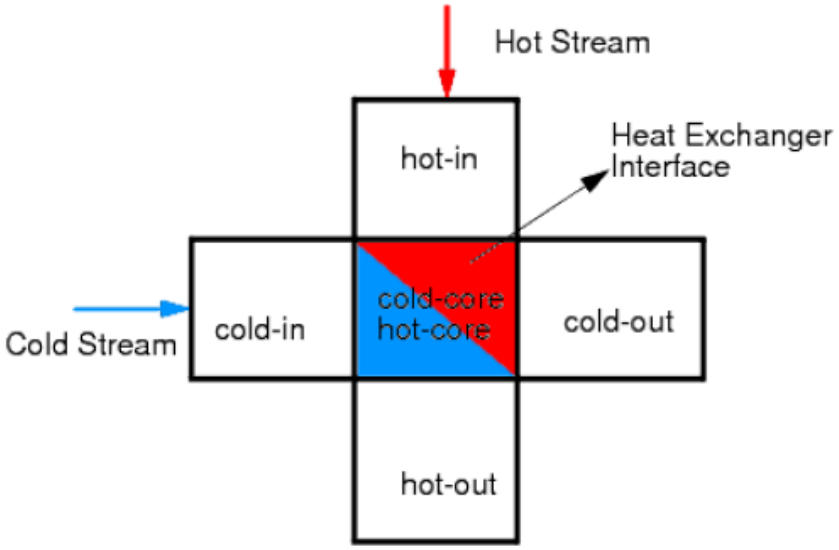

Figure 10: Heat exchanger interface layout (CD-Adapco, 2018)

Heat transfer between the cells, within the heat transfer interface, takes place by adding a local energy source or sink term to the fluid energy equation, used by the simulation. Star-CCM+ uses a local heat transfer coefficient (UAL) to calculate this local energy source. The UAL can be defined in different combinations that uses velocities, mass flow rates and the overall heat transfer of the system, which is typically obtained through experimental measurement.

The UAG (heat transfer coefficient) can be defined by varying the cold fluid stream of a system for a constant hot fluid stream. The UAG value is then converted into the UAL that can be used by the heat exchanger model to transfer heat within the system.

2.1.4 CFD analyses on Heat Exchangers

A literature review has been done to investigate how heat exchangers are simulated in CFD, how experimental tests are done and how different parameters influence the performance of a radiator.

Čarija and Franković (2008) did a study on the heat exchange and airflow through a fin-and-tube heat exchanger. The characteristics of the radiators were compared with different fin configurations. The heat exchange of the radiator was calculated using CFD. Due to the periodic

and symmetric nature of the geometry of the radiator, the CFD domain consisted of a section cut of the radiator (Figure 11).

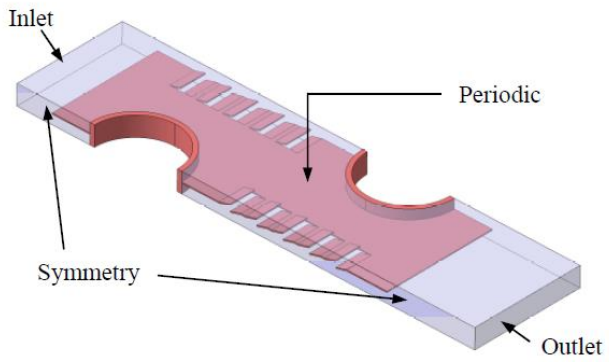

Figure 11: Radiator section cut (Čarija & Franković, 2008)

By using only a section cut of the radiator, the computational power required was reduced by a large extent. A trimmed volume mesh with prism layers was used, consisting of almost 300 000 cells. The simulation assumed laminar airflow over the fins in a steady state condition. The air was simulated as an ideal gas.

The pressure drop over the radiator was used to validate the CFD results. It is common to use the pressure drop for validation, as it is easy to measure. The CFD results compared well with the experimental results, all within 10%. It was concluded that the louver fin configuration significantly increases the heat exchange capabilities of the radiator.

Kang *et al.* (2004) simulated a number of radiators with louver fins at different angles. The airflow over a small section of each radiator was simulated, and the porous coefficients were determined. The radiator was then simulated as a porous block using the porous coefficients. By using a porous model to represent the radiator, the simulation time was reduced.

The CFD mesh consisted of a tetrahedral and hexahedral mesh. A relative error of 6.94% was obtained on the coolant outlet temperature. It was found that the radiator with an angle of 23° at a spacing of 1.4 mm, yielded the best cooling performance out of all the tested radiators.

Junjanna *et al.* (2012) performed a numerical study on a heat exchanger. CFD was used to analyse changes made in the flow parameters and the geometry of the radiator. The computational domain was confined to one fin and pipe pitch, due to the symmetric nature of the radiator (Figure 12).

Different turbulence models were considered, and it was found that the k-ω turbulence model was the most suitable model to use for simulating the heat exchanger. This was due to the ability of the model to capture large fluid strains accurately. A tetrahedral mesh consisting of 1.5 million cells was used. The boundaries that were implemeted in the computational domain can be seen in Figure 13, which includes various solid surfaces, air and water inlets and outlets.

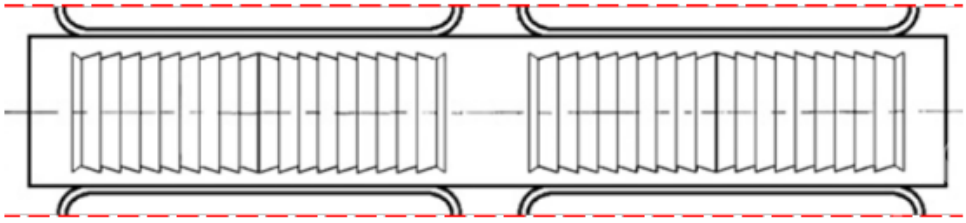

Figure 12: Periodic flow domain (Junjanna et al., 2012)

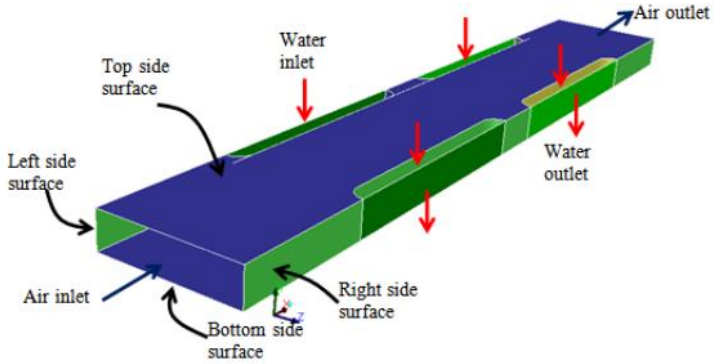

Figure 13: Boundaries of the computational domain (Junjanna et al., 2012)

The results of the CFD simulation proved to be in good agreement with the experimental data. It was found that by increasing the flow rate of the air, a prominent increase in the heat transferred was observed. An increase in the water flow rate showed an increase in the water outlet temperature and a decrease in the outlet air temperatures. This increase in the outlet water temperature was due to the decreased time the water and air had to transfer heat, as a result of the increased water flow.

A parametric study on automotive radiators was done by Oliet *et al.* (2007). The influence of different parameters on the heat exchange capabilities of the radiators was analysed. Figure 14 shows how the mass flow of the air and coolant influenced the cooling capacity of the radiator. It was found that the cooling capacity was more dependent on the mass flow rate of the air, when compared to the flow rate of the coolant. This occurred because the air has a higher thermal resistance than that of the coolant.

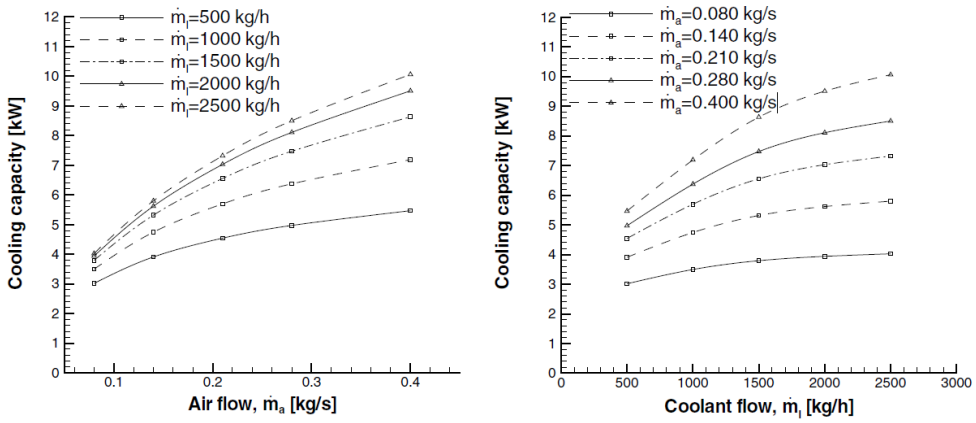

Figure 14: Influence of the mass flow of the air and coolant on the performance of a radiator (Oliet *et al.*, 2007)

The experimental tests revealed that water was the most efficient coolant used in the tests and that adding ethylene glycol or propylene glycol decreased the cooling capability of the radiator.

The influence of different inlet air temperatures of the radiator was also studied. It was observed that a noticeable decrease in the cooling capacity of the radiator was obtained when the inlet air temperatures of the radiator were increased.

Recently, the thermal balance of a vehicle engine bay was investigated by Lidar (2018) using CFD. The CFD simulation was based on a steady state Reynolds-Averaged Navier-Stokes approach, and the SST $k-\omega$ turbulence model was used.

The radiator of the vehicle was simulated as a simplified porous block. The model was created in Star CCM+ and a dual flow heat exchanger interface was used to simulate the heat transfer of the radiator. The inlet temperature and mass flow rate of the coolant were set equal to that of the experimental values. The local heat transfer coefficients needed by the heat exchanger interface were calculated by creating a local heat transfer polynomial. The polynomial was adjusted until the coolant outlet temperature was equal to the value measured during the experiment.

The mesh consisted of polyhedral and prism layers, and consisted of 57 million cells. Due to the size and complexity of the geometry and the physics, the complexity of the simulation was gradually increased. The heat exchanged by the radiator was initially overpredicted by the CFD

simulation and the local heat transfer polynomial was then adjusted to deliver a more accurate heat transfer prediction.

Kim *et al.* (2014) conducted experiments to characterise the heat exchange performance of heat exchangers having oval tubes. Figure 15 shows a detailed diagram of the experimental setup that was used. The heat exchanger was placed inside a suction-type wind tunnel, with a constant temperature and humidity chamber. A water pump circulated the flow between the radiator and a constant temperature bath. The temperatures of the water and air were measured by resistance thermometers. The pressure drop over the radiator was measured using a pressure transducer, and the airflow was measured using a nozzle pressure difference.

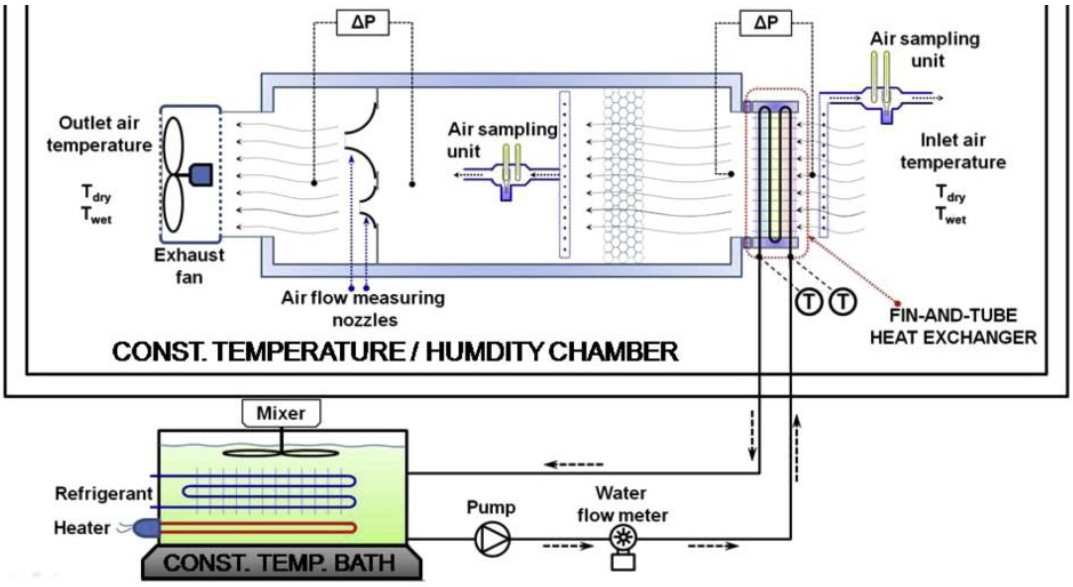

Figure 15: Experiment setup (Kim *et al.*, 2014)

The experiments showed that the oval tubes delivered a smaller heat transfer coefficient, as well as a smaller pressure drop when compared to round tubes. Changes made to the fin pitch of the oval tube had an insignificant effect on the *j* and *f* factors of the heat exchanger.

Ng *et al.* (2001) measured the local timed-average airflow velocity through the radiator of a car. The air velocity through the radiator was determined using the pressure drop over the radiator. Measuring the velocity through the radiator was a challenging and expensive experiment. The measured velocity showed a complex and non-uniform airflow through the radiator. A total of 24 pairs of pressure tubes were used to capture the pressure distribution through the radiator and the velocity field was then determined from that by using a pressure

drop correlation. The non-uniform airflow through the radiator was mainly due to the wake created by the bumper bar in front of the radiator.

Figure 16 and Figure 17 show a visualisation of the airflow behind the radiator using wool tufts and smoke trace, respectively.

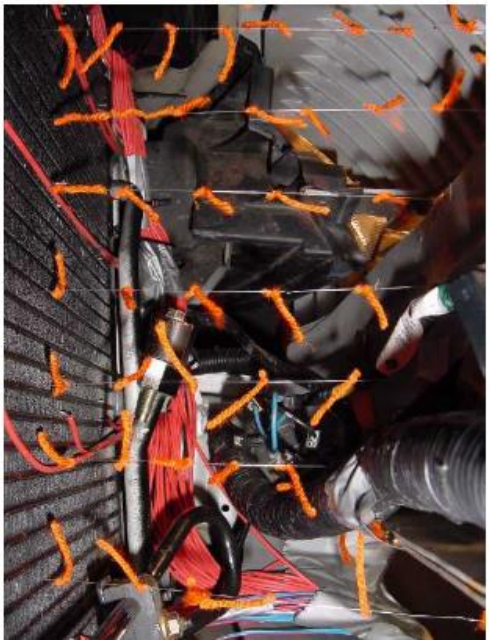

Figure 16: Flow visualisation behind the radiator (Ng et al., 2001)

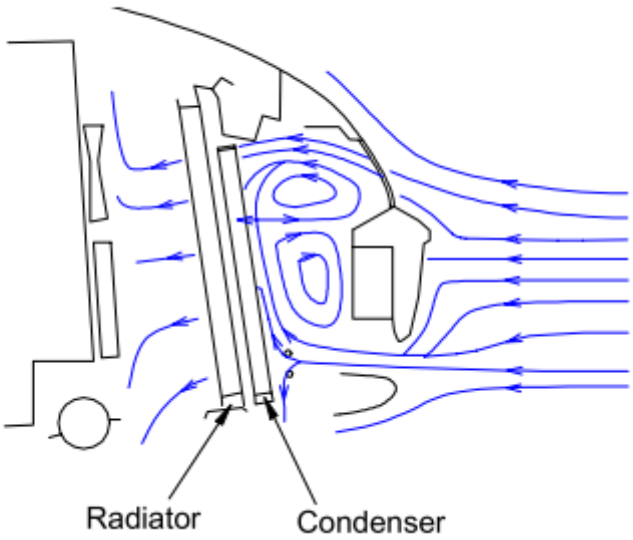

Figure 17: Smoke trace flow visualisation behind the radiator (Ng et al., 2001)

The 24 pressure data points were interpolated over the face of the radiator, and the resultant flow distribution can be seen in Figure 18. A highly non-uniform velocity field was measured with a three-fold increase between low velocity and high velocity regions. This will off course also impact the heat exchange properties of the radiator and highlights why accurate flow distribution information is needed.

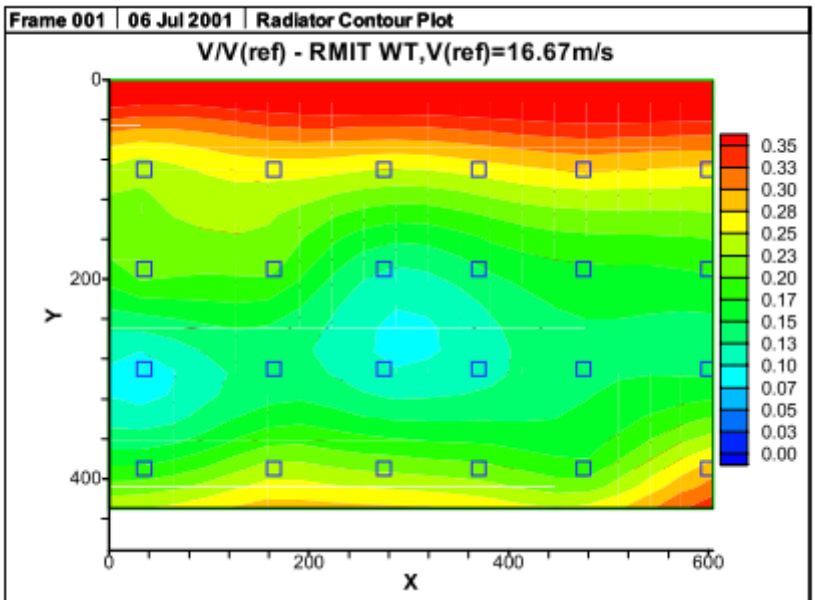

Figure 18: Velocity profile of the air on the face of the radiator (Ng et al., 2001)

2.2 Propellers

A propeller is a device that delivers force by converting mechanical energy into thrust, which can propel an object attached to the propeller (Gudmundsson, 2013).

2.2.1 Basic Principles of a Propeller.

A propeller consists of several airfoil sections that can have a variation in cord length and twist along the blade of the propeller. The propeller is rotated at a rapid rate. A lift force, similar to that of a wing, is created. A CAD model of the propeller used in the self-launch system can be seen in Figure 19.

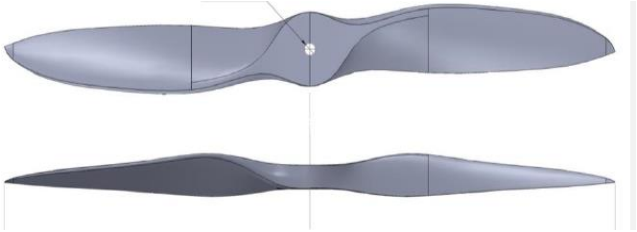

Figure 19: A CAD of the propeller used by the self-launch system

Propellers are usually designed for a specific airspeed. Low speed operations typically require a low pitch, whereas high speed operations require a larger pitch (Gudmundsson, 2013). A fixed-pitch propeller has fixed blade pitch angles that cannot be altered. A fixed-pitch propeller is inexpensive and light, but has only a small range in airspeed where the efficiency of the propeller is adequate.

A variable pitch propeller has a changing pitch distance which changes span wise of the propeller. In Figure 20 the geometry of a fixed pitch and variable pitch propeller are compared.

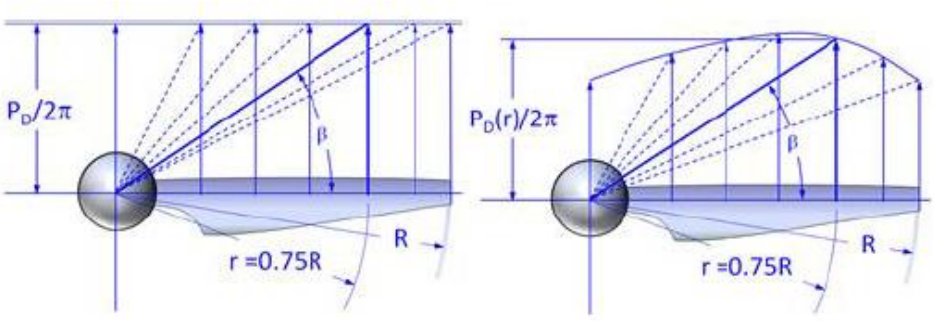

Figure 20: Geometry of a fixed and a variable pitch propeller (Gudmundsson, 2013)

Constant pitch propellers are heavier and more expensive than fixed pitch propellers. The airspeed range which provides a high propeller with efficiency is a great deal larger when

compared to fixed pitch propellers (Figure 21). A governor utilises flyweights and throttles the fuel setting to keep the rpm of a propeller constant.

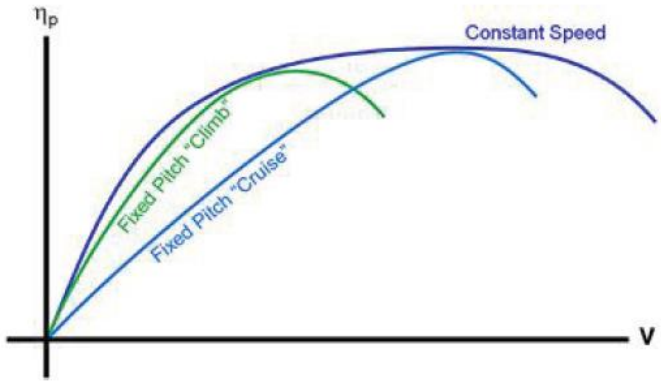

Figure 21: Efficiency of different propellers (Gudmundsson, 2013)

2.2.2 Propeller Performance

The blade element theory was first developed by Stefan Drzewiecki who used airfoil theory to determine the thrust delivered by a propeller (Monk, 2010). Blade element theory estimates the thrust created by the propeller, by dividing the propeller into sections that are treated as independent two-dimensional airfoils. Aerodynamic forces are then locally determined at each section and summed up to determine the aerodynamic forces of the whole propeller (Gudmundsson, 2013). The BEM does not explicitly take into account the lift weakening at the tip and hub of the propeller, where Prandtl's tip and hub loss corrections are used to estimate these losses.

The momentum theory, also known as the disk actuator theory can also be used to determine the performance of a propeller. This mathematical model can estimate the induced velocity of the propeller (Gudmundsson, 2013). The model represents the propeller as an infinitesimally thin actuator disk where the air can pass through without resistance (Figure 22). The flow passing through the disk is uniform, and the far field streamlines in front and behind the propeller, are parallel. The model assumes the flow to be inviscid and incompressible with no rotational flow.

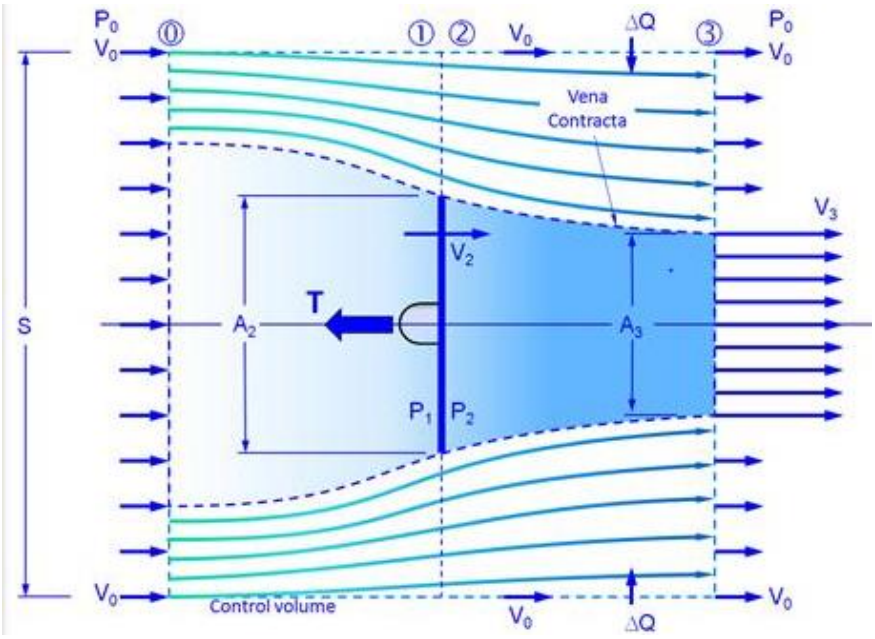

Figure 22: Momentum theory model (Gudmundsson, 2013)

Being able to estimate the induced velocity of the propeller, enables one to determine the resulting change in the angle of attack used by the BEM method. By using the BE method in conjunction with momentum theory, improved results can be obtained for design purposes.

2.2.3 Modelling Propellers in CFD

A number of numerical methods exist to analyse the performance of a propeller in Star CCM+. The most relevant methods concerning this study are discussed below.

2.2.3.1. Actuator Disk / Virtual Disk

A rotating object can also be modelled as a Virtual disk in CFD. The rotating object is simulated as an actuator disk. The motion of the propeller is represented as a source term, which is used in the momentum equation of the simulated domain (Monk, 2010). It is not necessary to include the geometry of the rotating object when using the virtual disk model. The lack of necessity in meshing the propeller, decreases the number of cells in the mesh and as a result, decreases the computational power needed. The virtual disk model can utilise BEM theory to determine the performance of propeller where the BEM method can capture the wake structure of the propeller well enough to make design decisions (CD-Adapco, 2018). The model is a cost-effective and dependable model to use when simulating a rotating propeller.

2.2.3.2. Constant Rigid Motion

A rotating object can be modelled in CFD by rotating the cell vertices of the mesh. This can be applied only in a transient analysis where the mesh is rotated a fixed amount for each time step. The rotating body is rigid with no deformation during rotation. This method of modelling a rotating object is the most accurate method, but also requires the most computational power (Reynolds, 2018).

2.2.3.3. Rotating Reference Frame

A rotating reference frame can be used to simulate a rigid rotating object in a steady state simulation. The induced forces created by the rotating object are implemented without explicitly rotating the cell vertices of the mesh and thus provides one with a time-averaged representation of the rotating object's flow. The rotating reference frame delivers a good balance between computational cost and accuracy.

2.2.4 The Simulation of Propellers

A literature review has been done to investigate how propellers are simulated in CFD.

Kutty and Parvathy (2017) did a study on numerical methods to predict the performance of a propeller blade. CFD was used to simulate the rotating propeller as a rotating reference frame. The domain consisted of a stationary and a rotating region enclosing the propeller (Figure 23). The flow between the two regions was connected with interfaces. The boundaries of the domain were created far enough from the propeller to ensure that the fully developed flow of the propeller would not influence the results.

The mesh used in the simulation domain consisted of a mesh consisting of 4 million cells. Three different turbulence models were used, namely standard $k-\varepsilon$, k - ω, SST k - ω. The torque and power coefficients obtained from experimental results were used to validate the CFD simulations. The different turbulence models delivered very similar results. The SST k - ω turbulence model was judged to be the most suitable turbulence model to simulate the propeller, as it has the ability to capture transitional flow well. The results were compared with experimental results and proved that the simulations were capable of providing reliable results. Lidar (2018) also successfully used a rotating reference frame in a similar manner to simulate a rotating fan of a radiator.

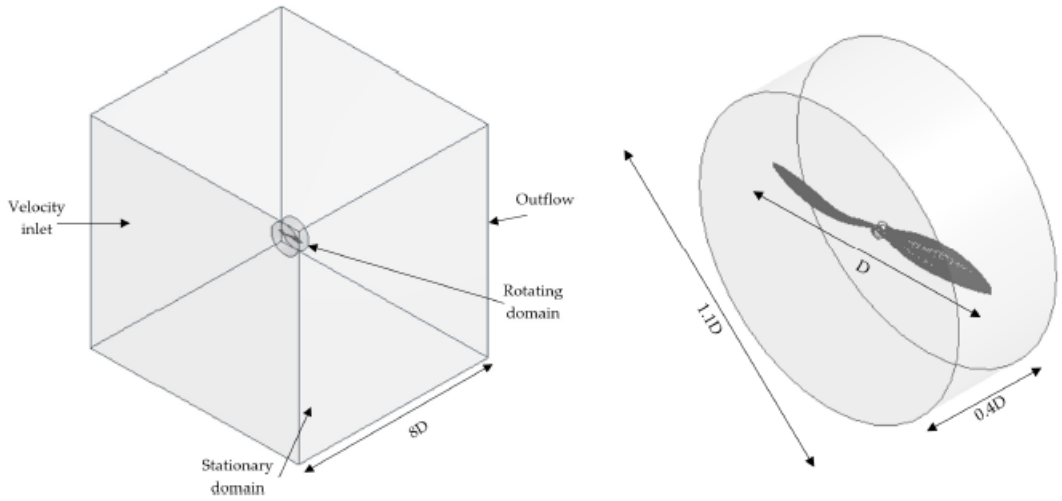

Figure 23: Propeller domain (Kutty & Parvathy, 2017)

The accuracy of a CFD model coupled with BEM theory was tested by Guo *et al.* (2014). The CFD modelled the flow of a marine current turbine. The turbine was simulated using a rotating reference (with the full geometry of the propeller captured in the mesh) and a BEM-CFD model, respectively.

A steady-state RANS solution was used for both the BEM-CFD and rotating reference model. Figure 24 shows the geometry of the computational domain. The mesh consisted of 1.2 million nodes. Figure 25 shows the mesh generation in the ZX plane.

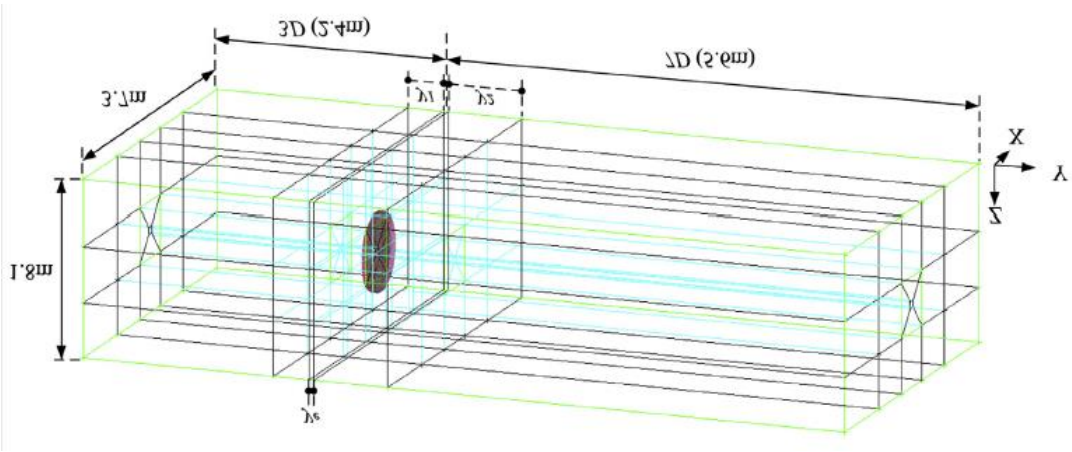

Figure 24: Computational domain of turbine (Guo *et al.*, 2014)

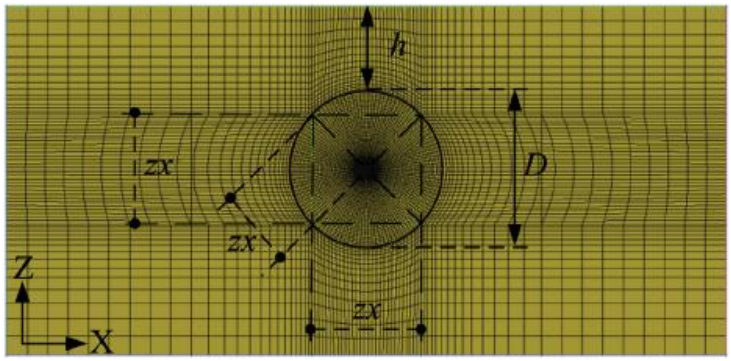

Figure 25: Mesh of flow domain (Guo *et al.*, 2014)

In Figure 26 one can see the BEM-CFD method compared to the experimental data and the full rotor CFD model. Note that BEM-CFD N refers to C_l and C_d values obtained numerically using XFoil. BEM-CFD E refers to C_l and C_d values obtained from experimental data.

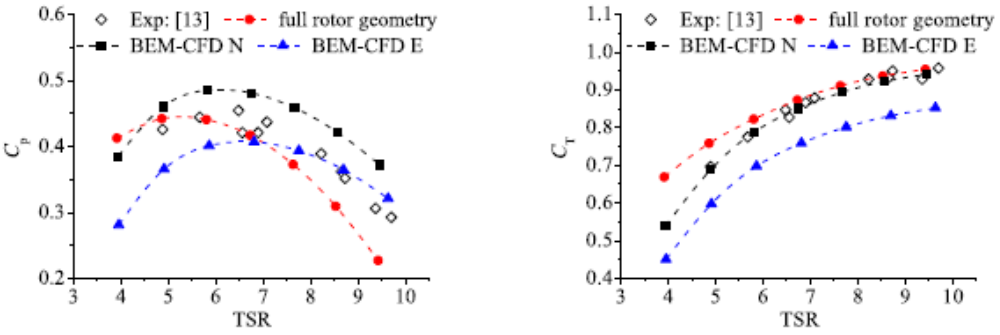

Figure 26: Propeller coefficients comparison (Guo *et al.*, 2014)

Figure 27 shows both the δC_p values of the BEM-CFD model and the full rotor geometry model.

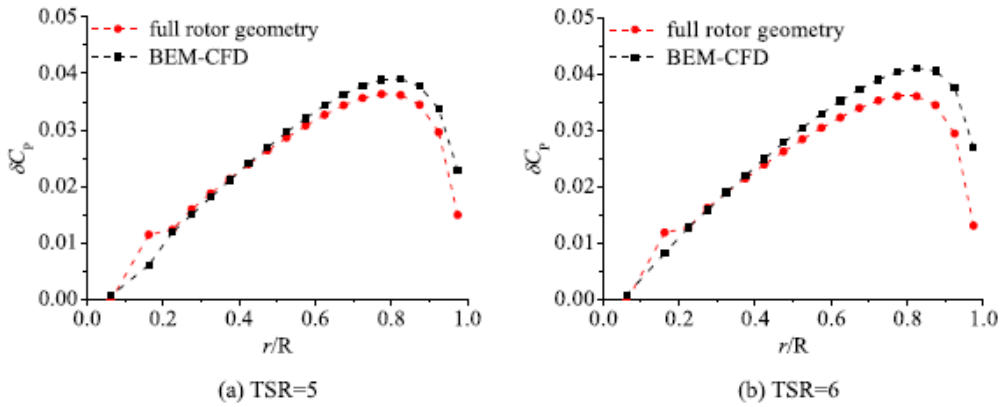

Figure 27: Radial variations of dCP (Guo et al., 2014)

It was found that that the C_l and C_d values used in the BEM-CFD model had a noticeable effect on the thrust and power coefficients predicted for the propeller. A difference in these values was noted when the C_l and C_d values were obtained numerically using XFoil and experimentally (by using a wind tunnel).

The BEM-CFD N method was successful in predicting the thrust of the rotor accurately but overpredicted the power of the rotor. BEM-CFD E method underpredicted the thrust of the rotor but was more successful in predicting the power of the rotor at higher tip speed ratios. The rotor geometry and BEM-CFD dCP values compared well at lower radial lengths.

A tidal turbine was simulated by Malki *et al.* (2012) using a CFD BEM method. The domain consisted of a trimmer mesh with 250 000 cells. The domain can be seen in Figure 28. It was found that the CFD BEM method needed notably less computational power when compared to other CFD simulations.

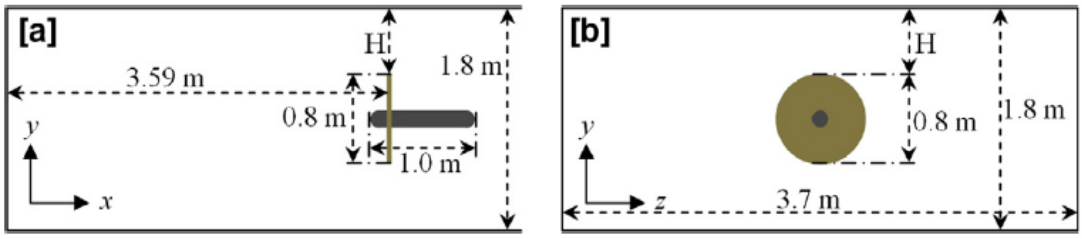

Figure 28: Computational domain of the tidal turbine

The CFD simulation was validated with experimental data obtained from Bahaj *et al.* (2006), and results obtained from a classic blade element model. The results obtained by the CFD simulation compared well with the aforementioned. It was found that the classic BE method had a few shortcomings when compared to the CFD-BEM method, beacause the classic BE method relies on the various empirical corrections and does not resolve local flow around the propeller.

Rao and Sahitya (2015) completed a numerical and experimental study on the lift and drag coefficients of a NACA 0012 airfoil. A low speed, open circuit wind tunnel was used to complete the experimental tests. The airfloil was tested at an angle of attack ranging from -20° to 20°, with increments of 2°. A two-dimensional quadratic mesh consisting of 80 000 elements was used by the CFD simulation (Figure 29).

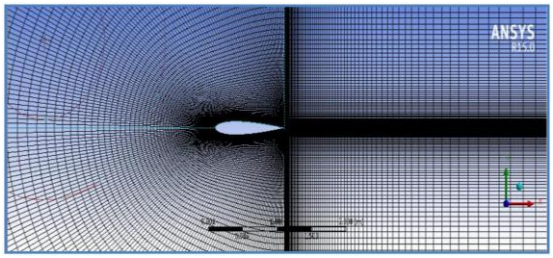

Figure 29: The two-dimensional quadratic mesh used by the CFD simulation

Two Reynolds-averaged turbulence models namely, *k* - ω and Spalart-Allmaras were used to simulate the airflow over the airfoil. The lift and drag coefficients of the airfloil were measured in the experiments and by means of CFD simulation. A comparison was made between the results obtained by the experimental tests and CFD simulations.

If was found that both the *k* - ω and Spalart-Allmaras predicted the lift coefficient particularity well at angles of attack lower than the stall angle. At the stall angle both the *k* - ω and Spalart-Allmaras models overpredicted the lift. The *k* - ω model showed a superior similarity towards the experimental results when compared to the Spalart-Allmaras.

The drag coefficient was in agreement with the turbulence models, but near the stall angle the drag was overpredicted by both models. The overprediction in the drag was due to the inability of the turbulence models to simulate transition in the boundary layer from laminar to turbulence flow. The total length of the boundary layer was simulated to be turbulent, as opposed to the actual airfoil having a laminar flow over the first half of the airfoil. It was concluded that the *k* - ω SST model was more accurate when compared to the Spalart-Allmaras model.

2.3 Aerodynamics

A basic understanding of aerodynamics is needed to enable one to set up an accurate CFD simulation, capable of capturing the interaction between fluids and bodies.

2.3.1 Boundary Layers

A boundary layer consists of a very thin layer adjacent to the surface of a moving body. Directly next to the surface of a moving body, the velocity of the particles is zero. The velocity increases as one moves away from the body until it reaches a velocity equal to the free stream (Anderson, 2001). The boundary layer that develops can consist of two stable states; a laminar boundary layer or a turbulent boundary layer. The type of boundary layer that develops on the surface of

a moving body, has a substantial effect on the drag the body experience, as well as on the size of the wake that is formed.

A laminar boundary layer consists of an orderly and steady flow where the particles flow in parallel lanes. The ordered nature of a laminar boundary layer makes it possible to be calculated mathematically and when compared to a turbulent boundary layer, it produce smaller drag counts. A laminar boundary layer gradually degrades as it increases in thickness, until a transition into a turbulent boundary layer takes place (McCormick, 1995).

A turbulent boundary layer can be seen as an irregular and erratic flow. To estimate the behaviour of this flow, empirical data is required (Schlichting, 1973). Figure 30 compares the velocity profile of a laminar and turbulent boundary layer, where one can see a superior rounded curve in the velocity profile of the turbulent boundary layer. The rounded curve indicates that the near wall particles contain more energy when compared to the flatter velocity profile of the laminar boundary layer (Munson *et al.*, 2010).

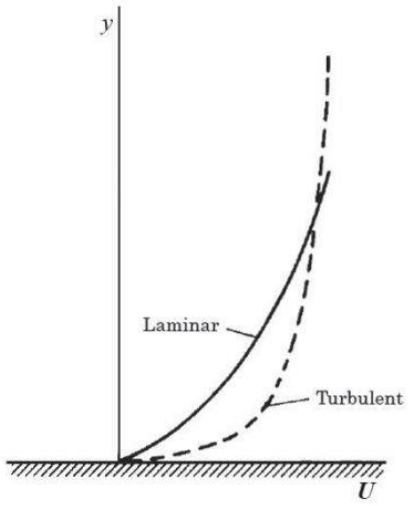

Figure 30: Turbulent and laminar boundary layer (Munson *et al.*, 2010).

The increased energy in the velocity profile of the turbulent boundary layer increases its stability and decreases its sensitivity to adverse pressure gradients. The increased energy in the velocity profile increases shear force. A turbulent boundary layer can be utilised to delay or eliminate the flow separation that can significantly reduce the wake and drag of a moving object.

2.3.2 Flow Separation

When the boundary layer of a fluid travels along an adverse pressure gradient, the shear stress due to viscosity retards the flow. The retarding effect is stronger near the surface where the flow is further away from the acceleration of the mainstream (Houghton & Carpenter, 2003). A point downstream is reached where the gradients of the velocity and the shear stress become zero and flow separation takes place (Munson *et al.*, 2010). Behind the point of separation, the direction of the flow near the surface reverses and a region of recirculation flow forms.

As a result, the flow can detach from the body and a region of highly retarded flow, also known as a wake, forms behind the body. Flow separation increases the size of the wake created by the body and as a result, increases form drag.

2.3.3 Drag

Drag is a force that is generated in the opposite direction of the velocity vector of a moving body due to the interaction between a solid body and a fluid. According to McCormick (McCormick, 1994), the two main components of the total drag of an airplane are induced drag and parasite drag.

Induced drag is the result of a trailing vortex created downstream of a lifting surface with a finite aspect ratio. Parasite drag is the total drag experienced by an airplane excluding induced drag. Parasite drag consists of a few different types of drag, including skin friction drag, form drag and interference drag.

Skin friction drag is the drag experience due to the viscous shearing stresses over the wetted surface of an object. As seen in Figure 31, a laminar boundary layer is developed at the leading edge. The laminar boundary grows downstream due to the surface roughness and becomes unstable. As a result, a transition to a turbulent layer takes place (McCormick, 1994). Ensuring a smooth surface on bodies will reduce the skin friction drag.

Figure 31: Skin friction drag (McCormick, 1994)

Form or pressure drag is the static pressure experienced normal to a body's surface, resolved in the drag direction. By changing the form of a body, one can decrease the drag coefficient of the body, as seen in Figure 32.

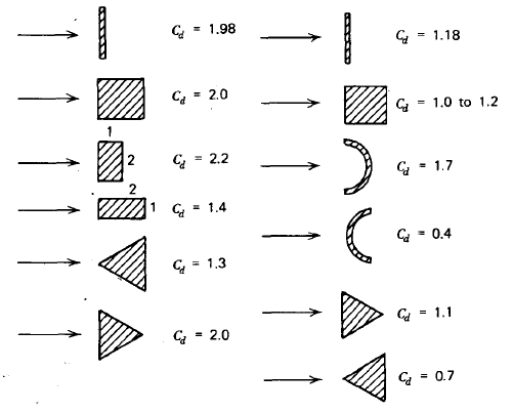

Figure 32: Drag coefficient of different shapes (McCormick, 1994)

Interference drag is the increased drag due to different bodies being close to one another. With the bodies being close to each other, their pressure distribution and boundary layers interact and the combination of the drag of the bodies, is greater than the sum of the drag of the bodies separately.

In some instances, interference drag can lead to a decrease in total drag. A shielding effect occurs when bodies are aligned behind each other at a certain distance, relative to the oncoming air. The drag of the second body is less than that of the leading body, because the leading body creates a wake with a reduced dynamic pressure in the area of the second body (Hoerner, 1965). In some instances, the drag of the second body can become negative as suction forms behind the leading body. The shielding effects can be seen in Figure 33.

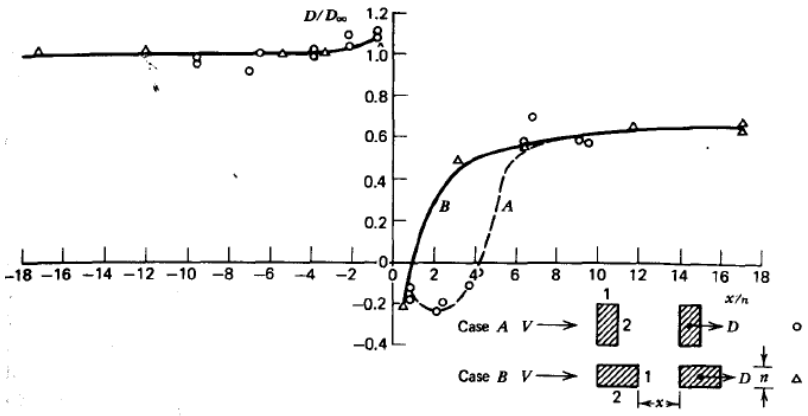

Figure 33: Shielding effect (McCormick, 1994)

2.3.4 Reduction in Drag

Streamlined bodies can reduce drag as it considerably decreases the wake formed by the body. In Figure 34 a larger body creates the same amount of drag compared to a much smaller body. This occurrence is made possible by the streamlined shape of the larger body where the adverse pressure gradients are smaller compared to the small body.

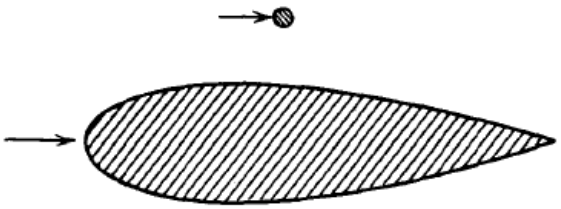

Figure 34: Objects with an equal amount of drag (McCormick, 1994)

By increasing the corner radius of the leading edge of the pylon, the drag coefficient will decrease noticeably, as seen in Figure 35.

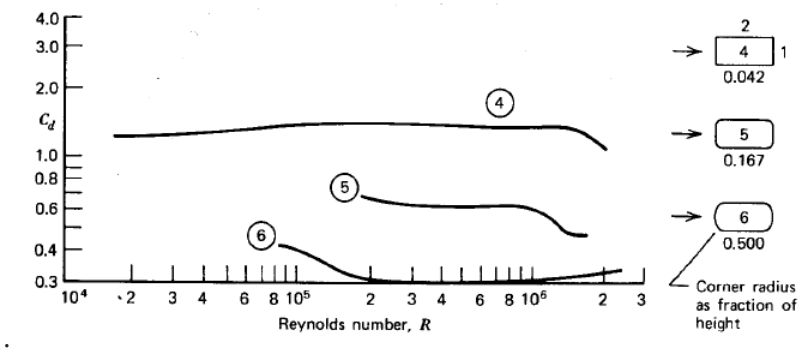

Figure 35: Drag coefficients of different size corner radius (McCormick, 1994)

Non-streamlined bodies of airplanes use fairings to make them more streamlined. Fairings can be used at the leading edge of the pylon to decrease the drag and wake created by the pylon. A large wake created by the pylon, which is located in front of the radiator, can thus reduce the airflow going through the radiator.

The square shape of the leading edge of pylons used in Self-luanch systems (Figure 36), can also be rounded to a more streamlined shape to reduce drag and the size of the wake.

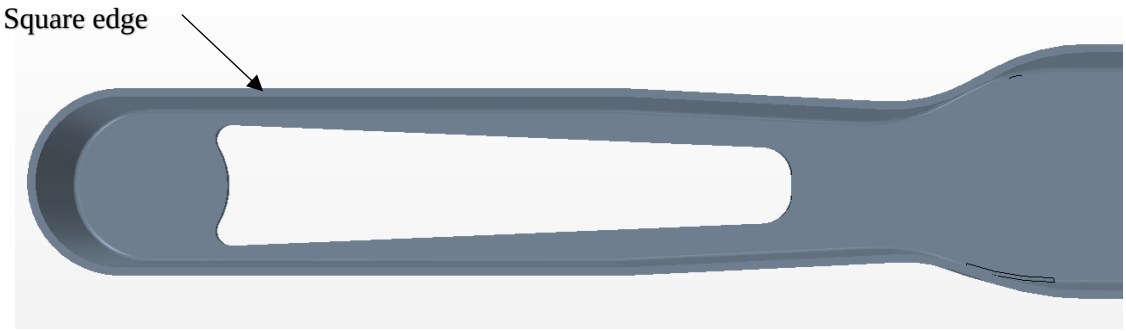

Figure 36: Typical self-launcher pylon

2.4 CFD

Computational fluid dynamics uses numerical methods together with algorithms to solve and analyse problems in fluid flows. CFD has become a common tool to solve aerodynamic and heat transfer problems and is a viable alternative to expensive experiments. CFD can be more efficient than experimental tests, as more iterations of a test can be completed in less time. To setup a CFD analysis, one needs to understand the fundamentals of developing a CFD simulation that is accurate enough and using numerical models that are descriptive but still efficient.

2.4.1 Mesh Construction

A mesh is a mathematical representation of space and geometry that is composed out of vertexes, faces and cells. The mesh type is size is critical to ensure that a proper balance between accurate results and simulation runtime is achieved. CD-Adapco (2018) recommends that the following factors should be considered when creating a mesh:

- The turnaround time for generating a mesh
- The amount of memory available for the simulation
- The desired accuracy and convergence rate required
- Whether the domain consists of a single or multi-region mesh
- The initial surface mesh quality
- Whether the geometry of the simulated part is mainly thin or not

STAR-CCM+ has three different meshing techniques available for generating a mesh, namely polyhedral, tetrahedral and trimmed mesh. A prism layer mesh is used to capture boundary layer flow.

Tetrahedral meshes have been successfully used over the past few decades in a large number of CFD simulations. It is a mesh technique that is relatively easy to generate and has become a standard practice in automatic mesh generation in CFD (Peric & Ferguson, 2005).

In recent years the use of polyhedral meshes increased as it shows advantages over tetrahedral meshes (Balafas, 2014). Polyhedral meshes are more efficient than tetrahedral meshes regarding cell count, as it uses up to five times fewer cells (Peric & Ferguson, 2005). Convergence is also achieved faster with fewer cells in comparison to a tetrahedral mesh (Balafas, 2014). Polyhedral cells have an average of 12 faces and as a result has 12 neighbours. 12 Neighbours give the cells the ability to capture swirling and recirculation flow particularly well due to a greater likelihood that local flow vectors can be orthogonal to the connecting faces (Peric & Ferguson, 2005).

The size of the mesh has a direct influence on the accuracy and simulation run time. Up to a certain point, a mesh refinement can deliver more accurate simulation results. By using a mesh independency test, one can determine the point where making the mesh successively smaller no longer affects the simulation results.

2.4.2 Turbulence Models

Turbulence models are used to simulate the effect of turbulence on a moving fluid. Turbulence is present in most flows of engineering interest. Star CCM+ uses three different approaches to model turbulence; Direct Numerical Simulation, Large Eddy Simulations and Reynolds-Averaged Navier-Stokes equations.

DNS (Direct Numerical Simulation) uses full unsteady-state Navier-Stokes equations. These full unsteady-state Navier-Stokes equations can be extremely demanding when an irregular turbulent flow is present. To capture the smallest eddies accurately, a fine mesh size is needed. In Figure 37 one can see that a fine mesh and time resolution are needed to capture the fine details. DNS is not an effective way to compute transitional flow over an object yet, as it requires too much computational power and a very fine level of detail.

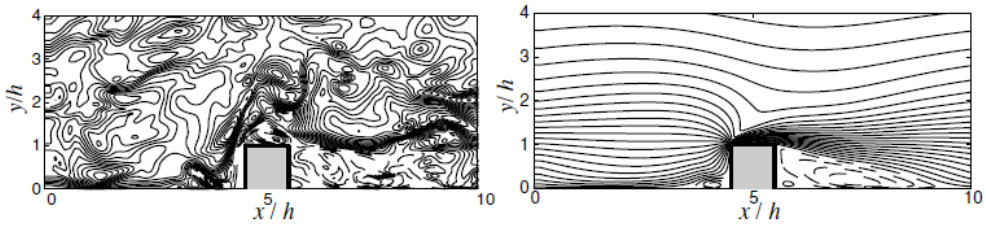

Figure 37: Instantaneous turbulent contours versus averaged contours. (McCormick, 1994)

With the high computational cost of DNS, an alternative, less demanding method was required. The need was satisfied with Large Eddy Simulations (LES). This method uses filtered Navier-Stokes equations (Kariadakis, 1999). It works on the same principle as DNS, but at a lower resolution compared to DNS. Only the large scale eddies are computed and the small scale eddies are taken into account by using a viscosity assumption. This makes LES a more efficient alternative to DNS.

Reynolds-Averaged Navier-Stokes (RANS) Turbulence model creates averaged and fluctuating components in an attempt to solve a modified set of transport equations. Additional equations of known quantities are needed to ensure that the number of equations is equal to the number of unknown variables. Using the RANS model highly reduces the computational cost when compared to DNS (CD-Adapco, 2018). Many CFD models rely on the RANS approach, and a number of turbulence models exist that are based on thereon. The most often used turbulence models based on the RANS approach are discussed below.

2.4.3 SST (Menter *et al.*) $k - \omega$ Model

The SST (Menter *et al.*) $k - \omega$ model is a turbulence model that can be used with simulations based on a steady state RANS approach. The model utilises the most significant advantages of both the $k - \varepsilon$ and $k - \omega$ models. (Menter *et al.*, 2003)

The $k - \varepsilon$ model is one of the most used turbulence models in CFD. The model consists of two equations that solves the transport equations for the turbulent kinetic energy, k, and the turbulent dissipation rate, ε (CD-Adapco, 2018). The model can capture free stream flow well, but lacks the ability to capture near wall flow. The k - ε model requires fewer computational resources to run in comparison with the $k - \omega$ model.

The $k - \omega$ model is capable of capturing near wall and free stream flow well, but at a higher computational cost when compared to the $k - \omega$ model (Menter *et al.*, 2003). The second equation solved for from by the $k - \varepsilon$ model (turbulent dissipation rate), is replaced with ω (specific turbulent dissipation rate). The $k - \omega$ model is sensitive to changes of ω in the free stream, making it sensitive to inlet boundary conditions for internal flow.

The SST (Menter *et al.*) $k - \omega$ model uses the $k - \omega$ model for near wall flow and the k - ε model for flow further away from the wall. The model switches between the $k - \omega$ and k - ε as needed and uses a blending function to unite the two models.

2.5 Summary

After completing the literature review concerning heat exchangers, propellers, CFD and aerodynamics, the necessary knowledge was gained to complete the objectives of this study. The following main conclusions were reached and are summarized for convenience:

- Modelling the complete detailed geometry of the radiator is unnecessary. Only a small section of the detailed radiator is needed, in order to obtain the characteristics with which to represent the complete radiator region as simplified porous block (Lidar, 2018; Ning *et al.*, 2004).
- The porous resistance coefficients can be determined by measuring the pressure drop over the radiator, as it changes for various flow velocities (Ning *et al.*, 2004).
- The presence of an object in front of the radiator can lead to a non-uniform airflow and temperature distribution over the radiator. To capture this non-uniform flow accurately, a large number of pressure and temperature sensors are ideally required (Ng *et al.*, 2001).
- The CFD simulation used to simulate a heat exchanger can be based on a steady RANS approach. The SST $k-\omega$ turbulence model yielded more accurate results than other turbulence models (Junjanna *et al.*, 2012; Lidar, 2018).

- A rotating propeller can be modelled as a rotating reference frame or a virtual disk in a steady state simulation. BEM virtual disk method does not require a mesh of the propeller to be modelled, only geometry detail of the propeller is needed. (CD-Adapco, 2018).
- The BEM virtual disk model is an economical model which utilises BEM theory, and is able to capture the wake structure of the propeller well enough to make design decisions (CD-Adapco, 2018; Guo *et al.*, 2014). The results of the BEM virtual disk model are compareable to the rotating reference frame model.
- The rotating reference frame method is one of the most widely used methods to simulate rotating fans, propellers and rotors in steady state simulations.
- Simulating a rotating propeller to use the constant rigid motion method, consists of rotating the cell vertices which requires a computational heavy transient simulation (Reynolds, 2018).
- The drag and wake created by an object can be greatly reduced by using streamlined bodies of fairings (McCormick, 1994).

- The boundary layer of a fluid that travels along an adverse pressure gradient, will retard the flow due to shear stress created by viscosity. The retarded flow can lead to flow separation or recirculation flow (Munson *et al.*, 2010).

- The size of a mesh used by a CFD simulation, has a direct influence on the accuracy and simulation run time.
- A polyhedral mesh is more efficient than a tetrahedral mesh (Balafas, 2014). Polyhedral meshes are also better suited to capture swirling and recirculation flow, due to its high number of faces (Peric & Ferguson, 2005).
- The SST $k - \omega$ turbulence model utilises the greatest advantages of the $k - \omega$ and $k - \varepsilon$ turbulence models (Menter et al., 2003).

The conclusions made above, assisted in making informed decisions concerning the modelling strategy used in the setup of the self-launcher system flow and heat transfer simulation.

3. EXPERIMENTAL TESTS

Three different experimental tests were completed in this study, as seen in Figure 38. The propeller static thrust as well as the radiator wind tunnel tests were required to obtain the necessary data to setup and validate the simplified CFD simulations, as discussed in section 4. The self-launch radiator characterisation test was done to determine the heat transfer capabilities of the radiator, and to determine whether the radiator could cool the engine sufficiently. The measured data was used to investigate the effects of different components (such as the pylon) on the heat transfer capabilities of the radiator as well as to validate the integrated CFD simulation.

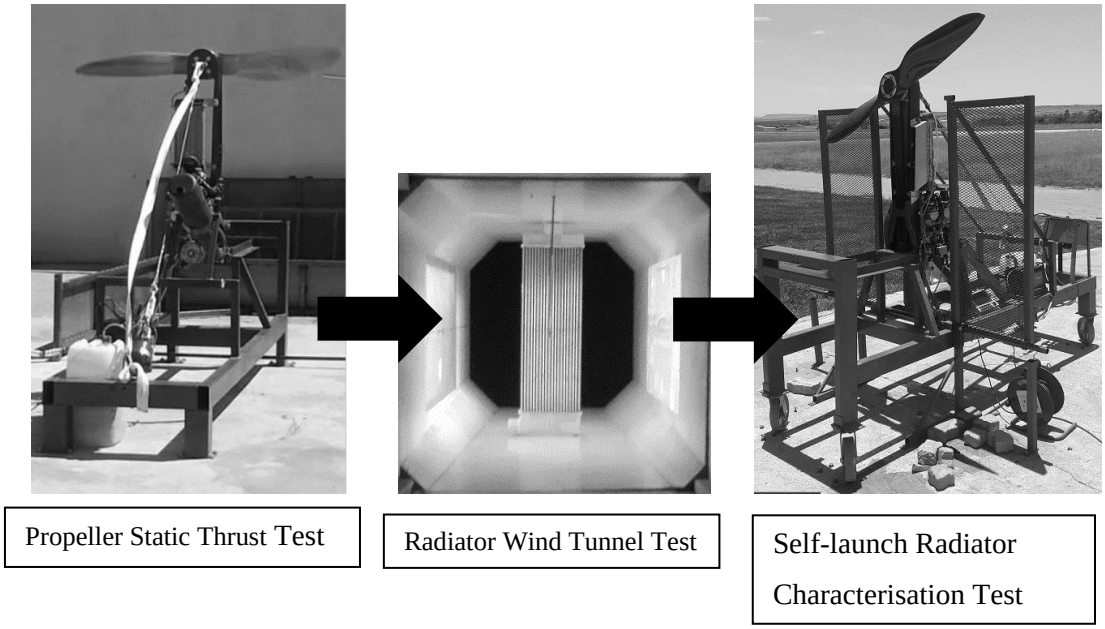

Figure 38: Experimental tests breakdown

3.1 Propeller Static Thrust

The static thrust of the propeller was chosen as the primary parameter with which to validate the CFD propeller model. Measuring the static thrust of the propeller can be done with sufficient accuracy and is an uncomplicated and cost-efficient experiment.

3.1.1 Experimental Setup

The experimental tests were done on a self-launch system (SLS) test bench as seen in Figure 39. The self-launch system was securely mounted on the test bench, and the pylon was supported on hinges. A restraining cable connected to the pylon prevented it from falling forward as the propeller delivered thrust. The hinges and cable system is similar to the design which will eventually be used in the production version of the self-launch sailplane. Strict experimental procedures were followed to ensure that the experiment took place in an orderly and safe manner.

The rpm of the engine was measured with a magnetic pickup located at the alternator of the engine. A secondary tachometer was used from a pickup sensor around the spark plug wire. Measurements from the two sensors consistently read within a band of 50 rpm from each other. The propeller was connected to the engine by a pulley and belt system. As a result, the propeller rotated at a reduction ratio of 2.32, when compared to the rpm of the engine.

A calibrated load cell was connected to the restraining cable to measure the static thrust of the propeller at an angle. The geometry of the system was used to determine the horizontal static thrust (Figure 39).

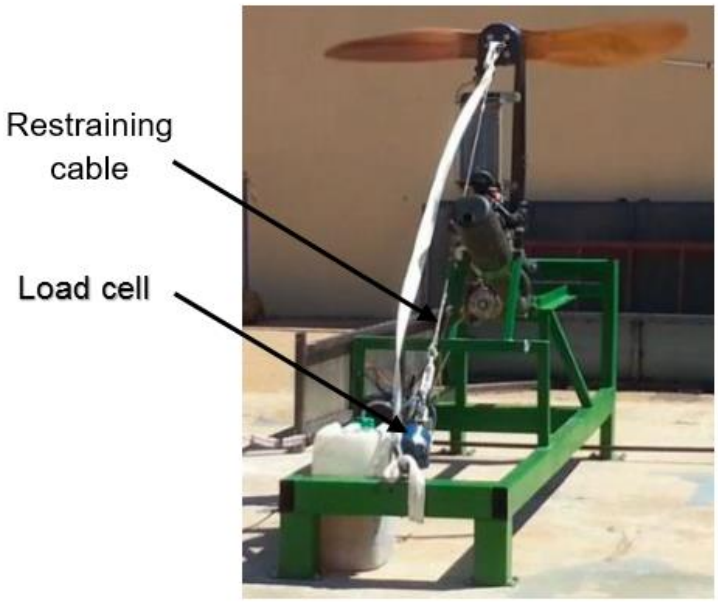

Figure 39: Static thrust experiment setup

After all necessary safety checks were completed, the engine was started. The engine was set to different rpm values, ranging from idle to full throttle, with the load cell measurements taken at each rpm setting. After every change in rpm, the engine was allowed enough time to stabilise at the new operating point. Readings of the load cell oscillated by 1kg during the experiment. Vibrations as well as a slow refresh rate (1 second) could have contributed to the fluctuation in the measurements. With the original cooling system (before the modifications investigated in this study), the engine could not reach its intended power peak and started to overheat when run at high rpm for long periods of time.

3.1.2 Results

The static thrust of the propeller was measured at an angle with a load cell. The force diagram in Figure 40 was used together with equation 4 to determine the static thrust of the propeller. Figure 41 shows the measured static thrust of the propeller.

$$\frac{T_{propeller}}{F_{load\ cell}} = cos \propto \quad \ldots (4)$$

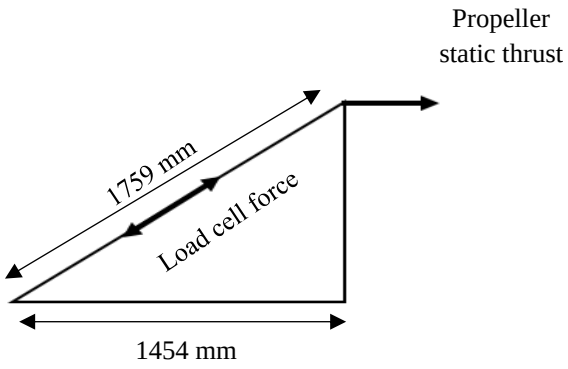

Figure 40: Force diagram of propeller

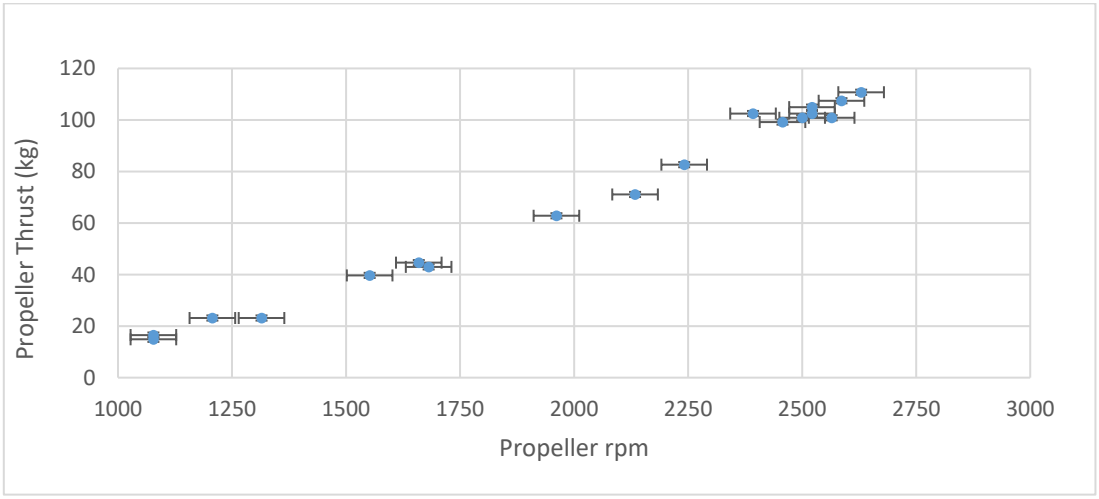

Figure 41: Propeller static thrust measured

The static thrust of the propeller steadily increased up to a maximum of 111 kg at a propeller rpm of 2600. The engine of the self-launch system could not reach its intended power peak.

The highest rpm that the engine could reach, at full throttle, was just over 6000 rpm. The original prototype exhaust layout was identified as the main cause for the engine not reaching its maximum rpm. The static thrust can be used to validate the propeller CFD simulation used in section 4.

3.2 Radiator Wind Tunnel Test

In the CFD simulation of the integrated self-launch system, the radiator was represented by a porous region model. The model coefficients required a pressure drop versus flow rate correlation across the radiator, to calculate the calibration values.

3.2.1 Setup

A pressure drop experiment was performed inside a subsonic, open-circuit suction wind tunnel (Appendix D). The radiator was placed inside a wind tunnel capable of delivering a velocity of up to 30m/s. Two pitot tubes were placed in front and behind the radiator and were connected to a digital 32-way pressure display unit (Figure 42). The 32-way pressure display unit has 32 calibrated pressure transducers, accurate to +- 0.5%, which measures pressure with respect to atmosphere (Appendix D). The pitot tubes measured the total and static pressure inside the wind tunnel. A calibrated anemometer (Appendix D) with an accuracy of 2%, was also used to measure the velocity in the wind tunnel to verify the readings of the pitot tube. Figure 43 shows the placement of the radiator inside the wind tunnel.

Figure 42: Pitot tube connected to the digital 32-way pressure display unit

Figure 43: Radiator placement inside the wind tunnel

The total and static pressure were measured by a pitot tube in front of the radiator. The air velocity was calculated by using Bernoulli's equation. A calibrated anemometer was used to verify the was calculated with the pitot tubes.

3.2.2 Results

The results of the measured airflow can be seen in Table 1.

Table 1: Wind velocity measurements

Anemometer	15	17	19	21	23
Pitot Tubes (m/s)	14.46	17.44	19	20.91	22.65
% Difference	3.6	2.59	0	0.43	1.52

The pitot tube setup delivered accurate velocity readings when compared to the readings of the anemometer. Figure 44 presents the results of the pressure drop measured with the pitot tubes.

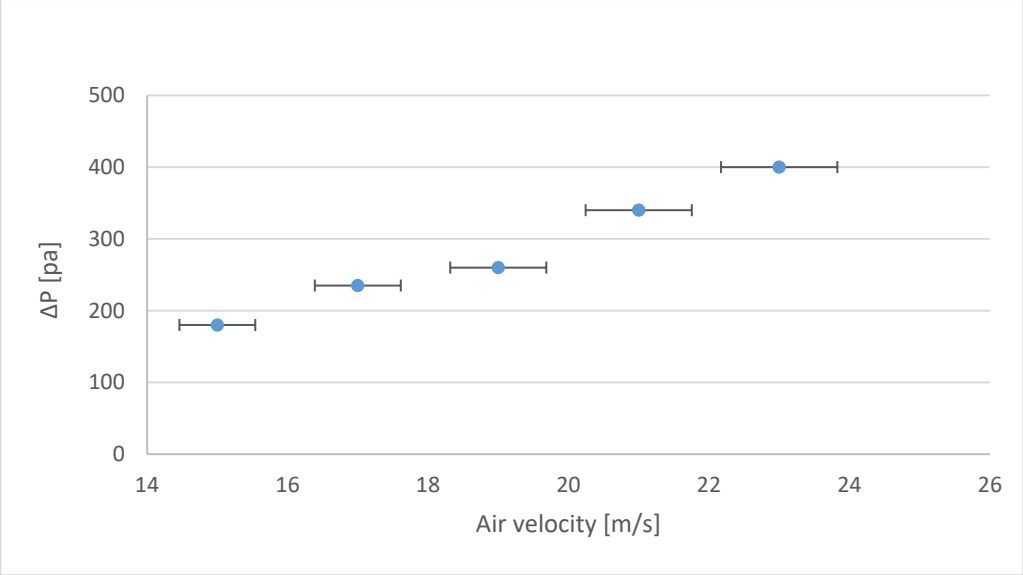

Figure 44: Pressure drop versus flow rate across the radiator (pitot tube measurements)

The pressure drop, as function of flow rate, was determined in a wind tunnel experiment. As the velocity increased, the pressure drop over the radiator steadily increased as well. The results can be used to characterise and validate the detailed CFD radiator model, as well as the porous region approximate model.

3.3 Self-Launcher Radiator Characterisation Test

To characterise the radiator of the self-launch system, numerous parameters had to be measured. The experiment was done on a grounded self-launcher test bench (Figure 45).

3.3.1 Setup

A twin-cylinder inline two-stroke engine manufactured by Solo™ is used by the self-launch system. The engine has a rated power of 47 kW and a continuous maximum rpm of 6500. See Appendix D for the data sheet of engine.

A data logger equipped with 20 channels was used to gather data during the experiment. The data gathered included the air flow rate into the radiator, the inlet and outlet temperatures of the air/coolant, as well as the mass flow rate of the coolant. All the channels of the data logger were used in order to log the maximum amount of data from the self-launch test.

18 type K thermocouples, with an accuracy of ± 1°C were used to measure the temperatures of the air and water. The calibration of the thermocouples is discussed in Appendix B. In order to measure the temperature change of the coolant, separate thermocouples were inserted into the inlet and outlet pipes of the radiator. Eight thermocouples were installed at the front and back face of the radiator respectively (Figure 46). The thermocouples were installed on a mesh and care was taken to ensure the signal wires did not touch any metal. All the wires were secured in a wire harness to prevent any interference with other components. The wires were then connected to the corresponding electronic interference of the data logger.

A water turbine flow sensor, with a ± 2% accuracy, was installed in line with the pipes of the radiator to measure the mass flow rate of the water (Appendix D). The flow sensor was installed in the longest straight pipe section available, to try and eliminate swirling flow effects as far as possible (in Appendix B the calibration process of the flow meter is described). In Figure 47, the coolant's flow path through the double pass radiator is illustrated. The hot coolant flowing out of the engine enters the inlet at the bottom manifold of the tank and then flows upwards in the first pass to reach the top manifold. The coolant is then rotated 180° in the upper tank and flows downwards in the second pass of the tank towards the outlet.

Figure 45: Self-launch test bench setup

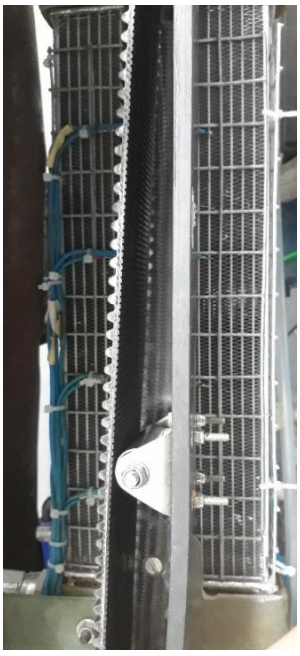

Figure 46: Thermocouples installed on a wire mesh located alongside the radiator.

Figure 47: Coolant flow path through the double-pass radiator. Flow enters from the right-hand side in the image and exits on the left.

After all the necessary safety checks were completed, the self-launch system was started and allowed to idle until the coolant reached the operating temperature and stabilised at idle. The throttle of the engine was then gradually opened as necessary to reach the rpm specified in the speed range settings of a test. When a rpm value was reached, the throttle setting was kept constant and the system was given enough time to achieve stable water and air temperatures at the new conditions.

3.3.2 Results and Discussion

Figure 48 to Figure 51 show the results of the recorded data logger after the temperatures had stabilised. Tests were completed at 2500, 3700 and 5100 engine rpm.

An uncertainty analysis was done on all the measurement of the experiment, using a method described by Taylor (1999), which can be seen in Appendix F. The error bars in the graphs show the amount of uncertainty in the measurements.

The heat load transferred by the radiator increased as the rpm of the propeller increased (Figure 48). The increase in the heat exchanged was due two factors; to an increase in the airflow through the radiator, and a higher temperature difference in the coolant between the inlet and the outlet.

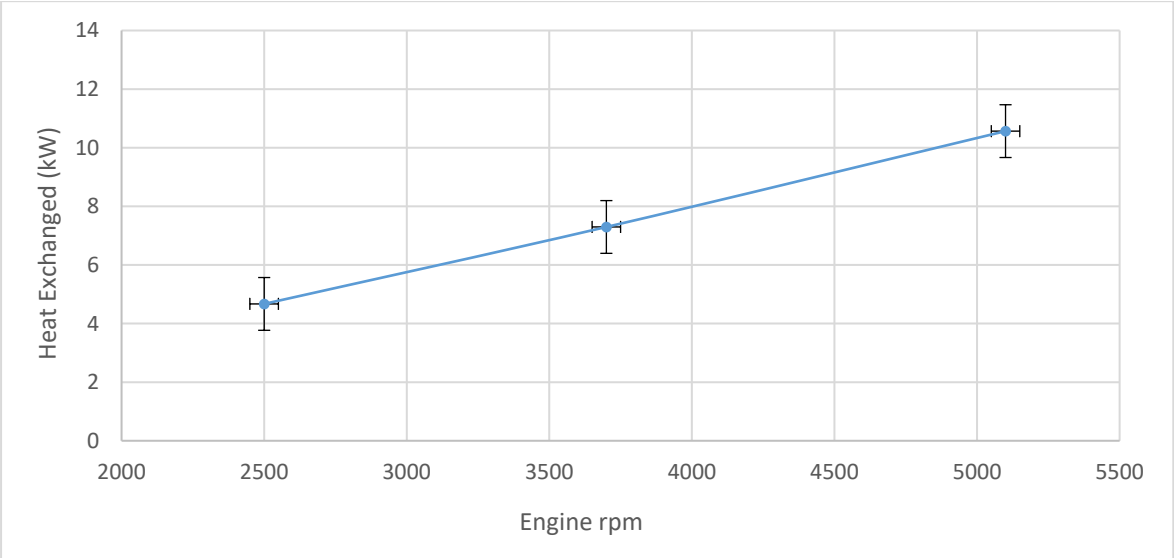

Figure 48: Heat exchanged by the system

.

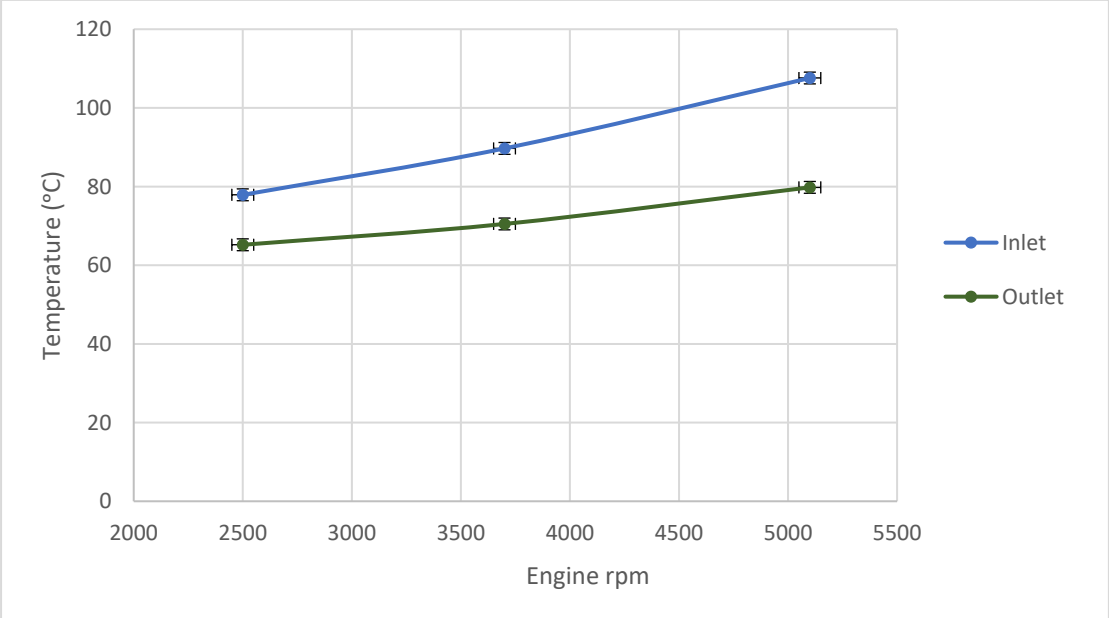

Figure 49: Radiator water temperatures

The measured temperatures of the water and air at both the inlets and outlets increased as the air flow rate increased due to the propeller turning faster which is linked to the engine speed increase (Figure 49, Figure 50).

At an engine rpm of 5100, the water temperature rose to an uncomfortably high level of 107.6 °C. The Solo™ two stroke engine has a maximum operating temperature of 115 °C (engine ref Apendex?). The pressure cap of the radiator allowed coolant temperatures above 100 °C, without the fluid boiling. The cooling capacity of the system was therefore determined to be inadequate, since the safety limits of the equipment were reached.

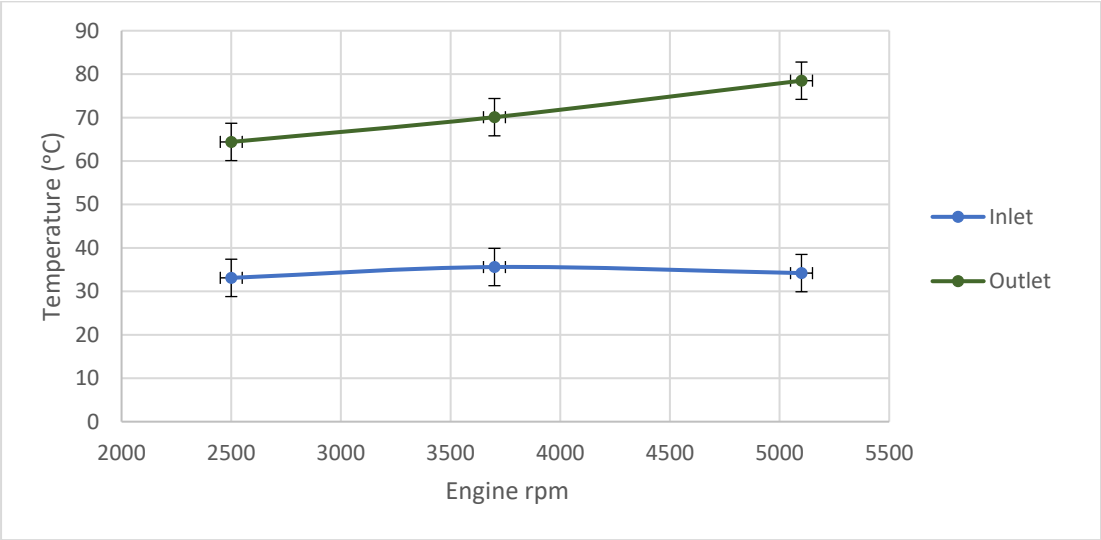

Figure 50: Radiator air temperatures

Literature has shown that measuring the air inlet velocity of a radiator where the flow has been disrupted, can be a formidable task (Ng *et al.*, 2001). A high number of pressure sensors would be needed to capture the non-uniform velocity over the radiator created by the wake of the pylon. The radiator was located only a few centimeters behind the rotating propeller. Using handheld flow rate measuring devices (e.g. vane anemometer) could not be considered, due to the limited space as well as safety concerns. It was decided on using an analytical approach to calculate the air mass flow rate at the inlet face of the radiator. The conservation of energy equation as seen in equation 5 was used.

$$q = \dot{m}_h \, c_{p,\,h}(T_{h,\,in} - T_{h,\,out}) = \dot{m}_c \, c_{pc}(T_{c,\,out} - T_{c,\,in}) \qquad \ldots 5$$

Where q is the heat exchanged (kW), $\dot{m}_h$ the mass flow of the hot fluid (kg/s), $c_{p\ h}$ (kJ/kg. ^{o}C), the specific heat of the hot fluid, $T_{h\ in}$ the inlet temperature of the hot fluid, $T_{h,\,out}$ the outlet temperature of the hot fluid (McCormick).

All the variables, excluding for the mass flow rate of the air in equation 5, were measured during the experiment. Consequently, the air mass flow rate could be calculated by substituting the measured data into equation 5. For equation 5 to be valid, the system was assumed to be adiabatic. The calculated mass flow of the air at the inlet face of the radiator, can be seen in Figure 51.

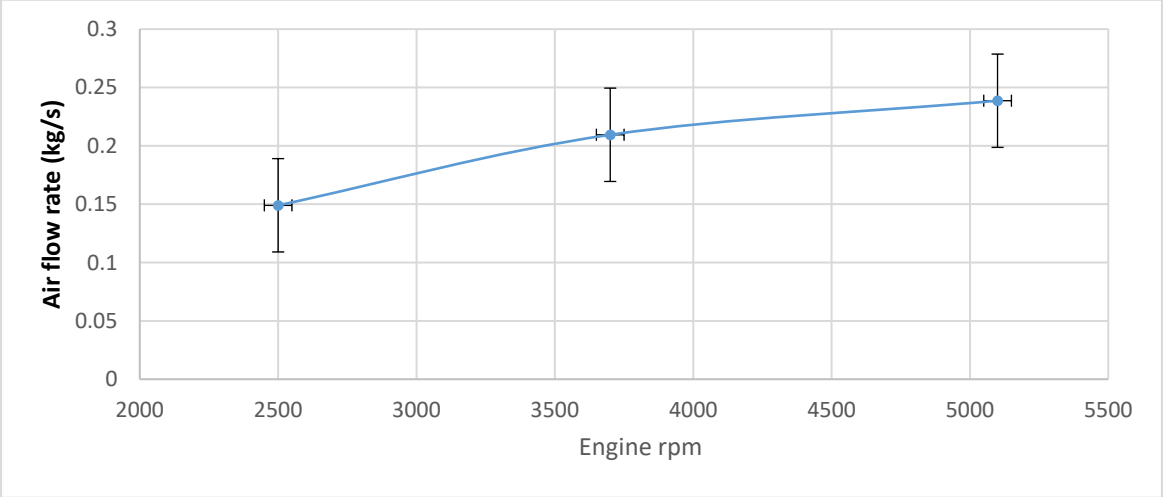

Figure 51: Radiator inlet air mass flow

The inlet air mass flow rate of the radiator was somewhat lower than expected. It is therefore postulated that the pylon located in front of the radiator obstructed a large portion of the airflow approaching the radiator.

Figure 52 shows the inlet and outlet air temperatures measured by the thermocouples. Note that the inlet temperatures are displayed as seen from the front of the radiator and the outlet temperatures as seen from behind the radiator. The hot coolant inlet is indicated using red arrows, and the cooled coolant outlet is indicated using blue arrows below in Figure 52.

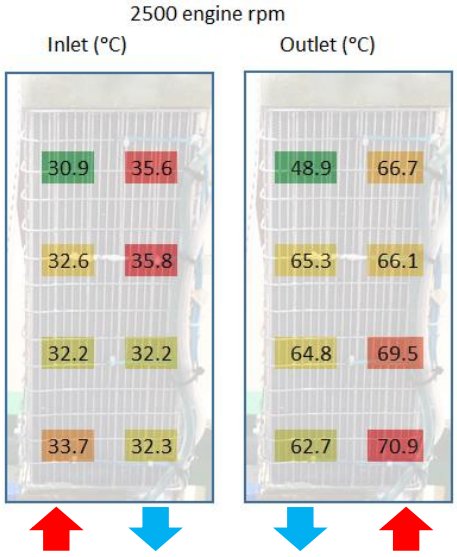

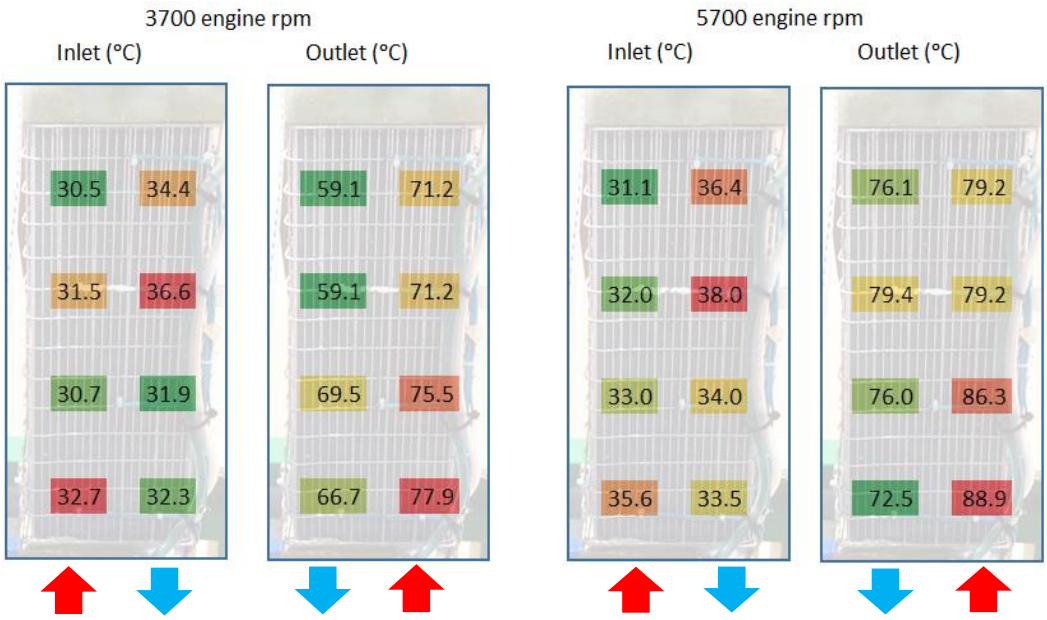

Figure 52: Temperatures over the face of the radiator

The air temperatures varied in agreement with the coolant's flow directions. The outlet air temperatures located near the inlet tank of the radiator, were high due to the hot coolant just entering the radiator. As one moves further along the path of the coolant, the outlet air temperatures lowered as the coolant became colder.

At all the engine rpm settings tested, the temperatures of the inlet air delivered a hot spot located at the top right portion of the radiator (Figure 52). A possible explanation of this hot spot may be that the air is moving slower at the location of the hot spot, due to the wake created by the pylon. Recirculating air can also be a cause of the hot spot. The slower moving and/or the recirculating air allows more time for heat transfer to take place and results in an increased air temperature.

3.4 Summary

A number of experiments were done to characterize the airflow and temperature distributions of the self-launch system and to provide empirical data required to setup and validate the CFD simulations used in section 4.

Experiments were completed to determine the static thrust of the propeller. The static thrust of the propeller was the chosen parameter to validate the propeller model used in CFD simulation.

The pressure drop over the radiator was determined in a wind tunnel test. These results provided the needed data to calibrate the porous region model used for the radiator in the integrated CFD simulation. (The calculation of detailed coefficients are described in the following chapter).

The effectiveness of the radiator was investigated on the self-launcher test bench where all the needed parameters were measured to determine the heat transferred by the radiator. The engine could not be run at full rpm, as the temperature of the engine rose to 107.6°C at an rpm of 5100, which is above the safety limit for the coolant temperature, but well below the maximum rpm of the engine.

The heat transfer specifications of the radiator used in the self-launch system is comparable to various other radiators used by self-launch sailplanes. Further investigation is needed to identify possible reasons as to why the radiator does not achieve the adequate heat transfer required. CFD simulation can be used to do an in-depth analysis of the heat transfer and airflow of the self-launch system. These models can significantly assist in obtaining a better understanding of how the different components of the self-launch system influence one another.

4. CFD VALIDATION AND ANALYSIS

By utilising CFD simulations, one can analyse the self-launch system in more depth. To gain confidence and trust in the CFD simulation, CFD methodology must be validated by comparing the results with experimental test data. After the models have been validated, one can make changes to the system in the CFD simulation, to determine how it will affects the heat exchange capabilities of the cooling system. Using CFD in such a manner can save time and money when compared to performing experimental tests.

4.1 CFD Roadmap

To determine the heat transfer of the radiator, a systematic approach was needed. The main CFD simulation consisted of several sub-models, as seen in Figure 53. These sub-models were developed with efficiency in mind, in an attempt to keep the overall computational cost at acceptable levels. The sub-models must be developed and validated before they can be integrated into the main CFD simulation. By following this CFD roadmap, one can have confidence in the final integrated CFD simulation. This model can then be used to make alterations to the self-launch system and determine in detail the effect of the alterations. By using CFD, one can save time and reduce cost by keeping experimental tests to a minimum.

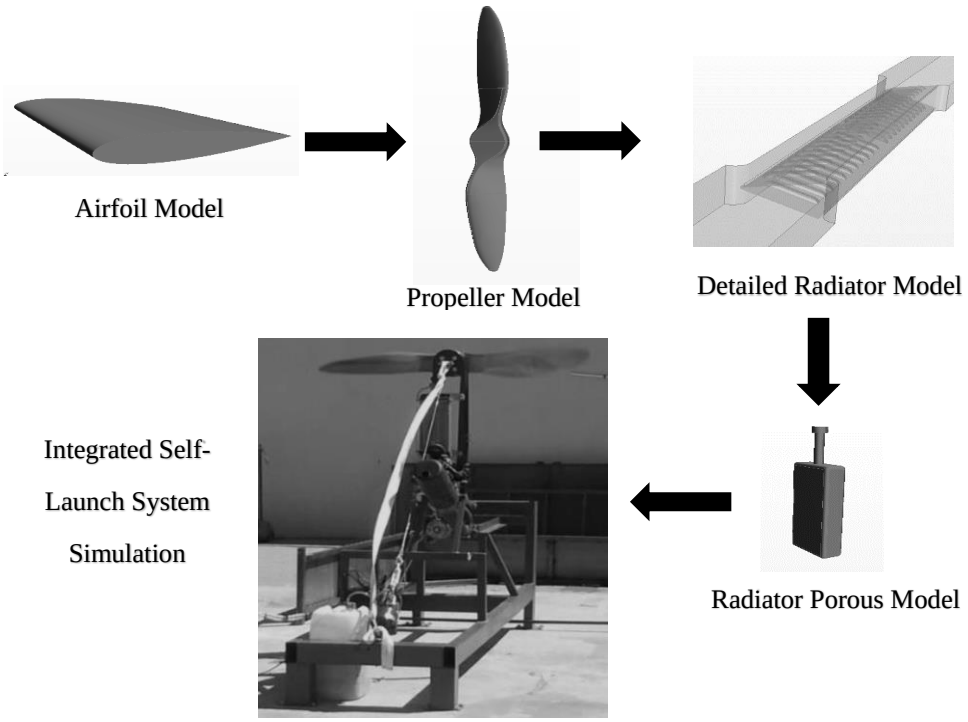

Figure 53: CFD roadmap

4.2 Methodology

To create CFD simulations that are accurate and reliable, the methodology as described below, was applied to all the CFD simulations.

4.2.1 Geometry

The geometry of the objects that were imported into the CFD simulations had a clean surface to ensure that a good quality mesh could be created. When an object had a high level of detail and a small impact on the simulation, a simplified geometry was used. The geometry of the engine with all its bolts, nuts and spark plugs was simplified. The distance between the simulated objects and the far field boundaries was set at an adequate distance. This ensured that the flow had already recovered from the wake when it arrived at the boundary.

4.2.2 Mesh

Polyhedral cells were used in all the CFD simulations. Literature showed the advantages it has over a tetrahedral mesh and its ability to capture complex swirling and rotating flow (Balafas, 2014). Prism layers were used at surface boundaries in order to capture boundary layer flow profiles with sufficient accuracy.

A lower mesh resolution was used at the far field boundaries with finer mesh resolutions at detailed geometries and points of interest. Wake refinements were also used where applicable. A mesh independence study was performed with each CFD simulation to ensure the results are independent of the mesh size. All the mesh independency studies can be seen in Appendix E.

4.2.3 Physics

All the CFD simulations are based on a steady state Reynolds-Averaged Navier Stokes approach. A transient approach was not considered as the needed resource and time were not available. The SST k - ω turbulence model was used in an attempt to capture boundary flow more accurately. The SST k - ω model proved to be a capable and reliable turbulence model that has been used successfully to solve similar CFD simulations as covered in this study (Junjanna *et al.*, 2012; Lidar, 2018)

The air domain in the CFD simulations was simulated as an ideal gas and the coolant as a non-compressible fluid (water). Interfaces were used to connect the different continua's. CFD simulations that used specialised models and physics will be discussed in more detail when the specific CFD simulation is discussed.

4.3 NACA 0012 Airfoil

A propeller consists of many cross-section airfoils. By successfully validating the aerodynamic coefficients of an airfoil, the performance of a propeller can be simulated with more confidence. The NACA 0012 is a popular airfoil used to validate simulated flow and the modelling methodology of flow over an airfoil, as plentiful experimental data is available.

4.3.1 Setup

A small section of a NACA 0012 airfoil was simulated. The domain consisted of a velocity inlet, pressure outlet and symmetry outer walls (Figure 54). A numerical mesh consisting of 2 million polyhedral cells was used. A prism layer consisting of 20 layers and a thickness of 7 mm were used to capture the boundary layers of the flow. The prism layer was chosen to keep the y+ wall values below one over the majority of the airfoil section. The flow over the airfoil was simulated at different angles of attack where the aerodynamic coefficients were measured and for conditions of a Reynolds number of 3.6×10^6.

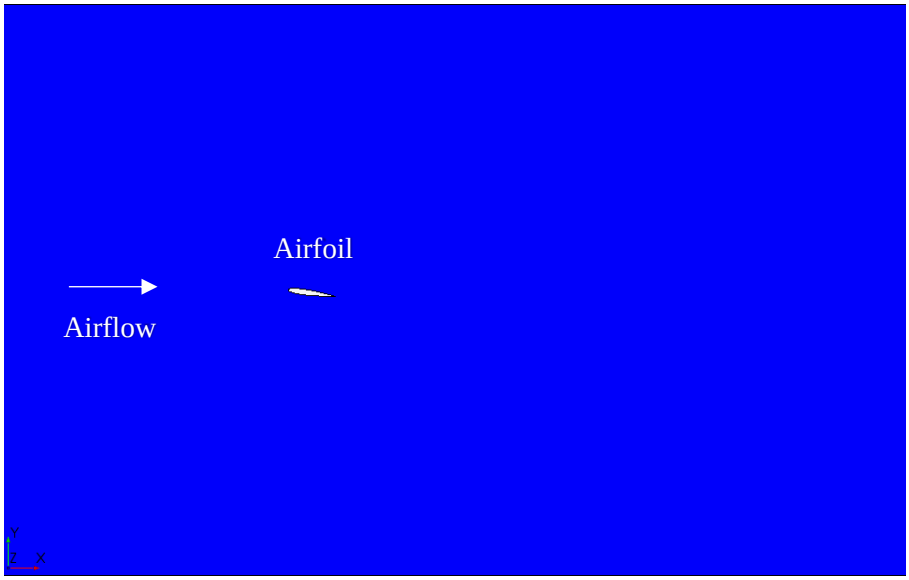

Figure 54: Computation flow domain

Figure 55 shows the mesh that was used in the computational flow domain. A wake refinement region was defined to improve the wake detail behind the airfoil to improve accurate drag prediction. The $\gamma - Re\theta$ transition model was added to the SST(Menter *et al.*) k - ω turbulence model in order to improve the boundary layer prediction.

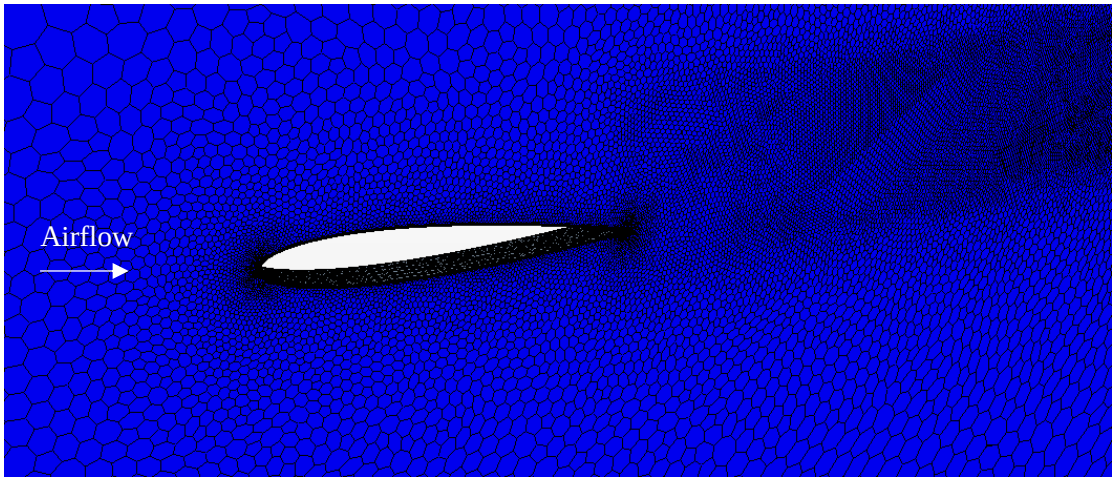

Figure 55: Mesh of the domain

4.3.2 Results and Discussion

The results of the drag and lift coefficients of the CFD simulation can be seen in Figure 56 and Figure 57. Numerical data obtained from XFoil and wind tunnel data (Smith & Schaefer, 1945) was also plotted on the same graph.

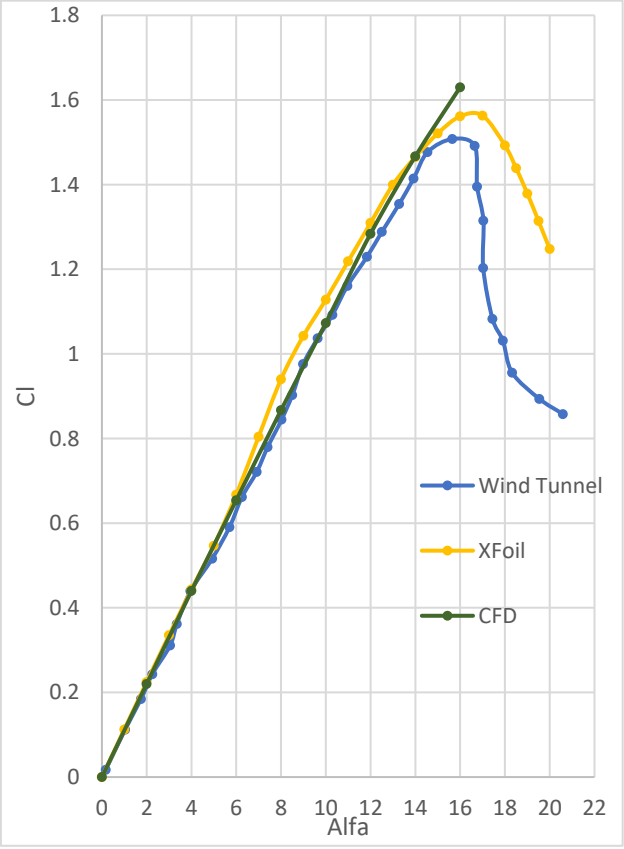

Figure 56: Lift polar of the airfoil

Figure 56 shows how the lift coefficient increased linearly with the angle of attack, at lower angles of attack. As a result the flow is attached to the airfloil in this region. At about an angle of attack of 16°, the flow separated from the airfoil, and is known as the stall angle.

At lower angles of attack, both methods predicted the lift coefficient especially well. At higher angles of attack, the XFoil and CFD data slightly overpredicted the lift coefficient. The overprediction in the lift coefficient, was the largest at the stall angle. Literature shows that XFoil tends to overpredict the lift coefficient by as much as 6% (Gopalarathnam & Selig, 2001).

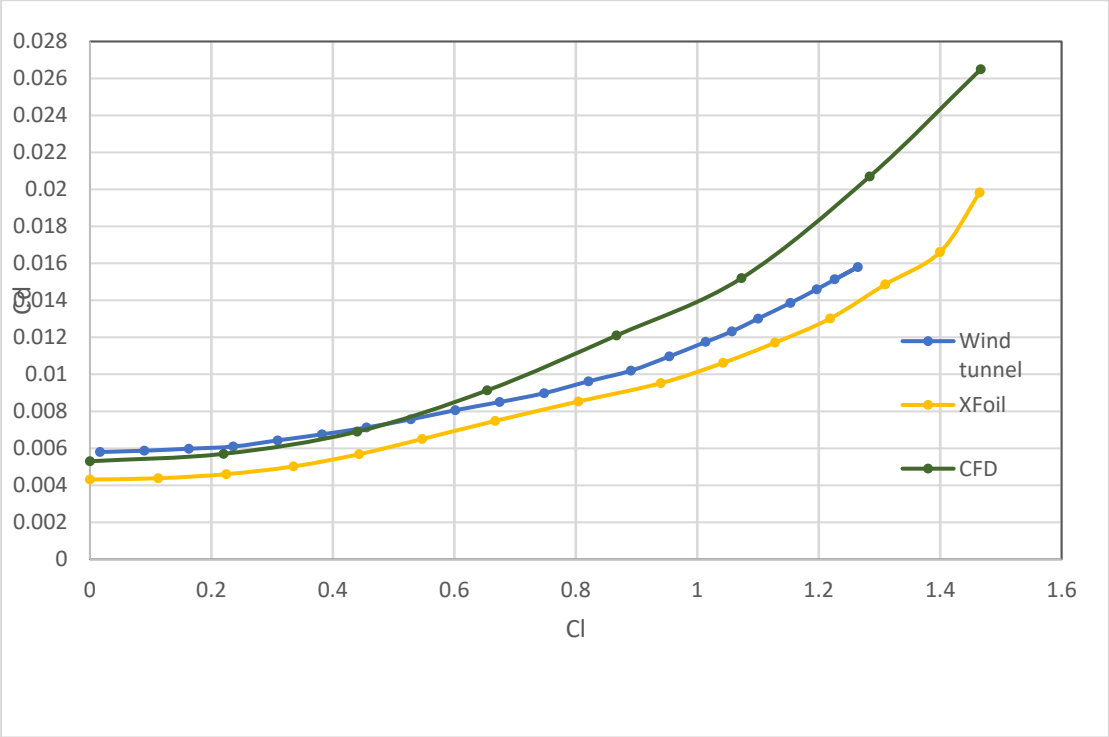

Figure 57: Drag polar of the airfoil

In Figure 57 one can see how the CFD and XFoil data does not agree well with the wind tunnel data at higher angles of attack. In the low drag bucket shape, the CFD results are very similar to the wind tunnel data. As the angle of attack approaches the stall angle, the drag coefficient was overpredicted progressively. Similar findings are confirmed by a study done by Bosman (2012), who simulated a three-dimensional section of a NACA 653418 airfoil.

This occurrence may indicate that the transition in the boundary layer was not simulated accurately by the CFD simulation. It was not further investigated as it did not fall within the scope of this study to predict transition flow in the boundary layer accurately.

The CFD simulation setup proved to be capable of predicting the aerodynamic coefficients of an airfoil, at lower angles of attack. The CFD setup also shows potential to simulate a propeller, as a propeller consists of a number of cross sectional airfoils.

The CFD simulation proved to be able of predicting the lift coefficient more accurately than the drag coefficient. Therefore, it is recommended to validate the propeller CFD simulation with the static thrust of the propeller.

4.4 Propeller (Rotating Reference)

The wake behind the propeller has a considerable influence on the airflow going through the radiator. The rotating reference frame method promises a good balance between accuracy and fast solution speed, and is investigated in this section to determine if it is a suitable method to simulate the flow of the rotating propeller.

4.4.1 Setup

Literature shows that a rotating propeller can successfully be simulated by using a rotating reference frame technique in CFD (Kutty & Parvathy, 2017).

The propeller of the self-launch system was thus simulated using the same approach and the CAD (Figure 58) geometry can be seen.

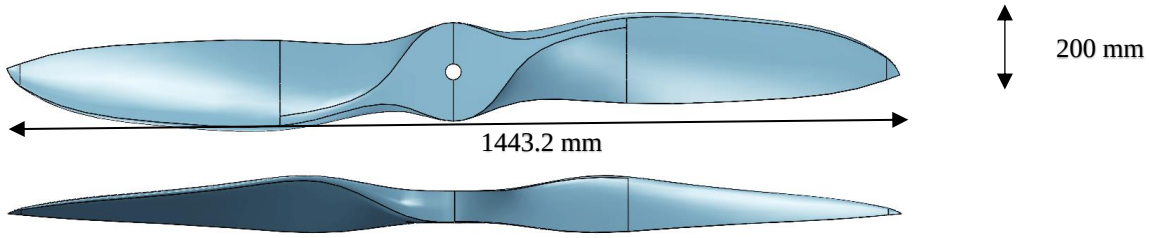

Figure 58: Geometry of propeller

The flow domain consists of a cylinder with a velocity inlet, pressure outlet and slip side walls as seen in Figure 59. Inside the flow domain, the propeller was enclosed by a smaller cylindrical region which was used to specify the rotating reference frame.

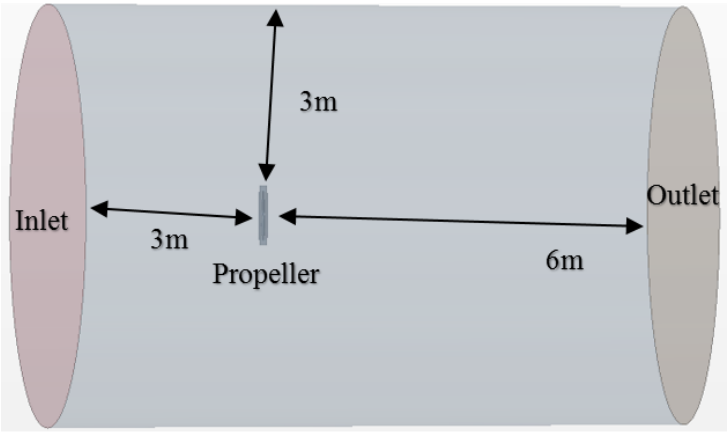

Figure 59: Computational domain of the propeller

A high mesh resolution was used to capture the detail of the propeller with emphasis on the leading edge of the airfoil. In an attempt to capture the boundary layers of the flow, prism layers were used on the boundaries of the propeller. The prism layers consisted of 16 layers (5mm thick), which yielded a y+ wall range of one or less over the majority of the propeller's body (Figure 60).

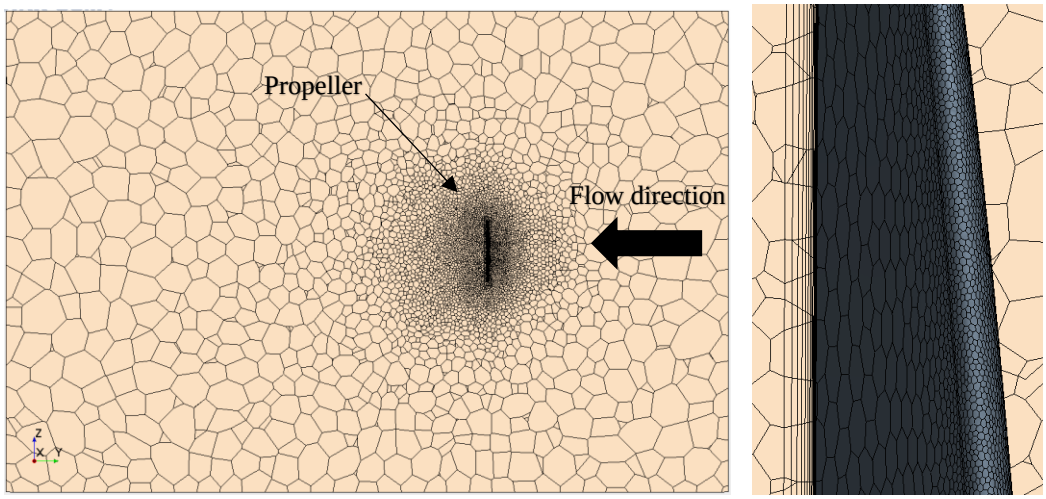

Figure 60: Mesh of the domain with detail, a close up of the propeller mesh.

4.4.2 Results and Discussion

The reference frame was rotated through a range of speed values, to simulate the movement of the propeller, and the static thrust was measured. The static thrust values were then converted to kg and compared with the experimental measurements as seen in Figure 61.

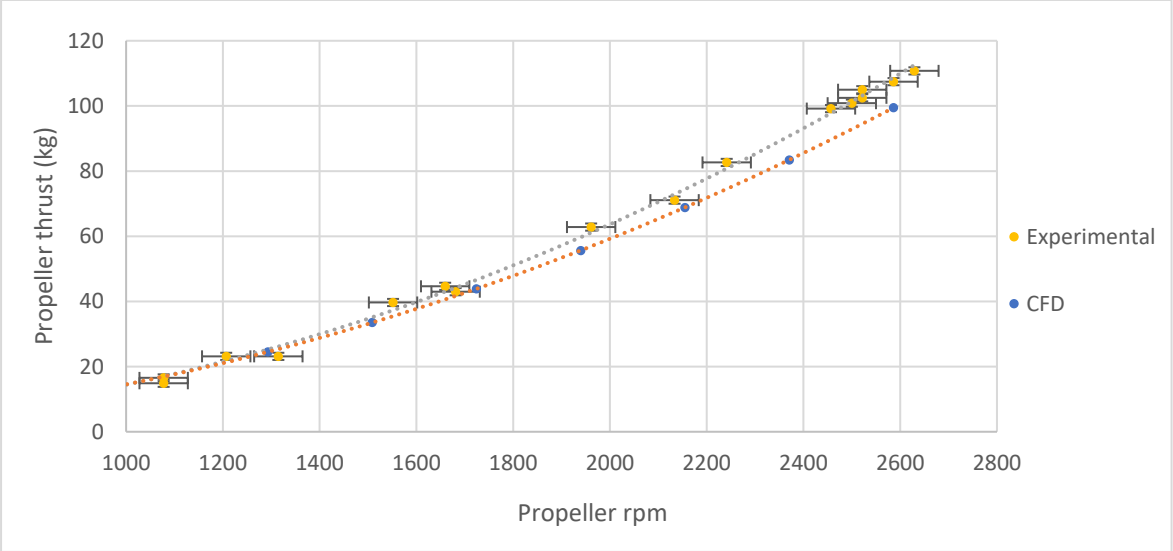

Figure 61: Comparison of simulated thrust values with measured values for the rotating reference frame method.

The values compare favourably, especially at lower propeller rpm. At higher rpm the simulation underpredicts the static thrust of the propeller, with the largest percentage difference at approximately 7%, when the propeller's rpm is at 2590. The Difference can be explained by the inaccuracy of the CFD simulation to predict lift and drag coefficients at high angle of attack, which exist near the hub of the propeller.

The pressure distribution over the front and back of the propeller can be seen in Figure 62. A propeller creates lift in a similar manner as an airfoil. The front of the propeller has a lower pressure distribution compared with the back; this is a result from the blade angle and rotation causing a momentum change of the airstream flowing through the propeller disk. The pressure difference and the change in momentum direction as air flows across the blades, create the forwards force also known as thrust.

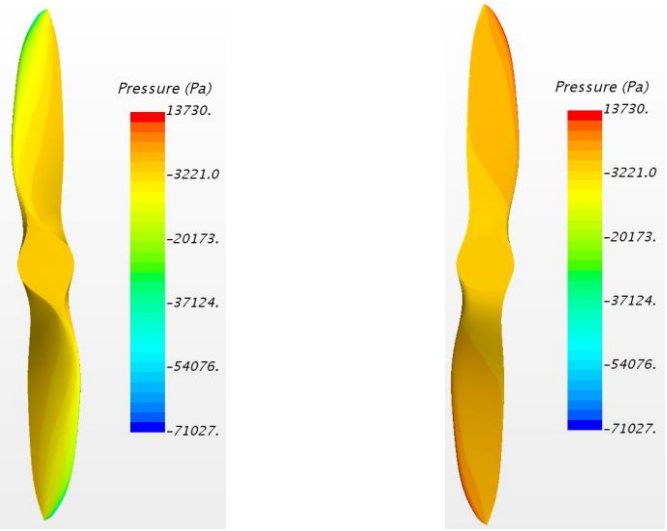

Figure 62: Left-hand side: Pressure distribution on the front of the propeller
Right-hand side: Pressure distribution on the back of the propeller

Figure 63 shows the line integral convolution velocity vector of the propeller at a 90° and 180° sectional cut. Closer examination of the CFD results indicated a significant shortcoming of the rotating reference frame method, in that the steady-state wake pattern varies and is determined by the stationary position of the geometry in the simulation scene. When the propeller is thus at 90°, the wake pattern would differ from that of the sectional cut at 180°, as seen in Figure 63. When the propeller is at 90°, the wake of the propeller would differ from a wake at 180°, as seen in Figure 63. The velocity profile directly behind the propeller (90°) has a higher velocity range when compared to the velocity profile at 180°, where it is expected that the velocity pattern should have an evenly distributed spiral character.

This finding demonstrated that the rotating reference frame would not be suitable for the purpose of the study, as the stationary position of the propeller will have a large influence on the flow entering the radiator, and flow patterns subsequently change as the stationary orientation of the propeller is modified. A method to simulate the rotating motion of the propeller independent of the position of the propeller was thus needed.

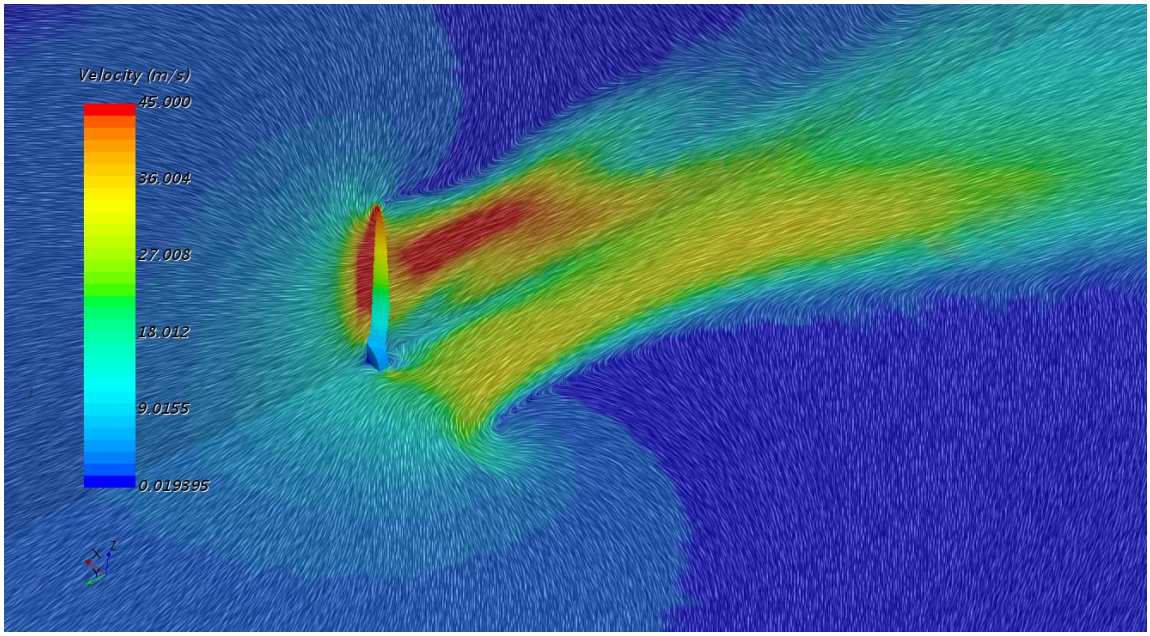

Figure 63: Line integral convolution velocity vector with a 90° and 180° sections cut

The rotating reference frame model can be used to simulate radiator fans with decent results Lidar (2018). The fans used by radiators used a high number of blades which makes the above-mentioned problem less prominent as opposed to the propeller consisting of only two blades.

In summary, the propeller was semi-successfully simulated using a rotating reference frame approach. The average static thrust values from the simulation compared well with experimental results, but the wake position is not modelled realistically and would result in erroneous airflow distributions entering the radiator. This in turn would affect the accuracy of the heat transfer calculations.

4.5 Propeller (Virtual Disk BEM)

An alternative method to simulate a rotating propeller in Star CCM+, is to use the virtual disk model. The propeller is simulated as an actuator disk where the motion of the propeller will be represented as a source term that is used in the momentum equation of the simulated domain. This method also utilises BEM theory to obtain the aerodynamic quantities from the rotating propeller.

4.5.1 Setup

The same setup used in section 5.4 was used here, with the only exception being that the geometry of the propeller was not explicitly modelled. This lead to a noticeable decrease in the number of cells used in the simulation. The rotating reference frame CFD simulation used 1.2 million cells, where the virtual disk CFD simulation only used 680 thousand cells. The geometric parameters of the propeller required by the virtual disk model included the following; chord distribution, sweep angle, twist distribution, rotation rate and disk geometry.

4.5.2 Results and Discussion

The CFD results of the propeller rotated at a range of rpm which can be seen in
Figure 64. The results were compared to experimental data, as well as results of the moving reference CFD simulation. The result of a spreadsheet utilising BEM theory to predict the static thrust of the propeller is also included and served as an additional tool to validate the static thrust of the propeller and the implementation of it in CFD.

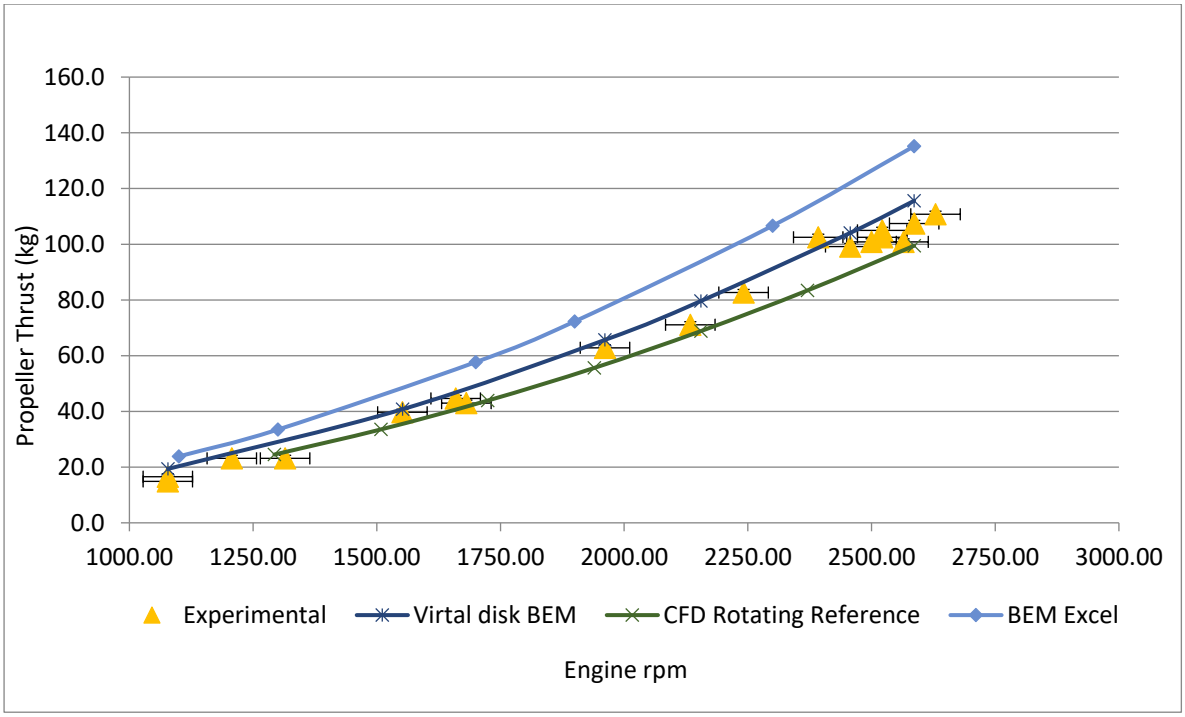

Figure 64: Static thrust comparison of different methods used

The virtual disk method proved to deliver accurate static thrust results. A small overprediction in thrust was observed when the CFD results were compared to the experimental results. The same overprediction of the thrust of the propeller was observed when compared to the BEM theory spreadsheet, only to a greater extent.

The overprediction in the BEM theory spreadsheet was expected as tip and hub losses were not taken into account when the static thrust was calculated. The Prandtl tip and hub corrections are dependent on having a helix (ϕ) angle, which needs a forward velocity of the propeller, and is not present when static thrust is measured.

The overprediction in static thrust of the virtual disk BEM method, can be as a result of the geometry and lift coefficients used by the BEM method. The lift coefficients were obtained through XFoil, which is known to overpredict the lift coefficient by as much as 6% (Gopalarathnam & Selig, 2001). A good correlation between the numerical (CFD) and the analytical (BEM theory spreadsheet) was obtained.

In Figure 65, one can see the velocity vector from the propeller, at a 90° and 180° sectional cut.

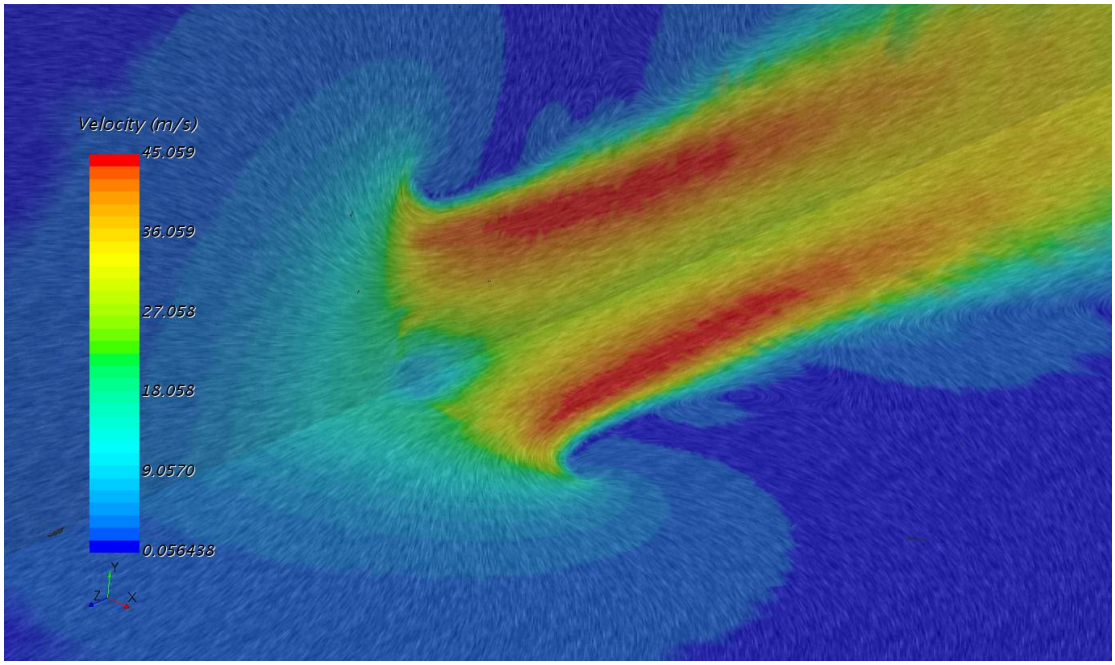

Figure 65: Line integral convolution velocity vector of the rotating reference model, with 90° and 180° sections cut.

The virtual disk method does not explicitly model the geometry of the propeller and is therefore independent of the location of the propeller. Thus, the resulting flow of the propeller is averaged out over the virtual disk. The method also reduces the number of cells in the mesh, which decreases the computational power needed when compared to the rotating reference method. Consequently, the virtual disk method was the method chosen to simulate the rotating propeller, as the flow entering the radiator was deemed more realistic and the heat transfer calculations would thus be more accurate.

Figure 66 shows the difference in the geometry of the propeller which was used by the models based on BEM theory and the geometry of the propeller used in the experiments. The BEM models slightly simplified the geometry near the centre of the propeller. These simplifications resulted in an increase of thrust delivered by the propeller. The increase of thrust is small, because the simplifications were made near the centre of rotation where little thrust is produced by the propeller.

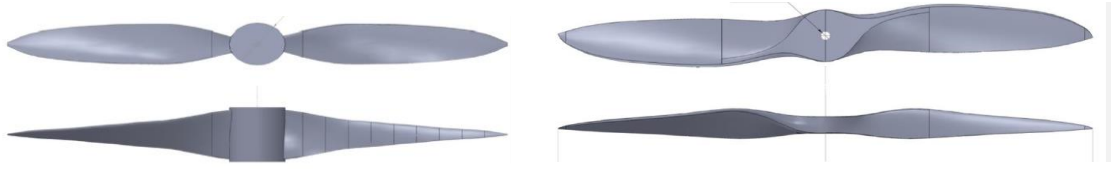

Figure 66: Simplified versus real propeller geometry

4.6 Detailed Radiator

The amount of detail in the geometry of the radiator tubes and fins is excessively high. To mesh such high detail takes a large number of cells. This level of detail increases the computational power required by the simulations to a great extent. To keep the computational power required by the simulation to manageable levels, only a small part of the radiator was simulated, because of the periodic nature of the geometry also makes it suitable to simulate only a small part of the radiator. In order to simulate the radiator as a simplified porous block, the porous coefficients obtained from the pressure drop characterisation (simulated with the detailed radiator CFD simulation) were required.

4.6.1 Setup

A cutout section (of a periodic nature) from the detailed radiator geometry used in the CFD simulation can, be seen in Figure 67. A fine mesh was used to capture the small details of the perforated fins. The flow domain consisted of a velocity inlet, pressure outlet and periodic planes. The periodic plane was used at the side, top and bottom of the flow domain. By using periodic planes at these locations, the influence of neighbouring fins and pipes can be simulated. The periodic planes achieved this by working in pairs and allowing the flow to transfer from one plane to another.

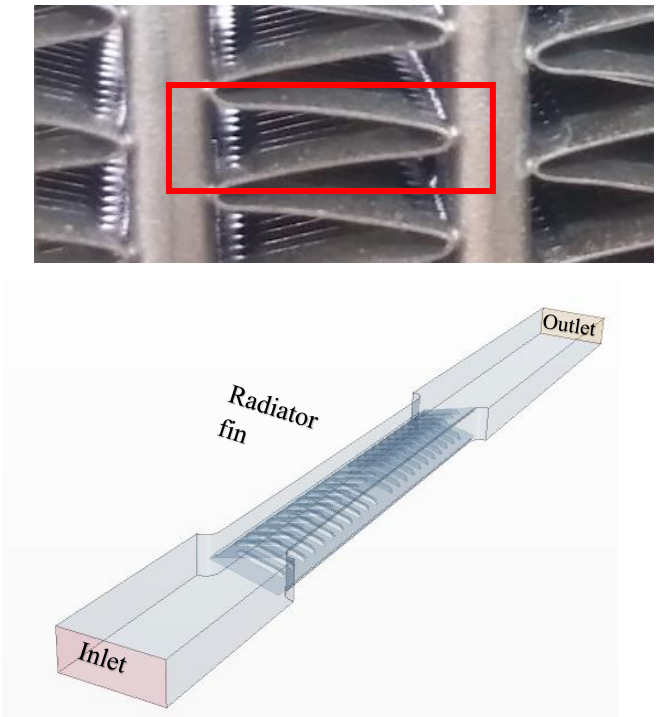

Figure 67: Radiator section used in the CFD simulation

The inertial and viscous porous coefficients can be determined by the pressure drop over the radiator, measured at different velocities.

4.6.2 Results and Discussion

The airflow through a section cut of the radiator was simulated, and the results of the pressure drop over the inlet and outlet face of the radiator are displayed in Figure 68. A second-order polynomial curve was fitted on the graph. Equation 6, together with the coefficients of the graph's equation were used to determine the porous resistance coefficients of the detailed radiator section.

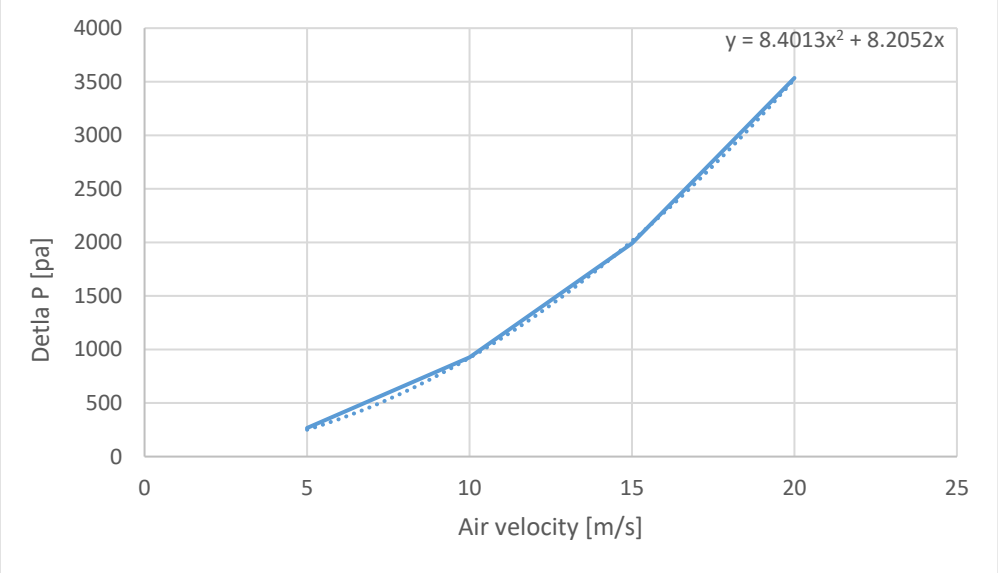

Figure 68: Pressure drop over radiator

When observing Figure 68, one can see that as the air velocity increased, so did the pressure drop over the radiator.

By using equation 6, the porous inertial and viscous coefficients were calculated in accordance to the heat exchanger interface used by the CFD simulation (CD-Adapco, 2018).

$$\frac{\Delta p}{L} = -(P_i|v| + P_v) \qquad \ldots 6$$

Where v is the velocity through the radiator, L the length of the radiator in the air flow direction and P_i , P_v the inertial and viscous resistance coefficients, respectively.

The inertial and viscous porous coefficients were determined to be 262.5 and 256.4 respectively. The airflow through the radiator can be seen in Figure 69 where three periodic planes are displayed next to one another.

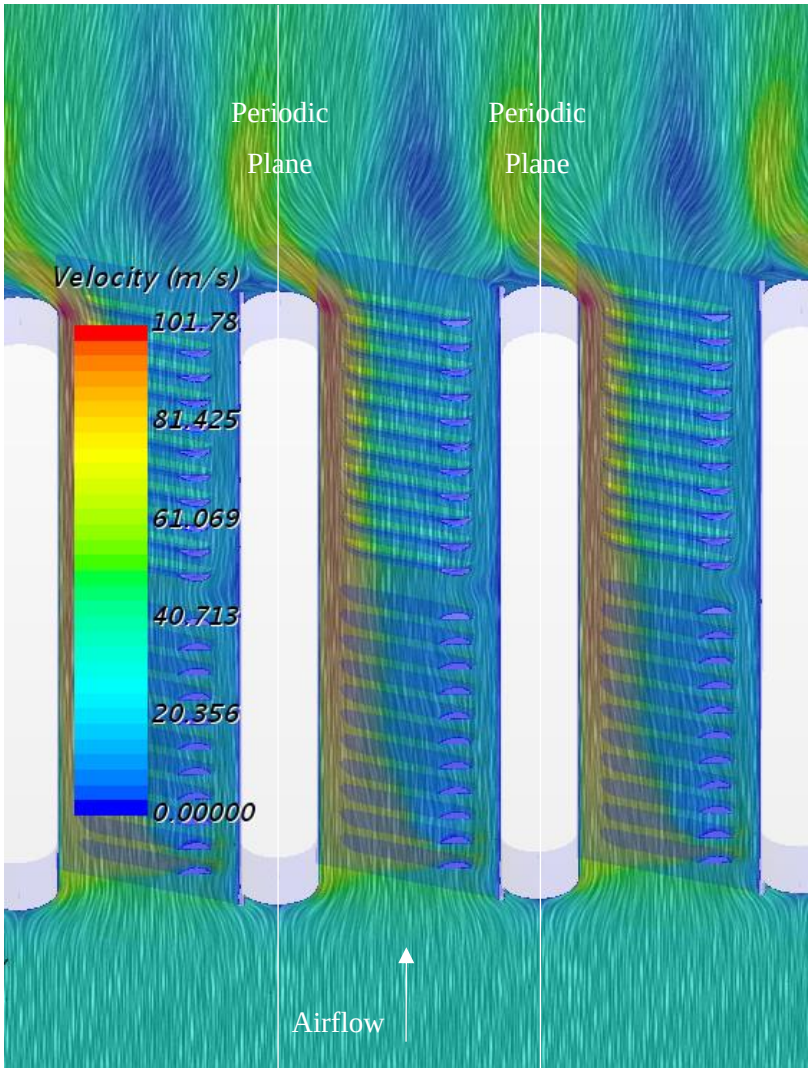

Figure 69: Line integral convolution velocity vector on the periodic planes of the airflow

The periodic planes assisted in creating a more realistic airflow, where one can observe the flow being influenced by the neighbouring tube and fins (Figure 69).

The porous coefficients will be validated in the next section, where the radiator will be simulated as a porous block using the porous coefficients obtained from this CFD simulation and results compared with measurements from wind tunnel experiments.

4.7 Porous Medium Radiator Model

A porous medium is a medium where the flow experiences a resistance in specific directions. The flow resistance is modelled by the pressure drop equation shown in the previous section, and the resistance can be specified as anisotropic values.

4.7.1 Setup

The pressure drop over the radiator was measured at different velocities. The flow domain consisted of a portion of the wind tunnel and the porous radiator. The simplistic geometry of the porous radiator consists of only a block, reducing the number of cells used in the mesh by a remarkable amount (Figure 70). The simulation domain boundaries consisted of a velocity inlet, pressure outlet, wind tunnel walls and a porous region to represent the radiator. Care was taken to measure the pressure drop over the simulated porous radiator, at the same physical locations where the pitot tubes were used in the wind tunnel experiments.

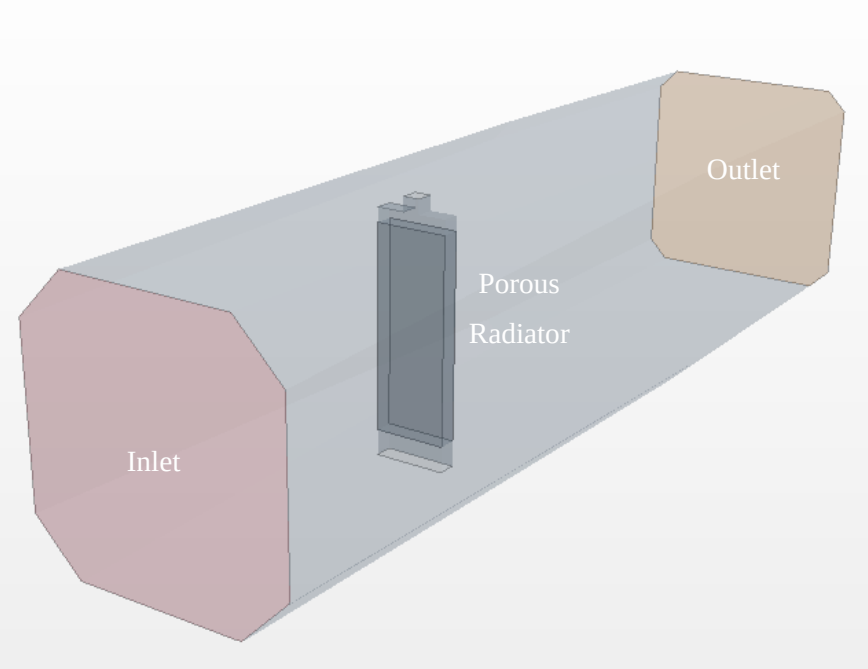

Figure 70: Computational domain of radiator in the wind tunnel

4.7.2 Results and Discussion

The porous coefficients obtained in section 4.6 were used in this CFD simulation to emulate the resistance of the radiator. The results of the pressure drop over the radiator can be seen in Figure 71.

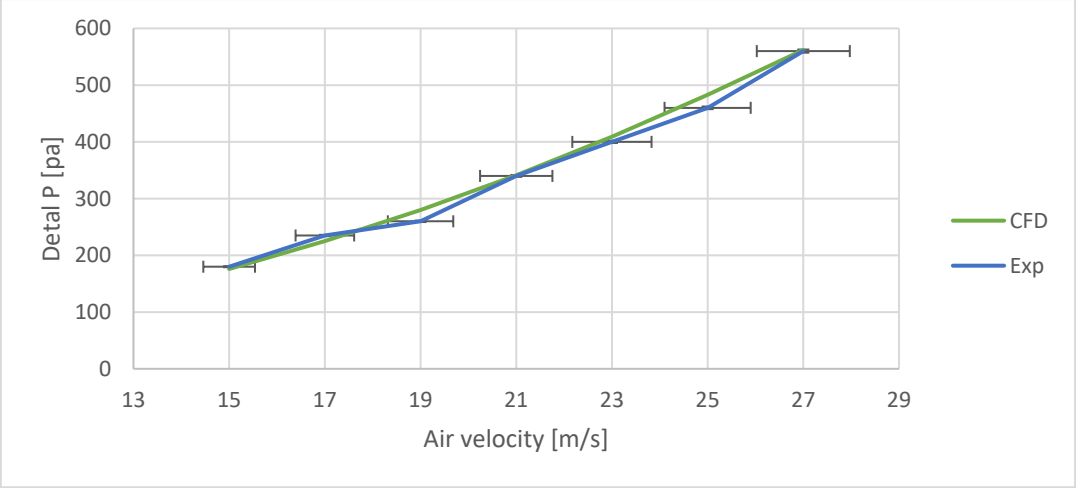

Figure 71: Pressure drop over radiator

The simplified porous block used the porous flow resistance coefficients determined in section 4.6, and the effect thereof on the static pressure in the flow domain can be seen in Figure 72.

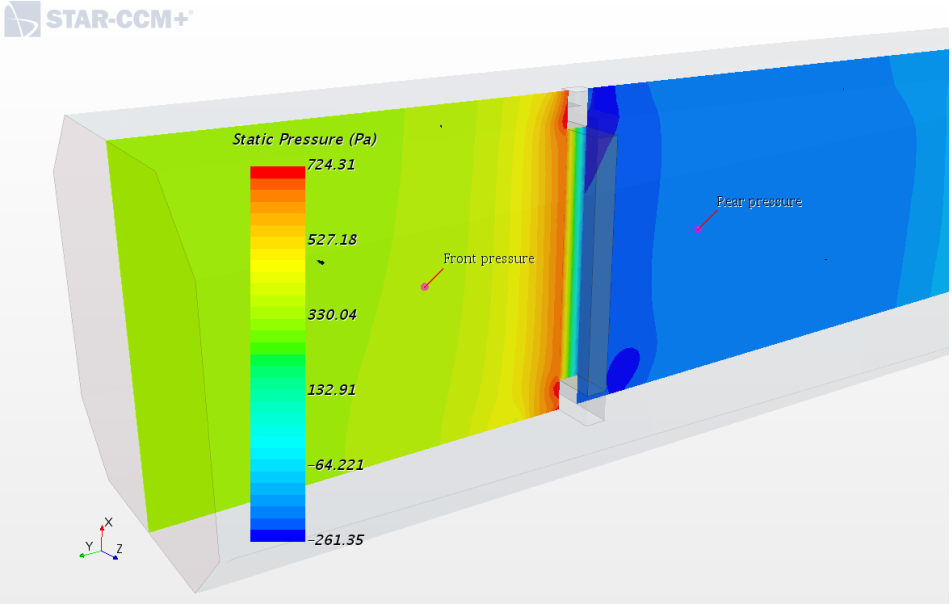

Figure 72: Static pressure drop over the porous radiator

The experimental results compared well with the CFD results, and thus the porous medium model is an accurate representation of the flow resistance created by the radiator, and can be used with confidence in an integrated simulation model.

4.8 Integrated Self-launch System Simulation

The integrated self-launch system simulation consisted of a CFD simulation that incorporated the CFD simulations previously described in chapter 4, into one integrated CFD simulation. Using CFD, the self-launch system can be analysed in much more detail when compared to experimental tests. The CFD simulation will also assist in making insightful alterations to the system, which can improve the heat exchange capabilities of the radiator.

4.8.1 Setup

The flow domain consists of the cylinder containing the self-launch system. The boundaries consist of a velocity inlet, pressure outlet, symmetric outer wall and a heat exchanger interface (Figure 73).

The self-launch system consisted of a pylon, exhaust, radiator, simplified engine and a virtual disk propeller. The polyhedral mesh used by the model can be seen in Figure 74. The mesh consisted of 4 million cells and an in-depth summary report of the simulation can be seen in Appendix F. The number of cells in the mesh was greatly reduced due to it being unnecessary to mesh the detailed geometry of the propeller.

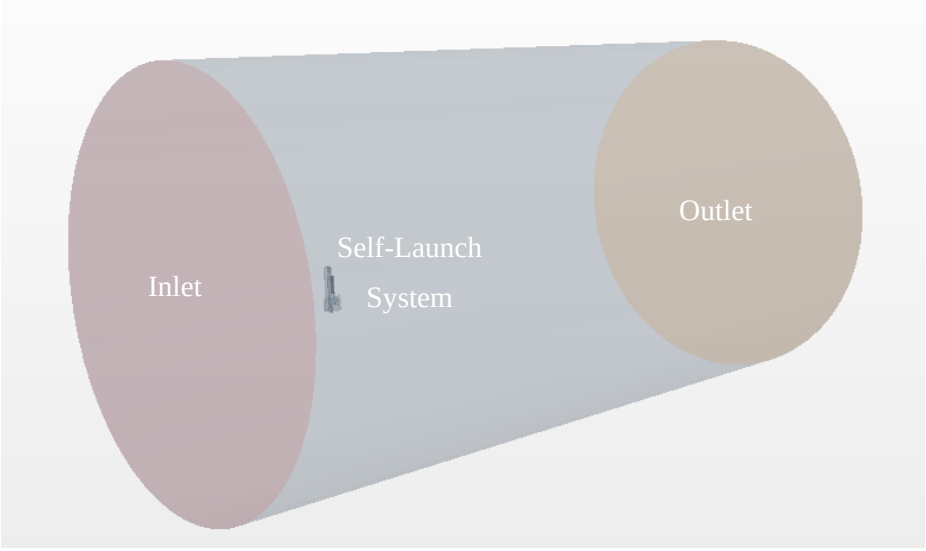

Figure 73: Computational domain of the self-launch system

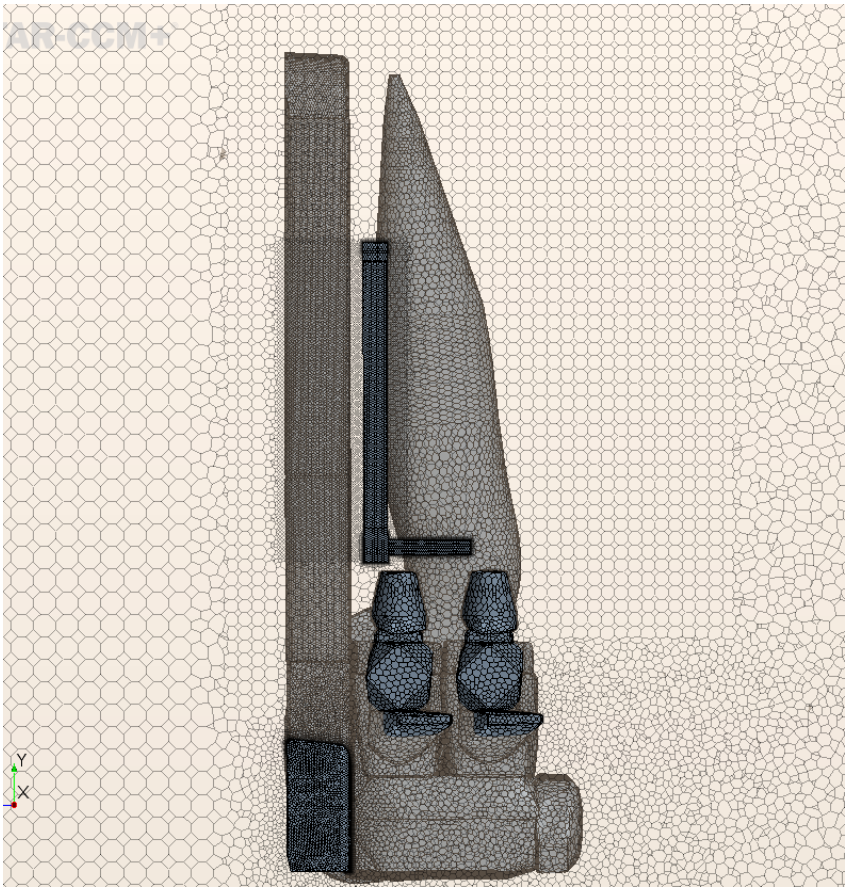

Figure 74: Components of self-launch system

The heat exchanger interface consisted of an overlapping cool air and hot coolant region. The coolant and air domain were connected to each other by using interfaces.

The radiator which is used in the self-launch system has a double pass coolant flow configuration. A baffle interface was used to divide the lower tank into an inlet and outlet tank. Using a baffle interface to divide the radiator core into two regions to simulate the double configuration, was not compatible with the heat exchanger interface. Instead, high porous resistance coefficients were used in the x and z direction to direct the water to flow only in a vertical direction, as seen in Figure 79.

4.8.2 Results and Discussion

A CFD simulation was set up to simulate the heat transfer of the self-launch system's radiator. The parameters measured were compared to data obtained from the integrated self-launch

system simulation, radiator characterisation experiments. Table 2 presents data obtained from the CFD results as well as the experimental results.

Table 2: CFD results of the self-launch system

	Engine rpm	Airflow (kg/s)	Coolant Flow (kg/s)	Coolant Inlet Temp. (°C)	Coolant Outlet Temp. (°C)	Air Inlet Temp. (°C)	Air Outlet Temp. (°C)	Heat Transfer Air (kW)	Heat Transfer Water (kW)
Experiment	5100	0.239	0.9	107.6	79.8	34.2	78.1	10.6	
CFD	5100	0.203	0.9	107.6	84.5	32.9	75.4	8.7	
% Difference	-	16.3	-	-	5.7	3.9	3.5	19.7	

A good correlation exists between the results predicted by the CFD simulation and the experimental data. All the results were within their allocated margin of uncertanty, except for the coolant outlet and the heat transfer, where a larger deviation in the results was observed. The airfow was underpredicted by 16%, but was still within the allocated uncertanties of the measurement, and was the main cause for the underpridiction of 20% in the heat transfer.

The ability for the CFD simulation to predict the coolant temperatures accurately, is of great importance in order to determine if the engine will be adequately cooled. To improve the accuracy of the coolant's outlet temperature, the UAG values can be adjusted to calibrate the model (Lidar, 2018). Thus, adjustments to the UAG values of the heat exchanger model available in the software code, were made to calibrate the model for more accurate outlet coolant temperatures. The UAG value was adjusted until the outlet temperature of the coolant was equal to the experiment value. The results of the adjustment in the UAG values can be seen in Table 3.

Table 3: Results of the CFD adjusted UAG self-launch system

	Engine rpm	Airflow (kg/s)	Coolant Flow (kg/s)	Coolant Inlet Temp. (°C)	Coolant Outlet Temp. (°C)	Air Inlet Temp. ('C)	Air Outlet Temp. (°C)	Heat Transfer Air (kW)	Heat Transfer Water (kW)
Experiment	5100	0.239	0.9	107.6	79.8	34.2	78.1	10.6	
CFD UAG Adjusted	5100	0.197	0.9	107.6	79.7	32.9	85.4	10.5	
% Difference	-	19.0	-	-	0.1	3.9	9.5	1.0	

The results of the adjustments in the UAG values lead to an increase in the outlet temperature of the air and a decrease in the coolant outlet temperature. As a result, a distinct increase in

the heat transfer of the system was observed. All the values of the adjusted UAG CFD simulation were within their respective margins of uncertainty except for the air outlet temperature, which was overpredicted by 9.5%. Errors in the air temperatures was expected, as only eight thermocouples could be used to capture the non-uniform temperatures over, the face of the radiator during the experiments. The outlet air temperature does not influence design deisions and therfore was the 9.5% overprediction was acceptable.

The results shown in Table 2 and Table 3 is represented in Figure 75 to Figure 78 for the sake a visual comparison reasons, where the marign of uncertainty is represented by the error bars.

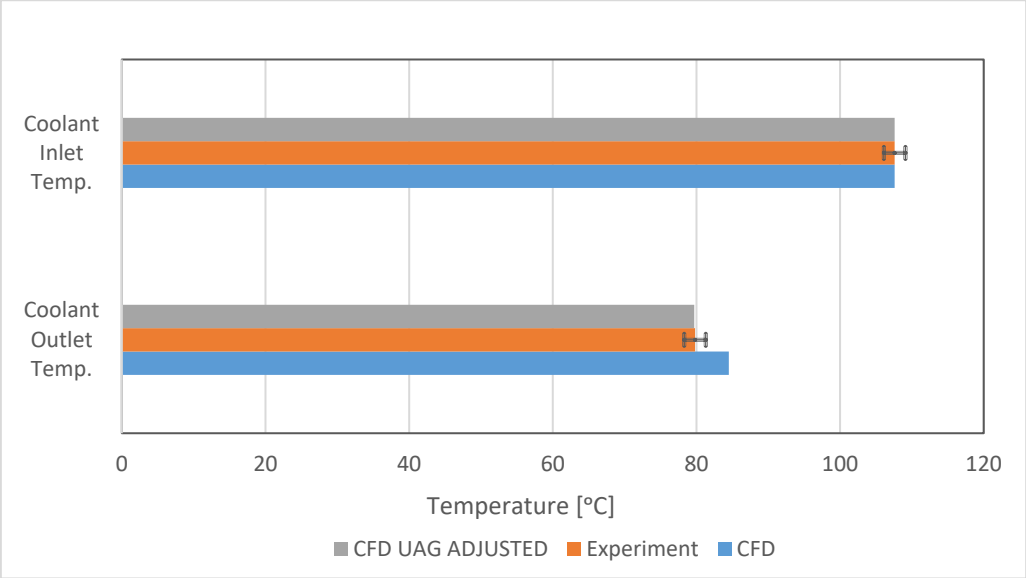

Figure 75: Coolant temperatures of the radiator

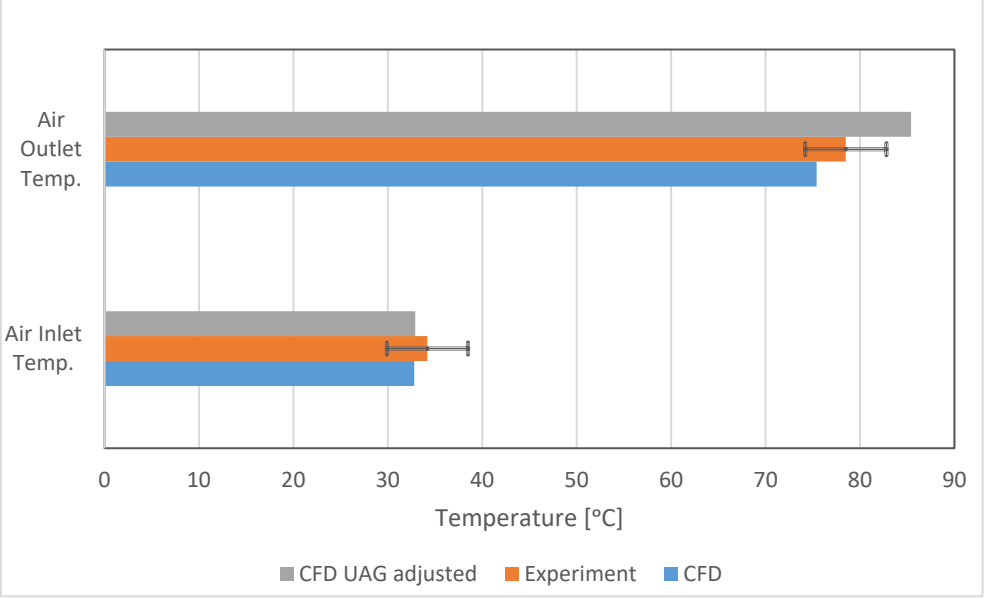

Figure 76: Air temperatures of the radiator

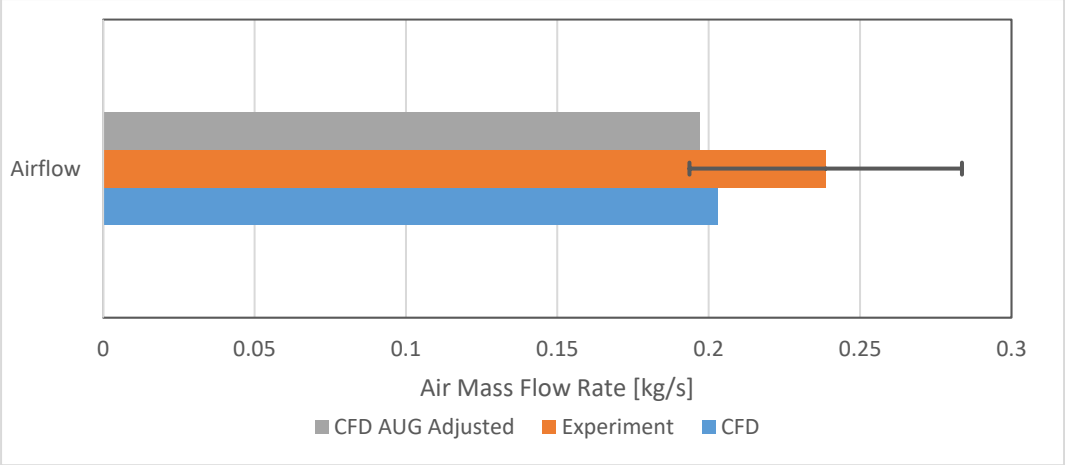

Figure 77: Airflow through the radiator

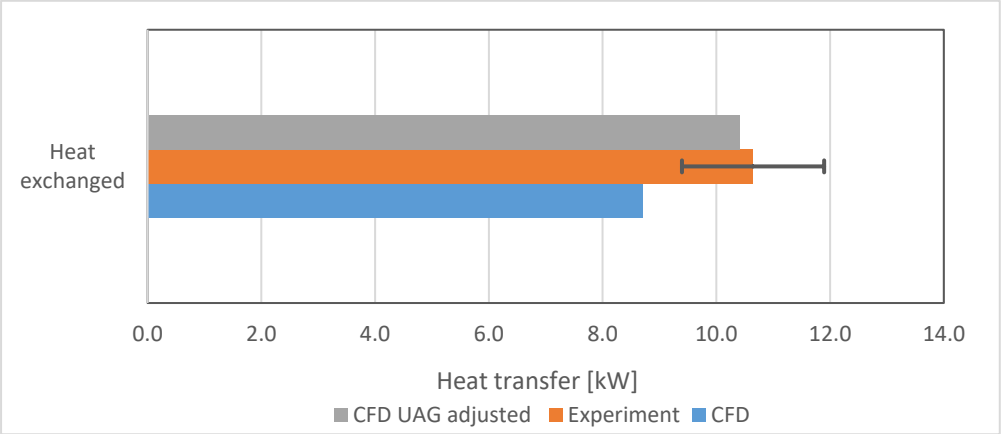

Figure 78: Heat transfer of the system

A CFD analysis was performed to investigate the various phenomena of the system and to acquire a better comprehension of the system.

The double pass configuration of the radiator was simulated using high porous resistance coefficients in the x and z directions, which forced the coolant to only flow in a vertical direction within the radiator core, to simulate coolant flowed in a similar manner only being able to flow y direction (vertical). In the upper and lower tank the coolant could flow freely (in any direction). After the coolant entered the inlet tank it was forced to flow vertically upwards until it reached the top tank of the radiator where it could flow freely again. The coolant was then forced to flow downwards towards the exit of the bottom tank. The coolant flow can be seen in Figure 79. In Figure 80, one can clearly see how the temperature of the coolant was reduced as the water flowed through the radiator.

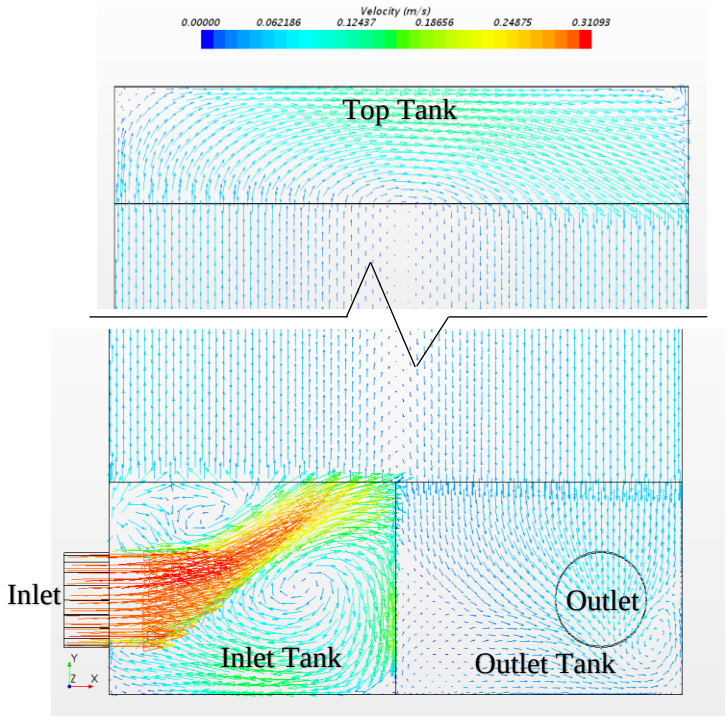

Figure 79: Sectional cut of the velocity vector coolant flow through the radiator.

Observing Figure 80, one can see how the temperature of the coolant was reduced as the water flowed through the radiator. A cool region is observed lengthwise in the second pass portion of the radiator, which was due to the mass flow rate being slower in that region.

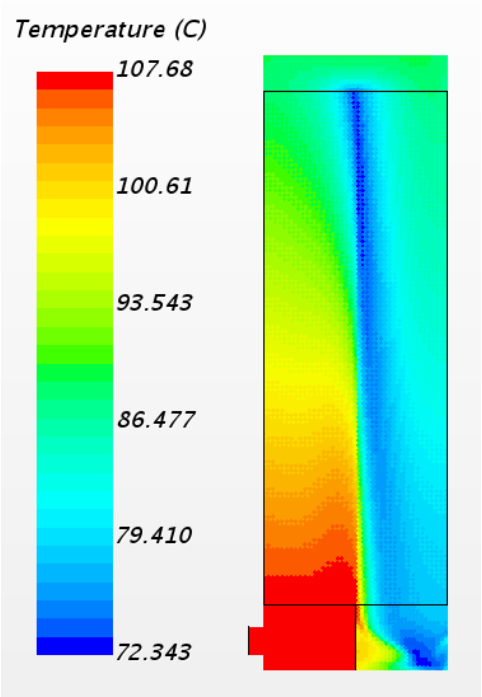

Figure 80: Left: Coolant temperature inside radiator

Figure 81 shows the velocity scalar (perpendicular to the face of the radiator) of the airflow at the front face of the radiator. After inspection, one can clearly see that the velocity on the right-hand side of the pylon was noticeably reduced. Further analysis is required to determine the cause of this phenomena.

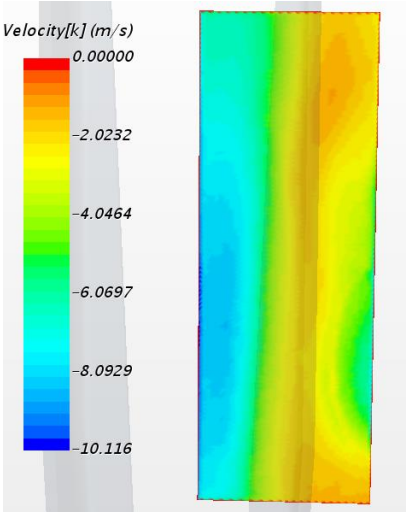

Figure 81: Velocity at the inlet face of the radiator

The path and the velocity magnitude of streamlines near the surface of the pylon (Figure 82) show a region where an upwards vortex was formed. The region corresponded to the reduction in the velocity, normal to the face of the radiator, also included in Figure 82. A noticeable recirculation zone was observed in the top right corner of the radiator.

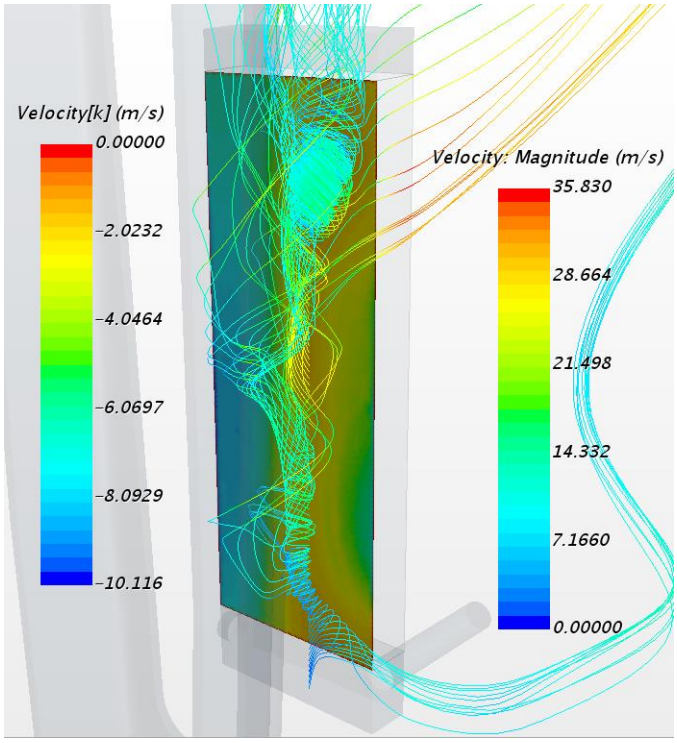

Figure 82: Flow of streamlines near the radiator inlet face and the velocity scalar on the radiator

A horizontal sectional cut (see Figure 83 for the location of the sectional cut) of the airflow can be seen in Figure 84. The wake created by the pylon resulted in a region of recirculation which started at the leading edge of the pylon where flow separation took place. The incoming airflow to the radiator was redirected past the radiator, instead of flowing through it.

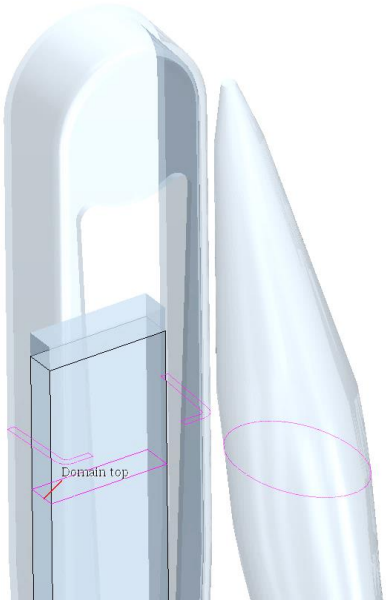

Figure 83: Horizontal sectional cut location

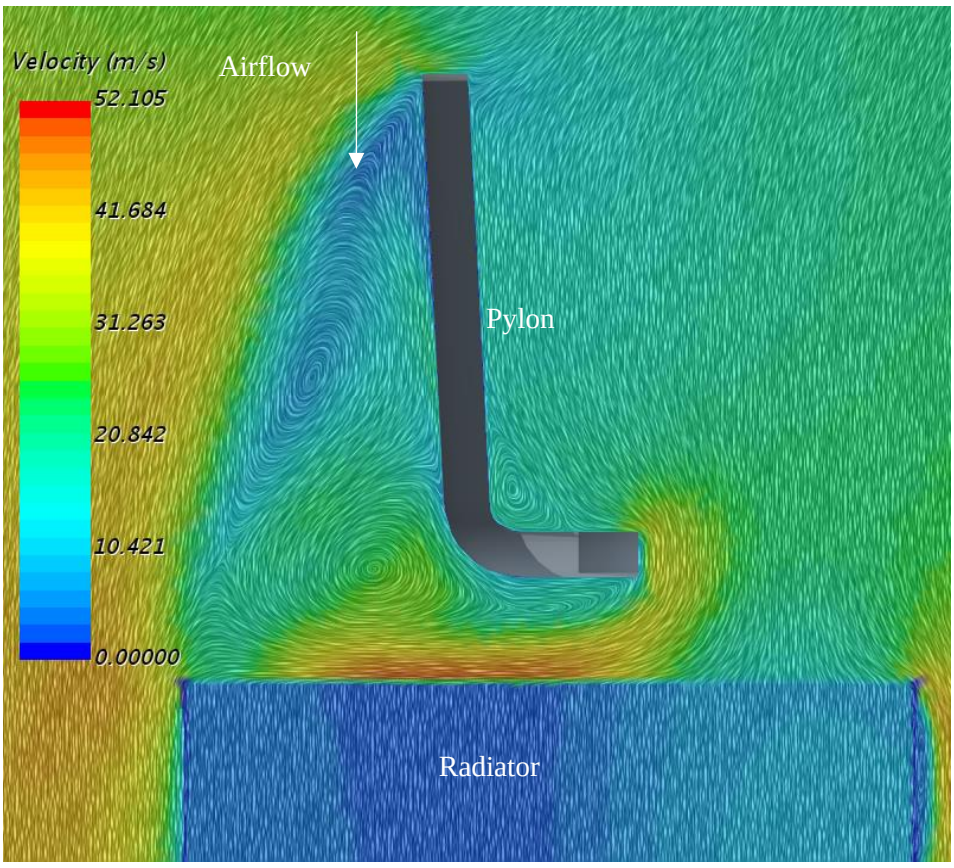

Figure 84: Velocity vectors of the airflow near the radiator

In a similar manner, a vertical sectional cut (see Figure 85 for the location of the sectional cut) of the airflow is presented by Figure 86: Velocity vector of the airflow near the self-launch system and shows how a large portion of the airflow flowed over the top of the radiator and not contributing to the heat removal from the radiator core. Figure 86 also shows how the porous resistance coefficients forced the airflow in a straight line through the radiator.

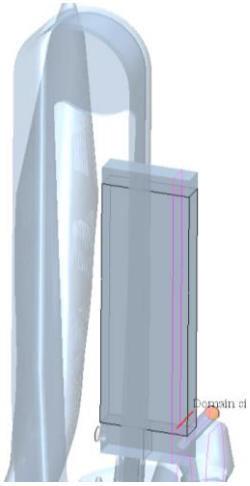

Figure 85: Vertical sectional cut location

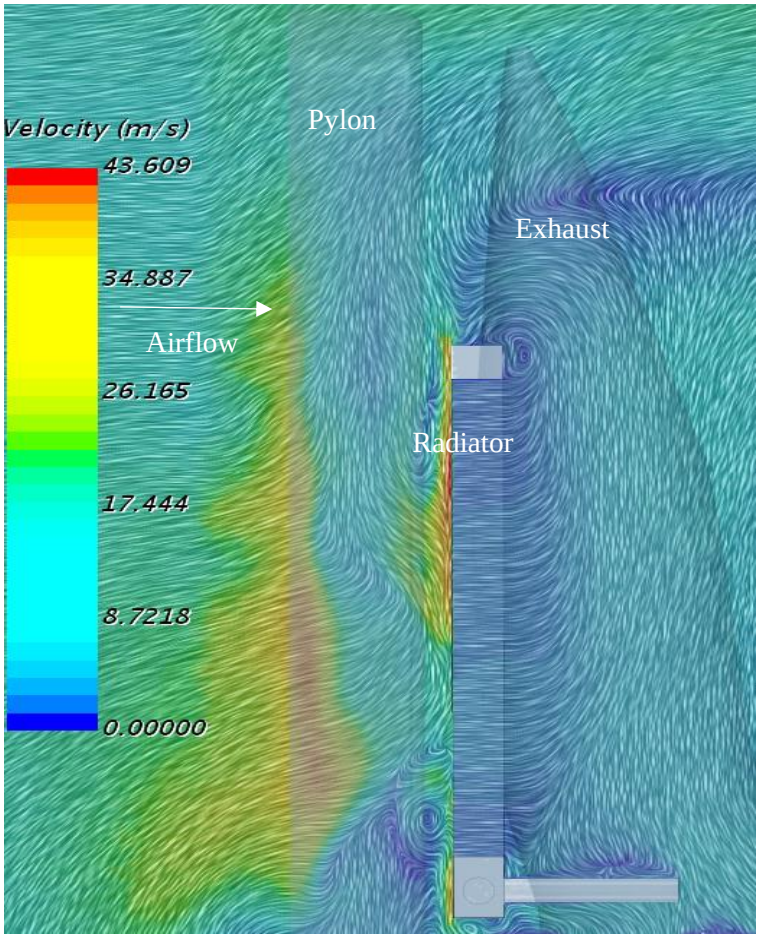

Figure 86: Velocity vector of the airflow near the self-launch system

The temperature distribution on the inlet and outlet face of the radiator is displayed in Figure 87. A hot spot was created by the recirculating airflow (Figure 82), was due to the poor airflow through the radiator at this region. A similar hot spot was observed in the experimental data (Figure 52). A correlation can be seen between the outlet air temperature of the simulation and the experiment. The outlet air temperate is in accordance to the coolant's temperate distribution in the radiator (Figure 80).

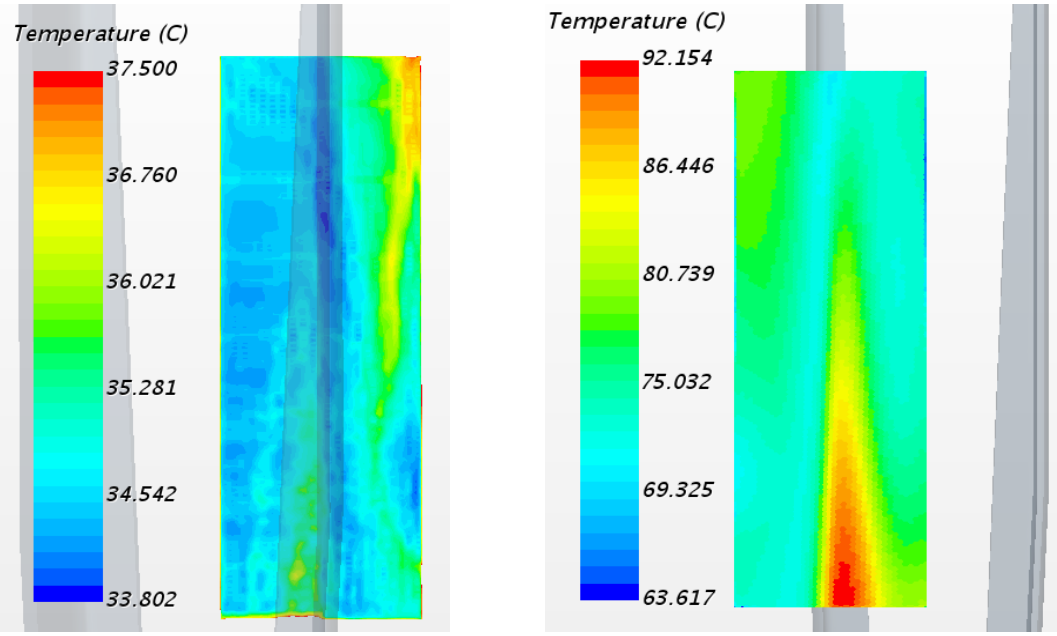

Figure 87: Left: Temperature distribution of the inlet air on the face of the radiator, Right: Temperature distribution of the inlet air on the face of the radiator

The airflow near the location of the hotspot is in a recirculation region. The air is moving slower at the location of the hot spot, due to the wake and the recirculating air. The air spend an increased period near the warm radiator and an increase in the temperature of the air is observed.

A small oscillation was observed in a few of the quantities that were monitored. The outlet temperature of the radiator, oscillated at 84.5°C by an average of 0.5°C, as seen in Figure 88.

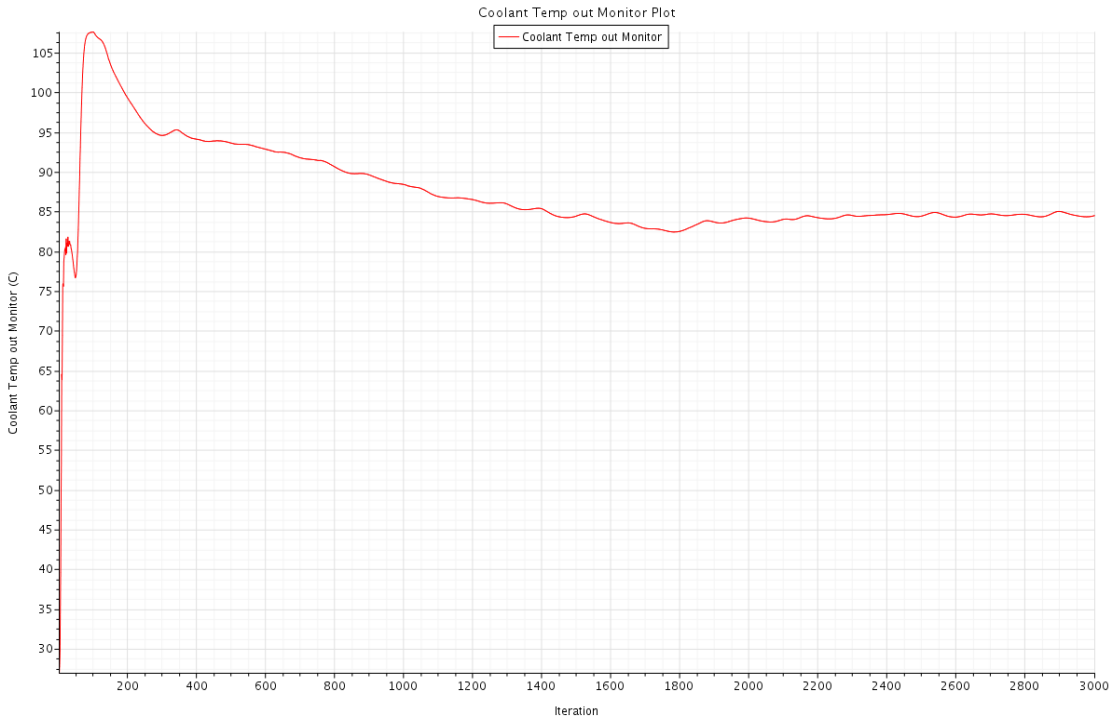

Figure 88: Oscillating coolant outlet temperature

Lidar (2018) used the same heat exchanger model of Star CCM+, to simulate the heat transfer of a car's radiator, and observed similar minor fluctuations in the temperatures of the radiator monitored. Lidar (2018) reasoned that vortex shedding could have caused the oscillation in the results, and recommended running the CFD simulation as a transient simulation or alternatively taking the mean value of the last few hundred iterations after convergence was met.

To determine if a similar vortex shedding behaviour in the integrated self-launch system simulation occurred, the velocity vectors of flow behind the radiator was inspected and plotted at different iteration steps. Figure 89 confirms that vortex shedding was present in the simulation. It is suspected that the vortex shedding may have caused the minor oscillation in few quantities that were monitored. The oscillation in the values of the parameter may indicate the presence of transient effects, such as vortex shedding in the flow, which is incapable of being captured by a steady state solution (Koren, 2015).

The geometry of the self-launch system were also further simplified and a high quality geometry surface was used to create an extensive fine mesh consisting of triple the amount of cells (12 million) used by current polyhedral mesh, to determine if the mesh used may have caused the minor oscillating quantities that were monitored. No noticeable difference in the oscillation was observed using the finer mesh.

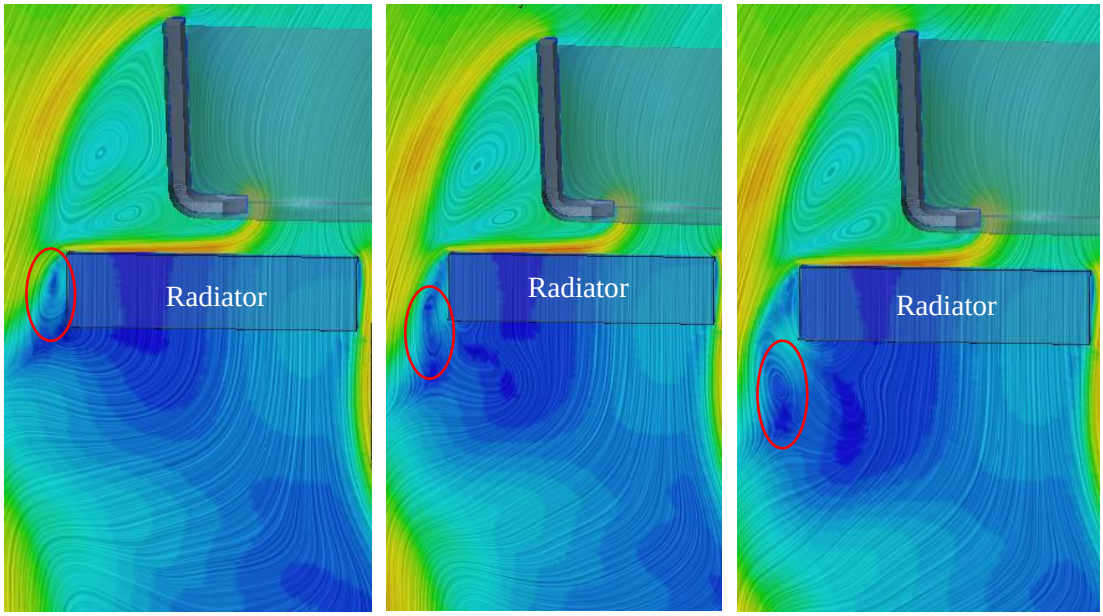

Figure 89: Velocity vector plotted at different iteration steps showing vortex shedding

According to CD-Adapco (2018), using very large porous resistance coefficients can lead to minor instabilities in the CFD simulation. The highly energised airflow behind the propeller met the inlet face of the radiator at an angle. To force the airflow in straight line through the porous radiator, high porous resistance coefficients (in the x and y direction of the simulation) had to be used.

The value of the oscillation was smaller than the instrumental uncertainty of the thermocouple used to measure the outlet temperature of the coolant. Thus, the mean value over the last few hundred iterations was chosen to provide a single value for the outlet temperature of the coolant.

4.9 Summary

The heat transfer of the self-launch system was simulated with the aid of CFD. The final integrated CFD simulation, utilised several sub-models to provide an efficient and accurate representation of the complete machine and the relevant phenomena.

First, the airflow over an NACA 0012 airfoil was simulated using CFD, to determine the aerodynamic coefficients of the airfoil. An airfoil was chosen, as it is the basis of a propeller consisting of several airfoil sections. The resultant static thrust predictions were found to be in agreement with that of experimental tests.

Thereafter, two methods were investigated to identify a computationally efficient method to simulate the airflow from a rotating propeller. The rotating reference frame used the exact geometry of the propeller and a stationary mesh. By effectively 'rotating' the momentum source terms inside the governing equations, the method delivers acceptable results at a reasonably efficient computational cost. After inspecting the wake of the propeller, it was found that the method was dependant on the angle in rotation of the propeller.

An alternative method to simulate the propeller, was to use the virtual disk method. The method did not need to mesh the exact propeller geometry. Instead it used various geometry parameters of the propeller to model the momentum source terms for the airflow, representing the effect from the rotating propeller as an actuator disk. This method utilised BEM theory to simulate the rotating propeller. The results were accurate when compared to experimental results and were not dependent on the location in the rotation of the propeller. The method also used significantly fewer cells than the rotating reference models. It was for these reasons that the virtual disk method was chosen as sub-model to simulate the propeller in the integrated system simulation.

The last sub model concerned an approximation of the radiator geometry and the heat transfer characteristics. A small section of the radiator was simulated in full detail to determine the porous resistance coefficients of the radiator. The porous coefficients were then used to approximate the radiator as a simplified porous block. The pressure drop predicted by the simplified radiator sub-model, compared very well with the experimental results.

The final CFD simulation model incorporating all the sub-models gave satisfactory results when compared to the experimental results. Adjustment to the UAG values of the heat transfer

model available in the software code, was necessary to calibrate the model for an accurate outlet coolant temperature.

The airflow through the radiator was examined, and the influence of the wake of the propeller and the location of the radiator behind the pylon revealed insightful results. It was clear from an inspection of the simulation results, that the airflow pattern through the radiator is far from optimal, and that this maldistribution negatively impacts the heat removal from the radiator. The engine is restricted from running at full speed, due to this significant effect. It is therefore crucial to investigate mechanisms with which to improve the flow distribution over the radiator's face.

5. RADIATOR HEAT EXCHANGE IMPROVEMENTS

Different approaches to improve the heat removal capabilities of the self-launcher radiator were explored by using the results and findings of the CFD analysis in section 4.8.

5.1 Identified Areas for Improvement

The self-launch system overheated when running at high engine rpm. It soon became evident that the heat removal capabilities of the radiator were inadequate. In section 4.8 it was determined that the airflow through the radiator was remarkably poor, and that one must improve the airflow through the radiator to increase the heat transfer of the radiator. The air mass flow rate of the radiator is calculated by equation 7.

$$\dot{m} = \rho\, v\, A \qquad \ldots 7$$

The air mass flow rate ($\dot{m}$) is equal to the product of the density (ρ), the bulk air velocity (v), and A the area of the inlet face of the radiator.

The confined space in which the self-launch system must fit, limits the choice parameters of the system that can be modified. The aerodynamic effects that a self-launch system has on a sailplane, as discussed in section 1.4, must also be kept in mind when making design changes to the system.

The air mass flow rate through the radiator can be improved by enlarging the area of the radiator, increasing the density of the air or increasing the velocity of flow through the radiator. Due to the limited space available for a larger radiator, it was not considered. Increasing the density of the air, has only a small influence on the heat transfer of the system and is difficult to control. Thus, the largest room for improvement was to increase the velocity of the air flowing through the radiator.

By utilising CFD, the effects of proposed design changes to the self-launch system could be determined. The integrated CFD simulation of the system (described in section 4.8) was used as a baseline to determine how the heat transfer capabilities of the self-launch system could be improved by design modifications made to the self-launch system.

5.2 Radiator Scoop

The self-launch system had space next to the pylon available, where a scoop could be fitted to improve the airflow through the radiator. The space was limited, and the scoop could therefore not be any wider than the radiator, in order to still fit inside the engine bay.

5.2.1 Design Concept

A radiator scoop attached to the pylon can be used to force the separated air, at the leading edge of the pylon, through the radiator. The basic design concept of the proposed radiator scoop can be seen in Figure 90. The main function of the scoop is to capture and redirect the flow that was separated by the leading edge of the pylon, to flow through the radiator.

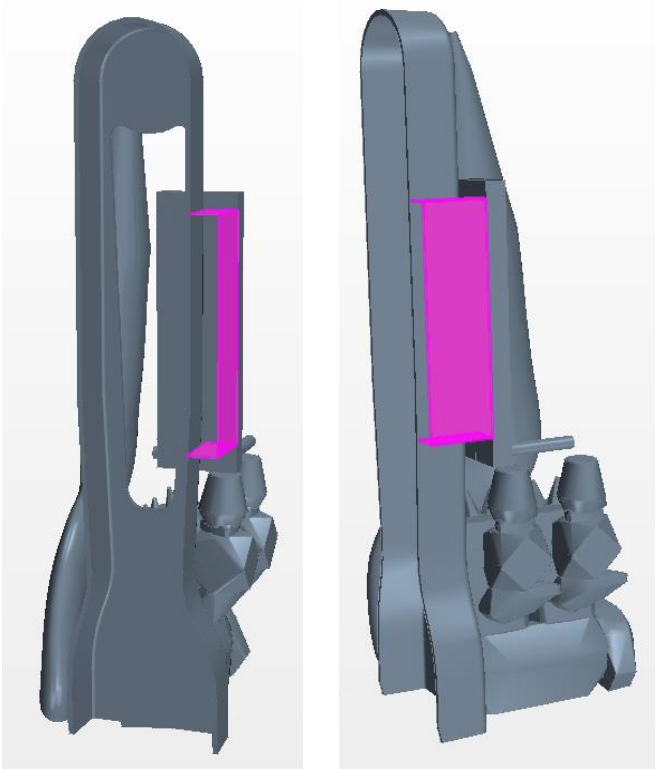

Figure 90: Basis of the proposed radiator scoop

The upward flowing air near the inlet face of the radiator (Figure 82) can be forced through the radiator by adjusting the horizontal faces of the radiator scoop to be in better alignment with streamlines, as shown in Figure 91. The adjustment made to the lower face of the scoop assists in directing more air through the lower section of the radiator.

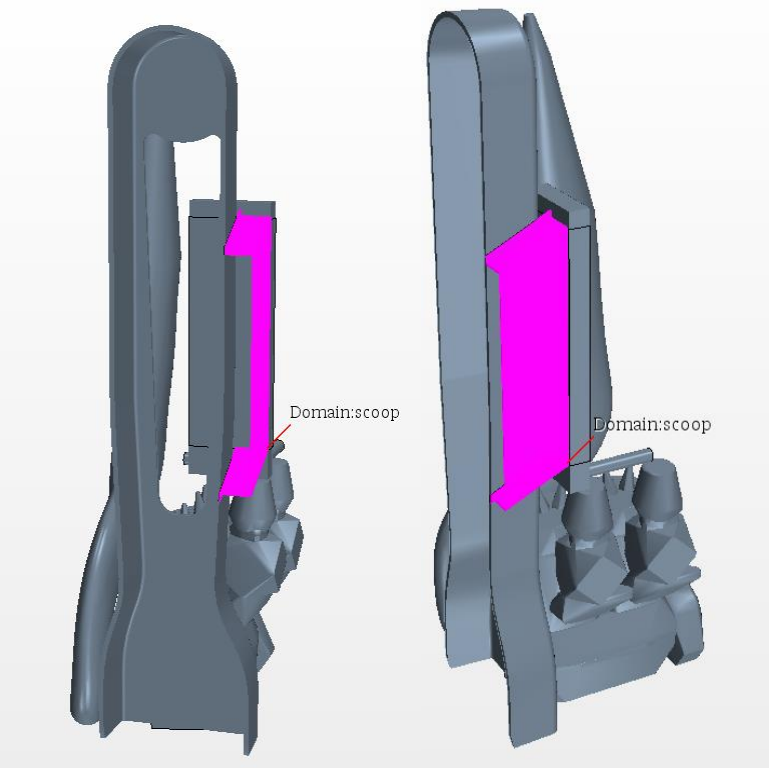

Figure 91: Geometry of the radiator scoop

Figure 92 shows the detailed drawing of the radiator scoop. The radiator scoop was made out of aluminium 6080 and bent into shape. The proposed scoop is thus uncomplicated and robust, as well as and quick and affordable to manufacture.

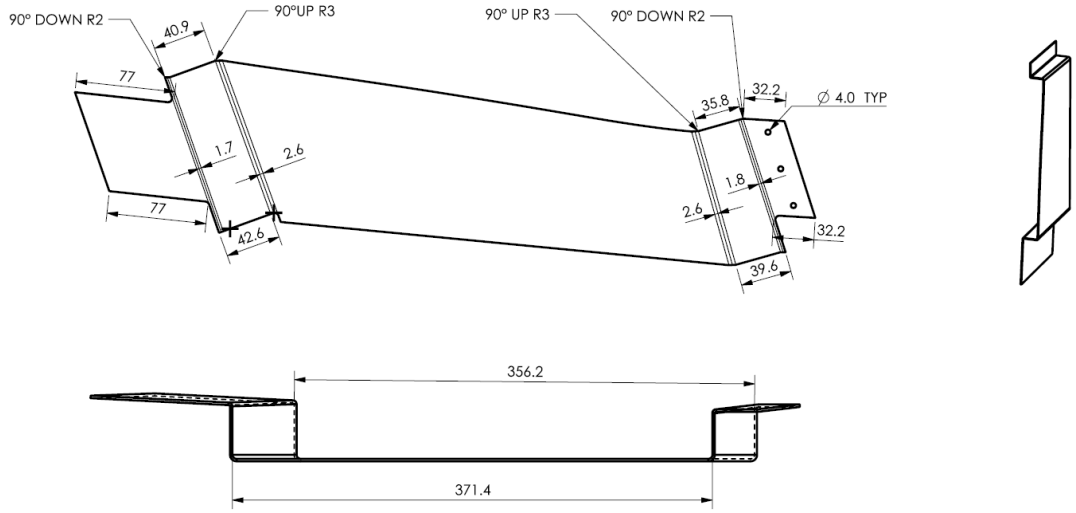

Figure 92: Detailed drawing of the radiator scoop, indicating the uncomplicated design layout results

5.2.2 Results and Discussion

The influence the radiator scoop had on the heat transfer characteristics of the self-launch system can be seen in Table 4.

Table 4: Radiator scoop results

	Engine Speed (rpm)	Airflow (kg/s)	Coolant Flow (kg/s)	Coolant Inlet Temp. (°C)	Coolant Outlet Temp. (°C)	Air Inlet Temp. (°C)	Air Outlet Temp. (°C)	Heat Exchanged Air (kW)	Heat Exchanged Coolant (kW)
Experiment Baseline	5100	0.24	0.90	107.6	79.8	34.2	78.5	10.6	
Radiator Scoop (CFD)	5100	0.30	0.90	107.6	76.0	32.9	74.4	11.9	

In Figure 93 one can see how the recirculate flow was noticeably decreased by the additional captured by the radiator scoop. Figure 94 shows a significant improvement in the air velocity over the radiator. The increased velocity was especially noticeable on the right-hand side of the radiator, where the radiator scoop was installed and the recirculation region was reduced (although not fully eliminated yet).

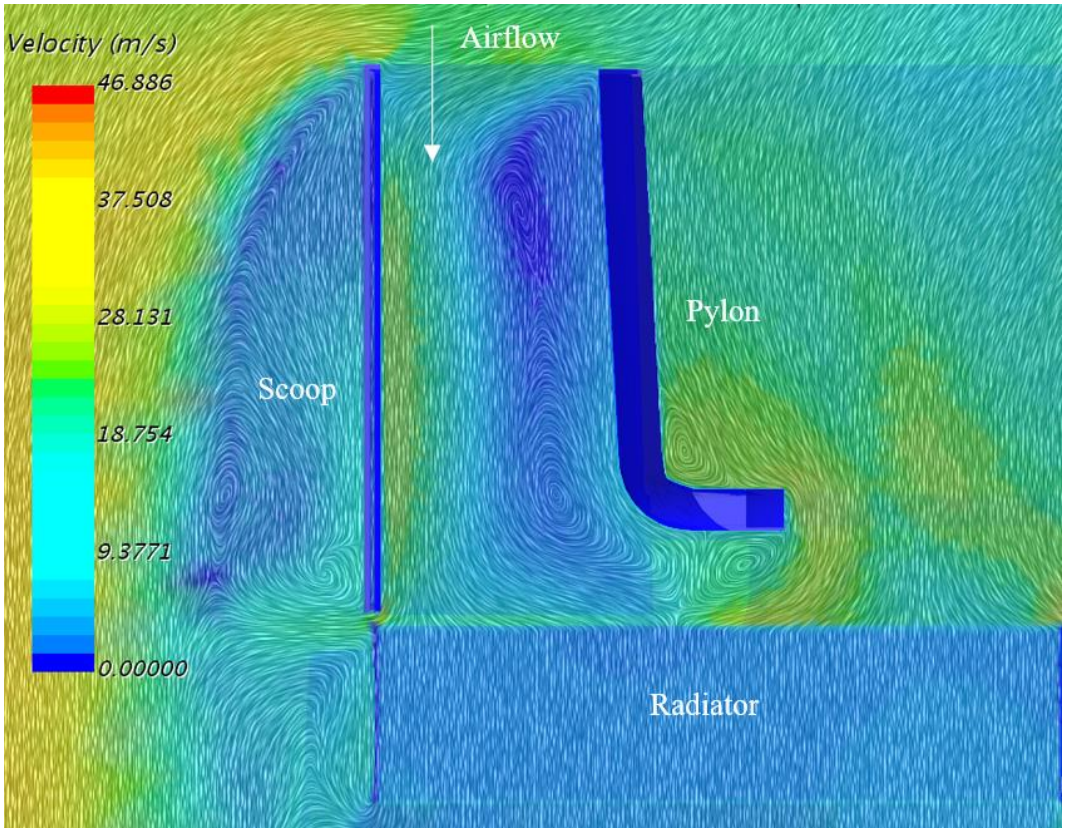

Figure 93: Velocity vector of the flow near the leading edge of the pylon

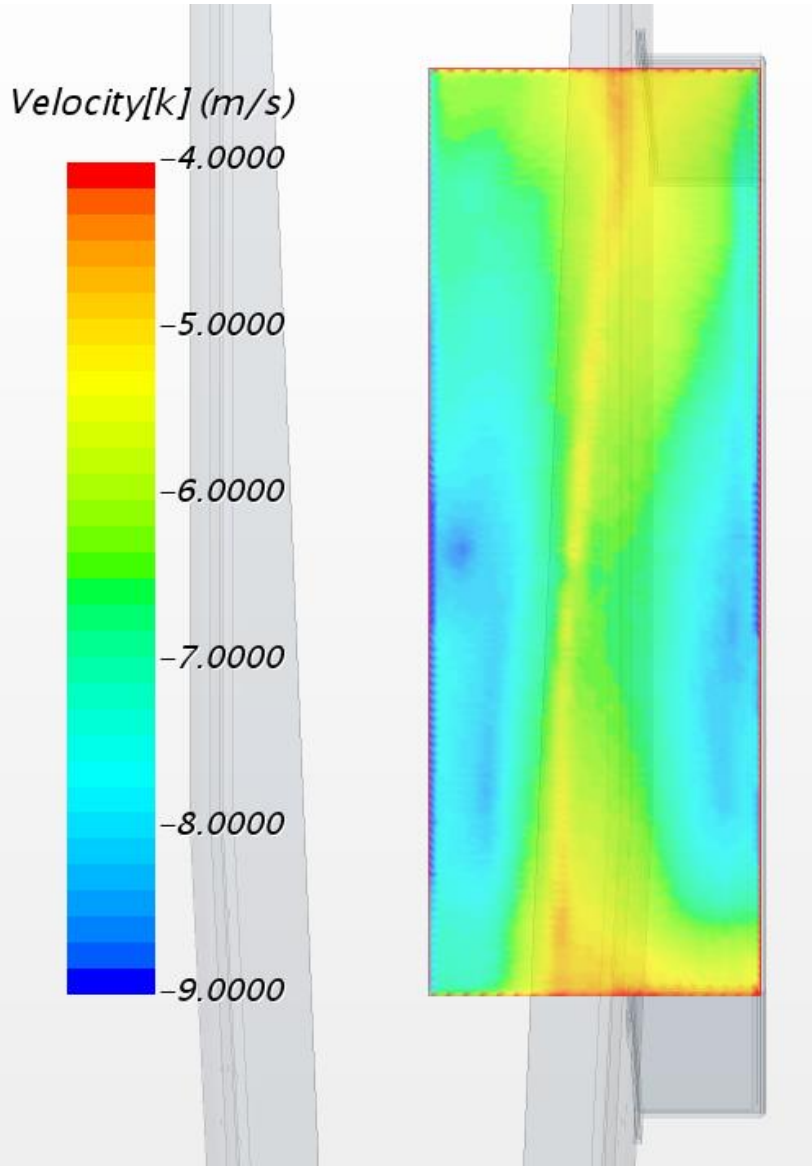

Figure 94: Velocity magnitude of flow entering the inlet face of the radiator

Figure 95 shows how the airflow was successfully redirected through the radiator. One can see how the diagonal upper face of the radiator scoop prevents the airflow from flowing flow over the top of the radiator, as it did without the scoop installed (Figure 95).

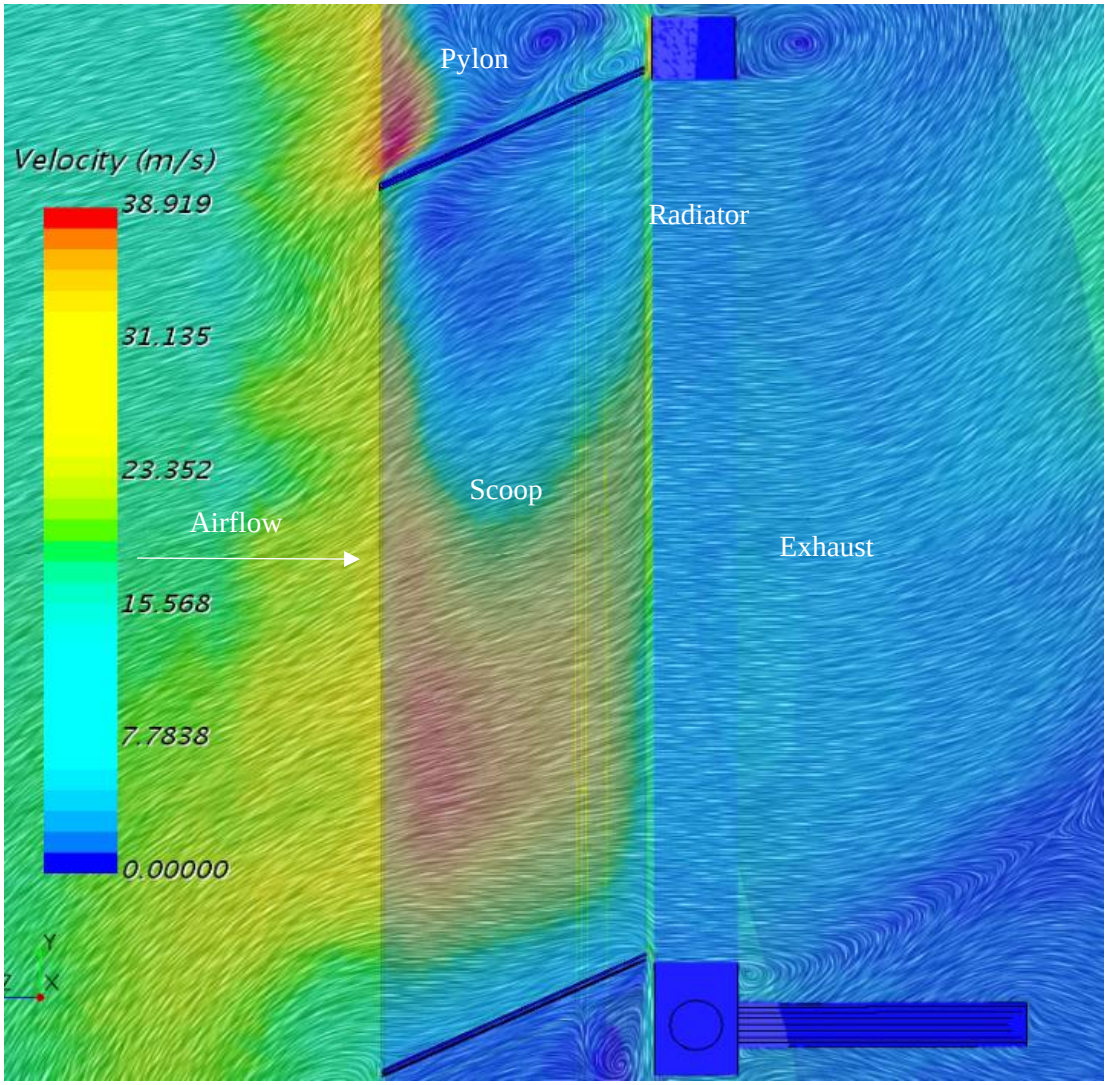

Figure 95: Velocity vector of the airflow within the radiator scoop

The improved results of the radiator scoop were indeed promising. The airflow through the radiator increased from 0.24 kg/s to 0.3 kg/s (25% increase). The increased airflow resulted in a 12% increase in the heat exchanged by the radiator and a 5% decrease in the coolant outlet temperature.

5.3 Pylon Fairing

Fairings can be used to reduce the drag and the size of the wake created by a body, as discussed in section 2.3.4.

5.3.1 Design Concept

A fairing can be installed at the leading edge of the pylon in an attempt to reduce the flow separation that occurred at the leading edge (Figure 84). Figure 96 shows a proposed fairing profile projected over the current pylon. Note how the leading edge of the fairing is pointing in the direction of the incoming flow and how a gentle gradient was used. The fairing could assist in reducing the adverse pressure gradients of the airflow, which can decrease flow separation and the size of the wake created by the pylon and the fairing.

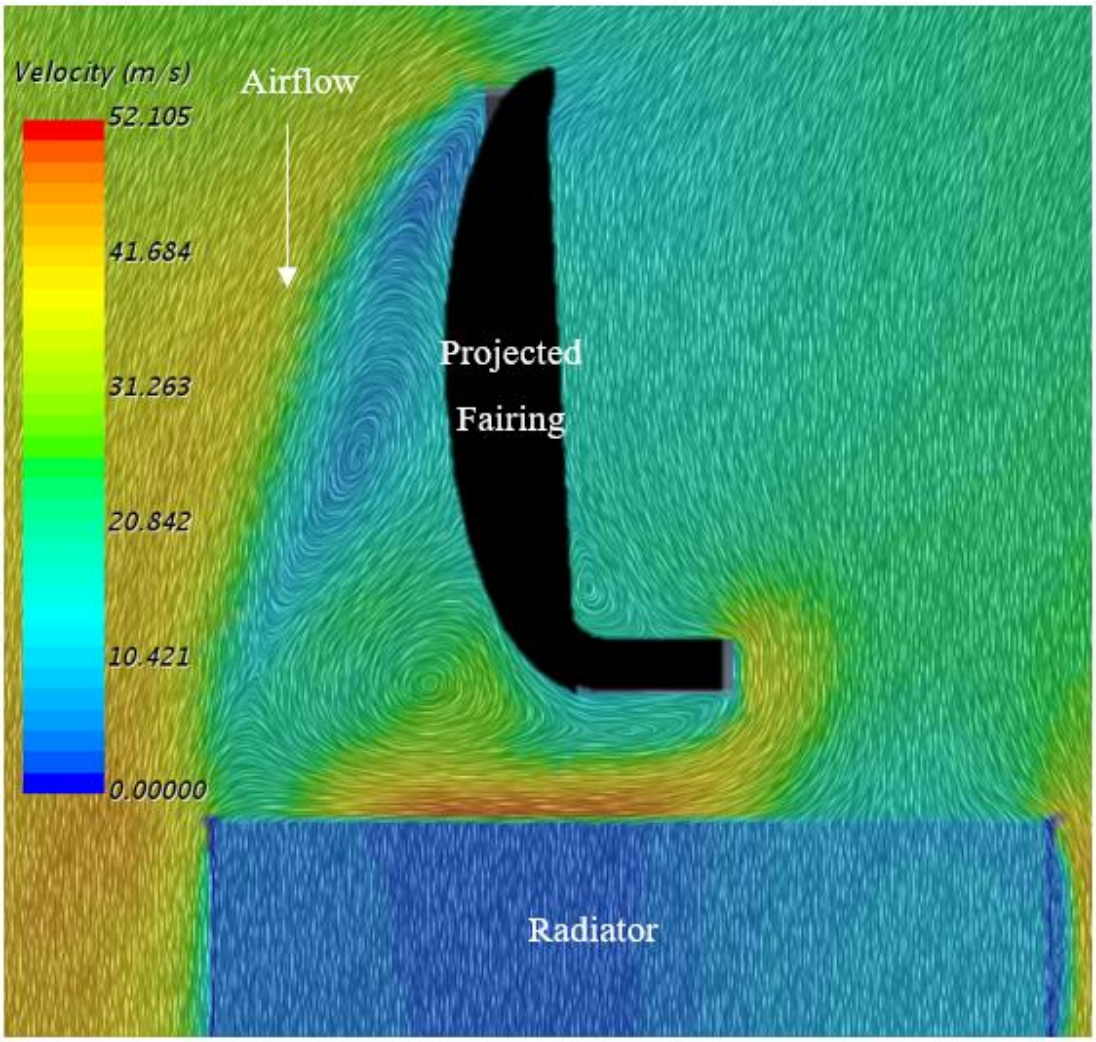

Figure 96: Sectional cut through the radiator and pylon with the proposed fairing profile projected on the velocity vector of the unmodified pylon.

The second modification was thus proposed to be a fairing installation on the leading edge of the pylon, as presented in Figure 97.

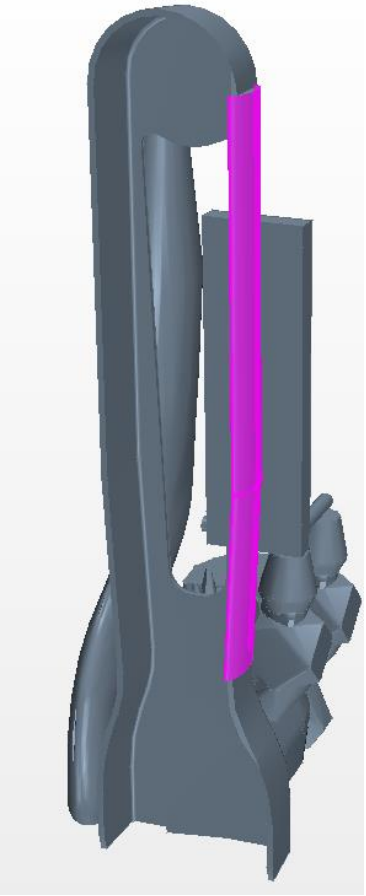

Figure 97: Location of the pylon fairing

5.3.2 Results and Discussion

The effect that the pylon fairing had on the airflow can be seen in Figure 98 and Figure 99. Table 5 presents the CFD results with the pylon fairing installed.

Table 5: Radiator fairing results

	Engine Speed (rpm)	Airflow (kg/s)	Coolant Flow (kg/s)	Coolant Inlet Temp. (°C)	Coolant Outlet Temp. (°C)	Air Inlet Temp. (°C)	Air Outlet Temp. (°C)	Heat Exchanged Air (kW)	Heat Exchanged Water (kW)
Experiment Baseline	5100	0.239	0.9	107.6	79.8	34.2	78.5	10.6	10.6
Pylon Fairing (CFD)	5100	0.285	0.9	107.6	75.9	32.9	74.4	11.9	11.9

The increase in the airflow through the radiator resulted in a 12% increase in the amount of heat exchanged by the radiator. The airflow distribution over the inlet face of the radiator was improved considerably (Figure 98). A large increase on the right-hand side of the radiator was observed. Figure 99 further shows how the recirculation region had been notably reduced, by providing a more streamlined flow path around the pylon's edges.

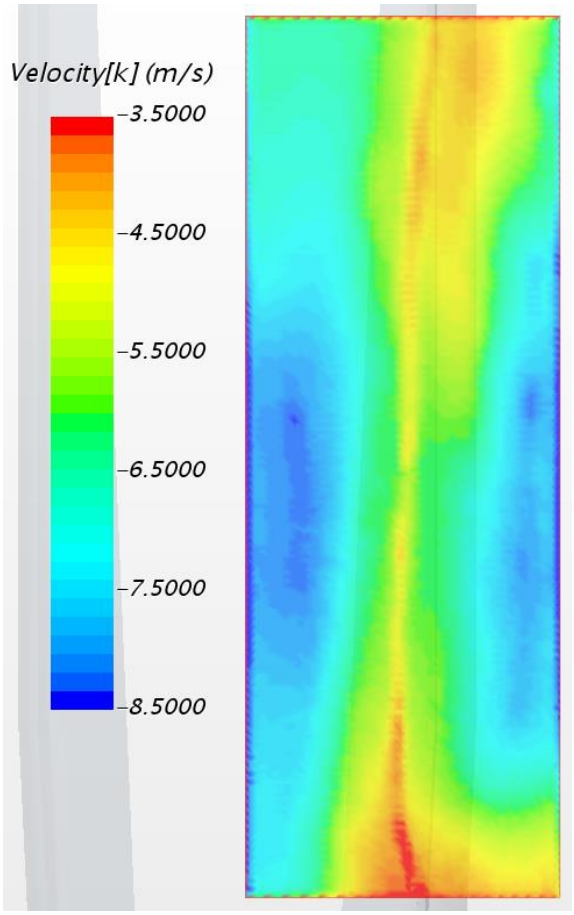

Figure 98: Velocity scalar of the air over the inlet face of the radiator

The use of a fairing at the leading edge of the pylon was indeed noticeable. The mass air flow rate increased from 0.24 kg/s to 0.29 kg/s (19% increase). Flow separation still took place near the leading edge, but the recirculation region was clearly reduced when compared to the baseline, as seen in Figure 99.

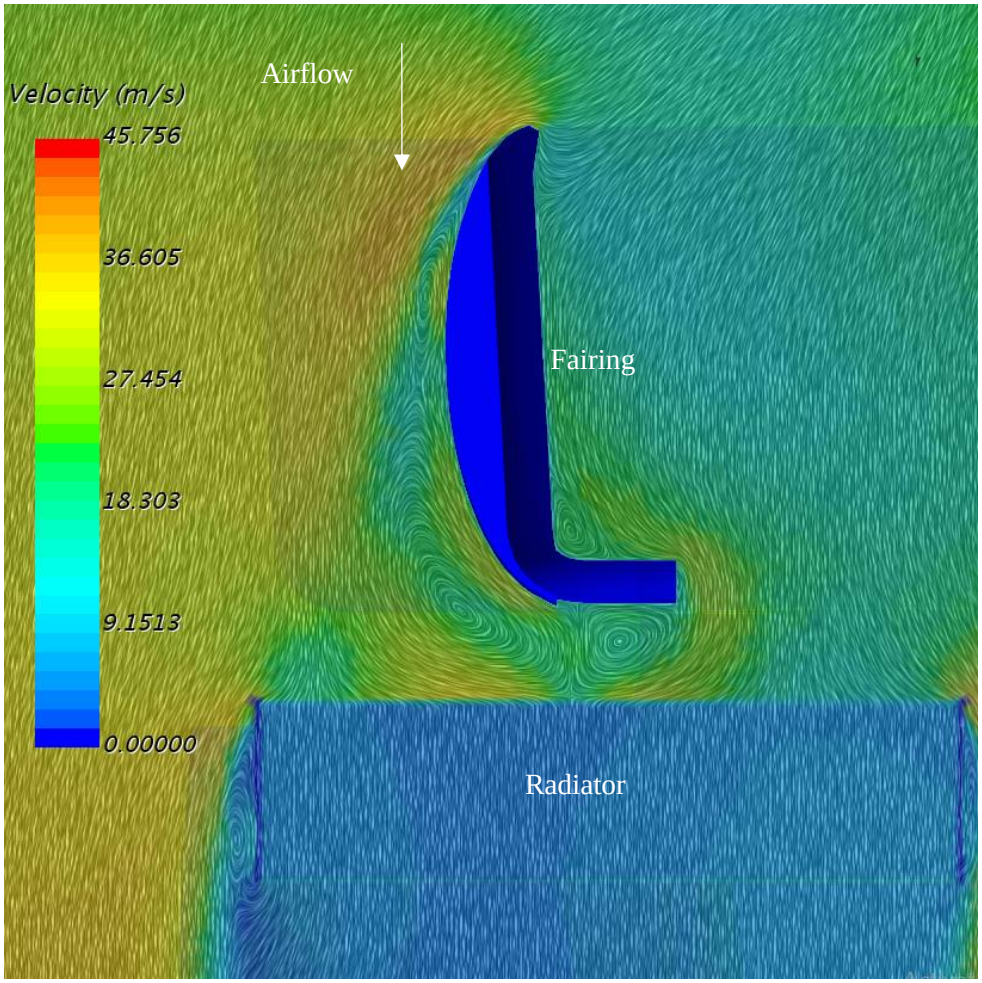

Figure 99: Airflow influenced by the fairing

5.4 Chosen Concept

Different concepts were investigated to determine the most effective method to keep the temperature of the engine at acceptable levels. The radiator scoop and pylon fairing delivered very similar results. The radiator scoop and pylon fairing both increased the airflow through the radiator by 25 % and 19 %, respectively.

The radiator scoop was ultimately identified as the concept of choice to reduce the temperature of the engine, due to its ease of manufacturing and low cost and for its large improvement in the mass air flow rate through the radiator. It is expected that the radiator scoop will increase the drag of the system by a small amount and one should take note of it, however with the large amount of drag created by the self-launch system when deployed, the change in drag is insignificant for this study. The heat exchanger interface model delivered satisfactory results. A drawback of the model, as used in this study, is that the hot inlet coolant temperature had to be specified. Thus, experiments are needed to determine the hot inlet coolant temperatures.

5.5 Radiator Scoop Concept Validation

The radiator scoop CFD simulation revealed that the radiator scoop can greatly assist in improving the heat exchange capabilities of the self-launch system. The heat exchange interface method used to simulate the heat exchange of the radiator, requires the hot inlet coolant temperature at the radiator to be specified. With the coolant's temperature unknown, an experimental test was required to determine if the improved airflow created by the radiator scoop was indeed significant enough to cool the engine at full throttle.

5.5.1 Setup

A similar setup as described in section 3.3 was used to determine the heat transfer of the system. Figure 100 shows the radiator scoop installed on the self-launch system.

Figure 100: Radiator scoop installed on the pylon

5.5.2 Results and Discussion

The various performance characteristics of the radiator, with and without the scoop, is compared in Figure 101 to Figure 104.

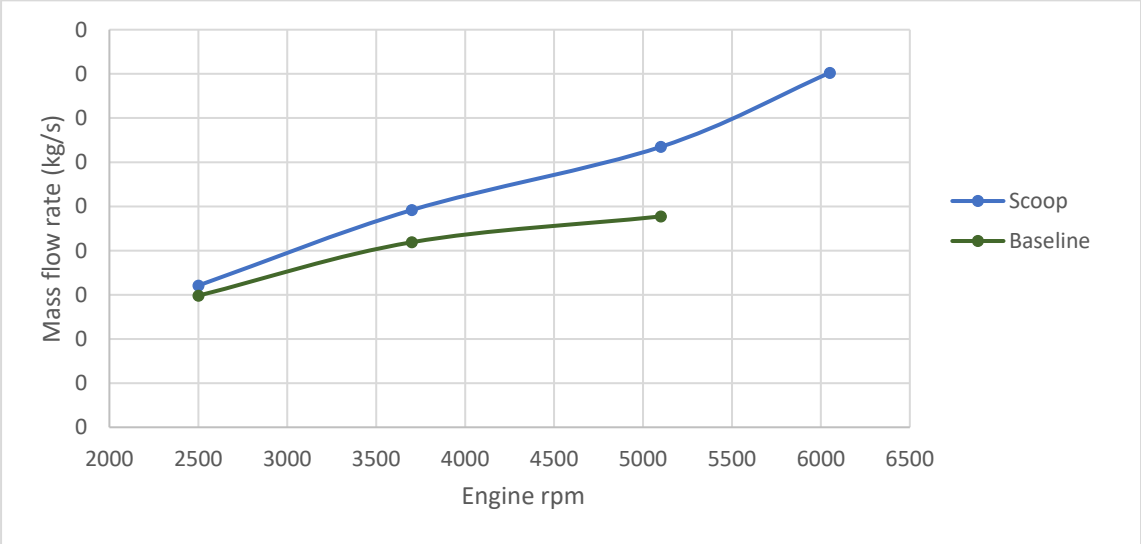

Figure 101: Radiator inlet mass airflow

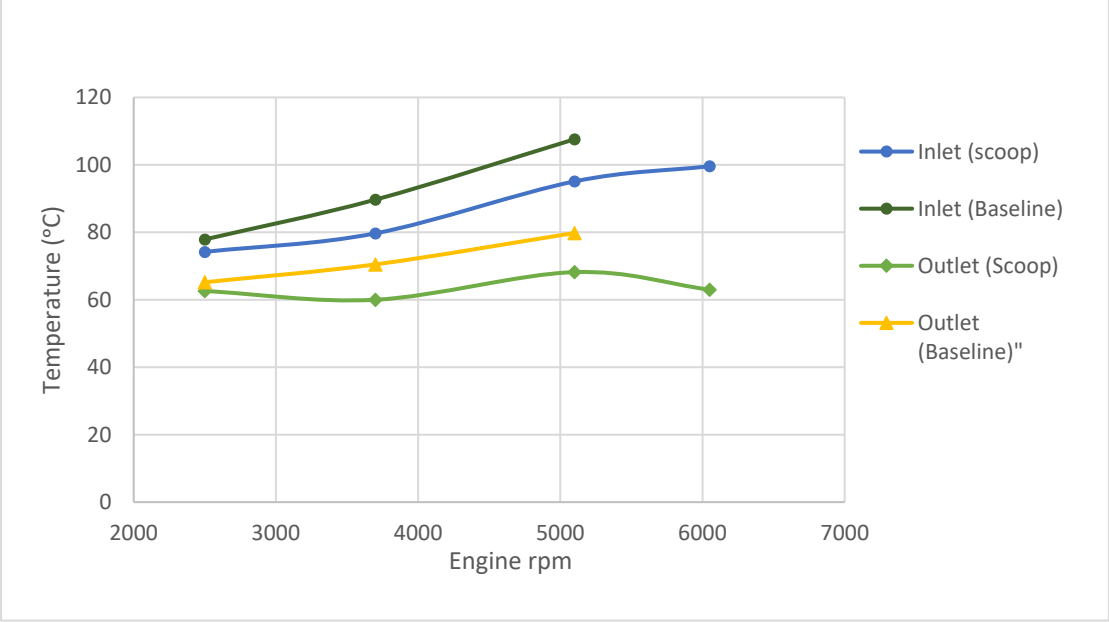

Figure 102: Water inlet temperatures

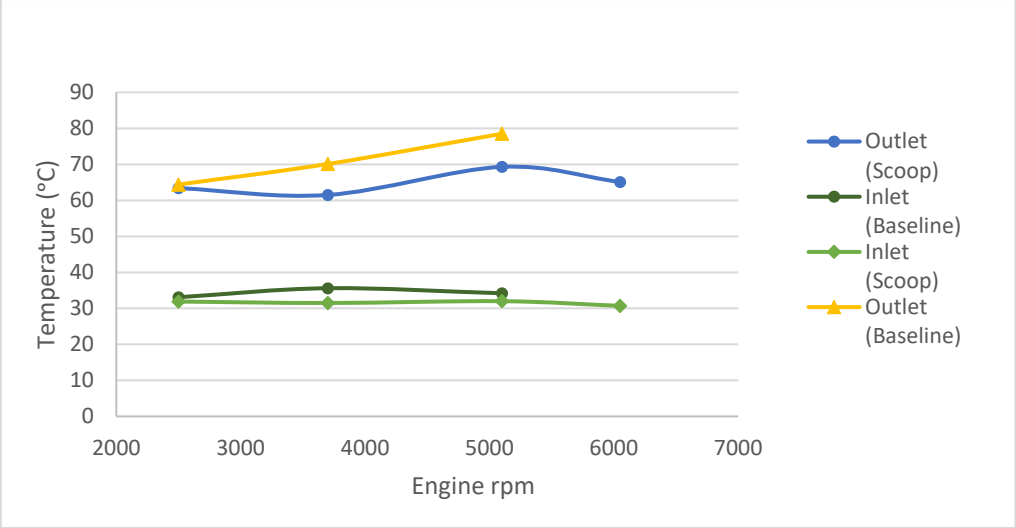

Figure 103: Air temperatures of the radiator

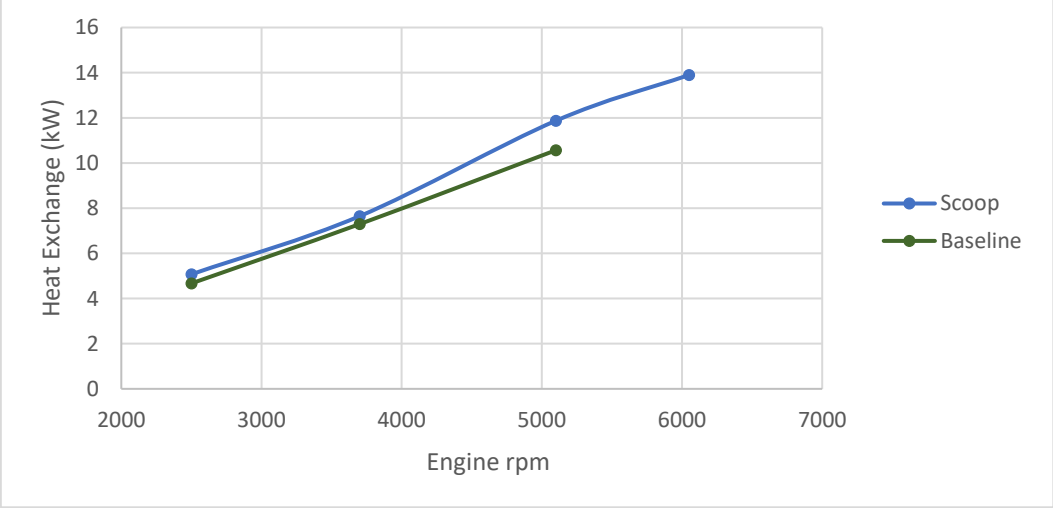

Figure 104: Heat load removal by the radiator at different engine speeds

An increase in the air mass flow rate through the radiator can be seen in Figure 101. The increased airflow was small at low rpm, but became more prominent as the rpm of the propeller increased.

The increase in the air mass flow rate through the radiator, confirmed that the radiator scoop forced additional air through the radiator. In Figure 95 one can see how the flow is directed through the radiator by utilising the radiator scoop. This increase in airflow through the radiator also leads to a decrease in the inlet and outlet temperatures of the water and air, as seen in Figure 102 and Figure 103. An increase in the heat transfer is also observed as presented in Figure 104. The addition of the radiator scoop proved to be successful in keeping the temperature of the engine below its maximum rated temperature of 115°C.

6. CONCLUSION AND RECOMMENDATIONS

6.1 Summary of the Project

During the design phase of a new high performance self-launch sailplane, engine overheating problems occurred. To understand how the different components of the self-launch system influenced the heat transfer of the radiator, a CFD heat transfer analysis was performed on the radiator, within the context of its operation as part of the integrated self-launcher mechanism.

The objectives of the study were as follows:

- To determine the heat transfer of the radiator used in the self-launch system, both experimentally and by means of numerical simulation.
- To develop a computationally efficient CFD simulation which can assist in making design decisions
- To validate CFD results with experimental data obtained from a ground test rig
- To use CFD simulations to analyse the influence of the heat exchange capabilities of the radiator, pertaining to the following parameters:
    - The wake of the propeller
    - The position of the radiator
    - The airflow through the radiator
- To ensure that adequate cooling of the engine is obtained

The heat transfer of the radiator was determined by experimental tests performed on a grounded test bench. All the required parameters were measured during the experiment to determine the heat transferred by the radiator. Experimental tests revealed that the radiator did not adequately cool the engine. Additional experiments were performed where the static thrust of the propeller and the pressure drop over the radiator were measured. The data of the experiments were used to validate and to setup the CFD sub-models.

A computationally efficient CFD simulation was created to perform a CFD analysis of the heat transfer from the radiator. A systematic approach was followed, where all the different sub-models that were included in the final integrated model, were first simulated and validated as separate models. Simulating the models separately made it easier to identify errors and improve stability. To create a computationally efficient CFD simulation, a few simplified CFD simulations were utilised.

The propeller was simulated as a BEM virtual disk which utilised BEM theory to simulate the rotating propeller. No detailed mesh of the propeller geometry is required by this method, which reduced the mesh of the simulation greatly.

The radiator was simulated as a porous medium by using porous resistance coefficients determined by using the pressure drop over the radiator. It is not required to mesh the fine detail of the radiator using this method, once again, further saving computational effort. A dual stream heat exchange interface was created in Star CCM+ to simulate the heat transfer of the system.

Using the data measured during the experiments, the CFD simulations was validated. The CFD sub-models compared especially well with the experimental data. The main integrated CFD simulation also compared well to the experimental data, but to a lesser extent. With the high level of simplification of the system, a decrease in accuracy was expected. The overall heat transfer coefficient determined during the experiments, was adjusted to calibrate the simulation to deliver a more accurate outlet coolant temperature.

An in-depth analysis of the self-launch system was done using the integrated self-launch system CFD simulation. The influence of the rotating airflow of the propeller, the wake created by the pylon, as well as the airflow through the radiator were determined. A particularly poor airflow through the radiator was revealed by the CFD simulation.

The CFD simulation was utilised to make design decisions, which improved the flow through the radiator. In an attempt to improve the airflow through the radiator, a radiator scoop and pylon fairing was added separately to the CFD simulation. Both the radiator scoop and pylon fairing increased the airflow though the radiator by 25% and 19% respectively. The radiator scoop was chosen as the superior concept design, as it was uncomplicated and robust, quick and more economical to manufacture, compared to the pylon fairing.

The radiator scoop was manufactured and installed onto the pylon. With the radiator scoop installed, the engine could be run at full throttle (6050 rpm) without overheating. Without the radiator scoop, the engine could only be run at 5100 rpm before overheating.

By using the radiator scoop, the radiator could sufficiently cool the engine. The application of CFD as design tool was thus validated by its successful use in the integrated self-launch system simulation.

6.2 Recommendations and Future Work

The data logger used in the experiments had only 20 channels. With eight channels available to the air inlet and outlet faces, more channels are needed to improve the resolution of the inlet and outlet air temperature distributions. The non-uniform airflow through the radiator, makes it even more compelling to have plentiful thermocouples spread across the face of the radiator.

Using instruments with a higher accuracy is also recommended. When certain engineering quantities had to be calculated using measured data, the combined margin of uncertainty turned out to be rather large, due to the accumulative error propagation.

The difference in accuracy of more robust and less simplified models could be investigated and compared to the simplified CFD models used. The effects of simulating the self-launch system as a transient case can also be investigated, to validate the steady state assumptions used for the current approach.

It would be valuable if a visual validation of the airflow can be displayed. By using wool tufts at the side of the pylon, one can visually confirm the recirculation flow region.

Lastly the geometry of the sailplane can be included in the CFD simulation, and the interaction between the self-launch system and the fuselage can be studied at a non-static stance. Subsequently, the influence in the drag of the system with the proposed changes to the radiator can be investigated.

If an even larger increase in the airflow through the radiator is required, the pylon fairing and radiator scoop can be used in combination. That would provide a greater margin of safety when considering the engine at full throttle operation and increase the heat removal capacity of the radiator.

7. BIBLIOGRAPHY

Anderson, J.D. 2001. Fundamentals of Aerodynamics. New York: McGraw-Hill.

Bahaj, A.S., Molland, A.F., Chaplin, J.R. & Batten, W.M.J. 2006. Power and thrust measurements of marine current turbines under various hydrodynamic flow conditions in a cavitation tunnel and towing tank. Renewable Energy, 32(32):407–426.

Balafas, G. 2014. Polyhedral Mesh Generation for CFD-Analysis of Complex Structures.

Bergman, T.L., Lavine, A.S., Incropera, F.P. & DeWitt, D.P. 2011. Fundamentals of Heat and Mass Transfer. 7th. New York: Wiley.

Borgnakke, C. & Sonntag, R.E. 2010. Fundamentals of Thermodynamics. 8th: Wiley.

Bosman, J.J. 2012. Evaluation of New Aerodynamic Concepts using CFD for the Improvement of a Glider Fuselage.

Čarija, Z. & Franković, B. 2008. Heat Transfer Analysis of Flatland Louvered Fin-and-Tube Heat Exchangers using CFD. Paper presented at the HEFAT2008, Pretoria, South Africa, 30 June to 2 July.

CD-Adapco. 2018. User Guide Star CCM+.

EASA. 2009. Certification Specifications for Sailplanes and Powered Sailplanes.

Gopalarathnam, A. & Selig, M.S. 2001. Low-Speed Natural-Laminar-Flow Airfoils: Case Study in Inverse Airfoil Design. *Journal of Aircraft*, 38(1):57–63.

Greenwell, E. 2004. A Guide to Self-Launching Sailplane Operation.

Gudmundsson, S. 2013. General Aviation Aircraft Design: Applied Methods and Procedures: Elsevier Science.

Guo, Q., Zhou, L. & Wang, Z. 2014. Comparison of BEM-CFD and Full Rotor Geometry Simulations for the Performance and Flow Field of a Marine Current Turbine. *Renewable Energy*, 75:640-648.

Hoerner, S.F. 1965. Fluid-Dynamic Drag: Practical Information on Aerodynamic Drag and Hydrodynamic Resistance: Hoerner Fluid Dynamics.

Houghton, E.L. & Carpenter, P.W. 2003. Aerodynamics for engineering students. 5th. Oxford: Butterworth-Heineman.

HPH. 2018. The Lowest cost quality self-launch sailplane on the market today. http://hphuk.co.uk/hph-products/shark-sj-ms/ Date of access: 18 October 2017. [Image].

Junjanna, G.C., Kulasekharan, N. & Purushotham, H.R. 2012. Performance Improvement Of A Louver-Finned Automobile Radiator Using Conjugate Thermal CFD Analysis. *International Journal of Engineering Research & Technology (IJERT)*, 1(8).

Kang, N., Mo, N. & Zheng, W. 2004. Three Dimensional Simulation of the Heat Dissipation of an Automotive Radiator Based on Porous Media Method. *Applied Mechanics and Materials*, 543:207-210.

Kim, N.H., Lee, K., J. & Jeong, Y.B. 2014. Airside Performance of Oval Tube Heat Exchangers Having Sinewavefins under Wet Conditions. *Applied Thermal Engineering*, 66:580-589.

Koren, D. 2015. Computational Fluid Dynamics unstructured mesh optimization for the Siemens 4rd generation DLE burner. Royal Institute of Technology (Thesis: M. Ing.).

Kutty, H.A. & Parvathy, R. 2017. 3D CFD Simulation and Experimental Validation of Small APC Slow Flyer Propeller Blade. *Aerospace*, 4(10).

Lidar, J. 2018. Thermal Analysis of Engine Bay in Star-CCM+. Gothenburg, Sweden: Chalmers University of Technology (Thesis: M. Ing.).

Malki, R., Williams, A.J., Croft, T.N., Togneri, M. & Masters, I. 2012. A Coupled Blade Element Momentum – Computational Fluid Dynamics Model for Evaluating Tidal Stream Turbine Performance. *Applied Mathematical Modelling*, 37:3006–3020.

McCormick, B.W. 1994. Aerodynamics, Aeronautics, and Flight Mechanics: Wiley.

McCormick, B.W. 1995. Aerodynamics, aeronautics and flight mechanics. Danvers: John Wiley & Sons , Inc.

Menter, F.R., Kuntz, M. & Langtry, R. 2003. Ten years of industrial experience with the sst turbulence model: Bergell House.

Monk, J.S. 2010. A Propeller Design and Analysis Capability Evaluation for High Altitude Application.

Munson, B.R., Young, D.F., Okiishi, T.H. & Huebsch, W.Q. 2010. Fundamentals of Fluid Mechanics. Asia: John Wiley & Sons.

Ng, E.Y., Watkins, S., Johnson, P.W. & Mole, L. 2001. Measuring Local Time-Averaged Airflow Velocity through

an Automotive Heat Exchanger. Paper presented at the 14th Australasian Fluid Mechanics Conference Adelaide University, Adelaide, Australia, 10-14 December.

Ning, K., Nika, M. & Weiqi, Z. 2004. Three Dimensional Simulation of the Heat Dissipation of an Automotive Radiator Based on Porous Media Method. *Applied Mechanics and Materials*, 543:207-210.

Oliet, C., Oliva, A., Castro, J. & Pe´rez-Segarra, C.D. 2007. Parametric Studies on Automotive Radiators. *Applied Thermal Engineering*, 1(27):2033–2043.

Peric, M. & Ferguson, S. 2005. The Advantage of Polyhedral Meshes: CD-adapco.

Rao, B.R. & Sahitya, R. 2015. Numerical And Experimental Investigation of The Flow Field Around

NACA 0012 Aerofoil. *International Journal on Theoretical and Applied Research in Mechanical Engineering (IJTARME)*, 1.

Reynolds, B. 2018. Should I Use Moving Reference Frames or Rigid Body Motion for My Simulation?

Sachs, G., Lenz, J. & Holzapfel, F. 2010. Range Maximization by Saw-Tooth Mode Optimization for Motor Gliders with Retractable Engines. Paper presented at the Technical Soaring, Garching, Germany, 6-13 August.

Schlichting, H. 1973. Boundary Layer Theory. New York: McGraw-Hill.

Smith, H.A. & Schaefer, R.F. 1945. Aerodynamic Characteristics of 15 NACA Airfoil Sections at Seven Reynols Numbers from 0.7 x 10^6 to 9.0 x 10^6. Washington.

Transportation, U.S.D.o. 2015. Glider Flying Handbook: SKYHORSE PUB.

U.S. Department of Transportation. 2013. Aircraft Weight and Balance Handbook: Skyhorse Publishing Company, Incorporated.

Appendix

A Blade Element Moment Theory spreadsheet

A spreadsheet was developed in MS Excel that utilises BEM theory, as discussed in section 2.2.2, to predict the thrust of the propeller. The methodology that was followed to create this spreadsheet is explained in great detail by Gudmundsson (2013). The spreadsheet consists of a number of sections and will be discussed below (Figure 105).

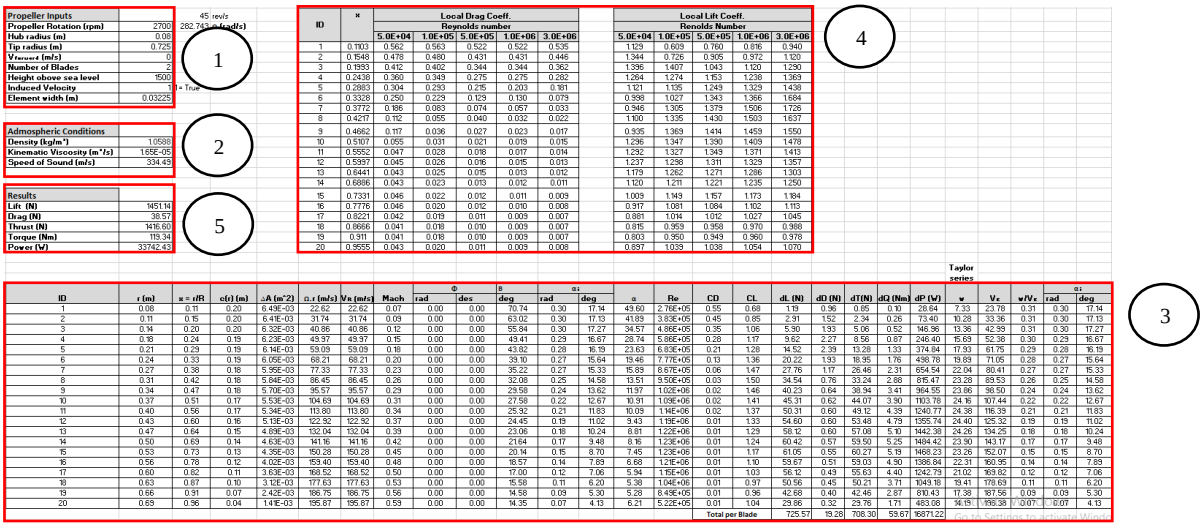

Figure 105: Overview of the BEM theory main spreadsheet, 1: Propeller input, 2: Atmospheric conditions, 3: Main results, 4: Lift and drag coefficients, 5: Blade element calculations.

The propeller input section requires the user to specify the propeller's rotations rate, hub radius, tip radius, forward velocity and the height above sea level (Figure 106). The atmospheric conditions are then calculated based on the height above sea level (Figure 107). The user can also decide if the spreadsheet should take induced velocity into account.

Propeller Inputs	
Propeller Rotation (rpm)	2700
Hub Radius (m)	0.08
Tip Radius (m)	0.725
Vforward (m/s)	0
Number of Blades	2
Height Above Sea Level	1500
Induced Velocity	1
Element Width (m)	0.03225

Figure 106: BEM inputs

Atmospheric Conditions					
Altitude	Temperture	Density	Speed of Sound	Kinematic Viscosity	Atmospheric Pressure
[m]	[K]	kg/m^3	m/s	m^2/s	Pa
0	299.16	1.225	340.29	1.46E-05	1.01E+05
900	282.31	1.1226	336.82	1.5687E-05	90971
1800	276.46	1.0269	333.32	1.6869E-05	81494
2700	270.62	0.93765	329.77	1.8167E-05	72835
3600	264.77	0.85445	326.77	1.9595E-05	64939
4500	258.92	0.77704	322.57	2.1167E-05	57752
5400	253.09	0.70513	318.91	2.2903E-05	51226
6300	247.25	0.63845	315.21	2.4824E-05	45311
7200	241.41	0.57671	311.47	2.6953E-05	39963
8100	235.58	0.51967	307.68	0.00002932	35140
9000	229.74	0.46706	303.85	3.1957E-05	30800
9900	223.91	41864	299.97	3.4903E-05	26906
10800	218.08	0.37417	296.03	3.8202E-05	23422

Atmospheric Conditions	
Density (kg/m³)	1.0588
Kinematic Viscosity (m²/s)	1.65E-05
Speed of Sound (m/s)	334.49

Figure 107: Atmospheric conditions

The blade chord and twist distribution of the propeller are also required as an input by the user. A graph is created from the data, and a polynomial curve is fitted onto the data. The spreadsheet inserts the value of the position of the blade element into the equation of the fitted curve. The blade chord and twist distribution can then be calculated at any point along the blade.

The blade element calculation section divides the propeller into 20 sections. It utilises BEM theory to calculate the performance over each blade element of the propeller (Figure 108).

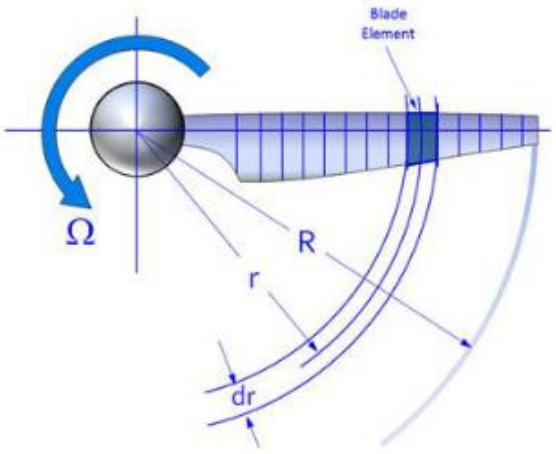

Figure 108: Blade divided into elements (Gudmundsson, 2013)

The first part of the element calculation section contains the position, area, velocities, Mach number and several airfoil angles of the blade elements (Figure 110). To distinguish between the different angles and velocities of a propeller section, Figure 109 can be used.

Figure 109 shows the different kind of velocities and angles of a non-static rotating propeller that were used in the calculations.

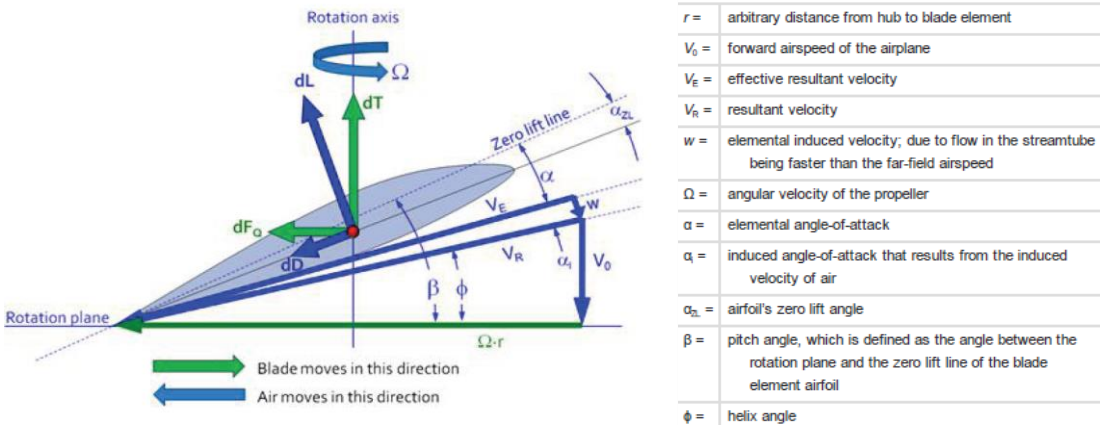

r =	arbitrary distance from hub to blade element
V_0 =	forward airspeed of the airplane
V_E =	effective resultant velocity
V_R =	resultant velocity
w =	elemental induced velocity; due to flow in the streamtube being faster than the far-field airspeed
Ω =	angular velocity of the propeller
α =	elemental angle-of-attack
α_i =	induced angle-of-attack that results from the induced velocity of air
α_{ZL} =	airfoil's zero lift angle
β =	pitch angle, which is defined as the angle between the rotation plane and the zero lift line of the blade element airfoil
ϕ =	helix angle

Figure 109: Velocity angles of a rotating propeller (Gudmundsson, 2013)

								Φ		B	αi	
ID	r (m)	x = r/R	c(r) (m)	ΔA (m^2)	Ω.r (m/s)	VR (m/s)	Mach	rad	des	deg	rad	deg
1	0.08	0.11	0.20	6.49E-03	22.62	22.62	0.07	0.00	0.00	70.74	0.30	17.14
2	0.11	0.15	0.20	6.41E-03	31.74	31.74	0.09	0.00	0.00	63.02	0.30	17.13
3	0.14	0.20	0.20	6.32E-03	40.86	40.86	0.12	0.00	0.00	55.84	0.30	17.27
4	0.18	0.24	0.19	6.23E-03	49.97	49.97	0.15	0.00	0.00	49.41	0.29	16.67
5	0.21	0.29	0.19	6.14E-03	59.09	59.09	0.18	0.00	0.00	43.82	0.28	16.19
6	0.24	0.33	0.19	6.05E-03	68.21	68.21	0.20	0.00	0.00	39.10	0.27	15.64
7	0.27	0.38	0.18	5.95E-03	77.33	77.33	0.23	0.00	0.00	35.22	0.27	15.33
8	0.31	0.42	0.18	5.84E-03	86.45	86.45	0.26	0.00	0.00	32.08	0.25	14.58
9	0.34	0.47	0.18	5.70E-03	95.57	95.57	0.29	0.00	0.00	29.58	0.24	13.62
10	0.37	0.51	0.17	5.53E-03	104.69	104.69	0.31	0.00	0.00	27.58	0.22	12.67
11	0.40	0.56	0.17	5.34E-03	113.80	113.80	0.34	0.00	0.00	25.92	0.21	11.83
12	0.43	0.60	0.16	5.13E-03	122.92	122.92	0.37	0.00	0.00	24.45	0.19	11.02
13	0.47	0.64	0.15	4.89E-03	132.04	132.04	0.39	0.00	0.00	23.06	0.18	10.24
14	0.50	0.69	0.14	4.63E-03	141.16	141.16	0.42	0.00	0.00	21.64	0.17	9.48
15	0.53	0.73	0.13	4.35E-03	150.28	150.28	0.45	0.00	0.00	20.14	0.15	8.70
16	0.56	0.78	0.12	4.02E-03	159.40	159.40	0.48	0.00	0.00	18.57	0.14	7.89
17	0.60	0.82	0.11	3.63E-03	168.52	168.52	0.50	0.00	0.00	17.00	0.12	7.06
18	0.63	0.87	0.10	3.12E-03	177.63	177.63	0.53	0.00	0.00	15.58	0.11	6.20
19	0.66	0.91	0.07	2.42E-03	186.75	186.75	0.56	0.00	0.00	14.58	0.09	5.30
20	0.69	0.96	0.04	1.41E-03	195.87	195.87	0.59	0.00	0.00	14.35	0.07	4.13

Figure 110: Blade element calculation part one

The second part of the blade element calculation section calculates the propeller performance of each blade element as seen in Figure 111.

α	Re	CD	CL	dL (N)	dD (N)	dT(N)	dQ (Nm)	dP (W)	w	Vε	w/Vε	αi	
												rad	deg
49.60	2.76E+05	0.55	0.68	1.19	0.96	0.85	0.10	28.64	7.33	23.78	0.31	0.30	17.14
41.89	3.83E+05	0.45	0.85	2.91	1.52	2.34	0.26	73.40	10.28	33.36	0.31	0.30	17.13
34.57	4.86E+05	0.35	1.06	5.90	1.93	5.06	0.52	146.96	13.36	42.99	0.31	0.30	17.27
28.74	5.86E+05	0.28	1.17	9.62	2.27	8.56	0.87	246.40	15.69	52.38	0.30	0.29	16.67
23.63	6.83E+05	0.21	1.28	14.52	2.39	13.28	1.33	374.84	17.93	61.75	0.29	0.28	16.19
19.46	7.77E+05	0.13	1.36	20.22	1.93	18.95	1.76	498.78	19.89	71.05	0.28	0.27	15.64
15.89	8.67E+05	0.06	1.47	27.76	1.17	26.46	2.31	654.54	22.04	80.41	0.27	0.27	15.33
13.51	9.50E+05	0.03	1.50	34.54	0.76	33.24	2.88	815.47	23.28	89.53	0.26	0.25	14.58
11.97	1.02E+06	0.02	1.46	40.23	0.64	38.94	3.41	964.55	23.86	98.50	0.24	0.24	13.62
10.91	1.09E+06	0.02	1.41	45.31	0.62	44.07	3.90	1103.78	24.16	107.44	0.22	0.22	12.67
10.09	1.14E+06	0.02	1.37	50.31	0.60	49.12	4.39	1240.77	24.38	116.39	0.21	0.21	11.83
9.43	1.19E+06	0.01	1.33	54.60	0.60	53.48	4.79	1355.74	24.40	125.32	0.19	0.19	11.02
8.81	1.22E+06	0.01	1.29	58.12	0.60	57.08	5.10	1442.38	24.26	134.25	0.18	0.18	10.24
8.16	1.23E+06	0.01	1.24	60.42	0.57	59.50	5.25	1484.42	23.90	143.17	0.17	0.17	9.48
7.45	1.23E+06	0.01	1.17	61.05	0.55	60.27	5.19	1468.23	23.26	152.07	0.15	0.15	8.70
6.68	1.21E+06	0.01	1.10	59.67	0.51	59.03	4.90	1386.84	22.31	160.95	0.14	0.14	7.89
5.94	1.15E+06	0.01	1.03	56.12	0.49	55.63	4.40	1242.79	21.02	169.82	0.12	0.12	7.06
5.38	1.04E+06	0.01	0.97	50.56	0.45	50.21	3.71	1049.18	19.41	178.69	0.11	0.11	6.20
5.28	8.49E+05	0.01	0.96	42.68	0.40	42.46	2.87	810.43	17.38	187.56	0.09	0.09	5.30
6.21	5.22E+05	0.01	1.04	29.86	0.32	29.76	1.71	483.08	14.19	196.38	0.07	0.07	4.13
		Total per Blade		725.57	19.28	708.30	59.67	16871.22					

Figure 111: Blade element calculation part 2

The lift and drag coefficients are computed at each element at a given Reynolds number. The lift and drag coefficients were calculated using XFoil and tabulated as seen in Figure 112. The Reynolds number at each blade element was calculated, and the corresponding lift and drag coefficients were interpolated using the tables in Figure 112. The lift, drag, power and thrust of the propeller was calculated using the aforementioned coefficients.

The influence of the induced velocity was also taken into account and was calculated using a Taylor series finite difference scheme, as described by Gudmundsson (2013).

ID	x	Local Drag Coeff. Reynolds number					Local Lift Coeff. Renolds Number				
		5.0E+04	1.0E+05	5.0E+05	1.0E+06	3.0E+06	5.0E+04	1.0E+05	5.0E+05	1.0E+06	3.0E+06
1	0.110345	0.748	0.749	0.725	0.725	0.732	0.650	0.351	0.438	0.470	0.541
2	0.154828	0.664	0.665	0.633	0.633	0.643	0.866	0.467	0.583	0.626	0.721
3	0.19931	0.586	0.588	0.549	0.548	0.561	1.066	0.576	0.718	0.771	0.888
4	0.243793	0.516	0.518	0.472	0.472	0.487	1.246	0.673	0.839	0.901	1.038
5	0.288276	0.456	0.458	0.406	0.406	0.422	1.402	0.757	0.944	1.014	1.168
6	0.332759	0.416	0.407	0.351	0.350	0.368	1.406	1.353	1.033	1.109	1.278
7	0.377241	0.382	0.373	0.305	0.304	0.323	1.324	1.335	1.106	1.188	1.368
8	0.421724	0.352	0.343	0.268	0.267	0.272	1.245	1.259	1.165	1.251	1.365
9	0.466207	0.326	0.315	0.238	0.238	0.228	1.177	1.188	1.212	1.302	1.371
10	0.51069	0.303	0.292	0.214	0.202	0.180	1.120	1.133	1.250	1.329	1.441
11	0.555172	0.280	0.270	0.176	0.175	0.138	1.064	1.079	1.304	1.331	1.530
12	0.599655	0.261	0.250	0.146	0.149	0.102	1.021	1.039	1.331	1.346	1.624
13	0.644138	0.246	0.217	0.122	0.122	0.071	0.990	1.026	1.348	1.376	1.707
14	0.688621	0.228	0.159	0.103	0.092	0.049	0.962	1.114	1.349	1.431	1.744
15	0.733103	0.201	0.087	0.078	0.062	0.035	0.900	1.302	1.373	1.500	1.732
16	0.777586	0.100	0.068	0.053	0.042	0.026	1.237	1.311	1.417	1.513	1.684
17	0.822069	0.138	0.049	0.034	0.029	0.020	0.941	1.347	1.432	1.494	1.610
18	0.866552	0.093	0.034	0.025	0.022	0.017	1.079	1.361	1.406	1.441	1.524
19	0.911034	0.052	0.030	0.020	0.018	0.015	1.295	1.339	1.373	1.393	1.452
20	0.955517	0.049	0.029	0.019	0.018	0.014	1.293	1.334	1.362	1.383	1.434

Figure 112: Lift and drag coefficients at different Reynolds numbers

Lastly, the final results of the performance of the propeller are presented in section 5, as seen in Figure 113.

Results	
Lift (N)	1451.14
Drag (N)	38.57
Thrust (N)	1416.60
Torque (Nm)	119.3394
Power (W)	33742.43

Figure 113: BEM theory results

B Calibration

Instruments connected to the memograph required calibration before they could be used in the experiments.

Turbine flow sensor

A Gems™ turbine flow sensor was connected in line with a water pipe. A container was placed on a calibrated load cell, and the amount of water that flowed into the container within one minute, was weighed (Figure 114). The necessary adjustments were made to the memograph which ensured the flow rate (l/min) logged was in correspondence with the water weighed. This process was repeated until the difference between the measured and logged value converged. Figure 115 shows the setup used during calibration. Figure 115 shows the percent difference between the value measured by the load cell and the value measured by the turbine flow sensor.

Figure 114: Water flow sensor calibration

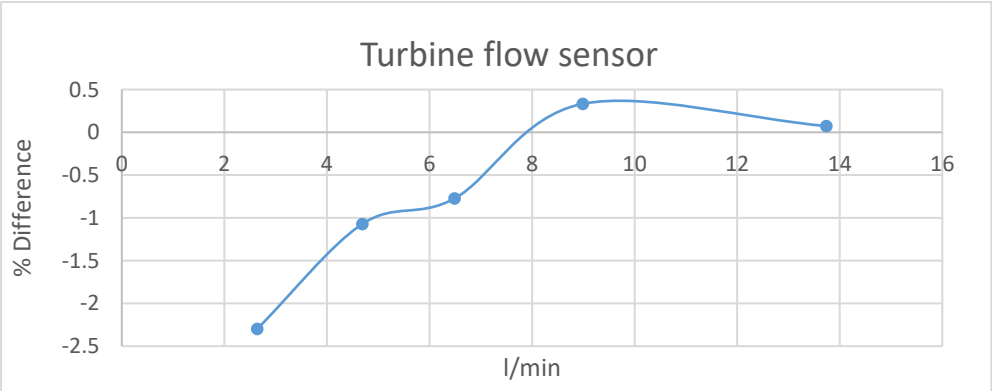

Figure 115: Percent difference measured between the value logged and measured

Thermocouples

The thermocouples were connected to a memograph and placed in an ice bath. The necessary adjustments were made to the memograph to ensure the thermocouples were within 0.5° of 0°. The thermometers were placed in an ice bath (Figure 116) where the necessary adjustments were made to ensure the termocouples measured zero. A tolorance of +- 0.5℃ was allowed. To ensure the thermocouples measured correctly, the thermocouples were then inserted into a controlled heat bath (Figure 117) at different temperatures. The temperature of the controlled heat bath, was confirmed with a calibrated thermometer.

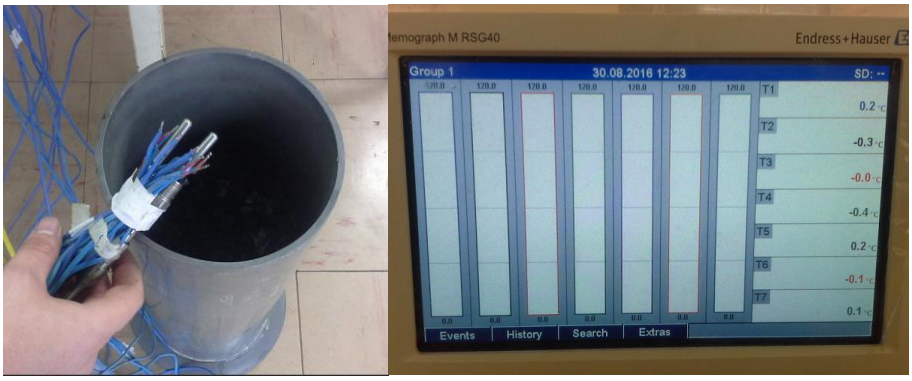

Figure 116: Calibration of type-K thermocouples in ice bath

Figure 117: Calibration of type K thermocouples inside a control heat bath

C Load Cell Calibration Certificate

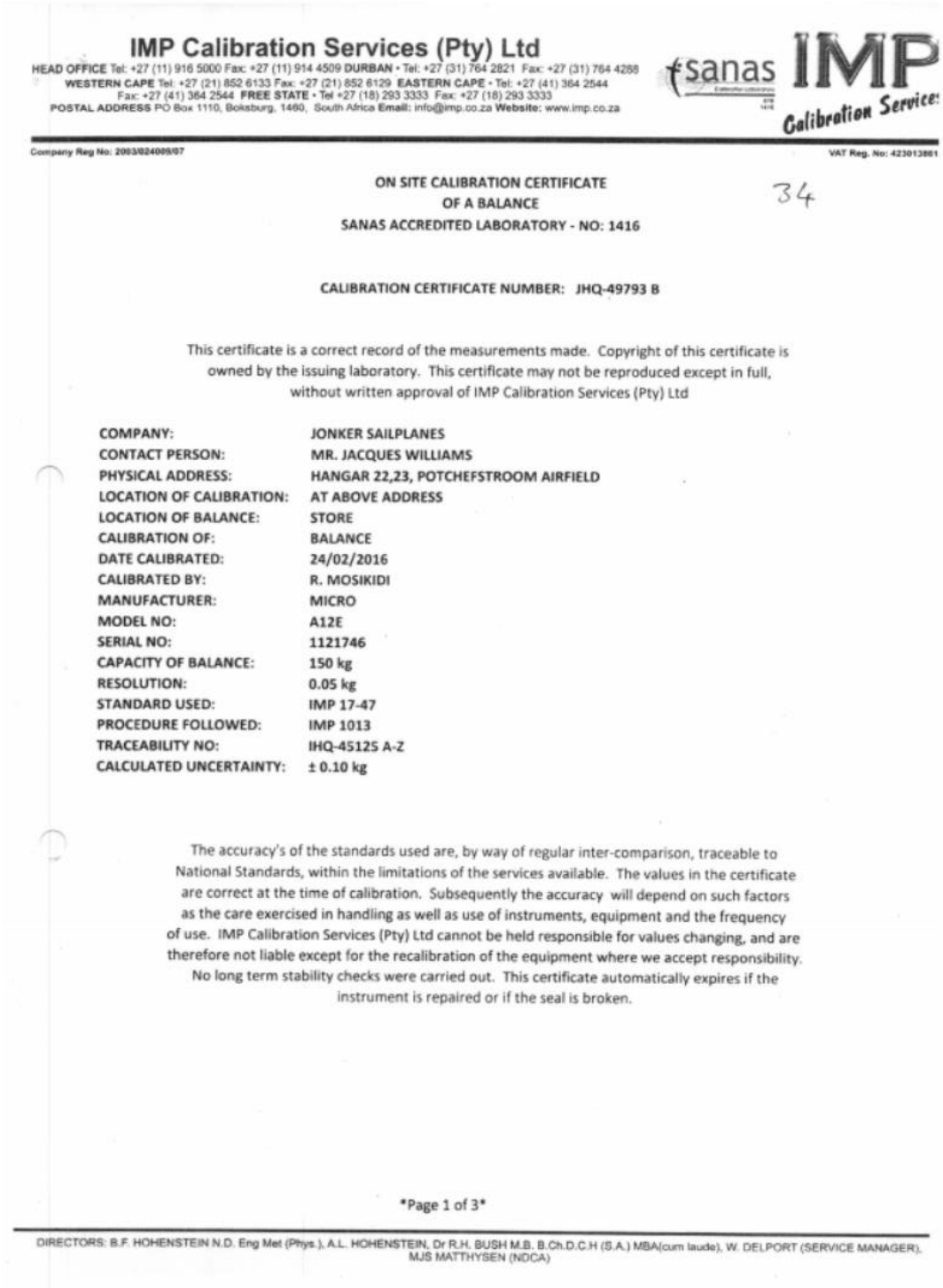

IMP Calibration Services (Pty) Ltd

HEAD OFFICE Tel: +27 (11) 916 5000 Fax: +27 (11) 914 4509 DURBAN • Tel: +27 (31) 764 2821 Fax: +27 (31) 764 4268
WESTERN CAPE Tel: +27 (21) 852 6133 Fax: +27 (21) 852 6129 EASTERN CAPE • Tel: +27 (41) 364 2544
Fax: +27 (41) 364 2544 FREE STATE • Tel +27 (18) 293 3333 Fax: +27 (18) 293 3333
POSTAL ADDRESS PO Box 1110, Boksburg, 1460, South Africa Email: info@imp.co.za Website: www.imp.co.za

sanas IMP Calibration Services

Company Reg No: 2003/024009/07 VAT Reg. No: 4230138B1

34

ON SITE CALIBRATION CERTIFICATE
OF A BALANCE
SANAS ACCREDITED LABORATORY - NO: 1416

CALIBRATION CERTIFICATE NUMBER: JHQ-49793 B

This certificate is a correct record of the measurements made. Copyright of this certificate is owned by the issuing laboratory. This certificate may not be reproduced except in full, without written approval of IMP Calibration Services (Pty) Ltd

COMPANY:	**JONKER SAILPLANES**
CONTACT PERSON:	**MR. JACQUES WILLIAMS**
PHYSICAL ADDRESS:	**HANGAR 22,23, POTCHEFSTROOM AIRFIELD**
LOCATION OF CALIBRATION:	**AT ABOVE ADDRESS**
LOCATION OF BALANCE:	**STORE**
CALIBRATION OF:	**BALANCE**
DATE CALIBRATED:	**24/02/2016**
CALIBRATED BY:	**R. MOSIKIDI**
MANUFACTURER:	**MICRO**
MODEL NO:	**A12E**
SERIAL NO:	**1121746**
CAPACITY OF BALANCE:	**150 kg**
RESOLUTION:	**0.05 kg**
STANDARD USED:	**IMP 17-47**
PROCEDURE FOLLOWED:	**IMP 1013**
TRACEABILITY NO:	**IHQ-45125 A-Z**
CALCULATED UNCERTAINTY:	**± 0.10 kg**

The accuracy's of the standards used are, by way of regular inter-comparison, traceable to National Standards, within the limitations of the services available. The values in the certificate are correct at the time of calibration. Subsequently the accuracy will depend on such factors as the care exercised in handling as well as use of instruments, equipment and the frequency of use. IMP Calibration Services (Pty) Ltd cannot be held responsible for values changing, and are therefore not liable except for the recalibration of the equipment where we accept responsibility. No long term stability checks were carried out. This certificate automatically expires if the instrument is repaired or if the seal is broken.

Page 1 of 3

DIRECTORS: B.F. HOHENSTEIN N.D. Eng Met (Phys.), A.L. HOHENSTEIN, Dr R.H. BUSH M.B. B.Ch.D.C.H (S.A.) MBA(cum laude), W. DELPORT (SERVICE MANAGER), MJS MATTHYSEN (NDCA)

Figure 118: Load cell calibration certificate page 1

CALIBRATION CERTIFICATE NUMBER: JHQ-49793 B

Results:

1. Off Centre Error Test:

Off centre error tested at	40 kg
The maximum error was found to be	0.00 kg

2. Precision Test:

Precision test carried out at	80 kg
The standard deviation was	± 0.05 kg

3. Linearity Test

BALANCE READING (kg)	STANDARD VALUE (kg)	BALANCE CORRECTION (kg)
0.00	0.00	0.00
5.00	5.00	0.00
10.00	10.00	0.00
30.00	30.00	0.00
59.95	59.99	0.05
89.95	89.99	0.05
119.95	119.98	0.05
149.90	149.98	0.10
MAXIMUM ERROR		**0.10 kg**

Remarks:

1.) The reported expanded uncertainty is based on a standard uncertainty multiplied by a coverage factor k = 2 providing a level of confidence of approximately 95%, the uncertainty of measurement has been estimated in accordance with the principles defined in the GUM, Guide to Measurement, ISO, Geneva, 1993.

2.)The balance was not adjusted.

3.) Single range balance.

Figure 119: Load cell calibration certificate page 2

CALIBRATION CERTIFICATE NUMBER: JHQ-49793 B

Checked by:

R. Mositheli	Technician	
Name	Designation	Signature

Authorized by:

F. CLASSEN	Technical Signatory	
Name	Designation	Signature

Date issued: 2016/03/03

**********END**********

Figure 120: Load cell calibration certificate page 3

D Apparatus Specifications

solo KLEINMOTOREN GMBH Postfach 60 01 52 , D 71050 Sindelfingen	Manual for engine 2625 02	

Table of contents

1. General engine description

- Twin - cylinder in line - two - stroke - engine
- Lquid cooling
- Lubrication by fuel-oil-mixture
- Two diaphragm carburetors
- Dual electronic high-voltage ignition
- Crankshaft layout for belt transmission
- Electric starter
- AC generator

2. Technical data

Displacement	625 cm^3 bore 76 mm stroke 69 mm
Compression ratio	9,5 : 1
Ignition unit	Dual electronic high-voltage ignition (Ducati Energia)
Spark plugs	BOSCH W5 AC, gap at electrodes 0.5 mm
Carburetor	Mikuni diaphragm carburetor Typ BN 38
Sence of rotation	Clockwise in flight direction
Fuel	Premium unleaded Min. 95 RON , AVGAS100LL
Lubrication	Fuel oil mixture 1:50 (2%),CASTROL Super TT oder TTS For USA SOLO Two Stroke oil (SOLO Inc. Newport News VA)
Dry weight	24 kg
Generator	12 V 150 W

edition 2 January 5th, 2001	revised edition September 24th, 1997	page - no. 1

Figure 121: Solo™ engine 2625 02 engine specification page 1

3. Operational data and limitations

Take-off-speed,power	6 500 rpm with a power of 47 kW (64 hp)
Max. cont. speed, power	6 500 rpm with a power of 47 kW (64 hp) /
Max. rpm	7 000 rpm
Idle rpm	approx .2 500 rpm
Max. temp. cooling liquid	115 °C (240°F) measured in the cylinder - head
Fuel consumption	Max. continous power approx. 24,5 l/h

4. Installing Instructions

Installing Instructions

The engine can be mounted at the driveside flange with 4 bolts M8. At the cylinder heads there are 4 more threads M8 and at the bottom of the crankcase there are 4 threads M10.
The cylinders have to be in vertical position when the engine is its operating position.
The load on the mounting threads can be 5 kN each.
The fuel line has to be protected against fire.
A fuel pump with a fuel pressure of min.0,2 bar and a maximum pressure of 0,4 bar is to be used.
A fuel filter with 6 to 7 µm has to be installed in the fuel line.
A watercooler with a cooling capability of 14 kW has to be used.
If an electric starter is used, its power has to be at least 400 W.
If an electric starter is used, its power has to be at least 400 W.
If the propeller is driven by a belt the belt tension may not be higher than 2 000 N at engines up to No. 19. If the belt tension must be higher, the use of an additional bearing is necessary.
At higher engine-numbers (from 20) the belt tension can be 2 500 N max.

Table of torques

Spark plug	20 Nm
Drive pully on crankshaft	100 Nm
Bolts and nuts M 6	12 Nm
Bolts and nuts M 8	20 Nm
Bolts and nuts M 10	40 Nm
Magneto on crankshaft	80 Nm

Figure 122: Solo™ engine 2625 02 engine specification page 2

VDAS® AF1450S

SUBSONIC WIND TUNNEL 450 MM

DESCRIPTION

Air passes into the wind tunnel through a honeycomb flow straightener and a grille. It then passes into an aerodynamically designed effuser (cone) that accelerates the air in a linear manner before it moves through the working section. Finally it passes through a diffuser, then into the variable speed axial fan. The grille protects the fan from damage by loose objects. The air leaves the fan, passes through a silencer unit and then back out to atmosphere.

The speed of the axial fan (and therefore the air velocity in the working section) is controlled by an electronic drive control in the separate On/Off unit mounted on the tunnel's associated instrument frame along with other ancillaries.

WORKING SECTION

The working section is of a square section with an acrylic roof and floor. The sides are full length acrylic panels and can be removed. The whole unit is supported in an aluminium framework. Each side panel has a holder to support wind tunnel models. On the top of the working section are two Pitot devices and a wall tapping to measure the static pressure upstream and downstream of the working section.

INCLUDED WITH THE WIND TUNNEL:

- **THREE-COMPONENT BALANCE (AF1450T)**

  The Three-Component Balance measures lift, drag and pitching moment exerted on the model.

- **BALANCE ANGLE FEEDBACK UNIT (AFA4)**

  (Included with AF1450T). Measures the angular position of models mounted on the balance in the wind tunnel.

- **NACA 0012 AEROFOIL WITH TAPPINGS (AF1450B)**

  A 150 mm chord 450 mm span NACA0012 aerofoil with pressure tappings.

- **DUAL DIFFERENTIAL PRESSURE DISPLAY (DP6)**

  Measures and displays pressures with respect to the atmosphere or differential pressures.

- **32-WAY PRESSURE DISPLAY UNIT (AFA6)**

  Measures and displays up to 32 different pressures from models, Pitot-static tubes and other measuring instruments fitted to the wind tunnel.

- **PITOT STATIC TRAVERSE X2 (AF1450X)**

  Two traversing Pitot-static tube with electronic position measurement for use with TecQuipment's Subsonic Wind Tunnels.

- **PROTRACTOR**

  For assisting with setting up models and rotating them during experiments.

- **MODEL HOLDER**

  To hold models when the three component balance is not used. Also for use with the user's own models.

- **VERSATILE DATA ACQUISITION SYSTEM (VDAS-F)**

  A frame mounting versatile data acquisition system (VDAS®) to allow computer-based data capture.

OPTIONAL EXTRAS INCLUDE:

- **MULTITUBE MANOMETER (AFA1)**

  A tilting 36-tube manometer

- **SMOKE GENERATOR (AFA11)**

  To assist with visualising air flow

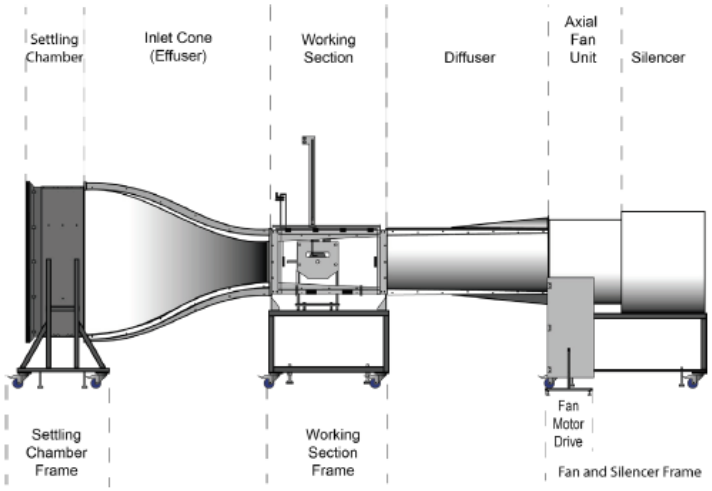

TECQUIPMENT LTD, BONSALL STREET, LONG EATON, NOTTINGHAM NG10 2AN, UK
TECQUIPMENT.COM +44 115 972 2611 SALES@TECQUIPMENT.COM

TECQUIPMENT

Figure 123: Subsonic wind tunnel specifications page

AFA6

32-Way Pressure Display Unit

Microprocessor-controlled 32-way pressure measurement and display unit for use with TecQuipment's Subsonic Wind Tunnel (AF100)

Works with VDAS®

- Optional ancillary to TecQuipment's modular Subsonic Wind Tunnel (AF100)
- Measures and displays up to 32 differential pressures from models, Pitot-static tubes and other devices
- Quicker, easier and more versatile than using liquid manometers
- Integral LCD allows direct pressure measurement
- Measures pressures with respect to atmosphere
- Fully compatible with TecQuipment's Versatile Data Acquisition System (VDAS®) to enable accurate real-time data capture, monitoring and display on a computer

TecQuipment Ltd, Bonsall Street, Long Eaton, Nottingham NG10 2AN, UK

T +44 115 972 2611 • F +44 115 973 1520 • E info@tecquipment.com • W www.tecquipment.com

TecQuipment

Figure 124: 32-Way pressure display unit specifications page 1

AFA6 32-Way Pressure Display Unit

Description

The 32-Way Pressure Display Unit is an optional ancillary to TecQuipment's modular Subsonic Wind Tunnel (AF100). It measures and displays up to 32 different pressures from models, Pitot-static tubes and other measuring instruments fitted to a wind tunnel. It is ideally suited in applications where multiple pressure measurements are required, for example in boundary layer and tapped aerofoil model investigations.

The unit mounts onto the control and instrumentation frame of the AF100 wind tunnel. The microprocessor-controlled unit contains 32 calibrated pressure transducers. Input connection to each of the pressure transducers is via quick-release pressure inputs mounted on the front panel of the unit. This allows easy and quick connection between the unit and an experiment mounted in a wind tunnel. All pressures are measured with respect to atmosphere.

The unit has an integral liquid crystal display with a scroll switch that allows all 32 channels to be viewed in groups of four at any time.

The conditioned outputs of the pressure sensors, and any other connected compatible electronic instruments, may be output to TecQuipment's Versatile Data Acquisition System (VDAS®, available separately) to allow computer-based data acquisition and display. Using VDAS® enables accurate real-time data capture, monitoring, display, calculation and charting of all relevant parameters on a suitable computer (computer not included). When the 32-Way Pressure Display Unit is used with the system it allows laboratory time to be used more efficiently because data can be captured and processed much more quickly than when using manual techniques. The facility in the software to average data to remove the fluctuations inherent in wind tunnel measurements, enhances the quality of the results by making their interpretation much easier. This option provides significant experimental advantages over conventional instruments such as manometers.

Standard Features

- Supplied with comprehensive user guide
- Five-year warranty
- Made in accordance with the latest European Union directives

Ancillary For

- Subsonic Wind Tunnel (AF100)
- NACA 0012 Aerofoil With Tappings (AF102)
- Boundary Layer Model (AF106)

Essential Services

Electrical supply:
100 V a.c. to 240 V a.c., 50 Hz to 60 Hz
Note: A suitable electrical supply outlet is included at the rear of the Subsonic Wind Tunnel controller.

Specification

Dimensions:
Nett: height 450 mm x width 350 mm x depth 220 mm
Packed: 0.11m^3

Weight:
Nett: 10 kg
Packed: 20 kg

Pressure sensors:
32 pressure transducers calibrated at a maximum of ± 7 kPa

Operating Conditions

Operating environment:
Well ventilated laboratory

Storage temperature range:
–25°C to +55°C (when packed for transport)

Operating temperature range:
+5°C to +40°C

Operating relative humidity range:
80% at temperatures < 31°C decreasing linearly to 50% at 40°C

TecQuipment Ltd, Bonsall Street, Long Eaton, Nottingham NG10 2AN, UK
T +44 115 972 2611 • F +44 115 973 1520 • E info@tecquipment.com • W www.tecquipment.com

TecQuipment

Figure 125: 32-Way pressure display unit specifications page 2

with Temp. Measurement

DIGITAL ANEMOMETER

Model : AM-4202 *ISO-9001, CE, IEC1010*

FEATURES

* The portable anemometer provides fast accurate readings with digital readability and the convenience of a remote sensor separately.
* Multi-functions for air flow measurement:
  m/s, km/h, ft/min, knots.
* ℃, ℉ temperature measurement.
* Low-friction ball-bearing design resulting in accuracy at both high and low velocities.
* Conventional twisted vane arms, always a source of unreliability have been eliminated.
* DATA HOLD.
* Compact housing cabinate.
* Wide applications: use this anemometer to check air conditioning & heating systems, measure air velocities, wind speeds, temperature...etc.

LUTRON ELECTRONIC

The Art of Measurement

Figure 126: Digital anemometer specifications page

Gems Sensors

FLOW SENSORS

FT-110 Series – TurboFlow™
Economical Flow-Rate Sensors

- Low Cost Plus High Accuracy ±3% of Reading
- Measures Low Liquid Flow Rates of .1 to 8 GPM
- FDA Approved Materials
- Lightweight Plastic Design Enables Mounting in any Position

Gems hall effect turbine flow rate sensor is ideal for OEM applications involving low flow liquid monitoring. The low cost coupled with 1/2% repeatability makes it an ideal candidate for replacing dispensing timer systems. Unlike existing timing systems, turbine technology is not influenced by changes in system pressure caused by aging filters. The sensor's standard power and output specifications make it easy to retrofit to existing controllers.

Specifications

Wetted Materials	
Body	Nylon 12
Turbine	Nylon 12 Composite
Bearings	PTFE/15% Graphite
Operating Pressure	200 PSIG
Burst Pressure	2500 PSIG
Operating Temperature	-4°F to 212°F (-20°C to 100°C)
Viscosity	32 to 81 SSU (.8 to 16 Centistokes)
Filter	<50 Microns
Input Power	5 to 24 VDC @ 8mA
Output	NPN Sinking Open Collector @ 50mA Maximum (1 to 2.2K Ohm Pull-Up Resistor Required) (Hz Output)
Accuracy	±3% of Reading
Repeatability	0.5% of Full Scale
Electrical Connection	Spade Terminals .110"/.248" x .031" (2.8/6.3 x .8 mm)
Inlet/Outlet Ports	3/8" NPT Male and 3/8" G Male

Dimensions

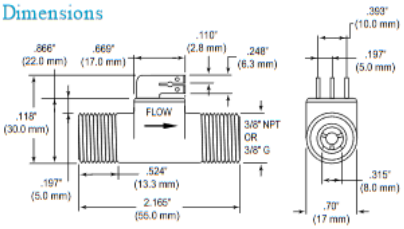

Wiring

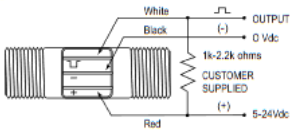

How To Order – Standard Models

Specify Part Number based on desired body material and port size.

Flow Range		Pulses per		Frequency Output	Part Number	
GPM	Liters/m	Gallon	Liter		3/8" NPT	3/8" G
.13-1.3	.5-5	26100	6900	58-575 Hz	173931	173936
.26-2.6	1-10	12500	3300	55-550 Hz	173932	173937
.26-4.0	1-15	17400	4600	76-1150 Hz	173933	173938
.26-4.0	1-15	8300	2200	37-550 Hz	173934 ⚡	173939
.53-7.9	2-30	3800	1000	33-500 Hz	173935 ⚡	173940

⚡ – Stock Items.

Pressure Drop—Typical

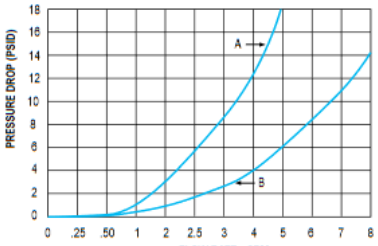

Tests conducted with water flow at 68°F (20°C).

A) Part # 173931 173936 B) Part # 173934 173935
173932 173937 173939 173940
173933 173938

FT-110 Accessories

Description	Part Number
Mating connector w/3 feet, 3 conductor, PVC pigtail leads	173941
Mating connector w/10 feet, 3 conductor, PVC pigtail leads	173942

K-7

Figure 127: Gems turbine flow meter

E Mesh Independence Studies

A mesh independency study was done for each CFD simulation. The amount of cells in the mesh was increased until the change in the engineering quantity being monitored, was negligible small. The results can be seen in Figure 128 tot Figure 134, where the red markers indicate the number of cells that were used in the in the simulations .

Rotating reference frame propeller

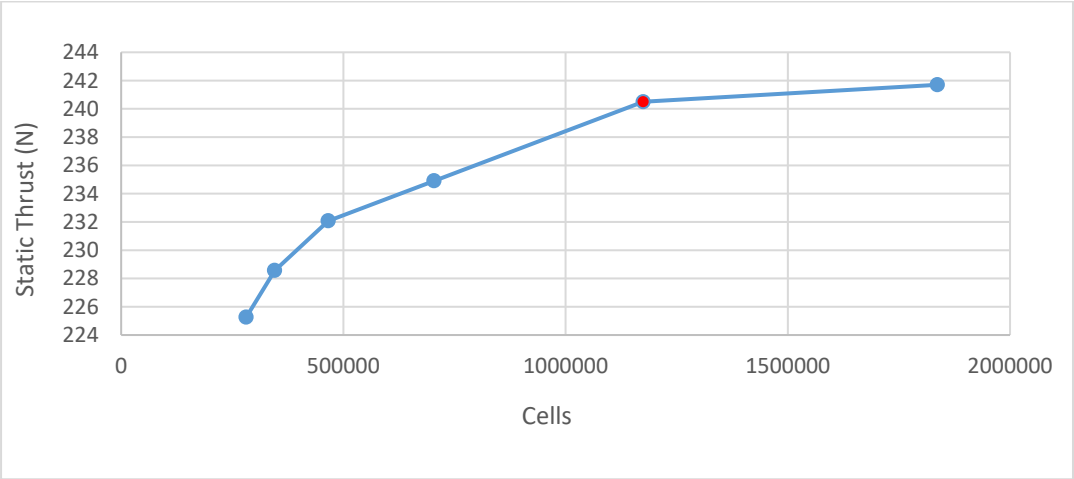

Figure 128: Rotating reference frame propeller mesh independence study

Virtual disk BEM

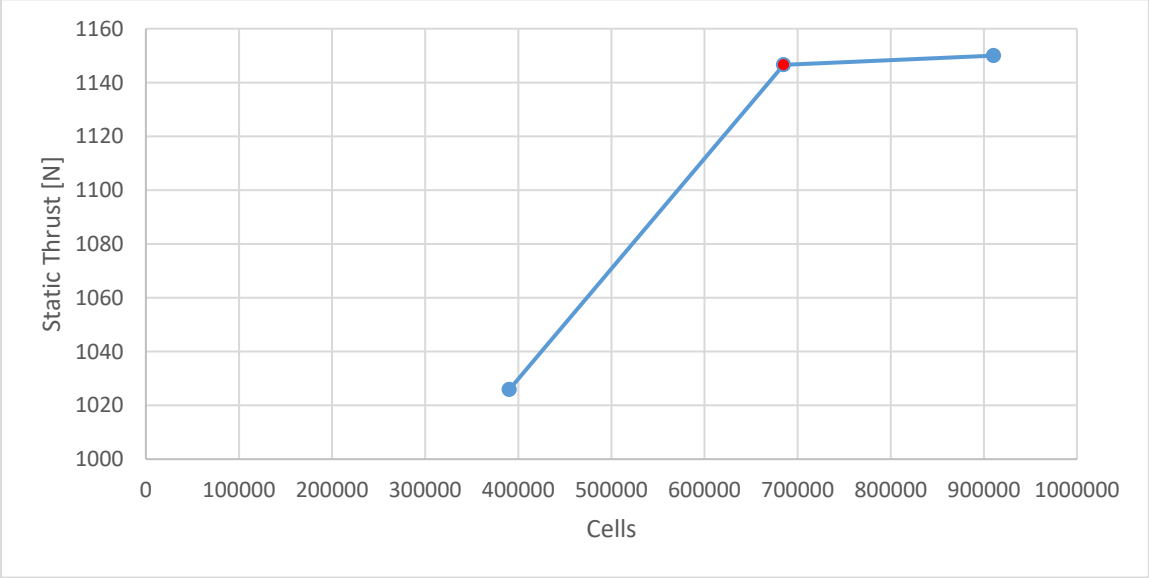

Figure 129: Virtual Disk BEM mesh independence study

Porous radiator model

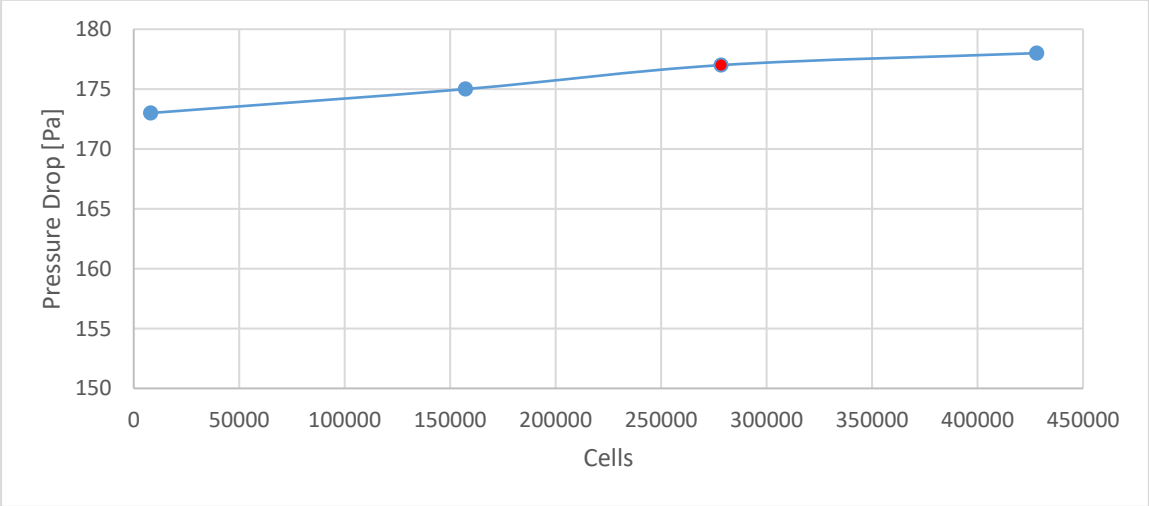

Figure 130: Virtual Disk BEM mesh independence study

Self-launch radiator characterisation model

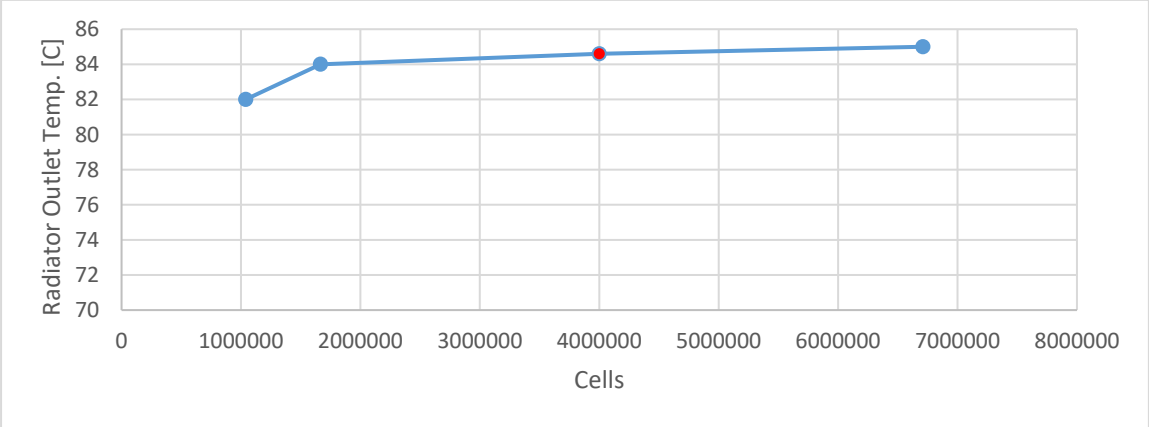

Figure 131: Virtual Disk BEM mesh independence study

Detailed radiator model

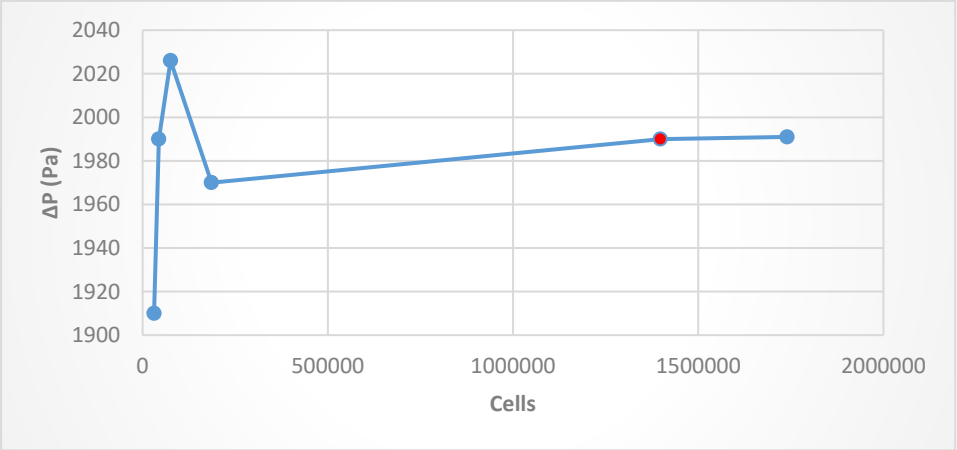

Figure 132: Virtual Disk BEM mesh independence study

Airfoil model

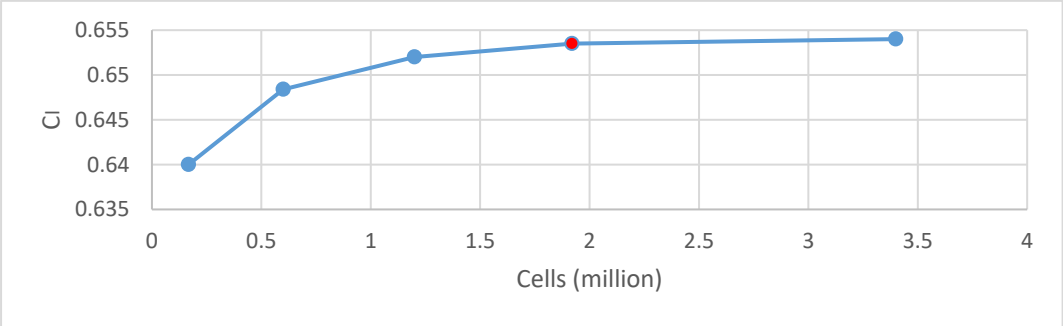

Figure 133: Lift coefficient mesh independence study of the NACA 0012 airfoil

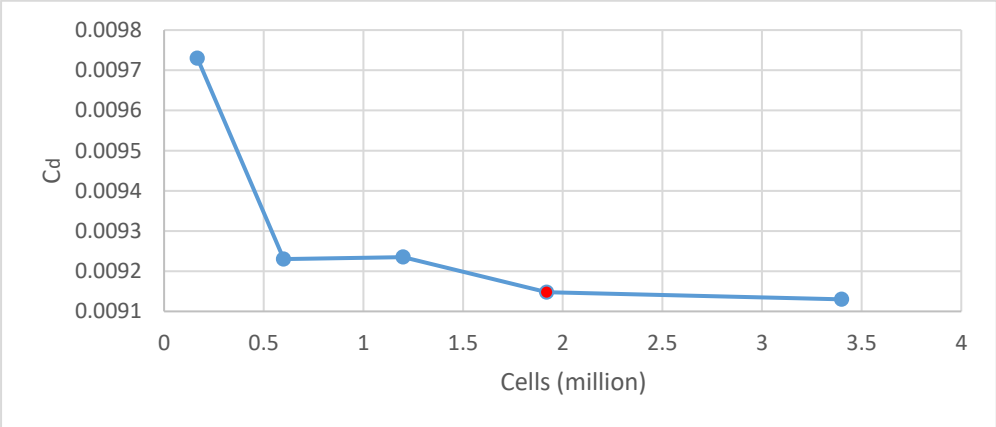

Figure 134: Drag coefficient airfoil mesh independence study

F Propagation of Errors

During the experiments, numerous quantities were measured with instruments that have a specified measurement accuracy. Quantities measured during the experiments are used to calculate other quantities of interest. The influence of the measured quantities' uncertainties when used in calculations, needs to be determined.

A method proposed by (Taylor, 1997), is discussed below to determine the uncertainties of calculated quantities.

Suppose two quantities, X and Y, have an uncertainty of ΔX and ΔY respectively: then the quantities are added or subtracted, and the total uncertainty, ΔU, is determined by equation 8

$$\Delta U = \sqrt{(\Delta A)^2 + (\Delta B)^2} \quad \ldots 8$$

When the above-mentioned quantities are multiplied or divided, the total uncertainty is determined as in equation 9.

$$\Delta U = U\sqrt{(\frac{\Delta A}{A})^2 + (\frac{\Delta B}{B})^2} \quad \ldots 9$$

By using the above the equations, the uncertainty was determined for calculated quantities using experimental measurements.

G Main Integrated CFD Simulation: Summary Report

1. Summary Report: Final SL 1.0

Session Summary

Date	Nov 19, 2018 7:56:20 AM
Simulation	I:\liefvirjouaimee\Final SL 1.0.sim
File size	1.8e+03 MB
Number of Partitions	1
Number of Restored Partitions	1

Software Summary

Version	BuildArch: win64 BuildEnv: intel16.3 ReleaseDate: Wed Feb 7 22:25:17 UTC 2018 ReleaseNumber: 13.02.011

Hardware Summary

Hosts	Number Processes: 1 Rank[0]: DESKTOP-BV36G1T

2. Simulation Properties

1 **Final SL 1.0**		
+-1 Continua	Continua	3
| +-1 **Air**	Regions	[Domain, Air Core]
| | |	Interfaces	[Interface 4, Interface 5, Heat Exchanger 1]
| | |	Point Sets	[]
| | |	Active	true
| | |	Tags	[]
| | +-1 Models		
| | | +-1 All y+ Wall Treatment	Iterative Ustar	false
| | | +-2 Cell Quality Remediation		
| | | +-3 Exact Wall Distance		
| | | +-4 Gas		
| | | | `-1 **Air**	Database Material	Air (Air) [Standard/Gases]
| | | | |	Tags	[]
| | | | `-1 Material Properties		
| | | | +-1 Dynamic Viscosity	Method	Constant
| | | | | `-1 Constant	Value	1.85508E-5 Pa-s
| | | | +-2 Molecular Weight	Method	Constant
| | | | | `-1 Constant	Value	28.9664 kg/kmol
| | | | +-3 Specific Heat	Method	Constant
| | | | | `-1 Constant	Value	1003.62 J/kg-K
| | | | +-4 Thermal Conductivity	Method	Constant
| | | | | `-1 Constant	Value	0.0260305 W/m-K
| | | | `-5 Turbulent Prandtl Number	Method	Constant
| | | | `-1 Constant	Value	0.9
| | | +-5 Gradients	Gradient Method	Hybrid Gauss-LSQ
| | | |	Limiter Method	Venkatakrishnan
| | | |	Custom Accuracy Level Selector	2.0
| | | |	Verbose	false
| | | |	Least-Squares Quality Criterion	true
| | | |	Flat Cells Curvature Criterion	true

Cell Skewness Criterion	true
Chevron-Cell Criterion	true
Least-Squares Tensor Minimum Eigenvalues Ratio	0.1
Normalized Flat Cells Curvature Factor	1.0
Maximum Safe (Positive) Skewness Angle (deg)	75.0
Minimum Unsafe (Positive) Skewness Angle (deg)	88.0
Use TVB Gradient Limiting	false
Acceptable Field Variation (Factor)	0.05
+-6 Ideal Gas	Incompressible	false
Density Limiting	false
+-7 K-Omega Turbulence		
+-8 Reynolds-Averaged Navier-Stokes		
+-9 Segregated Flow	Minimum Absolute Pressure	1000.0 Pa
Positivity Rate Limit	0.2
Flow Boundary Diffusion	true
Unsteady Flux Dissipation Corrections	false
Limit Acoustic-CFL Option	Per-Model
Secondary Gradients	On
Convection	2nd-order
Delta-V Dissipation	Off
+-10 Segregated Fluid Enthalpy	Secondary Gradients	On
Convection	2nd-order
Flow Boundary Diffusion	true
+-11 SST (Menter *et al.*) K-Omega	Curvature Correction Option	Off
Realizability Option	Durbin Scale Limiter
Compressibility Correction	true
Low Re Damping Modification	false
Convection	2nd-order
Normal Stress Term	false
Tke Minimum	1.0E-10
Sdr Minimum	1.0E-10
Secondary Gradients	On
Kappa	0.41
BetaStar	0.09
Beta1	0.075
Sigma_k1	0.85
Sigma_w1	0.5
Beta2	0.0828
Sigma_k2	1.0
Sigma_w2	0.856
Constitutive Option	Linear
a1	0.31
+-1 Compressibility Parameters	Zeta_Star	1.5
`-2 Realizability Coefficient	Realizability Coefficient	0.6000000238418579
+-12 Steady	Continuum Iteration	2999
+-13 Three Dimensional		
+-14 Turbulent		
`-15 Virtual Disk		
`-1 Virtual Disks		
`-1 **Virtual Disk**	Method	Blade Element Method
Display Source Term	false
Verbosity	NONE

Tags	[]
1 Airfoil Sections	
1 **Airfoil Section 1**	Airfoil Section Function Specification: Reynolds Number
Normalized Disk Span	0.7
Tags	[]
1 Cl (AoA, Reynolds)	Table: Reynolds Number: Reynolds
Table: Angle Of Attack	AOA_rad
Table: Cl	Cl
Input Table	calrk y v4
Columns	[AOA_deg, AOA_rad, Cd, Cl, Reynolds]
Table Format	Unstructured
Verbose	false
Cubic Interpolation	false
2 Cd (AoA, Reynolds)	Table: Reynolds Number: Reynolds
Table: Angle Of Attack	AOA_rad
Table: Cd	Cd
Input Table	calrk y v4
Columns	[AOA_deg, AOA_rad, Cd, Cl, Reynolds]
Table Format	Unstructured
Verbose	false
Cubic Interpolation	false
2 Chord Distribution	Method: Table (r/R)
1 Table (r/R)	
3 Sweep Angle Distribution	Method: Constant
1 Constant	Value: 0.0 radian
4 Twist Distribution	Method: Table (r/R)
1 Table (r/R)	
5 Disk Geometry	Number of Blades: 2
Inner Radius	0.08 m
Outer Radius	0.7216 m
Thickness	0.024 m
Origin	[0.0, 0.0, 0.05] m,m,m
Local Coordinate System	Laboratory->Virtual Disk-CSys 1
Orientation Specification	Disk Normal and Coordinate System
1 Normal And Coordinate System	Coordinate System: Laboratory
Disk Normal	[0.0, 0.0, 1.0]
6 Rotation Rate	Rotation Rate: 2198.0 rpm
Ramp Method	Linear Ramp
1 Linear Ramp	Start Iteration: 1
End Iteration	20
Initial Value	0.1
7 Disk Stick Specification	Collective Pitch: 0.0 radian
Cyclic Pitch : Cosine Component	0.0 radian
Cyclic Pitch : Sine Component	0.0 radian
Virtual Disk Trim Option	No Trimming
8 Disk Flap Specification	Coning Angle: 0.0 radian
Cyclic Flap : Cosine Component	0.0 radian
Cyclic Flap : Sine Component	0.0 radian
Flap Hinge Eccentricity	0.0
9 Virtual Disk Resolution	

				+- 1 Azimuthal Resolution	Azimuthal Resolution	18
				`- 2 Radial Resolution	Radial Resolution	18
					Radial Distribution Function	Constant
					Radial Stretch Mode	None
			+- 10 Tip-Loss Correction		Method	Cosine
				`- 1 Cosine	Radial Start Point	1.0
			`- 11 Source Convergence Control		Source Under Relaxation Factor	0.01
					Source Tolerance	0.5
		+-2 Reference Values				
			+-1 Minimum Allowable Wall Distance		Value	1.0E-6 m
			+-2 Minimum Allowable Temperature		Value	100.0 K
			+-3 Maximum Allowable Temperature		Value	5000.0 K
			`-4 Reference Pressure		Value	87000.0 Pa
		`-3 Initial Conditions				
			+-1 Pressure		Method	Constant
				`- 1 Constant	Value	0.0 Pa
			+-2 Static Temperature		Method	Constant
				`- 1 Constant	Value	300.0 K
			+- 3 Turbulence Intensity		Method	Constant
				`- 1 Constant	Value	0.01
			+- 4 Turbulence Specification		Method	Intensity + Viscosity Ratio
			+-5 Turbulent Velocity Scale		Method	Constant
				`- 1 Constant	Value	1.0 m/s
			+-6 Turbulent Viscosity Ratio		Method	Constant
				`- 1 Constant	Value	10.0
			`-7 Velocity		Method	Constant
					Coordinate System	Laboratory
				`- 1 Constant	Value	[0.0, 0.0, 0.0] m/s
		+-2 **Coolant**			Regions	[Outlet Tank, Top tank, Inlet tank, Coolant core]
					Interfaces	[Inlet tank/Outlet Tank, Interface 1, Interface 2, Interface 3, Heat Exchanger 1]
					Point Sets	[]
					Active	true
					Tags	[]
		+-1 Models				
			+-1 Constant Density			
			+-2 Exact Wall Distance			
			+-3 Gradients		Gradient Method	Hybrid Gauss-LSQ
					Limiter Method	Venkatakrishnan
					Custom Accuracy Level Selector	2.0
					Verbose	false
					Least-Squares Quality Criterion	true

Flat Cells Curvature Criterion	true
Cell Skewness Criterion	true
Chevron-Cell Criterion	true
Least-Squares Tensor Minimum Eigenvalues Ratio	0.1
Normalized Flat Cells Curvature Factor	1.0
Maximum Safe (Positive) Skewness Angle (deg)	75.0
Minimum Unsafe (Positive) Skewness Angle (deg)	88.0
Use TVB Gradient Limiting	false
Acceptable Field Variation (Factor)	0.05
K-Epsilon Turbulence	
Liquid	
H2O	Database Material	H2O (Water) [Standard/Liquids]
Tags	[]
Material Properties	
Density	Method	Constant
Constant	Value	997.561 kg/m^3
Dynamic Viscosity	Method	Constant
Constant	Value	8.8871E-4 Pa-s
Specific Heat	Method	Constant
Constant	Value	4181.72 J/kg-K
Thermal Conductivity	Method	Constant
Constant	Value	0.620271 W/m-K
Turbulent Prandtl Number	Method	Constant
Constant	Value	0.9
Realizable K-Epsilon Two-Layer	Buoyancy Production of Dissipation	Boundary Layer Orientation
Cmu	0.09
C1e	1.44
C2e	1.9
Ct	1.0
Sigma_k	1.0
Sigma_e	1.2
Sarkar	2.0
Tke Minimum	1.0E-10
Tdr Minimum	1.0E-10
Secondary Gradients	On
Convection	2nd-order
Normal Stress Term	false
Curvature Correction Option	Off
Two-Layer Type	Shear Driven (Wolfstein)
Two-Layer ReY*	60.0
Two-Layer Delta ReY	10.0
Reynolds-Averaged Navier-Stokes	
Segregated Flow	Minimum Absolute Pressure	1000.0 Pa
Positivity Rate Limit	0.2
Flow Boundary Diffusion	true
Unsteady Flux Dissipation Corrections	false
Limit Acoustic-CFL Option	Per-Model
Secondary Gradients	On
Convection	2nd-order
Delta-V Dissipation	Off

| | | +- 9 Segregated Fluid Temperature	Secondary Gradients: On
| | | |	Convection: 2nd-order
| | | |	Flow Boundary Diffusion: true
| | | +-10 Steady	Continuum Iteration: 2999
| | | +-11 Three Dimensional	
| | | +- 12 Turbulent	
| | | `-13 Two-Layer All y+ Wall Treatment	Iterative Ustar: false
| | +-2 Reference Values	
| | | +-1 Minimum Allowable Wall Distance	Value: 1.0E-6 m
| | | +-2 Minimum Allowable Temperature	Value: 100.0 K
| | | +-3 Maximum Allowable Temperature	Value: 5000.0 K
| | | `-4 Reference Pressure	Value: 101325.0 Pa
| | `-3 Initial Conditions	
| | +-1 Pressure	Method: Constant
| | | `- 1 Constant	Value: 0.0 Pa
| | +-2 Static Temperature	Method: Constant
| | | `- 1 Constant	Value: 300.0 K
| | +- 3 Turbulence Intensity	Method: Constant
| | | `- 1 Constant	Value: 0.01
| | +- 4 Turbulence Specification	Method: Intensity + Viscosity Ratio
| | +-5 Turbulent Velocity Scale	Method: Constant
| | | `- 1 Constant	Value: 1.0 m/s
| | +-6 Turbulent Viscosity Ratio	Method: Constant
| | | `- 1 Constant	Value: 10.0
| | `-7 Velocity	Method: Constant
| | |	Coordinate System: Laboratory
| | `- 1 Constant	Value: [0.0, 0.0, 0.0] m/s
| `-3 **Parts Meshes**	Interpolation Option: Nearest neighbor
|	Regions: [Domain, Outlet Tank, Air Core, Inlet tank, Top tank, Coolant core]
|	Interfaces: [Inlet tank/Outlet Tank, Interface 4, Interface 5, Interface 1, Interface 2, Interface 3, Heat Exchanger 1]
|	Tags: []
+-2 Interfaces	Verbosity: false
| |	Contact Selection Priority: [Inlet tank/Outlet Tank, Interface 4, Interface 5, Interface 1, Interface 2, Interface 3]
| |	Interfaces: 7
| +-1 **Heat Exchanger 1**	Allow Per-Part Values: false
| | |	Region-0 (Cold Region): Air Core
| | |	Region-1 (Hot Region): Coolant core
| | |	Type: Heat Exchanger Interface
| | |	Tags: []

| | +-1 Physics Conditions		
| | | +-1 Heat Exchanger Data Specification	Method	UAG Table
| | | +-2 Heat Exchanger Method	Option	Actual Flow Dual Stream
| | | `-3 Hot Stream Inlet Temperature Specification	Hot Inlet Temperature	Specified
| | `-2 Physics Values		
| | +-1 Heat Exchanger First Iteration	First Heat Exchanger Iteration	100
| | `-2 UAG Table	Cold Fluid Inlet Temperature	293.0 K
| | |	Hot Fluid Inlet Temperature	373.0 K
| | |	Cold Upstream Boundaries	[Air Core: Radiator Inlet [Interface 4]]
| | |	Hot Upstream Boundaries	[Coolant core: Radiator Bot Inet inteface [Interface 3]]
| | |	Hot Mass Flow Rate Specified	false
| | |	UAG Table	AUG FINAL
| | |	UAG Table: Mass Flow Rate	Massflow
| | |	UAG Table: UAG	UAG
| | |	UAG Table: Heat Transfer Units	kW
| | |	Inlet Temperature Averaging	Area Averaged
| | `-1 UAL Table	Table Columns	[mCold, UAL]
| +-2 **Inlet tank/Outlet Tank**	Allow Per-Contact Values	false
| | |	Geometry	Boundaries
| | |	Boundary-0	Outlet Tank: Outletank Divider
| | |	Boundary-1	Inlet tank: Inlet Tank Divider
| | |	Contacts	[]
| | |	Type	Baffle Interface
| | |	Topology	In-place
| | |	Connectivity	Imprinted
| | |	Tags	[]
| | +-1 Physics Conditions		
| | | `-1 Baffle Thermal Option	Baffle Thermal Option	Non-Conducting
| | `-2 Physics Values		
| | `-1 Intersection	Specify by Part Subgroup	false
| | `-1 Intersection tolerance	Value	0.05
| +-3 **Interface 1**	Allow Per-Contact Values	false
| | |	Geometry	Boundaries
| | |	Boundary-0	Top tank: Top Tank Interface
| | |	Boundary-1	Coolant core: Radiator Top inteface
| | |	Contacts	[]
| | |	Type	Internal Interface
| | |	Topology	In-place
| | |	Connectivity	Imprinted
| | |	Tags	[]
| | `-1 Physics Values		
| | `-1 Intersection	Specify by Part Subgroup	false
| | `-1 Intersection tolerance	Value	0.05
| +-4 **Interface 2**	Allow Per-Contact Values	false
| | |	Geometry	Boundaries
| | |	Boundary-0	Outlet Tank: Outlet Tank Interface
| | |	Boundary-1	Coolant core: Outlet Interface
| | |	Contacts	[]
| | |	Type	Internal Interface

				Topology	In-place
				Connectivity	Imprinted
				Tags	[]
		`-1 Physics Values			
		`-1 Intersection		Specify by Part Subgroup	false
		`-1 Intersection tolerance		Value	0.05
	+-5 **Interface 3**			Allow Per-Contact Values	false
				Geometry	Boundaries
				Boundary-0	Inlet tank: Inlet Tank Interface
				Boundary-1	Coolant core: Radiator Bot Inet inteface
				Contacts	[]
				Type	Internal Interface
				Topology	In-place
				Connectivity	Imprinted
				Tags	[]
		`-1 Physics Values			
		`-1 Intersection		Specify by Part Subgroup	false
		`-1 Intersection tolerance		Value	0.05
	+-6 **Interface 4**			Allow Per-Contact Values	false
				Geometry	Boundaries
				Boundary-0	Air Core: Radiator Inlet
				Boundary-1	Domain: Radiator Inlet
				Contacts	[]
				Type	Internal Interface
				Topology	In-place
				Connectivity	Imprinted
				Tags	[]
		`-1 Physics Values			
		`-1 Intersection		Specify by Part Subgroup	false
		`-1 Intersection tolerance		Value	0.05
	`-7 **Interface 5**			Allow Per-Contact Values	false
				Geometry	Boundaries
				Boundary-0	Air Core: Radiator Outlet
				Boundary-1	Domain: Radiator Outlet
				Contacts	[]
				Type	Internal Interface
				Topology	In-place
				Connectivity	Imprinted
				Tags	[]
		`-1 Physics Values			
		`-1 Intersection		Specify by Part Subgroup	false
		`-1 Intersection tolerance		Value	0.05
	+-3 Regions			Part Selection Priority	[Domain, Inlet tank, Outlet Tank, Air Core, Top tank, Coolant core]
				Regions	6
		+-1 **Air Core**		Index	3
				Mesh Continuum	Parts Meshes
				Physics Continuum	Air
				Parts	[Radiator]
				Type	Porous Region
				Allow Per-Part Values	false
				Tags	[]
			+-1 Boundaries	Part Surface Selection Priority	[Air Core: Outlet Interface, Air Core: Radiator Inlet, Air Core: Radiator Outlet, Air Core: Radiator Sides, Air Core: Radiator Top inteface, Air Core: Radiator Bot Inet inteface,

		Air Core: Radiator Inlet [Interface 4], Air Core: Radiator Outlet [Interface 5]]
| | | |	Boundaries	8
| | | +-1 **Outlet Interface**	Index	245
| | | | |	Interfaces	
| | | | |	Part Surfaces	[Radiator.Outlet Interface]
| | | | |	Type	Wall
| | | | |	Allow Per-Surface Values	false
| | | | |	Tags	[]
| | | | +-1 Physics Conditions		
| | | | | +-1 Reference Frame Specification	Option	Region Reference Frame
| | | | | +-2 Shear Stress Specification	Method	No-Slip
| | | | | +-3 Tangential Velocity Specification	Method	Fixed
| | | | | +-4 Thermal Specification	Condition	Adiabatic
| | | | | +-5 User Wall Heat Flux Coefficient Specification	Method	None
| | | | | `-6 Wall Surface Specification	Method	Smooth
| | | | `-2 Physics Values		
| | | | `-1 Blended Wall Function	E	9.0
| | | |	Kappa	0.42
| | | +-2 **Radiator Bot Inet inteface**	Index	250
| | | | |	Interfaces	
| | | | |	Part Surfaces	[Radiator.Radiator Bot Inet inteface]
| | | | |	Type	Wall
| | | | |	Allow Per-Surface Values	false
| | | | |	Tags	[]
| | | | +-1 Physics Conditions		
| | | | | +-1 Reference Frame Specification	Option	Region Reference Frame
| | | | | +-2 Shear Stress Specification	Method	No-Slip
| | | | | +-3 Tangential Velocity Specification	Method	Fixed
| | | | | +-4 Thermal Specification	Condition	Adiabatic
| | | | | +-5 User Wall Heat Flux Coefficient Specification	Method	None
| | | | | `-6 Wall Surface Specification	Method	Smooth
| | | | `-2 Physics Values		
| | | | `-1 Blended Wall Function	E	9.0
| | | |	Kappa	0.42
| | | +-3 **Radiator Inlet**	Index	246
| | | | |	Interfaces	Interface 4
| | | | |	Part Surfaces	[Radiator.Radiator Inlet]
| | | | |	Type	Wall
| | | | |	Allow Per-Surface Values	false
| | | | |	Tags	[]

| | | | +-1 Physics Conditions		
| | | | | +-1 Reference Frame Specification	Option	Region Reference Frame
| | | | | +-2 Shear Stress Specification	Method	No-Slip
| | | | | +-3 Tangential Velocity Specification	Method	Fixed
| | | | | +-4 Thermal Specification	Condition	Adiabatic
| | | | | +-5 User Wall Heat Flux Coefficient Specification	Method	None
| | | | | `-6 Wall Surface Specification	Method	Smooth
| | | | `-2 Physics Values		
| | | | `-1 Blended Wall Function	E	9.0
| | | |	Kappa	0.42
| | | +-4 **Radiator Inlet [Interface 4]**	Index	329
| | | |	Interfaces	
| | | |	Part Surfaces	[]
| | | |	Type	Internal Interface Boundary
| | | |	Allow Per-Contact Values	false
| | | |	Parent Interface	Interface 4
| | | |	Tags	[]
| | | +-5 **Radiator Outlet**	Index	247
| | | | |	Interfaces	Interface 5
| | | | |	Part Surfaces	[Radiator.RadiatorOutlet]
| | | | |	Type	Wall
| | | | |	Allow Per-Surface Values	false
| | | | |	Tags	[]
| | | | +-1 Physics Conditions		
| | | | | +-1 Reference Frame Specification	Option	Region Reference Frame
| | | | | +-2 Shear Stress Specification	Method	No-Slip
| | | | | +-3 Tangential Velocity Specification	Method	Fixed
| | | | | +-4 Thermal Specification	Condition	Adiabatic
| | | | | +-5 User Wall Heat Flux Coefficient Specification	Method	None
| | | | | `-6 Wall Surface Specification	Method	Smooth
| | | | `-2 Physics Values		
| | | | `-1 Blended Wall Function	E	9.0
| | | |	Kappa	0.42
| | | +-6 **Radiator Outlet [Interface 5]**	Index	331
| | | |	Interfaces	
| | | |	Part Surfaces	[]
| | | |	Type	Internal Interface Boundary
| | | |	Allow Per-Contact Values	false
| | | |	Parent Interface	Interface 5
| | | |	Tags	[]

| | | +-7 **Radiator Sides**	Index	248
| | | | |	Interfaces	
| | | | |	Part Surfaces	[Radiator.Radiator Sides]
| | | | |	Type	Wall
| | | | |	Allow Per-Surface Values	false
| | | | |	Tags	[]
| | | +-1 Physics Conditions		
| | | | | +-1 Reference Frame Specification	Option	Region Reference Frame
| | | | | +-2 Shear Stress Specification	Method	No-Slip
| | | | | +-3 Tangential Velocity Specification	Method	Fixed
| | | | | +-4 Thermal Specification	Condition	Adiabatic
| | | | | +-5 User Wall Heat Flux Coefficient Specification	Method	None
| | | | | `-6 Wall Surface Specification	Method	Smooth
| | | | `-2 Physics Values		
| | | | `-1 Blended Wall Function	E	9.0
| | | |	Kappa	0.42
| | | `-8 **Radiator Top inteface**	Index	249
| | | |	Interfaces	
| | | |	Part Surfaces	[Radiator.Radiator Top inteface]
| | | |	Type	Wall
| | | |	Allow Per-Surface Values	false
| | | |	Tags	[]
| | | +-1 Physics Conditions		
| | | | +-1 Reference Frame Specification	Option	Region Reference Frame
| | | | +-2 Shear Stress Specification	Method	No-Slip
| | | | +-3 Tangential Velocity Specification	Method	Fixed
| | | | +-4 Thermal Specification	Condition	Adiabatic
| | | | +-5 User Wall Heat Flux Coefficient Specification	Method	None
| | | | `-6 Wall Surface Specification	Method	Smooth
| | | `-2 Physics Values		
| | | `-1 Blended Wall Function	E	9.0
| | |	Kappa	0.42
| | +-2 Feature Curves	Part Curve Selection Priority	[Air Core:Default Feature Curve]
| | | |	Feature Curves	1
| | | `-1 **Default Feature Curve**	Part Curves	[Radiator.Default]
| | |	Tags	[]
| | +-3 Physics Conditions		
| | | +-1 Energy Source Option	Energy Source Option	None

| | | +-2 Initial Condition Option	Option	Use Continuum Values
| | | +-3 Mass Source Option	Mass Source Option	Disabled
| | | +-4 Momentum Source Option	Momentum Source Option	None
| | | +-5 Porous Media Flux Option	Discount Momentum Fluxes	Disabled
| | | `-6 Turbulence Specification	Method	Intensity + Viscosity Ratio
| | `-4 Physics Values		
| | +-1 Axis	Coordinate System	Laboratory
| | |	Origin	[0.0, 0.0, 0.0] m
| | |	Direction	[0.0, 0.0, 1.0]
| | +-2 Motion Specification	Motion	Stationary
| | |	Reference Frame	Lab Reference Frame
| | +-3 Porosity	Method	Constant
| | | `-1 Constant	Value	1.0
| | +-4 Porous Inertial Resistance	Method	Principal Tensor
| | | `-1 Principal Tensor		
| | | +-1 XX Axis	Method	Constant
| | | | |	Coordinate System	Laboratory
| | | | `-1 Constant	Value	[1.0, 0.0, 0.0]
| | | +-2 YY Axis	Method	Constant
| | | | |	Coordinate System	Laboratory
| | | | `-1 Constant	Value	[0.0, 1.0, 0.0]
| | | +-3 XX Component	Method	Constant
| | | | `-1 Constant	Value	0.0 kg/m^4
| | | +-4 YY Component	Method	Constant
| | | | `-1 Constant	Value	0.0 kg/m^4
| | | `-5 ZZ Component	Method	Constant
| | | `-1 Constant	Value	262.5 kg/m^4
| | +-5 Porous Viscous Resistance	Method	Principal Tensor
| | | `-1 Principal Tensor		
| | | +-1 XX Axis	Method	Constant
| | | | |	Coordinate System	Laboratory
| | | | `-1 Constant	Value	[1.0, 0.0, 0.0]
| | | +-2 YY Axis	Method	Constant
| | | | |	Coordinate System	Laboratory
| | | | `-1 Constant	Value	[0.0, 1.0, 0.0]
| | | +-3 XX Component	Method	Constant
| | | | `-1 Constant	Value	1000000.0 kg/m^3-s
| | | +-4 YY Component	Method	Constant

| | | | `-1 Constant	Value	1000000.0 kg/m^3-s
| | | `-5 ZZ Component	Method	Constant
| | | `-1 Constant	Value	256.4 kg/m^3-s
| | +-6 Solid Thermal Conductivity	Method	Isotropic Tensor
| | | `-1 Isotropic Tensor		
| | | `-1 Isotropic Component	Method	Constant
| | | `-1 Constant	Value	1.0 W/m-K
| | +-7 Tortuosity	Method	Constant
| | | `-1 Constant	Value	1.0
| | +-8 Turbulence Intensity	Method	Constant
| | | `-1 Constant	Value	0.01
| | `-9 Turbulent Viscosity Ratio	Method	Constant
| | `-1 Constant	Value	10.0
| +-2 **Coolant core**	Index	19
| | |	Mesh Continuum	Parts Meshes
| | |	Physics Continuum	Coolant
| | |	Parts	[]
| | |	Type	Porous Region
| | |	Allow Per-Part Values	false
| | |	Tags	[]
| | +-1 Boundaries	Part Surface Selection Priority	[Coolant core: Outlet Interface, Coolant core: Radiator Inlet, Coolant core: Radiator Outlet, Coolant core: Radiator Sides, Coolant core: Radiator Top inteface, Coolant core: Radiator Bot Inet inteface, Coolant core: Radiator Top inteface [Interface 1], Coolant core: Outlet Interface [Interface 2], Coolant core: Radiator Bot Inet inteface [Interface 3]]
| | | |	Boundaries	9
| | | +-1 **Outlet Interface**	Index	461
| | | | |	Interfaces	Interface 2
| | | | |	Part Surfaces	[]
| | | | |	Type	Wall
| | | | |	Allow Per-Surface Values	false
| | | | |	Tags	[]
| | | | +-1 Physics Conditions		
| | | | | +-1 Reference Frame Specification	Option	Region Reference Frame
| | | | | +-2 Shear Stress Specification	Method	No-Slip
| | | | | +-3 Tangential Velocity Specification	Method	Fixed
| | | | | +-4 Thermal Specification	Condition	Adiabatic
| | | | | +-5 User Wall Heat Flux Coefficient Specification	Method	None
| | | | | `-6 Wall Surface Specification	Method	Smooth
| | | | `-2 Physics Values		
| | | | `-1 Blended Wall Function	E	9.0

| | | |	Kappa	0.42
| | | +-2 **Outlet Interface [Interface 2]**	Index	470
| | | |	Interfaces	
| | | |	Part Surfaces	[]
| | | |	Type	Internal Interface Boundary
| | | |	Allow Per-Contact Values	false
| | | |	Parent Interface	Interface 2
| | | |	Tags	[]
| | | +-3 **Radiator Bot Inet inteface**	Index	466
| | | | |	Interfaces	Interface 3
| | | | |	Part Surfaces	[]
| | | | |	Type	Wall
| | | | |	Allow Per-Surface Values	false
| | | | |	Tags	[]
| | | | +-1 Physics Conditions		
| | | | | +-1 Reference Frame Specification	Option	Region Reference Frame
| | | | | +-2 Shear Stress Specification	Method	No-Slip
| | | | | +-3 Tangential Velocity Specification	Method	Fixed
| | | | | +-4 Thermal Specification	Condition	Adiabatic
| | | | | +-5 User Wall Heat Flux Coefficient Specification	Method	None
| | | | | `-6 Wall Surface Specification	Method	Smooth
| | | | `-2 Physics Values		
| | | | `-1 Blended Wall Function	E	9.0
| | | |	Kappa	0.42
| | | +-4 **Radiator Bot Inet inteface [Interface 3]**	Index	472
| | | |	Interfaces	
| | | |	Part Surfaces	[]
| | | |	Type	Internal Interface Boundary
| | | |	Allow Per-Contact Values	false
| | | |	Parent Interface	Interface 3
| | | |	Tags	[]
| | | +-5 **Radiator Inlet**	Index	462
| | | | |	Interfaces	
| | | | |	Part Surfaces	[]
| | | | |	Type	Wall
| | | | |	Allow Per-Surface Values	false
| | | | |	Tags	[]
| | | | +-1 Physics Conditions		
| | | | | +-1 Reference Frame Specification	Option	Region Reference Frame
| | | | | +-2 Shear Stress Specification	Method	No-Slip
| | | | | +-3 Tangential Velocity Specification	Method	Fixed
| | | | | +-4 Thermal Specification	Condition	Adiabatic

| | | | | +-5 User Wall Heat Flux Coefficient Specification	Method	None
| | | | | `-6 Wall Surface Specification	Method	Smooth
| | | | `-2 Physics Values		
| | | | | `-1 Blended Wall Function	E	9.0
| | | |	Kappa	0.42
| | | +-6 **Radiator Outlet**	Index	463
| | | | |	Interfaces	
| | | | |	Part Surfaces	[]
| | | | |	Type	Wall
| | | | |	Allow Per-Surface Values	false
| | | | |	Tags	[]
| | | | +-1 Physics Conditions		
| | | | | +-1 Reference Frame Specification	Option	Region Reference Frame
| | | | | +-2 Shear Stress Specification	Method	No-Slip
| | | | | +-3 Tangential Velocity Specification	Method	Fixed
| | | | | +-4 Thermal Specification	Condition	Adiabatic
| | | | | +-5 User Wall Heat Flux Coefficient Specification	Method	None
| | | | | `-6 Wall Surface Specification	Method	Smooth
| | | | `-2 Physics Values		
| | | | | `-1 Blended Wall Function	E	9.0
| | | |	Kappa	0.42
| | | +-7 **Radiator Sides**	Index	464
| | | | |	Interfaces	
| | | | |	Part Surfaces	[]
| | | | |	Type	Wall
| | | | |	Allow Per-Surface Values	false
| | | | |	Tags	[]
| | | | +-1 Physics Conditions		
| | | | | +-1 Reference Frame Specification	Option	Region Reference Frame
| | | | | +-2 Shear Stress Specification	Method	No-Slip
| | | | | +-3 Tangential Velocity Specification	Method	Fixed
| | | | | +-4 Thermal Specification	Condition	Adiabatic
| | | | | +-5 User Wall Heat Flux Coefficient Specification	Method	None
| | | | | `-6 Wall Surface Specification	Method	Smooth
| | | | `-2 Physics Values		
| | | | | `-1 Blended Wall Function	E	9.0
| | | |	Kappa	0.42

| | | +-8 **Radiator Top inteface**	Index	465
| | | | |	Interfaces	Interface 1
| | | | |	Part Surfaces	[]
| | | | |	Type	Wall
| | | | |	Allow Per-Surface Values	false
| | | | |	Tags	[]
| | | +-1 Physics Conditions		
| | | | | +-1 Reference Frame Specification	Option	Region Reference Frame
| | | | | +-2 Shear Stress Specification	Method	No-Slip
| | | | | +-3 Tangential Velocity Specification	Method	Fixed
| | | | | +-4 Thermal Specification	Condition	Adiabatic
| | | | | +-5 User Wall Heat Flux Coefficient Specification	Method	None
| | | | | `-6 Wall Surface Specification	Method	Smooth
| | | | `-2 Physics Values		
| | | | | `-1 Blended Wall Function	E	9.0
| | | |	Kappa	0.42
| | | `-9 **Radiator Top inteface [Interface 1]**	Index	468
| | |	Interfaces	
| | |	Part Surfaces	[]
| | |	Type	Internal Interface Boundary
| | |	Allow Per-Contact Values	false
| | |	Parent Interface	Interface 1
| | |	Tags	[]
| | +-2 Feature Curves	Part Curve Selection Priority	[Coolant core:Default Feature Curve]
| | | |	Feature Curves	1
| | | `-1 **Default Feature Curve**	Part Curves	[]
| | |	Tags	[]
| | +-3 Physics Conditions		
| | | +-1 Energy Source Option	Energy Source Option	None
| | | +-2 Initial Condition Option	Option	Use Continuum Values
| | | +-3 Mass Source Option	Mass Source Option	Disabled
| | | +-4 Momentum Source Option	Momentum Source Option	None
| | | +-5 Porous Media Flux Option	Discount Momentum Fluxes	Disabled
| | | `-6 Turbulence Specification	Method	Intensity + Viscosity Ratio
| | `-4 Physics Values		
| | +-1 Axis	Coordinate System	Laboratory
| | |	Origin	[0.0, 0.0, 0.0] m
| | |	Direction	[0.0, 0.0, 1.0]
| | +-2 Motion Specification	Motion	Stationary
| | |	Reference Frame	Lab Reference Frame
| | +-3 Porosity	Method	Constant

| | | `- 1 Constant	Value	1.0
| | +-4 Porous Inertial Resistance	Method	Principal Tensor
| | | `- 1 Principal Tensor		
| | | +-1 XX Axis	Method	Constant
| | | | |	Coordinate System	Laboratory
| | | | `- 1 Constant	Value	[1.0, 0.0, 0.0]
| | | +-2 YY Axis	Method	Constant
| | | | |	Coordinate System	Laboratory
| | | | `- 1 Constant	Value	[0.0, 1.0, 0.0]
| | | +-3 XX Component	Method	Constant
| | | | `- 1 Constant	Value	0.0 kg/m^4
| | | +-4 YY Component	Method	Constant
| | | | `- 1 Constant	Value	0.0 kg/m^4
| | | `-5 ZZ Component	Method	Constant
| | | `- 1 Constant	Value	0.0 kg/m^4
| | +-5 Porous Viscous Resistance	Method	Principal Tensor
| | | `- 1 Principal Tensor		
| | | +-1 XX Axis	Method	Constant
| | | | |	Coordinate System	Laboratory
| | | | `- 1 Constant	Value	[1.0, 0.0, 0.0]
| | | +-2 YY Axis	Method	Constant
| | | | |	Coordinate System	Laboratory
| | | | `- 1 Constant	Value	[0.0, 1.0, 0.0]
| | | +-3 XX Component	Method	Constant
| | | | `- 1 Constant	Value	1.0E8 kg/m^3-s
| | | +-4 YY Component	Method	Constant
| | | | `- 1 Constant	Value	100000.0 kg/m^3-s
| | | `-5 ZZ Component	Method	Constant
| | | `- 1 Constant	Value	1.0E8 kg/m^3-s
| | +-6 Solid Thermal Conductivity	Method	Isotropic Tensor
| | | `- 1 Isotropic Tensor		
| | | `- 1 Isotropic Component	Method	Constant
| | | `- 1 Constant	Value	1.0 W/m-K
| | +-7 Tortuosity	Method	Constant
| | | `- 1 Constant	Value	1.0
| | +- 8 Turbulence Intensity	Method	Constant
| | | `- 1 Constant	Value	0.01

| | `-9 Turbulent Viscosity Ratio	Method	Constant
| | `-1 Constant	Value	10.0
| +-3 **Domain**	Index	0
| | |	Mesh Continuum	Parts Meshes
| | |	Physics Continuum	Air
| | |	Parts	[Domain]
| | |	Type	Fluid Region
| | |	Allow Per-Part Values	false
| | |	Tags	[]
| | +-1 Boundaries	Part Surface Selection Priority	[Domain: Engine, Domain: Domain Inlet, Domain: Domain Outlet, Domain: Domain Sides, Domain: Exhaust, Domain: Pylon, Domain: Radiator Inlet, Domain: Radiator Outlet, Domain: Radiator Sides, Domain: Top Tank, Domain: Bot Tank, Domain: Radiator Inlet [Interface 4], Domain: Radiator Outlet [Interface 5]]
| | | |	Boundaries	13
| | | +-1 **Bot Tank**	Index	236
| | | | |	Interfaces	
| | | | |	Part Surfaces	[Domain.Bot Tank]
| | | | |	Type	Wall
| | | | |	Allow Per-Surface Values	false
| | | | |	Tags	[]
| | | | +-1 Physics Conditions		
| | | | | +-1 Reference Frame Specification	Option	Region Reference Frame
| | | | | +-2 Shear Stress Specification	Method	No-Slip
| | | | | +-3 Tangential Velocity Specification	Method	Fixed
| | | | | +-4 Thermal Specification	Condition	Adiabatic
| | | | | +-5 User Wall Heat Flux Coefficient Specification	Method	None
| | | | | `-6 Wall Surface Specification	Method	Smooth
| | | | `-2 Physics Values		
| | | | `-1 Blended Wall Function	E	9.0
| | | |	Kappa	0.42
| | | +-2 **Domain Inlet**	Index	227
| | | | |	Interfaces	
| | | | |	Part Surfaces	[Domain.Domain Inlet]
| | | | |	Type	Velocity Inlet
| | | | |	Allow Per-Surface Values	false
| | | | |	Tags	[]
| | | | +-1 Physics Conditions		
| | | | | +-1 Flow Direction Specification	Method	Boundary-Normal
| | | | | +-2 Reference Frame Specification	Option	Lab Frame
| | | | | +-3 Turbulence Specification	Method	Intensity + Viscosity Ratio
| | | | | `-4 Velocity Specification	Method	Magnitude + Direction
| | | | `-2 Physics Values		

| | | | +- 1 Static Temperature	Method	Constant
| | | | | `- 1 Constant	Value	33.0 C
| | | | +- 2 Turbulence Intensity	Method	Constant
| | | | | `- 1 Constant	Value	0.01
| | | | +- 3 Turbulent Viscosity Ratio	Method	Constant
| | | | | `- 1 Constant	Value	10.0
| | | | `- 4 Velocity Magnitude	Method	Constant
| | | | `- 1 Constant	Value	0.0 m/s
| | | +-3 **Domain Outlet**	Index	228
| | | | |	Interfaces	
| | | | |	Part Surfaces	[Domain.Domain Outlet]
| | | | |	Type	Pressure Outlet
| | | | |	Allow Per-Surface Values	false
| | | | |	Tags	[]
| | | | +-1 Physics Conditions		
| | | | | +- 1 Backflow Specification	Direction	Boundary-Normal
| | | | | |	Pressure	Environmental
| | | | | +- 2 Pressure Outlet Option	Option	None
| | | | | +- 3 Reference Frame Specification	Option	Lab Frame
| | | | | `- 4 Turbulence Specification	Method	Intensity + Viscosity Ratio
| | | | `-2 Physics Values		
| | | | +- 1 Pressure	Method	Constant
| | | | | `- 1 Constant	Value	0.0 Pa
| | | | +- 2 Static Temperature	Method	Constant
| | | | | `- 1 Constant	Value	33.0 C
| | | | +- 3 Turbulence Intensity	Method	Constant
| | | | | `- 1 Constant	Value	0.01
| | | | `- 4 Turbulent Viscosity Ratio	Method	Constant
| | | | `- 1 Constant	Value	10.0
| | | +-4 **Domain Sides**	Index	229
| | | |	Interfaces	
| | | |	Part Surfaces	[Domain.Domain Sides]
| | | |	Type	Symmetry Plane
| | | |	Allow Per-Surface Values	false
| | | |	Tags	[]
| | | +-5 **Engine**	Index	226
| | | | |	Interfaces	
| | | | |	Part Surfaces	[Domain.Engine]
| | | | |	Type	Wall
| | | | |	Allow Per-Surface Values	false
| | | | |	Tags	[]

| | | | +-1 Physics Conditions		
| | | | | +-1 Reference Frame Specification	Option	Region Reference Frame
| | | | | +-2 Shear Stress Specification	Method	No-Slip
| | | | | +-3 Tangential Velocity Specification	Method	Fixed
| | | | | +-4 Thermal Specification	Condition	Adiabatic
| | | | | +-5 User Wall Heat Flux Coefficient Specification	Method	None
| | | | | `-6 Wall Surface Specification	Method	Smooth
| | | | `-2 Physics Values		
| | | | `-1 Blended Wall Function	E	9.0
| | | |	Kappa	0.42
| | | +-6 **Exhaust**	Index	230
| | | | |	Interfaces	
| | | | |	Part Surfaces	[Domain.Exhaust]
| | | | |	Type	Wall
| | | | |	Allow Per-Surface Values	false
| | | | |	Tags	[]
| | | | +-1 Physics Conditions		
| | | | | +-1 Reference Frame Specification	Option	Region Reference Frame
| | | | | +-2 Shear Stress Specification	Method	No-Slip
| | | | | +-3 Tangential Velocity Specification	Method	Fixed
| | | | | +-4 Thermal Specification	Condition	Adiabatic
| | | | | +-5 User Wall Heat Flux Coefficient Specification	Method	None
| | | | | `-6 Wall Surface Specification	Method	Smooth
| | | | `-2 Physics Values		
| | | | `-1 Blended Wall Function	E	9.0
| | | |	Kappa	0.42
| | | +-7 **Pylon**	Index	231
| | | | |	Interfaces	
| | | | |	Part Surfaces	[Domain.Pylon]
| | | | |	Type	Wall
| | | | |	Allow Per-Surface Values	false
| | | | |	Tags	[]
| | | | +-1 Physics Conditions		
| | | | | +-1 Reference Frame Specification	Option	Region Reference Frame
| | | | | +-2 Shear Stress Specification	Method	No-Slip
| | | | | +-3 Tangential Velocity Specification	Method	Fixed

| | | | | +- 4 Thermal Specification	Condition	Adiabatic
| | | | | +-5 User Wall Heat Flux Coefficient Specification	Method	None
| | | | | `-6 Wall Surface Specification	Method	Smooth
| | | | `-2 Physics Values		
| | | | `- 1 Blended Wall Function	E	9.0
| | | |	Kappa	0.42
| | | +-8 **Radiator Inlet**	Index	232
| | | | |	Interfaces	Interface 4
| | | | |	Part Surfaces	[Domain.Radiator Inlet 2]
| | | | |	Type	Wall
| | | | |	Allow Per-Surface Values	false
| | | | |	Tags	[]
| | | | +-1 Physics Conditions		
| | | | | +- 1 Reference Frame Specification	Option	Region Reference Frame
| | | | | +- 2 Shear Stress Specification	Method	No-Slip
| | | | | +- 3 Tangential Velocity Specification	Method	Fixed
| | | | | +- 4 Thermal Specification	Condition	Adiabatic
| | | | | +-5 User Wall Heat Flux Coefficient Specification	Method	None
| | | | | `-6 Wall Surface Specification	Method	Smooth
| | | | `-2 Physics Values		
| | | | `- 1 Blended Wall Function	E	9.0
| | | |	Kappa	0.42
| | | +-9 **Radiator Inlet [Interface 4]**	Index	330
| | | |	Interfaces	
| | | |	Part Surfaces	[]
| | | |	Type	Internal Interface Boundary
| | | |	Allow Per-Contact Values	false
| | | |	Parent Interface	Interface 4
| | | |	Tags	[]
| | | +-10 **Radiator Outlet**	Index	233
| | | | |	Interfaces	Interface 5
| | | | |	Part Surfaces	[Domain.Radiator Outlet 2]
| | | | |	Type	Wall
| | | | |	Allow Per-Surface Values	false
| | | | |	Tags	[]
| | | | +-1 Physics Conditions		
| | | | | +- 1 Reference Frame Specification	Option	Region Reference Frame
| | | | | +- 2 Shear Stress Specification	Method	No-Slip
| | | | | +- 3 Tangential Velocity Specification	Method	Fixed

| | | | | +- 4 Thermal Specification	Condition	Adiabatic
| | | | | +-5 User Wall Heat Flux Coefficient Specification	Method	None
| | | | | `-6 Wall Surface Specification	Method	Smooth
| | | | `-2 Physics Values		
| | | | `- 1 Blended Wall Function	E	9.0
| | | |	Kappa	0.42
| | | +-11 **Radiator Outlet [Interface 5]**	Index	332
| | | |	Interfaces	
| | | |	Part Surfaces	[]
| | | |	Type	Internal Interface Boundary
| | | |	Allow Per-Contact Values	false
| | | |	Parent Interface	Interface 5
| | | |	Tags	[]
| | | +-12 **Radiator Sides**	Index	234
| | | | |	Interfaces	
| | | | |	Part Surfaces	[Domain.Radiator Sides 2]
| | | | |	Type	Wall
| | | | |	Allow Per-Surface Values	false
| | | | |	Tags	[]
| | | | +-1 Physics Conditions		
| | | | | +- 1 Reference Frame Specification	Option	Region Reference Frame
| | | | | +- 2 Shear Stress Specification	Method	No-Slip
| | | | | +- 3 Tangential Velocity Specification	Method	Fixed
| | | | | +- 4 Thermal Specification	Condition	Adiabatic
| | | | | +-5 User Wall Heat Flux Coefficient Specification	Method	None
| | | | | `-6 Wall Surface Specification	Method	Smooth
| | | | `-2 Physics Values		
| | | | `- 1 Blended Wall Function	E	9.0
| | | |	Kappa	0.42
| | | `-13 **Top Tank**	Index	235
| | | | |	Interfaces	
| | | | |	Part Surfaces	[Domain.Top Tank]
| | | | |	Type	Wall
| | | | |	Allow Per-Surface Values	false
| | | | |	Tags	[]
| | | +-1 Physics Conditions		
| | | | | +- 1 Reference Frame Specification	Option	Region Reference Frame
| | | | | +- 2 Shear Stress Specification	Method	No-Slip
| | | | | +- 3 Tangential Velocity Specification	Method	Fixed

| | | | +-4 Thermal Specification	Condition	Adiabatic
| | | | +-5 User Wall Heat Flux Coefficient Specification	Method	None
| | | | `-6 Wall Surface Specification	Method	Smooth
| | | `-2 Physics Values		
| | | `-1 Blended Wall Function	E	9.0
| | |	Kappa	0.42
| | +-2 Feature Curves	Part Curve Selection Priority	[Domain:Default Feature Curve]
| | | |	Feature Curves	1
| | | `-1 **Default Feature Curve**	Part Curves	[Domain.Default]
| | |	Tags	[]
| | +-3 Physics Conditions		
| | | +-1 Energy Source Option	Energy Source Option	None
| | | +-2 Initial Condition Option	Option	Use Continuum Values
| | | +-3 Mass Source Option	Mass Source Option	Disabled
| | | +-4 Momentum Source Option	Momentum Source Option	None
| | | `-5 Turbulence Source Option	Turbulence Source Option	None
| | `-4 Physics Values		
| | +-1 Axis	Coordinate System	Laboratory
| | |	Origin	[0.0, 0.0, 0.0] m
| | |	Direction	[0.0, 0.0, 1.0]
| | `-2 Motion Specification	Motion	Stationary
| |	Reference Frame	Lab Reference Frame
| +-4 **Inlet tank**	Index	1
| | |	Mesh Continuum	Parts Meshes
| | |	Physics Continuum	Coolant
| | |	Parts	[Inlet tank]
| | |	Type	Fluid Region
| | |	Allow Per-Part Values	false
| | |	Tags	[]
| | +-1 Boundaries	Part Surface Selection Priority	[Inlet tank: Inlet Tank Interface, Inlet tank: Inlet Tank Divider, Inlet tank: Inlet Tank, Inlet tank: Inlet Tank in, Inlet tank: Inlet Tank Divider [Inlet tank/Outlet Tank], Inlet tank: Inlet Tank Interface [Interface 3]]
| | | |	Boundaries	6
| | | +-1 **Inlet Tank**	Index	239
| | | | |	Interfaces	
| | | | |	Part Surfaces	[Inlet tank.Inlet Tank]
| | | | |	Type	Wall
| | | | |	Allow Per-Surface Values	false
| | | | |	Tags	[]
| | | | +-1 Physics Conditions		
| | | | | +-1 Reference Frame Specification	Option	Region Reference Frame
| | | | | +-2 Shear Stress Specification	Method	No-Slip

| | | | | +- 3 Tangential Velocity Specification	Method	Fixed
| | | | | +- 4 Thermal Specification	Condition	Adiabatic
| | | | | +-5 User Wall Heat Flux Coefficient Specification	Method	None
| | | | | `-6 Wall Surface Specification	Method	Smooth
| | | | `-2 Physics Values		
| | | | `- 1 Blended Wall Function	E	9.0
| | | |	Kappa	0.42
| | | +-2 **Inlet Tank Divider**	Index	238
| | | | |	Interfaces	Inlet tank/Outlet Tank
| | | | |	Part Surfaces	[Inlet tank.Inlet Tank Divider]
| | | | |	Type	Wall
| | | | |	Allow Per-Surface Values	false
| | | | |	Tags	[]
| | | | +-1 Physics Conditions		
| | | | | +- 1 Reference Frame Specification	Option	Region Reference Frame
| | | | | +- 2 Shear Stress Specification	Method	No-Slip
| | | | | +- 3 Tangential Velocity Specification	Method	Fixed
| | | | | +- 4 Thermal Specification	Condition	Adiabatic
| | | | | +-5 User Wall Heat Flux Coefficient Specification	Method	None
| | | | | `-6 Wall Surface Specification	Method	Smooth
| | | | `-2 Physics Values		
| | | | `- 1 Blended Wall Function	E	9.0
| | | |	Kappa	0.42
| | | +-3 **Inlet Tank Divider [Inlet tank/Outlet Tank]**	Index	269
| | | | |	Interfaces	
| | | | |	Part Surfaces	[]
| | | | |	Type	Baffle Boundary
| | | | |	Allow Per-Contact Values	false
| | | | |	Parent Interface	Inlet tank/Outlet Tank
| | | | |	Tags	[]
| | | | +-1 Physics Conditions		
| | | | | +- 1 Reference Frame Specification	Option	Region Reference Frame
| | | | | +- 2 Shear Stress Specification	Method	No-Slip
| | | | | +- 3 Tangential Velocity Specification	Method	Fixed
| | | | | `-4 Wall Surface Specification	Method	Smooth
| | | | `-2 Physics Values		

| | | | `-1 Blended Wall Function	E	9.0
| | | |	Kappa	0.42
| | +-4 **Inlet Tank Interface**	Index	237
| | | | |	Interfaces	Interface 3
| | | | |	Part Surfaces	[Inlet tank.Inlet Tank Interface]
| | | | |	Type	Wall
| | | | |	Allow Per-Surface Values	false
| | | | |	Tags	[]
| | | | +-1 Physics Conditions		
| | | | | +-1 Reference Frame Specification	Option	Region Reference Frame
| | | | | +-2 Shear Stress Specification	Method	No-Slip
| | | | | +-3 Tangential Velocity Specification	Method	Fixed
| | | | | +-4 Thermal Specification	Condition	Adiabatic
| | | | | +-5 User Wall Heat Flux Coefficient Specification	Method	None
| | | | | `-6 Wall Surface Specification	Method	Smooth
| | | | `-2 Physics Values		
| | | | `-1 Blended Wall Function	E	9.0
| | | |	Kappa	0.42
| | +-5 **Inlet Tank Interface [Interface 3]**	Index	471
| | | |	Interfaces	
| | | |	Part Surfaces	[]
| | | |	Type	Internal Interface Boundary
| | | |	Allow Per-Contact Values	false
| | | |	Parent Interface	Interface 3
| | | |	Tags	[]
| | | `-6 **Inlet Tank in**	Index	240
| | | | |	Interfaces	
| | | | |	Part Surfaces	[Inlet tank.Inlet Tank in]
| | | | |	Type	Mass Flow Inlet
| | | | |	Allow Per-Surface Values	false
| | | | |	Tags	[]
| | | +-1 Physics Conditions		
| | | | +-1 Flow Direction Specification	Method	Boundary-Normal
| | | | +-2 Mass Flow Option	Specification Option	Mass Flow Rate
| | | | +-3 Reference Frame Specification	Option	Lab Frame
| | | | `-4 Turbulence Specification	Method	Intensity + Viscosity Ratio
| | | `-2 Physics Values		
| | | +-1 Mass Flow Rate	Method	Constant
| | | | `-1 Constant	Value	0.09 kg/s
| | | +-2 Total Temperature	Method	Constant

| | | | `-1 Constant	Value: 107.6 C
| | | +-3 Turbulence Intensity	Method: Constant
| | | | `-1 Constant	Value: 0.01
| | | `-4 Turbulent Viscosity Ratio	Method: Constant
| | | `-1 Constant	Value: 10.0
| | +-2 Feature Curves	Part Curve Selection Priority: [Inlet tank:Default Feature Curve]
| | | |	Feature Curves: 1
| | | `-1 **Default Feature Curve**	Part Curves: [Inlet tank.Default]
| | |	Tags: []
| | +-3 Physics Conditions	
| | | +-1 Energy Source Option	Energy Source Option: None
| | | +-2 Initial Condition Option	Option: Use Continuum Values
| | | +-3 Mass Source Option	Mass Source Option: Disabled
| | | +-4 Momentum Source Option	Momentum Source Option: None
| | | `-5 Turbulence Source Option	Turbulence Source Option: None
| | `-4 Physics Values	
| | +-1 Axis	Coordinate System: Laboratory
| | |	Origin: [0.0, 0.0, 0.0] m
| | |	Direction: [0.0, 0.0, 1.0]
| | `-2 Motion Specification	Motion: Stationary
| |	Reference Frame: Lab Reference Frame
| +-5 **Outlet Tank**	Index: 2
| | |	Mesh Continuum: Parts Meshes
| | |	Physics Continuum: Coolant
| | |	Parts: [Outlet Tank]
| | |	Type: Fluid Region
| | |	Allow Per-Part Values: false
| | |	Tags: []
| | +-1 Boundaries	Part Surface Selection Priority: [Outlet Tank: Outletank Divider, Outlet Tank: Outlet Tank, Outlet Tank: Outlet Tank out, Outlet Tank: Outlet Tank Interface, Outlet Tank: Outletank Divider [Inlet tank/Outlet Tank], Outlet Tank: Outlet Tank Interface [Interface 2]]
| | | |	Boundaries: 6
| | | +-1 **Outlet Tank**	Index: 242
| | | | |	Interfaces
| | | | |	Part Surfaces: [Outlet Tank.Outlet Tank]
| | | | |	Type: Wall
| | | | |	Allow Per-Surface Values: false
| | | | |	Tags: []
| | | | +-1 Physics Conditions	
| | | | | +-1 Reference Frame Specification	Option: Region Reference Frame
| | | | | +-2 Shear Stress Specification	Method: No-Slip

| | | | | +- 3 Tangential Velocity Specification	Method	Fixed
| | | | | +- 4 Thermal Specification	Condition	Adiabatic
| | | | | +-5 User Wall Heat Flux Coefficient Specification	Method	None
| | | | | `-6 Wall Surface Specification	Method	Smooth
| | | | `-2 Physics Values		
| | | | `- 1 Blended Wall Function	E	9.0
| | | |	Kappa	0.42
| | | +-2 **Outlet Tank Interface**	Index	244
| | | | |	Interfaces	Interface 2
| | | | |	Part Surfaces	[Outlet Tank.Outlet Tank Interface]
| | | | |	Type	Wall
| | | | |	Allow Per-Surface Values	false
| | | | |	Tags	[]
| | | | +-1 Physics Conditions		
| | | | | +- 1 Reference Frame Specification	Option	Region Reference Frame
| | | | | +- 2 Shear Stress Specification	Method	No-Slip
| | | | | +- 3 Tangential Velocity Specification	Method	Fixed
| | | | | +- 4 Thermal Specification	Condition	Adiabatic
| | | | | +-5 User Wall Heat Flux Coefficient Specification	Method	None
| | | | | `-6 Wall Surface Specification	Method	Smooth
| | | | `-2 Physics Values		
| | | | `- 1 Blended Wall Function	E	9.0
| | | |	Kappa	0.42
| | | +-3 **Outlet Tank Interface [Interface 2]**	Index	469
| | | |	Interfaces	
| | | |	Part Surfaces	[]
| | | |	Type	Internal Interface Boundary
| | | |	Allow Per-Contact Values	false
| | | |	Parent Interface	Interface 2
| | | |	Tags	[]
| | | +-4 **Outlet Tank out**	Index	243
| | | | |	Interfaces	
| | | | |	Part Surfaces	[Outlet Tank.Outletank outlet]
| | | | |	Type	Pressure Outlet
| | | | |	Allow Per-Surface Values	false
| | | | |	Tags	[]
| | | | +-1 Physics Conditions		
| | | | | +- 1 Backflow Specification	Direction	Boundary-Normal
| | | | | |	Pressure	Environmental
| | | | | +- 2 Pressure Outlet Option	Option	None

| | | | | +- 3 Reference Frame Specification	Option	Lab Frame
| | | | | `- 4 Turbulence Specification	Method	Intensity + Viscosity Ratio
| | | | `-2 Physics Values		
| | | | +- 1 Pressure	Method	Constant
| | | | | `- 1 Constant	Value	0.0 Pa
| | | | +- 2 Static Temperature	Method	Constant
| | | | | `- 1 Constant	Value	300.0 K
| | | | +- 3 Turbulence Intensity	Method	Constant
| | | | | `- 1 Constant	Value	0.01
| | | | `- 4 Turbulent Viscosity Ratio	Method	Constant
| | | | `- 1 Constant	Value	10.0
| | | +-5 **Outletank Divider**	Index	241
| | | | |	Interfaces	Inlet tank/Outlet Tank
| | | | |	Part Surfaces	[Outlet Tank.Outletank Divider]
| | | | |	Type	Wall
| | | | |	Allow Per-Surface Values	false
| | | | |	Tags	[]
| | | | +-1 Physics Conditions		
| | | | | +- 1 Reference Frame Specification	Option	Region Reference Frame
| | | | | +- 2 Shear Stress Specification	Method	No-Slip
| | | | | +- 3 Tangential Velocity Specification	Method	Fixed
| | | | | +- 4 Thermal Specification	Condition	Adiabatic
| | | | | +-5 User Wall Heat Flux Coefficient Specification	Method	None
| | | | | `-6 Wall Surface Specification	Method	Smooth
| | | | `-2 Physics Values		
| | | | `- 1 Blended Wall Function	E	9.0
| | | |	Kappa	0.42
| | | `-6 **Outletank Divider [Inlet tank/Outlet Tank]**	Index	268
| | | |	Interfaces	
| | | |	Part Surfaces	[]
| | | |	Type	Baffle Boundary
| | | |	Allow Per-Contact Values	false
| | | |	Parent Interface	Inlet tank/Outlet Tank
| | | |	Tags	[]
| | | +-1 Physics Conditions		
| | | | +- 1 Reference Frame Specification	Option	Region Reference Frame

				+- 2 Shear Stress Specification	Method	No-Slip
				+- 3 Tangential Velocity Specification	Method	Fixed
				`-4 Wall Surface Specification	Method	Smooth
			`-2 Physics Values		
			`- 1 Blended Wall Function	E	9.0
				Kappa	0.42
		+-2 Feature Curves	Part Curve Selection Priority	[Outlet Tank:Default Feature Curve]
				Feature Curves	1
			`-1 **Default Feature Curve**	Part Curves	[Outlet Tank.Default]
				Tags	[]
		+-3 Physics Conditions		
			+-1 Energy Source Option	Energy Source Option	None
			+-2 Initial Condition Option	Option	Use Continuum Values
			+-3 Mass Source Option	Mass Source Option	Disabled
			+- 4 Momentum Source Option	Momentum Source Option	None
			`- 5 Turbulence Source Option	Turbulence Source Option	None
		`-4 Physics Values		
		+-1 Axis	Coordinate System	Laboratory
				Origin	[0.0, 0.0, 0.0] m
				Direction	[0.0, 0.0, 1.0]
		`-2 Motion Specification	Motion	Stationary
				Reference Frame	Lab Reference Frame
	`-6 **Top tank**	Index	4
		Mesh Continuum	Parts Meshes
		Physics Continuum	Coolant
		Parts	[Top tank]
		Type	Fluid Region
		Allow Per-Part Values	false
		Tags	[]
	+-1 Boundaries	Part Surface Selection Priority	[Top tank: Top Tank, Top tank: Top Tank Interface, Top tank: Top Tank Interface [Interface 1]]
			Boundaries	3
		+-1 **Top Tank**	Index	251
				Interfaces	
				Part Surfaces	[Top tank.Top Tank]
				Type	Wall
				Allow Per-Surface Values	false
				Tags	[]
			+-1 Physics Conditions		
				+- 1 Reference Frame Specification	Option	Region Reference Frame
				+- 2 Shear Stress Specification	Method	No-Slip
				+- 3 Tangential Velocity Specification	Method	Fixed

| | | | +- 4 Thermal Specification	Condition	Adiabatic
| | | | +-5 User Wall Heat Flux Coefficient Specification	Method	None
| | | | `-6 Wall Surface Specification	Method	Smooth
| | | `-2 Physics Values		
| | | `- 1 Blended Wall Function	E	9.0
| | |	Kappa	0.42
| | +-2 **Top Tank Interface**	Index	282
| | | |	Interfaces	Interface 1
| | | |	Part Surfaces	[Top tank.Top Tank interface]
| | | |	Type	Wall
| | | |	Allow Per-Surface Values	false
| | | |	Tags	[]
| | | +-1 Physics Conditions		
| | | | +- 1 Reference Frame Specification	Option	Region Reference Frame
| | | | +- 2 Shear Stress Specification	Method	No-Slip
| | | | +- 3 Tangential Velocity Specification	Method	Fixed
| | | | +- 4 Thermal Specification	Condition	Adiabatic
| | | | +-5 User Wall Heat Flux Coefficient Specification	Method	None
| | | | `-6 Wall Surface Specification	Method	Smooth
| | | `-2 Physics Values		
| | | `- 1 Blended Wall Function	E	9.0
| | |	Kappa	0.42
| | `-3 **Top Tank Interface [Interface 1]**	Index	467
| | | |	Interfaces	
| | | |	Part Surfaces	[]
| | | |	Type	Internal Interface Boundary
| | | |	Allow Per-Contact Values	false
| | | |	Parent Interface	Interface 1
| | | |	Tags	[]
| | +-2 Feature Curves	Part Curve Selection Priority	[Top tank:Default Feature Curve]
| | | |	Feature Curves	1
| | `-1 **Default Feature Curve**	Part Curves	[Top tank.Default]
| | | |	Tags	[]
| | +-3 Physics Conditions		
| | | +-1 Energy Source Option	Energy Source Option	None
| | | +-2 Initial Condition Option	Option	Use Continuum Values
| | | +-3 Mass Source Option	Mass Source Option	Disabled
| | | +- 4 Momentum Source Option	Momentum Source Option	None

		`-5 Turbulence Source Option	Turbulence Source Option	None
	`-4 Physics Values		
	+-1 Axis	Coordinate System	Laboratory
		Origin	[0.0, 0.0, 0.0] m
		Direction	[0.0, 0.0, 1.0]
	`-2 Motion Specification	Motion	Stationary
		Reference Frame	Lab Reference Frame
+-4 Representations			
	+-1 **Geometry**	Tags	[]
		+-1 **Automated Mesh.Remesh**	Tags	[]
		`-2 **Latest**	Tags	[]
	`-2 **Volume Mesh**	Cells	4005037
		Interior Faces	24311721
		Vertices	19120505
		Tags	[]
	+-1 Finite Volume Regions		
		+-1 Air Core	Cells	95000
				Interior Faces	644130
				Vertices	561796
				Edges	0
			`-1 Finite Volume Boundaries		
			+-1 Outlet Interface	Faces	270
			+-2 Radiator Bot Inet inteface	Faces	204
			+-3 Radiator Inlet	Faces	0
			+-4 Radiator Inlet [Interface 4]	Faces	4666
			+-5 Radiator Outlet	Faces	0
			+-6 Radiator Outlet [Interface 5]	Faces	4666
			+-7 Radiator Sides	Faces	2388
			`-8 Radiator Top inteface	Faces	468
		`-2 Coolant core	Cells	95000
				Interior Faces	644130
				Vertices	561796
				Edges	0
			`-1 Finite Volume Boundaries		
			+-1 Outlet Interface	Faces	0
			+-2 Outlet Interface [Interface 2]	Faces	270
			+-3 Radiator Bot Inet inteface	Faces	0
			+-4 Radiator Bot Inet inteface [Interface 3]	Faces	204
			+-5 Radiator Inlet	Faces	4666
			+-6 Radiator Outlet	Faces	4666

| | | +- 7 Radiator Sides	Faces	2388
| | | +- 8 Radiator Top inteface	Faces	0
| | | `- 9 Radiator Top inteface [Interface 1]	Faces	468
| | +-3 Domain	Cells	3788651
| | | |	Interior Faces	22849287
| | | |	Vertices	17843084
| | | |	Edges	0
| | | `-1 Finite Volume Boundaries		
| | | +-1 Bot Tank	Faces	3357
| | | +- 2 Domain Inlet	Faces	124
| | | +- 3 Domain Outlet	Faces	123
| | | +- 4 Domain Sides	Faces	810
| | | +- 5 Engine	Faces	19672
| | | +- 6 Exhaust	Faces	10281
| | | +- 7 Pylon	Faces	62777
| | | +- 8 Radiator Inlet	Faces	0
| | | +- 9 Radiator Inlet [Interface 4]	Faces	4666
| | | +- 10 Radiator Outlet	Faces	0
| | | +- 11 Radiator Outlet [Interface 5]	Faces	4666
| | | +- 12 Radiator Sides	Faces	2388
| | | `-13 Top Tank	Faces	1428
| | +-4 Inlet tank	Cells	6463
| | | |	Interior Faces	42786
| | | |	Vertices	37803
| | | |	Edges	0
| | | `-1 Finite Volume Boundaries		
| | | +-1 Inlet Tank	Faces	1071
| | | +-2 Inlet Tank Divider	Faces	0
| | | +-3 Inlet Tank Divider [Inlet tank/Outlet Tank]	Faces	182
| | | +-4 Inlet Tank Interface	Faces	0
| | | +-5 Inlet Tank Interface [Interface 3]	Faces	204
| | | `-6 Inlet Tank in	Faces	47
| | +-5 Outlet Tank	Cells	12618
| | | |	Interior Faces	83470
| | | |	Vertices	73510
| | | |	Edges	0
| | | `-1 Finite Volume Boundaries		
| | | +- 1 Outlet Tank	Faces	2179

| | | +- 2 Outlet Tank Interface	Faces	0
| | | +- 3 Outlet Tank Interface [Interface 2]	Faces	270
| | | +- 4 Outlet Tank out	Faces	60
| | | +- 5 Outletank Divider	Faces	0
| | | `- 6 Outletank Divider [Inlet tank/Outlet Tank]	Faces	182
| | `-6 Top tank	Cells	7305
| | |	Interior Faces	47918
| | |	Vertices	42516
| | |	Edges	0
| | `-1 Finite Volume Boundaries		
| | +-1 Top Tank	Faces	1428
| | +-2 Top Tank Interface	Faces	0
| | `-3 Top Tank Interface [Interface 1]	Faces	468
| `-2 Cell Sets		
+-5 Contacts		
| +-1 Domain/Inlet tank	Part 1	[Domain]
| | |	Part 2	[Inlet tank]
| | +-1 Bot Tank/Inlet Tank	Part Surface 1	Domain.Bot Tank
| | |	Part Surface 2	Inlet tank.Inlet Tank
| | |	Conformality	STRONG_CONTACT
| | |	Metadata	(Lidar, 2018)
| | |	Index	83
| | |	Interface	[]
| | |	Tags	[]
| | `-2 Bot Tank/Inlet Tank in	Part Surface 1	Domain.Bot Tank
| |	Part Surface 2	Inlet tank.Inlet Tank in
| |	Conformality	STRONG_CONTACT
| |	Metadata	(Lidar, 2018)
| |	Index	84
| |	Interface	[]
| |	Tags	[]
| +-2 Domain/Outlet Tank	Part 1	[Domain]
| | |	Part 2	[Outlet Tank]
| | +-1 Bot Tank/Outlet Tank	Part Surface 1	Domain.Bot Tank
| | |	Part Surface 2	Outlet Tank.Outlet Tank
| | |	Conformality	STRONG_CONTACT
| | |	Metadata	(Lidar, 2018)
| | |	Index	85
| | |	Interface	[]
| | |	Tags	[]
| | `-2 Bot Tank/Outletank outlet	Part Surface 1	Domain.Bot Tank
| |	Part Surface 2	Outlet Tank.Outletank outlet
| |	Conformality	STRONG_CONTACT
| |	Metadata	(Lidar, 2018)
| |	Index	107
| |	Interface	[]
| |	Tags	[]
| +- 3 Domain/Radiator	Part 1	[Domain]
| | |	Part 2	[Radiator]
| | +-1 Radiator Inlet 2/Radiator Inlet	Part Surface 1	Domain.Radiator Inlet 2

		Part Surface 2	Radiator.Radiator Inlet
		Conformality	STRONG_CONTACT
		Metadata	(Lidar, 2018)
		Index	101
		Interface	[]
		Tags	[]
| | +-2	Radiator Outlet 2/RadiatorOutlet	Part Surface 1	Domain.Radiator Outlet 2
		Part Surface 2	Radiator.RadiatorOutlet
		Conformality	STRONG_CONTACT
		Metadata	(Lidar, 2018)
		Index	102
		Interface	[]
		Tags	[]
| | `-3	Radiator Sides 2/Radiator Sides	Part Surface 1	Domain.Radiator Sides 2
		Part Surface 2	Radiator.Radiator Sides
		Conformality	STRONG_CONTACT
		Metadata	(Lidar, 2018)
		Index	103
		Interface	[]
		Tags	[]
| +-4	Domain/Top tank	Part 1	[Domain]
		Part 2	[Top tank]
| | `-1	Top Tank/Top Tank	Part Surface 1	Domain.Top Tank
		Part Surface 2	Top tank.Top Tank
		Conformality	STRONG_CONTACT
		Metadata	(Lidar, 2018)
		Index	88
		Interface	[]
		Tags	[]
| +-5	Outlet Tank/Inlet tank	Part 1	[Outlet Tank]
		Part 2	[Inlet tank]
| | `-1	Outletank Divider/Inlet Tank Divider	Part Surface 1	Outlet Tank.Outletank Divider
		Part Surface 2	Inlet tank.Inlet Tank Divider
		Conformality	STRONG_CONTACT
		Metadata	(Lidar, 2018)
		Index	82
		Interface	[]
		Tags	[]
| +-6	Outlet Tank/Radiator	Part 1	[Outlet Tank]
		Part 2	[Radiator]
| | `-1	Outlet Tank Interface/Outlet Interface	Part Surface 1	Outlet Tank.Outlet Tank Interface
		Part Surface 2	Radiator.Outlet Interface
		Conformality	STRONG_CONTACT
		Metadata	(Lidar, 2018)
		Index	87
		Interface	[]
		Tags	[]
| +-7	Radiator/Inlet tank	Part 1	[Radiator]
		Part 2	[Inlet tank]
| | `-1	Radiator Bot Inet inteface/Inlet Tank Interface	Part Surface 1	Radiator.Radiator Bot Inet inteface
		Part Surface 2	Inlet tank.Inlet Tank Interface
		Conformality	STRONG_CONTACT
		Metadata	(Lidar, 2018)
		Index	93
		Interface	[]
		Tags	[]

`-8 Radiator/Top tank	Part 1	[Radiator]
	Part 2	[Top tank]
`-1 Radiator Top inteface/Top Tank interface	Part Surface 1	Radiator.Radiator Top inteface
	Part Surface 2	Top tank.Top Tank interface
	Conformality	STRONG_CONTACT
	Metadata	(Lidar, 2018)
	Index	104
	Interface	[]
	Tags	[]
+-6 Parts		
+-1 **Domain**	Metadata	(Lidar, 2018)
	Index	20
	Region	[Domain]
	Contacts	[Outlet Tank, Radiator, Inlet tank, Top tank]
	Descriptions	[Root, Automated Mesh.Remesh]
	Face Count	38090
	Tags	[]
+-1 Surfaces		
+-1 **Bot Tank**	Metadata	(Lidar, 2018)
	Index	93
	Boundary	[Domain: Bot Tank]
	Tags	[]
+-2 **Domain Inlet**	Metadata	(Lidar, 2018)
	Index	77
	Boundary	[Domain: Domain Inlet]
	Tags	[]
+-3 **Domain Outlet**	Metadata	{}
	Index	78
	Boundary	[Domain: Domain Outlet]
	Tags	[]
+-4 **Domain Sides**	Metadata	{}
	Index	79
	Boundary	[Domain: Domain Sides]
	Tags	[]
+-5 **Engine**	Metadata	{}
	Index	72
	Boundary	[Domain: Engine]
	Tags	[]
+-6 **Exhaust**	Metadata	{}
	Index	80
	Boundary	[Domain: Exhaust]
	Tags	[]
+-7 **Pylon**	Metadata	{}
	Index	83
	Boundary	[Domain: Pylon]
	Tags	[]
+-8 **Radiator Inlet 2**	Metadata	{}
	Index	107
	Boundary	[Domain: Radiator Inlet]
	Tags	[]
+-9 **Radiator Outlet 2**	Metadata	{}
	Index	108
	Boundary	[Domain: Radiator Outlet]
	Tags	[]
+-10 **Radiator Sides 2**	Metadata	{}
	Index	109
	Boundary	[Domain: Radiator Sides]
	Tags	[]
`-11 **Top Tank**	Metadata	{}

				Index	92
				Boundary	[Domain: Top Tank]
				Tags	[]
		`-2	Curves		
		`-1	**Default**	Feature Curve	[Domain:Default Feature Curve]
				Index	20
				Tags	[]
	+-2		**Inlet tank**	Metadata	{}
				Index	23
				Region	[Inlet tank]
				Contacts	[Domain, Outlet Tank, Radiator]
				Descriptions	[Root, Automated Mesh.Remesh]
				Face Count	196
				Tags	[]
		+-1	Surfaces		
			+-1 **Inlet Tank**	Metadata	{}
				Index	95
				Boundary	[Inlet tank: Inlet Tank]
				Tags	[]
			+-2 **Inlet Tank Divider**	Metadata	{}
				Index	94
				Boundary	[Inlet tank: Inlet Tank Divider]
				Tags	[]
			+-3 **Inlet Tank Interface**	Metadata	{}
				Index	75
				Boundary	[Inlet tank: Inlet Tank Interface]
				Tags	[]
			`-4 **Inlet Tank in**	Metadata	{}
				Index	96
				Boundary	[Inlet tank: Inlet Tank in]
				Tags	[]
		`-2	Curves		
		`-1	**Default**	Feature Curve	[Inlet tank:Default Feature Curve]
				Index	23
				Tags	[]
	+-3		**Outlet Tank**	Metadata	{}
				Index	21
				Region	[Outlet Tank]
				Contacts	[Domain, Radiator, Inlet tank]
				Descriptions	[Root, Automated Mesh.Remesh]
				Face Count	196
				Tags	[]
		+-1	Surfaces		
			+-1 **Outlet Tank**	Metadata	{}
				Index	97
				Boundary	[Outlet Tank: Outlet Tank]
				Tags	[]
			+-2 **Outlet Tank Interface**	Metadata	{}
				Index	99
				Boundary	[Outlet Tank: Outlet Tank Interface]
				Tags	[]
			+-3 **Outletank Divider**	Metadata	{}
				Index	73
				Boundary	[Outlet Tank: Outletank Divider]
				Tags	[]
			`-4 **Outletank outlet**	Metadata	{}
				Index	117
				Boundary	[Outlet Tank: Outlet Tank out]
				Tags	[]
		`-2	Curves		

		`-1 **Default**	Feature Curve	[Outlet Tank:Default Feature Curve]
			Index	21
			Tags	[]
	+-4 **RAdiator inlet flow 2**		Metadata	{}
			Index	25
			Region	[]
			Contacts	[]
			Descriptions	[Root]
			Face Count	12
			Coordinate System	Laboratory
			Corner 1	[-0.018423802706225373, -0.5862185303852938, -0.08710683553396245] m,m,m
			Corner 2	[0.15400202865356863, -0.1634631370945906, 0.011463917466980167] m,m,m
			Tags	[]
		+-1 Surfaces		
		`-1 **Block Surface**	Metadata	{}
			Index	115
			Boundary	[]
			Tags	[]
		`-2 Curves		
		`-1 **Block Curve**	Feature Curve	[]
			Index	25
			Tags	[]
	+-5 **Radiator**		Metadata	{}
			Index	22
			Region	[Air Core]
			Contacts	[Domain, Outlet Tank, Inlet tank, Top tank]
			Descriptions	[Root, Automated Mesh.Remesh]
			Face Count	16
			Tags	[]
		+-1 Surfaces		
		+-1 **Outlet Interface**	Metadata	{}
			Index	74
			Boundary	[Air Core: Outlet Interface]
			Tags	[]
		+-2 **Radiator Bot Inet inteface**	Metadata	{}
			Index	105
			Boundary	[Air Core: Radiator Bot Inet inteface]
			Tags	[]
		+-3 **Radiator Inlet**	Metadata	{}
			Index	102
			Boundary	[Air Core: Radiator Inlet]
			Tags	[]
		+-4 **Radiator Sides**	Metadata	{}
			Index	103
			Boundary	[Air Core: Radiator Sides]
			Tags	[]
		+-5 **Radiator Top inteface**	Metadata	{}
			Index	104
			Boundary	[Air Core: Radiator Top inteface]
			Tags	[]
		`-6 **RadiatorOutlet**	Metadata	{}
			Index	101
			Boundary	[Air Core: Radiator Outlet]
			Tags	[]
		`-2 Curves		

		`-1 **Default**	Feature Curve	[Air Core:Default Feature Curve]
			Index	22
			Tags	[]
	+-6 **Radiator flow**		Metadata	{}
			Index	9
			Region	[]
			Contacts	[]
			Descriptions	[Root]
			Face Count	12
			Coordinate System	Laboratory
			Corner 1	[-0.2418481268729029, -0.6918509936667655, -0.5992989410518377] m,m,m
			Corner 2	[0.2759395270033004, 0.2244041709474055, 0.010687609143779142] m,m,m
			Tags	[]
		+-1 Surfaces		
		`-1 **Block Surface**	Metadata	{}
			Index	44
			Boundary	[]
			Tags	[]
		`-2 Curves		
		`-1 **Block Curve**	Feature Curve	[]
			Index	9
			Tags	[]
	+-7 **Radiator Inlet**		Metadata	{}
			Index	10
			Region	[]
			Contacts	[]
			Descriptions	[Root]
			Face Count	12
			Coordinate System	Laboratory
			Corner 1	[-0.018423802706225373, -0.5862185303852938, -0.10320994078965723] m,m,m
			Corner 2	[0.15400202865356863, -0.16451695572747638, -0.08710683553396242] m,m,m
			Tags	[]
		+-1 Surfaces		
		`-1 **Block Surface**	Metadata	{}
			Index	45
			Boundary	[]
			Tags	[]
		`-2 Curves		
		`-1 **Block Curve**	Feature Curve	[]
			Index	10
			Tags	[]
	+-8 **Radiator Outlet**		Metadata	{}
			Index	11
			Region	[]
			Contacts	[]
			Descriptions	[Root]
			Face Count	12
			Coordinate System	Laboratory
			Corner 1	[-0.018423802706225345, -0.5862185303852938, -0.16163986238844485] m,m,m
			Corner 2	[0.15360431116134454, -0.16451695572747638, -0.13750251250650358] m,m,m
			Tags	[]
		+-1 Surfaces		

				`-1 **Block Surface**	Metadata	{}
					Index	46
					Boundary	[]
					Tags	[]
				`-2 Curves		
				`-1 **Block Curve**	Feature Curve	[]
					Index	11
					Tags	[]
			+-9 **Radiator refinement**		Metadata	{}
					Index	26
					Region	[]
					Contacts	[]
					Descriptions	[Root]
					Face Count	12
					Coordinate System	Laboratory
					Corner 1	[-0.018423802706225345, -0.6014237073687284, -0.14790540511299524] m,m,m
					Corner 2	[0.15360431116134454, -0.14992751588898598, -0.08833546837177689] m,m,m
					Tags	[]
			+-1 Surfaces			
				`-1 **Block Surface**	Metadata	{}
					Index	119
					Boundary	[]
					Tags	[]
				`-2 Curves		
				`-1 **Block Curve**	Feature Curve	[]
					Index	26
					Tags	[]
			+-10 **Top tank**		Metadata	{}
					Index	24
					Region	[Top tank]
					Contacts	[Domain, Radiator]
					Descriptions	[Root, Automated Mesh.Remesh]
					Face Count	12
					Tags	[]
				+-1 Surfaces		
					+-1 **Top Tank**	Metadata	{}
						Index	100
						Boundary	[Top tank: Top Tank]
						Tags	[]
					`-2 **Top Tank interface**	Metadata	{}
						Index	116
						Boundary	[Top tank: Top Tank Interface]
						Tags	[]
				`-2 Curves			
					`-1 **Default**	Feature Curve	[Top tank:Default Feature Curve]
						Index	24
						Tags	[]
			+-11 **Virtual Prop**		Metadata	{}
					Index	8
					Region	[]
					Contacts	[]
					Descriptions	[Root]
					Face Count	308
					Coordinate System	Laboratory
					Start Coordinate	[0.0, 0.0, 0.01] m,m,m
					End Coordinate	[0.0, 0.0, 0.08] m,m,m
					Radius	0.8 m
					Tags	[]

		+-1 Surfaces	
			`-1 **Cylinder Surface**	Metadata	{}
				Index	43
				Boundary	[]
				Tags	[]
		`-2 Curves			
			`-1 **Cylinder Curve**	Feature Curve	[]
				Index	8
				Tags	[]
	`-12 **Virtual Prop inlet refinement**			Metadata	{}
				Index	27
				Region	[]
				Contacts	[]
				Descriptions	[Root]
				Face Count	300
				Coordinate System	Laboratory
				Start Coordinate	[0.0, 0.0, 0.8] m,m,m
				End Coordinate	[0.0, 0.0, 0.08] m,m,m
				Radius	1.6 m
				Tags	[]
		+-1 Surfaces			
			`-1 **Cylinder Surface**	Metadata	{}
				Index	120
				Boundary	[]
				Tags	[]
		`-2 Curves			
			`-1 **Cylinder Curve**	Feature Curve	[]
				Index	27
				Tags	[]
+-7 3D-CAD Models					
	`-1 **3D-CAD Model 1**			Part Update Method	UPDATE_GEOMETRY
				Tags	[]
		+-1 Bodies			
			+-1 **Top tank**	Tags	[]
			+-2 **Inlet Tank**	Tags	[]
			+-3 **Air Core**	Tags	[]
			+-4 **Domain**	Tags	[]
			`-5 **Outlet Tank**	Tags	[]
		+-2 Features			
			+-1 **XY**	Error Message	
				Origin	[0.0, 0.0, 0.0] m
				X-Axis	[1.0, 0.0, 0.0]
				Y-Axis	[0.0, 1.0, 0.0]
				Tags	[]
			+-2 **YZ**	Error Message	
				Origin	[0.0, 0.0, 0.0] m
				X-Axis	[0.0, 1.0, 0.0]
				Y-Axis	[0.0, 0.0, 1.0]
				Tags	[]
			+-3 **ZX**	Error Message	
				Origin	[0.0, 0.0, 0.0] m
				X-Axis	[0.0, 0.0, 1.0]
				Y-Axis	[1.0, 0.0, 0.0]
				Tags	[]
			+-4 **Global Origin**	Error Message	
				Position	[0.0, 0.0, 0.0]
				Tags	[]
			+-5 **Lab Coordinate System**	Error Message	

				Origin	[0.0, 0.0, 0.0]
				X-axis Direction	[1.0, 0.0, 0.0]
				Y-axis Direction	[0.0, 1.0, 0.0]
				Tags	[]
		+-6 **SL system**		Error Message	
				Tags	[]
		+-7 **Domian**		Error Message	
				Tags	[]
		+-8 **Sketch 1**		Error Message	
				Tags	[]
		+-9 **Extrude 1**		Error Message	
				Sketch	Sketch 1
				Method	Blind
				Direction Type	Normal
				Extrusion Options	TwoWayAsymmetric
				Distance	4.0 m
				Asym. Distance	30.0 m
				Draft	None
				Draft Angle	10.0 deg
				Offset Distance	0.1 m
				Body Type	Solid
				Body Interaction	None
				Bodies To Interact	All
				Tags	[]
		+-10 **SubtractBodies 1**		Error Message	
				Keep Tool Bodies	false
				Imprint	false
				Precision Type	Precise
				Tolerance	1.0E-5 m
				Transfer Face Names	true
				Transfer Body Names	false
				Tags	[]
		+-11 **DeleteBody 1**		Error Message	
				Delete Mode	Manual
				Solids	None
				Minimum Volume	0.001 m^3
				Maximum Volume	0.002 m^3
				Sheets	None
				Minimum Area	0.001 m^2
				Maximum Area	0.002 m^2
				Tags	[]
		+-12 **Sketch 2**		Error Message	
				Tags	[]
		+-13 **Extrude 2**		Error Message	
				Sketch	Sketch 2
				Method	Blind
				Direction Type	Normal
				Extrusion Options	TwoWayAsymmetric
				Distance	0.1 m
				Asym. Distance	0.015 m
				Draft	None
				Draft Angle	10.0 deg
				Offset Distance	0.1 m
				Body Type	Solid
				Body Interaction	Merge
				Bodies To Interact	Selected
				Tags	[]
		+-14 **SubtractBodies 2**		Error Message	
				Keep Tool Bodies	true
				Imprint	true
				Precision Type	Precise
				Tolerance	1.0E-5 m
				Transfer Face Names	true

| |	Transfer Body Names	false
| |	Tags	[]
| +- 15 **SubtractBodies 3**	Error Message	
| |	Keep Tool Bodies	true
| |	Imprint	true
| |	Precision Type	Precise
| |	Tolerance	1.0E-5 m
| |	Transfer Face Names	true
| |	Transfer Body Names	false
| |	Tags	[]
| `- 16 **ImportCad 1**	Error Message	
|	Tags	[]
| `-3 Design Parameters		
+-8 Operations		
| `-1 **Automated Mesh**	Per-Part Meshing	false
|	Mesher Execution Mode	Serial
|	Input Parts	[Domain, Inlet tank, Outlet Tank, Radiator, Top tank]
|	Perform Local Surface Meshing	false
|	Preserve Surface Perimeters	None
|	Verbose Output	false
|	Tags	[]
| +-1 Meshers		
| | +-1 Surface Remesher	Perform Curvature Refinement	true
| | |	Perform Proximity Refinement	true
| | |	Perform Compatibility Refinement	false
| | |	Create Aligned Meshes	true
| | |	Minimum Face Quality	0.05
| | +-2 Automatic Surface Repair	Connected Surface Count Limit	None
| | |	Connected Surface Size Limit(s)	None
| | |	Minimum Face Quality	0.05
| | +-3 Polyhedral Mesher	Run Optimizer	true
| | |	Optimize Boundary Vertices	false
| | |	Enable Growth Rate	false
| | |	Optimization Cycles	1
| | |	Quality Threshold	0.4
| | `-4 Prism Layer Mesher	Stretching Function	Geometric Progression
| |	Distribution Mode	Stretch Factor
| |	Boundary March Angle	50.0
| |	Gap Fill Percentage	25.0
| |	Minimum Thickness Percentage	10.0
| |	Layer Reduction Percentage	50.0
| |	Concave Angle Limit	0.0
| |	Convex Angle Limit	360.0
| |	Near Core Layer Aspect Ratio	0.0
| +-2 Default Controls		
| | +-1 Base Size	Value	1.0 m
| | +-2 CAD Projection	Project to CAD	true
| | +-3 Target Surface Size	Size Type	Relative to base
| | |	Percentage of Base	1000.0
| | |	Absolute Size	10.0 m
| | +-4 Minimum Surface Size	Size Type	Relative to base
| | |	Percentage of Base	0.5
| | |	Absolute Size	0.005 m
| | +-5 Surface Curvature	Enable Curvature Deviation Distance	false

| | # Pts/circle	36.0
| | Max # Pts/circle	200.0
| | Curvature Deviation Distance	0.01 m
| +-6 Surface Proximity	Search Floor	0.0 m
| | # Points in gap	2.0
| | Enable Search Ceiling	false
| | Search Ceiling	1.0E10 m
| +-7 Surface Growth Rate	Surface Growth Rate	1.1
| +-8 Auto-Repair Minimum Proximity	Minimum Proximity	0.01
| +-9 Number of Prism Layers	Number of Prism Layers	17
| +-10 Prism Layer Stretching	Prism Layer Stretching	1.3
| +-11 Prism Layer Total Thickness	Size Type	Absolute
| | Percentage of Base	0.5
| | Absolute Size	0.005 m
| +-12 Mesh Density	Density	1.0
| | Growth Factor	1.0
| `-13 Volumetric Control Blending	Blending Factor	5.0
`-3 Custom Controls	
+-1 **Bot Outlet Tank**	Enable Control	Enabled
| | Controls Display Mode	All
| | Parts	[Outlet Tank]
| | Tags	[]
| +-1 Controls	
| | +-1 Surface Remesher	Customize Size	Enabled
| | +-2 Prism Layer Mesher	Customize Number of Layers	Disabled
| | | Customize Total Thickness	Disabled
| | | Customize Stretching	Disabled
| | `-3 Polyhedral Mesher	Customize Polyhedral Mesher	Enabled
| `-2 Values	
| `-1 Custom Size	Size Type	Relative to base
| Percentage of Base	0.27999999999999997
| Absolute Size	0.0027999999999999995 m
+-2 **Engine and exhaust refinement**	Enable Control	Enabled
| | Controls Display Mode	All
| | Part Surfaces	[Domain.Engine, Domain.Exhaust]
| | Apply Only to Contacting Area	Disabled
| | Tags	[]
| +-1 Controls	
| | +-1 Target Surface Size	Target Surface Size	Custom
| | +-2 Minimum Surface Size	Minimum Surface Size	Custom
| | +-3 Surface Curvature	Curvature	Parent
| | +-4 Surface Proximity	Proximity	Parent
| | +-5 Edge Proximity	Proximity	Parent
| | +-6 Surface Growth Rate	Surface Growth Rate	Parent

| | | +- 7 Surface Remeshing	Surface Remeshing	Parent
| | | +- 8 Prism Layers	Prism Layers	Parent
| | | `- 9 Wake Refinement	Specify wake refinement options	Disabled
| | `-2 Values		
| | +- 1 Target Surface Size	Size Type	Relative to base
| | |	Percentage of Base	1.0
| | |	Absolute Size	0.01 m
| | `- 2 Minimum Surface Size	Size Type	Relative to base
| |	Percentage of Base	0.5
| |	Absolute Size	0.005 m
| +-3 **Prism Layer Control**	Enable Control	Enabled
| | |	Controls Display Mode	All
| | |	Part Surfaces	[Domain.Domain Inlet, Domain.Domain Outlet, Domain.Domain Sides, Domain.Engine, Domain.Radiator Inlet 2, Domain.Radiator Outlet 2, Inlet tank, Outlet Tank, Radiator, Top tank]
| | |	Apply Only to Contacting Area	Disabled
| | |	Tags	[]
| | +- 1 Controls		
| | | +- 1 Target Surface Size	Target Surface Size	Parent
| | | +- 2 Minimum Surface Size	Minimum Surface Size	Parent
| | | +- 3 Surface Curvature	Curvature	Parent
| | | +- 4 Surface Proximity	Proximity	Parent
| | | +-5 Edge Proximity	Proximity	Parent
| | | +- 6 Surface Growth Rate	Surface Growth Rate	Parent
| | | +- 7 Surface Remeshing	Surface Remeshing	Parent
| | | +- 8 Prism Layers	Prism Layers	Disable
| | | `- 9 Wake Refinement	Specify wake refinement options	Disabled
| | `-2 Values		
| +-4 **Propeller inlet refinement**	Enable Control	Enabled
| | |	Controls Display Mode	All
| | |	Parts	[Virtual Prop inlet refinement]
| | |	Tags	[]
| | +- 1 Controls		
| | | +- 1 Surface Remesher	Customize Size	Enabled
| | | +- 2 Prism Layer Mesher	Customize Number of Layers	Disabled
| | | |	Customize Total Thickness	Disabled
| | | |	Customize Stretching	Disabled
| | | `- 3 Polyhedral Mesher	Customize Polyhedral Mesher	Enabled
| | `-2 Values		
| | `- 1 Custom Size	Size Type	Relative to base
| |	Percentage of Base	3.0
| |	Absolute Size	0.03 m
| +-5 **Pylon refinement**	Enable Control	Enabled
| | |	Controls Display Mode	All

| |	Part Surfaces	[Domain.Pylon]
| |	Apply Only to Contacting Area	Disabled
| |	Tags	[]
| | +- 1 Controls		
| | | +- 1 Target Surface Size	Target Surface Size	Custom
| | | +- 2 Minimum Surface Size	Minimum Surface Size	Parent
| | | +- 3 Surface Curvature	Curvature	Custom
| | | +- 4 Surface Proximity	Proximity	Parent
| | | +-5 Edge Proximity	Proximity	Parent
| | | +- 6 Surface Growth Rate	Surface Growth Rate	Parent
| | | +- 7 Surface Remeshing	Surface Remeshing	Parent
| | | +- 8 Prism Layers	Prism Layers	Parent
| | | `- 9 Wake Refinement	Specify wake refinement options	Disabled
| | `-2 Values		
| | +- 1 Target Surface Size	Size Type	Relative to base
| | |	Percentage of Base	0.32
| | |	Absolute Size	0.0032 m
| | `- 2 Surface Curvature	Enable Curvature Deviation Distance	false
| |	# Pts/circle	88.0
| |	Max # Pts/circle	200.0
| |	Curvature Deviation Distance	0.01 m
| +-6 **Radiator core refinement**	Enable Control	Enabled
| | |	Controls Display Mode	All
| | |	Part Surfaces	[Domain.Radiator Inlet 2, Domain.Radiator Outlet 2, Domain.Radiator Sides 2]
| | |	Apply Only to Contacting Area	Disabled
| | |	Tags	[]
| | +- 1 Controls		
| | | +- 1 Target Surface Size	Target Surface Size	Custom
| | | +- 2 Minimum Surface Size	Minimum Surface Size	Custom
| | | +- 3 Surface Curvature	Curvature	Parent
| | | +- 4 Surface Proximity	Proximity	Parent
| | | +-5 Edge Proximity	Proximity	Parent
| | | +- 6 Surface Growth Rate	Surface Growth Rate	Parent
| | | +- 7 Surface Remeshing	Surface Remeshing	Parent
| | | +- 8 Prism Layers	Prism Layers	Parent
| | | `- 9 Wake Refinement	Specify wake refinement options	Disabled
| | `-2 Values		
| | +- 1 Target Surface Size	Size Type	Relative to base
| | |	Percentage of Base	0.32
| | |	Absolute Size	0.0032 m
| | `- 2 Minimum Surface Size	Size Type	Relative to base
| |	Percentage of Base	0.32
| |	Absolute Size	0.0032 m

+-7 **Radiator Flow**	Enable Control	Enabled
| |	Controls Display Mode	All
| |	Parts	[Radiator flow]
| |	Tags	[]
| +- 1 Controls		
| | +- 1 Surface Remesher	Customize Size	Enabled
| | +- 2 Prism Layer Mesher	Customize Number of Layers	Disabled
| | |	Customize Total Thickness	Disabled
| | |	Customize Stretching	Disabled
| | `- 3 Polyhedral Mesher	Customize Polyhedral Mesher	Enabled
| `-2 Values		
| `- 1 Custom Size	Size Type	Relative to base
|	Percentage of Base	1.78
|	Absolute Size	0.0178 m
+-8 **Radiator refinement**	Enable Control	Enabled
| |	Controls Display Mode	All
| |	Parts	[Inlet tank, Outlet Tank, Radiator, Top tank]
| |	Tags	[]
| +- 1 Controls		
| | +- 1 Surface Remesher	Customize Size	Enabled
| | +- 2 Prism Layer Mesher	Customize Number of Layers	Disabled
| | |	Customize Total Thickness	Disabled
| | |	Customize Stretching	Disabled
| | `- 3 Polyhedral Mesher	Customize Polyhedral Mesher	Enabled
| `-2 Values		
| `- 1 Custom Size	Size Type	Absolute
|	Percentage of Base	0.32
|	Absolute Size	0.0032 m
+-9 **Virtual Disk**	Enable Control	Enabled
| |	Controls Display Mode	All
| |	Parts	[Virtual Prop]
| |	Tags	[]
| +- 1 Controls		
| | +- 1 Surface Remesher	Customize Size	Disabled
| | +- 2 Prism Layer Mesher	Customize Number of Layers	Disabled
| | |	Customize Total Thickness	Disabled
| | |	Customize Stretching	Disabled
| | `- 3 Polyhedral Mesher	Customize Polyhedral Mesher	Enabled
| `-2 Values		
| `- 1 Custom Size	Size Type	Relative to base
|	Percentage of Base	1.7999999999999998
|	Absolute Size	0.018 m
+- 10 **Volumetric Control Radiator Inlet**	Enable Control	Enabled
| |	Controls Display Mode	All
| |	Parts	[Radiator Inlet]
| |	Tags	[]
| +- 1 Controls		

| | | +- 1 Surface Remesher	Customize Size	Enabled
| | | +- 2 Prism Layer Mesher	Customize Number of Layers	Disabled
| | |	Customize Total Thickness	Disabled
| | |	Customize Stretching	Disabled
| | | `- 3 Polyhedral Mesher	Customize Polyhedral Mesher	Enabled
| | `-2 Values		
| | `- 1 Custom Size	Size Type	Relative to base
| |	Percentage of Base	0.32
| |	Absolute Size	0.0032 m
| +- 11 **Volumetric Control Radiator Inlet 2**	Enable Control	Enabled
| | |	Controls Display Mode	All
| | |	Parts	[RAdiator inlet flow 2]
| | |	Tags	[]
| | +- 1 Controls		
| | | +- 1 Surface Remesher	Customize Size	Enabled
| | | +- 2 Prism Layer Mesher	Customize Number of Layers	Disabled
| | | |	Customize Total Thickness	Disabled
| | | |	Customize Stretching	Disabled
| | | `- 3 Polyhedral Mesher	Customize Polyhedral Mesher	Enabled
| | `-2 Values		
| | `- 1 Custom Size	Size Type	Relative to base
| |	Percentage of Base	0.5
| |	Absolute Size	0.005 m
| `- 12 **Volumetric Control RadiatorOutlet**	Enable Control	Enabled
| | |	Controls Display Mode	All
| | |	Parts	[Radiator Outlet]
| | |	Tags	[]
| +- 1 Controls		
| | | +- 1 Surface Remesher	Customize Size	Enabled
| | | +- 2 Prism Layer Mesher	Customize Number of Layers	Disabled
| | | |	Customize Total Thickness	Disabled
| | | |	Customize Stretching	Disabled
| | | `- 3 Polyhedral Mesher	Customize Polyhedral Mesher	Enabled
| | `-2 Values		
| | `- 1 Custom Size	Size Type	Relative to base
| |	Percentage of Base	0.32
| |	Absolute Size	0.0032 m
+-9 Descriptions	Number of Children	3
| +-1 Root	Described Parts	[Virtual Prop, Radiator flow, Radiator Inlet, Radiator Outlet, Domain, Outlet Tank, Radiator, Inlet tank, Top tank, RAdiator inlet flow 2, Radiator refinement, Virtual Prop inlet refinement]
| +-2 Automated Mesh.Remesh	Described Parts	[Domain, Outlet Tank, Radiator, Inlet tank, Top tank]
| |	Faces	233264
| |	Vertices	116636
| `-3 Latest	Described Parts	[Virtual Prop, Radiator flow, Radiator Inlet, Radiator Outlet, Domain, Outlet Tank, Radiator, Inlet tank, Top tank, RAdiator inlet

		flow 2, Radiator refinement, Virtual Prop inlet refinement]
|	Faces	233932
|	Vertices	116984
|	Preview Mesh Operation Parts	false
+-10 Coordinate Systems		
| `-1 **Laboratory**	Tags	[]
| `-1 Local Coordinate Systems		
| `-1 **Virtual Disk-CSys 1**	X Axis Direction	[1.0, 0.0, 0.0]
| |	Y Axis Direction	[0.0, 1.0, 0.0]
| |	Z Axis Direction	[0.0, 0.0, 1.0]
| |	Origin	[0.0, 0.0, 0.05] m,m,m
| |	Reference System	Laboratory
| |	Tags	[]
| `-1 Local Coordinate Systems		
+-11 Tables	Tables	12
| +-1 **AUG FINAL**	Extracted	[Massflow, UAG]
| |	Path	AUG FINAL.csv
| |	Tags	[]
| +-2 **AUG FINAL 10 velocity**	Extracted	[Massflow, UAG]
| |	Path	AUG FINAL 10 velocity.csv
| |	Tags	[]
| +-3 **AUG table**	Extracted	[Massflow, UAG]
| |	Path	AUG table.csv
| |	Tags	[]
| +-4 **AUG table adjusted**	Extracted	[Massflow, UAG]
| |	Path	AUG table adjusted.csv
| |	Tags	[]
| +-5 **AUG table adjusted 10 velocity**	Extracted	[Massflow, UAG]
| |	Path	AUG table adjusted 10 velocity.csv
| |	Tags	[]
| +-6 **AUG table adjusted 20%**	Extracted	[Massflow, UAG]
| |	Path	AUG table adjusted 20%.csv
| |	Tags	[]
| +-7 **AUG table adjusted 30%**	Extracted	[Massflow, UAG]
| |	Path	AUG table adjusted 30%.csv
| |	Tags	[]
| +-8 **AUG table final**	Extracted	[Massflow, UAG]
| |	Path	AUG table final.csv
| |	Tags	[]
| +-9 **AUG table lastest**	Extracted	[Massflow, UAG]
| |	Path	AUG table lastest.csv
| |	Tags	[]
| +-10 **AUG table lastest v -10%**	Extracted	[Massflow, UAG]
| |	Path	AUG table lastest v -10%.csv
| |	Tags	[]
| +-11 **calrk y v4**	Extracted	[AOA_deg, AOA_rad, Cl, Cd, Reynolds]
| |	Path	calrk y v4.csv
| |	Tags	[]
| `-12 **prop geometry v4**	Extracted	[r, r/R, c, alpha, alpha_final, Rad, rad_final]
|	Path	prop geometry v4.csv
|	Tags	[]
+-12 Tags		
+-13 Units	Preferred System	Systeme Internationale
+-14 Filters		
+-15 Custom Trees		

+-16 Field Functions		
| +-1 **ReTheta**	Function Name	ReTheta
| |	Inverse Distance Weight	false
| |	Type	Scalar
| |	Assembly Code	(if (> ${WallDistance} 0.005) 1 0)
| |	Definition	$WallDistance > 0.005?1:0
| |	Ignore Boundary Values	false
| |	Tags	[]
+-17 Parameters		
+-18 Volume Shapes		
+-19 Data Set Functions	Data Directory	function_data
+-20 Update Events	Event Count	0
|	Event Names	
+-21 User Code		
+-22 Data Focus		
+-23 Layouts		
| `-1 default		
+-24 Data Mappers		
+-25 Motions		
| `-1 **Stationary**	Tags	[]
+-26 Reference Frames		
| `-1 **Lab Reference Frame**	Tags	[]
+-27 Derived Parts	Derived Parts	21
| +-1 **Domain side**	Origin	[1.9369753792908284E-5, -6.526406188811507E-5, -14.99936444486957] m,m,m
| | |	Coordinate System	Laboratory
| | |	Normal	[1.0, 0.0, 0.0] m,m,m
| | |	Parts	[Air Core, Domain]
| | |	Section Mode	SINGLE
| | |	Displayed Index	-1
| | |	Tags	[]
| | `-1 Single section	Offset	0.107 m
| +-2 **Domain top**	Origin	[-5.259513854980469E-4, 8.58306884765625E-6, -13.0] m,m,m
| | |	Coordinate System	Laboratory
| | |	Normal	[0.0, 1.0, 0.0] m,m,m
| | |	Parts	[Domain, Inlet tank, Outlet Tank, Air Core, Top tank]
| | |	Section Mode	SINGLE
| | |	Displayed Index	-1
| | |	Tags	[]
| | `-1 Single section	Offset	-0.331 m
| +-3 **Radiator Front**	Origin	[1.9369753792908284E-5, -6.526406188811507E-5, -0.12252186564887292] m,m,m
| | |	Coordinate System	Laboratory
| | |	Normal	[0.0, 0.0, 1.0] m,m,m
| | |	Parts	[Coolant core, Inlet tank, Outlet Tank, Top tank]
| | |	Section Mode	SINGLE
| | |	Displayed Index	-1
| | |	Tags	[]
| | `-1 Single section	Offset	0.0 m
| +-4 **Streamline**	Parts	[Domain, Inlet tank, Outlet Tank, Air Core, Top tank, Coolant core]
| | |	Seed Type	LINE
| | |	Rotation Scale	1.0
| | |	Vector Field	Velocity
| | |	Integration Solver	RK2
| | |	Tags	[]

| | +-1 Line Seed	Point 1	[0.09894628730019728, -0.5588850698498431, -0.08134257452107235] m,m,m
| | |	Point 2	[0.10184453080535494, -0.16939103958892948, -0.08106906554597969] m,m,m
| | |	Coordinate System	Laboratory
| | |	Resolution	100
| | `-2 2nd Order Integrator	Initial Integration Step	0.5
| |	Maximum Propagation	68.00000000000001
| |	Max Steps	2000
| |	Integration Direction	FORWARD
| +-5 **Streamline 2**	Parts	[Domain, Inlet tank, Outlet Tank, Air Core, Top tank, Coolant core]
| | |	Seed Type	LINE
| | |	Rotation Scale	1.0
| | |	Vector Field	Velocity
| | |	Integration Solver	RK2
| | |	Tags	[]
| | +-1 Line Seed	Point 1	[0.0, -0.3, 0.05] m,m,m
| | |	Point 2	[0.15, -0.3, 0.05] m,m,m
| | |	Coordinate System	Laboratory
| | |	Resolution	100
| | `-2 2nd Order Integrator	Initial Integration Step	0.5
| |	Maximum Propagation	68.00000000000001
| |	Max Steps	2000
| |	Integration Direction	FORWARD
| +-6 **T2**	Parts	[Domain]
| |	Point	[0.0447, -0.344, -0.103] m,m,m
| |	Coordinate System	Laboratory
| |	Follow Motion	false
| |	Tags	[]
| +-7 **T3**	Parts	[Domain]
| |	Point	[0.0867, -0.344, -0.138] m,m,m
| |	Coordinate System	Laboratory
| |	Follow Motion	false
| |	Tags	[]
| +-8 **T4**	Parts	[Domain]
| |	Point	[0.0447, -0.419, -0.138] m,m,m
| |	Coordinate System	Laboratory
| |	Follow Motion	false
| |	Tags	[]
| +-9 **T5**	Parts	[Domain]
| |	Point	[0.0867, -0.494, -0.138] m,m,m
| |	Coordinate System	Laboratory
| |	Follow Motion	false
| |	Tags	[]
| +-10 **T6**	Parts	[Domain]
| |	Point	[0.0867, -0.344, -0.101] m,m,m
| |	Coordinate System	Laboratory
| |	Follow Motion	false
| |	Tags	[]
| +-11 **T7**	Parts	[Domain]
| |	Point	[0.0447, -0.494, -0.138] m,m,m
| |	Coordinate System	Laboratory
| |	Follow Motion	false
| |	Tags	[]
| +-12 **T8**	Parts	[Domain]
| |	Point	[0.0867, -0.419, -0.138] m,m,m
| |	Coordinate System	Laboratory
| |	Follow Motion	false
| |	Tags	[]
| +-13 **T9**	Parts	[Domain]
| |	Point	[0.0447, -0.269, -0.101] m,m,m
| |	Coordinate System	Laboratory
| |	Follow Motion	false

		Tags	[]
	+-14 **T10**	Parts	[Domain]
		Point	[0.0867, -0.269, -0.138] m,m,m
		Coordinate System	Laboratory
		Follow Motion	false
		Tags	[]
	+-15 **T11**	Parts	[Domain]
		Point	[0.0447, -0.419, -0.101] m,m,m
		Coordinate System	Laboratory
		Follow Motion	false
		Tags	[]
	+-16 **T12**	Parts	[Domain]
		Point	[0.0447, -0.494, -0.101] m,m,m
		Coordinate System	Laboratory
		Follow Motion	false
		Tags	[]
	+-17 **T13**	Parts	[Domain]
		Point	[0.0867, -0.494, -0.101] m,m,m
		Coordinate System	Laboratory
		Follow Motion	false
		Tags	[]
	+-18 **T14**	Parts	[Domain]
		Point	[0.0867, -0.419, -0.101] m,m,m
		Coordinate System	Laboratory
		Follow Motion	false
		Tags	[]
	+-19 **T15**	Parts	[Domain]
		Point	[0.0867, -0.269, -0.101] m,m,m
		Coordinate System	Laboratory
		Follow Motion	false
		Tags	[]
	+-20 **T17**	Parts	[Domain]
		Point	[0.0447, -0.269, -0.138] m,m,m
		Coordinate System	Laboratory
		Follow Motion	false
		Tags	[]
	`-21 **T20**	Parts	[Domain]
		Point	[0.0447, -0.344, -0.138] m,m,m
		Coordinate System	Laboratory
		Follow Motion	false
		Tags	[]
+-28 Summaries			
+-29 Monitors		Monitors	38
		Monitors To Print	[Continuity, X-momentum, Y-momentum, Z-momentum, Energy, Tke, Sdr, Tdr, Coolant Temp out Monitor, Heat Transfer Monitor, Mass flow air Monitor, Radiator Temp in Monitor, Radiator Temp out Monitor, Virtual Disk Force 1 Monitor, Coolant mass flow Monitor, Mass Flow 1 Monitor, T9 Monitor, T15 Monitor, T2 Monitor, T6 Monitor, T11 Monitor, T14 Monitor, T12 Monitor, T13 Monitor, T10 Monitor, T17 Monitor, T3 Monitor, T20 Monitor, T8 Monitor, T4 Monitor, T5 Monitor, T7 Monitor, Radiator Temp out Monitor 2, Coolant Temp in Monitor]
		Output Direction	Horizontal
		Heading Print Frequency	10
	+-1 **Coolant mass flow Monitor**	Report	[Coolant mass flow]
		Enabled	true
		Value Type	Total Value
		Trigger	Iteration
		Normalization Option	Off
		Maximum Plot Samples	5000
		Tags	[]
	`-1 Iteration Frequency	Iteration Frequency	1

		Start Iteration	0
		Enable Stop	false
		Stop Iteration	0
	+-2 **Coolant Temp in Monitor**	Report	[Coolant Temp in]
		Enabled	true
		Value Type	Total Value
		Trigger	Iteration
		Normalization Option	Off
		Maximum Plot Samples	5000
		Tags	[]
	`-1 Iteration Frequency	Iteration Frequency	1
		Start Iteration	0
		Enable Stop	false
		Stop Iteration	0
	+-3 **Coolant Temp out Monitor**	Report	[Coolant Temp out]
		Enabled	true
		Value Type	Total Value
		Trigger	Iteration
		Normalization Option	Off
		Maximum Plot Samples	5000
		Tags	[]
	`-1 Iteration Frequency	Iteration Frequency	1
		Start Iteration	0
		Enable Stop	false
		Stop Iteration	0
	+-4 **Heat Transfer Monitor**	Report	[Heat Transfer]
		Enabled	true
		Value Type	Total Value
		Trigger	Iteration
		Normalization Option	Off
		Maximum Plot Samples	5000
		Tags	[]
	`-1 Iteration Frequency	Iteration Frequency	1
		Start Iteration	0
		Enable Stop	false
		Stop Iteration	0
	+-5 **Iteration**	Maximum Plot Samples	5000
		Tags	[]
	+-6 **Mass Flow 1 Monitor**	Report	[Mass Flow 1]
		Enabled	true
		Value Type	Total Value
		Trigger	Iteration
		Normalization Option	Off
		Maximum Plot Samples	5000
		Tags	[]
	`-1 Iteration Frequency	Iteration Frequency	1
		Start Iteration	0
		Enable Stop	false
		Stop Iteration	0
	+-7 **Mass flow air Monitor**	Report	[Mass flow air]
		Enabled	true
		Value Type	Total Value
		Trigger	Iteration
		Normalization Option	Off
		Maximum Plot Samples	5000
		Tags	[]
	`-1 Iteration Frequency	Iteration Frequency	1
		Start Iteration	0

		Enable Stop	false
		Stop Iteration	0
| +-8 **Physical Time**		Maximum Plot Samples	5000
		Tags	[]
| +-9 **Radiator Temp in Monitor**		Report	[Radiator Temp in]
| |		Enabled	true
| |		Value Type	Total Value
| |		Trigger	Iteration
| |		Normalization Option	Off
| |		Maximum Plot Samples	5000
| |		Tags	[]
| | `-1 Iteration Frequency		Iteration Frequency	1
		Start Iteration	0
		Enable Stop	false
		Stop Iteration	0
| +-10 **Radiator Temp out Monitor**		Report	[T9]
| |		Enabled	true
| |		Value Type	Total Value
| |		Trigger	Iteration
| |		Normalization Option	Off
| |		Maximum Plot Samples	5000
| |		Tags	[]
| | `-1 Iteration Frequency		Iteration Frequency	1
		Start Iteration	0
		Enable Stop	false
		Stop Iteration	0
| +-11 **Radiator Temp out Monitor 2**		Report	[Radiator Temp out]
| |		Enabled	true
| |		Value Type	Total Value
| |		Trigger	Iteration
| |		Normalization Option	Off
| |		Maximum Plot Samples	5000
| |		Tags	[]
| | `-1 Iteration Frequency		Iteration Frequency	1
		Start Iteration	0
		Enable Stop	false
		Stop Iteration	0
| +-12 **T2 Monitor**		Report	[T2]
| |		Enabled	true
| |		Value Type	Total Value
| |		Trigger	Iteration
| |		Normalization Option	Off
| |		Maximum Plot Samples	5000
| |		Tags	[]
| | `-1 Iteration Frequency		Iteration Frequency	1
		Start Iteration	0
		Enable Stop	false
		Stop Iteration	0
| +-13 **T3 Monitor**		Report	[T3]
| |		Enabled	true
| |		Value Type	Total Value
| |		Trigger	Iteration
| |		Normalization Option	Off
| |		Maximum Plot Samples	5000
| |		Tags	[]
| | `-1 Iteration Frequency		Iteration Frequency	1
		Start Iteration	0
		Enable Stop	false
		Stop Iteration	0
| +-14 **T4 Monitor**		Report	[T4]

			Enabled	true
			Value Type	Total Value
			Trigger	Iteration
			Normalization Option	Off
			Maximum Plot Samples	5000
			Tags	[]
		`-1 Iteration Frequency	Iteration Frequency	1
			Start Iteration	0
			Enable Stop	false
			Stop Iteration	0
	+-15 **T5 Monitor**		Report	[T5]
			Enabled	true
			Value Type	Total Value
			Trigger	Iteration
			Normalization Option	Off
			Maximum Plot Samples	5000
			Tags	[]
		`-1 Iteration Frequency	Iteration Frequency	1
			Start Iteration	0
			Enable Stop	false
			Stop Iteration	0
	+-16 **T6 Monitor**		Report	[T6]
			Enabled	true
			Value Type	Total Value
			Trigger	Iteration
			Normalization Option	Off
			Maximum Plot Samples	5000
			Tags	[]
		`-1 Iteration Frequency	Iteration Frequency	1
			Start Iteration	0
			Enable Stop	false
			Stop Iteration	0
	+-17 **T7 Monitor**		Report	[T7]
			Enabled	true
			Value Type	Total Value
			Trigger	Iteration
			Normalization Option	Off
			Maximum Plot Samples	5000
			Tags	[]
		`-1 Iteration Frequency	Iteration Frequency	1
			Start Iteration	0
			Enable Stop	false
			Stop Iteration	0
	+-18 **T8 Monitor**		Report	[T8]
			Enabled	true
			Value Type	Total Value
			Trigger	Iteration
			Normalization Option	Off
			Maximum Plot Samples	5000
			Tags	[]
		`-1 Iteration Frequency	Iteration Frequency	1
			Start Iteration	0
			Enable Stop	false
			Stop Iteration	0
	+-19 **T9 Monitor**		Report	[T9]
			Enabled	true
			Value Type	Total Value
			Trigger	Iteration
			Normalization Option	Off
			Maximum Plot Samples	5000
			Tags	[]
		`-1 Iteration Frequency	Iteration Frequency	1

		Start Iteration	0
		Enable Stop	false
		Stop Iteration	0
	+-20 **T10 Monitor**	Report	[T10]
		Enabled	true
		Value Type	Total Value
		Trigger	Iteration
		Normalization Option	Off
		Maximum Plot Samples	5000
		Tags	[]
	`-1 Iteration Frequency	Iteration Frequency	1
		Start Iteration	0
		Enable Stop	false
		Stop Iteration	0
	+-21 **T11 Monitor**	Report	[T11]
		Enabled	true
		Value Type	Total Value
		Trigger	Iteration
		Normalization Option	Off
		Maximum Plot Samples	5000
		Tags	[]
	`-1 Iteration Frequency	Iteration Frequency	1
		Start Iteration	0
		Enable Stop	false
		Stop Iteration	0
	+-22 **T12 Monitor**	Report	[T12]
		Enabled	true
		Value Type	Total Value
		Trigger	Iteration
		Normalization Option	Off
		Maximum Plot Samples	5000
		Tags	[]
	`-1 Iteration Frequency	Iteration Frequency	1
		Start Iteration	0
		Enable Stop	false
		Stop Iteration	0
	+-23 **T13 Monitor**	Report	[T13]
		Enabled	true
		Value Type	Total Value
		Trigger	Iteration
		Normalization Option	Off
		Maximum Plot Samples	5000
		Tags	[]
	`-1 Iteration Frequency	Iteration Frequency	1
		Start Iteration	0
		Enable Stop	false
		Stop Iteration	0
	+-24 **T14 Monitor**	Report	[T14]
		Enabled	true
		Value Type	Total Value
		Trigger	Iteration
		Normalization Option	Off
		Maximum Plot Samples	5000
		Tags	[]
	`-1 Iteration Frequency	Iteration Frequency	1
		Start Iteration	0
		Enable Stop	false
		Stop Iteration	0
	+-25 **T15 Monitor**	Report	[T15]
		Enabled	true
		Value Type	Total Value
		Trigger	Iteration
		Normalization Option	Off

			Maximum Plot Samples	5000
			Tags	[]
		`-1 Iteration Frequency	Iteration Frequency	1
			Start Iteration	0
			Enable Stop	false
			Stop Iteration	0
	+-26 **T17 Monitor**		Report	[T17]
			Enabled	true
			Value Type	Total Value
			Trigger	Iteration
			Normalization Option	Off
			Maximum Plot Samples	5000
			Tags	[]
		`-1 Iteration Frequency	Iteration Frequency	1
			Start Iteration	0
			Enable Stop	false
			Stop Iteration	0
	+-27 **T20 Monitor**		Report	[T20]
			Enabled	true
			Value Type	Total Value
			Trigger	Iteration
			Normalization Option	Off
			Maximum Plot Samples	5000
			Tags	[]
		`-1 Iteration Frequency	Iteration Frequency	1
			Start Iteration	0
			Enable Stop	false
			Stop Iteration	0
	+-28 **Virtual Disk Force 1 Monitor**		Report	[Virtual Disk Force 1]
			Enabled	true
			Value Type	Total Value
			Trigger	Iteration
			Normalization Option	Off
			Maximum Plot Samples	5000
			Tags	[]
		`-1 Iteration Frequency	Iteration Frequency	1
			Start Iteration	0
			Enable Stop	false
			Stop Iteration	0
	+-30 Reports		Reports	25
		+-1 **Coolant mass flow**	Monitor Units	kg/s
			Monitor Value	Region-1 Mass Flux
			Heat Exchanger	Heat Exchanger 1
			Cold Downstream Boundaries	[Air Core: Radiator Outlet [Interface 5]]
			Hot Downstream Boundaries	[Coolant core: Outlet Interface [Interface 2]]
			Parts	[]
			Representation	Volume Mesh
			Smooth Values	false
			Tags	[]
		+-2 **Coolant Temp in**	Monitor Units	C
			Monitor Value	Region-1 Inlet Temperature
			Heat Exchanger	Heat Exchanger 1
			Cold Downstream Boundaries	[Air Core: Radiator Outlet [Interface 5]]
			Hot Downstream Boundaries	[Coolant core: Outlet Interface [Interface 2]]
			Parts	[]
			Representation	Volume Mesh
			Smooth Values	false
			Tags	[]
		+-3 **Coolant Temp out**	Monitor Units	C
			Monitor Value	Region-1 Outlet Temperature

		Heat Exchanger	Heat Exchanger 1
		Cold Downstream Boundaries	[Air Core: Radiator Outlet [Interface 5]]
		Hot Downstream Boundaries	[Coolant core: Outlet Interface [Interface 2]]
		Parts	[]
		Representation	Volume Mesh
		Smooth Values	false
		Tags	[]
	+-4 **Heat Transfer**	Monitor Units	kW
		Monitor Value	Heat Transfer
		Heat Exchanger	Heat Exchanger 1
		Cold Downstream Boundaries	[Air Core: Radiator Outlet [Interface 5]]
		Hot Downstream Boundaries	[Coolant core: Outlet Interface [Interface 2]]
		Parts	[]
		Representation	Volume Mesh
		Smooth Values	false
		Tags	[]
	+-5 **Mass Flow 1**	Units	kg/s
		Parts	[]
		Representation	Volume Mesh
		Smooth Values	false
		Tags	[]
	+-6 **Mass flow air**	Monitor Units	kg/s
		Monitor Value	Region-0 Mass Flux
		Heat Exchanger	Heat Exchanger 1
		Cold Downstream Boundaries	[Air Core: Radiator Outlet [Interface 5]]
		Hot Downstream Boundaries	[Coolant core: Outlet Interface [Interface 2]]
		Parts	[]
		Representation	Volume Mesh
		Smooth Values	false
		Tags	[]
	+-7 **Radiator Temp in**	Monitor Units	C
		Monitor Value	Region-0 Inlet Temperature
		Heat Exchanger	Heat Exchanger 1
		Cold Downstream Boundaries	[Air Core: Radiator Outlet [Interface 5]]
		Hot Downstream Boundaries	[Coolant core: Outlet Interface [Interface 2]]
		Parts	[]
		Representation	Volume Mesh
		Smooth Values	false
		Tags	[]
	+-8 **Radiator Temp out**	Monitor Units	C
		Monitor Value	Region-0 Outlet Temperature
		Heat Exchanger	Heat Exchanger 1
		Cold Downstream Boundaries	[Air Core: Radiator Outlet [Interface 5]]
		Hot Downstream Boundaries	[Coolant core: Outlet Interface [Interface 2]]
		Parts	[]
		Representation	Volume Mesh
		Smooth Values	false
		Tags	[]
	+-9 **T2**	Units	C
		Field Function	Temperature
		Collocated Field Functions	[]
		Parts	[T2]
		Representation	Volume Mesh
		Smooth Values	false
		Tags	[]
	+-10 **T3**	Units	C
		Field Function	Temperature
		Collocated Field Functions	[]
		Parts	[T3]
		Representation	Volume Mesh
		Smooth Values	false
		Tags	[]
	+-11 **T4**	Units	C
		Field Function	Temperature
		Collocated Field Functions	[]
		Parts	[T4]

		Representation	Volume Mesh
		Smooth Values	false
		Tags	[]
|	+-12 **T5**	Units	C
		Field Function	Temperature
		Collocated Field Functions	[]
		Parts	[T5]
		Representation	Volume Mesh
		Smooth Values	false
		Tags	[]
|	+-13 **T6**	Units	C
		Field Function	Temperature
		Collocated Field Functions	[]
		Parts	[T6]
		Representation	Volume Mesh
		Smooth Values	false
		Tags	[]
|	+-14 **T7**	Units	C
		Field Function	Temperature
		Collocated Field Functions	[]
		Parts	[T7]
		Representation	Volume Mesh
		Smooth Values	false
		Tags	[]
|	+-15 **T8**	Units	C
		Field Function	Temperature
		Collocated Field Functions	[]
		Parts	[T8]
		Representation	Volume Mesh
		Smooth Values	false
		Tags	[]
|	+-16 **T9**	Monitor Units	C
		Monitor Value	Region-0 Outlet Temperature
		Cold Downstream Boundaries	[]
		Hot Downstream Boundaries	[]
		Parts	[T9]
		Representation	Volume Mesh
		Smooth Values	false
		Tags	[]
|	+-17 **T10**	Units	C
		Field Function	Temperature
		Collocated Field Functions	[]
		Parts	[T10]
		Representation	Volume Mesh
		Smooth Values	false
		Tags	[]
|	+-18 **T11**	Units	C
		Field Function	Temperature
		Collocated Field Functions	[]
		Parts	[T11]
		Representation	Volume Mesh
		Smooth Values	false
		Tags	[]
|	+-19 **T12**	Units	C
		Field Function	Temperature
		Collocated Field Functions	[]
		Parts	[T12]
		Representation	Volume Mesh
		Smooth Values	false
		Tags	[]
|	+-20 **T13**	Units	C
		Field Function	Temperature
		Collocated Field Functions	[]
		Parts	[T13]
		Representation	Volume Mesh
		Smooth Values	false
		Tags	[]

| +-21 **T14**	Units	C
| |	Field Function	Temperature
| |	Collocated Field Functions	[]
| |	Parts	[T14]
| |	Representation	Volume Mesh
| |	Smooth Values	false
| |	Tags	[]
| +-22 **T15**	Units	C
| |	Field Function	Temperature
| |	Collocated Field Functions	[]
| |	Parts	[T15]
| |	Representation	Volume Mesh
| |	Smooth Values	false
| |	Tags	[]
| +-23 **T17**	Units	C
| |	Field Function	Temperature
| |	Collocated Field Functions	[]
| |	Parts	[T17]
| |	Representation	Volume Mesh
| |	Smooth Values	false
| |	Tags	[]
| +-24 **T20**	Units	C
| |	Field Function	Temperature
| |	Collocated Field Functions	[]
| |	Parts	[T20]
| |	Representation	Volume Mesh
| |	Smooth Values	false
| |	Tags	[]
| `-25 **Virtual Disk Force 1**	Units	N
|	Virtual Disk	Virtual Disk
|	Force Component Option	Z-Axis Force
|	Force Type Option	Action of the Fluid on the Virtual Disk
|	Tags	[]
+-31 Solvers		
| +-1 Partitioning	Solver Frozen	false
| |	Partitioning Method	Per-Continuum
| +-2 Wall Distance	Solver Frozen	false
| |	Wall Distance Solver Option	Kd-Tree
| |	Verbosity	0
| |	Minimum Tree Size Threshold	500000
| +-3 Segregated Flow	Freeze Flow	false
| | |	Reconstruction Frozen	false
| | |	Reconstruction Zeroed	false
| | |	Enable Enhanced Stability Treatment	false
| | |	Temporary Storage Retained	false
| | |	Pressure Corrections: Bad Cell Minimum Scaling	0.8
| | |	Pressure Corrections: Acceptable Cell Volume Change	0.001
| | |	Velocity Corrections: Maximum Unlimited Velocity	20.0 m/s
| | |	Velocity Corrections: Acceptable Velocity Increase Rate [<1]	0.15
| | |	Continuity Initialization	false
| | +-1 Velocity	Under-Relaxation Factor	0.7
| | | |	Dynamic Local Under-Relaxation	false
| | | +-1 Under-Relaxation Factor Ramp	Ramp Method	No Ramp
| | | `-2 AMG Linear Solver	Max Cycles	30
| | | |	Verbosity	NONE
| | | |	Enable Direct Solver	false
| | | |	Maximum Direct Solver Equations	32
| | | |	Convergence Tolerance	0.1
| | | |	Epsilon	0.0
| | | |	Cycle Type	Flex Cycle

				Group Size Control	Auto
				Group Size	4
				Relaxation Scheme	Gauss-Seidel
				Acceleration Method	None
				Scaling	Disabled
			`-1 Flex Cycle	Restriction Tolerance	0.9
				Prolongation Tolerance	0.5
				Sweeps	1
		`-2 Pressure		Number of Non-Orthogonality Correctors	0
				Under-Relaxation Factor	0.3
				Pressure Reference Location	Automatic Selection
		+-1 Under-Relaxation Factor Ramp		Ramp Method	No Ramp
		`-2 AMG Linear Solver		Max Cycles	30
				Verbosity	NONE
				Enable Direct Solver	false
				Maximum Direct Solver Equations	32
				Convergence Tolerance	0.1
				Epsilon	0.0
				Cycle Type	V Cycle
				Group Size Control	Auto
				Group Size	4
				Relaxation Scheme	Gauss-Seidel
				Acceleration Method	Bi Conjugate Gradient Stabilized
				Scaling	Auto
			`-1 V Cycle	Pre-Sweeps	1
				Post-Sweeps	1
				Max Levels	50
	+-4 Segregated Energy			Solver Frozen	false
				Reconstruction Frozen	false
				Reconstruction Zeroed	false
				Temporary Storage Retained	false
				Fluid Under-Relaxation Factor	0.9
				Solid Under-Relaxation Factor	0.99
				Enable High-Accuracy Temporal Discretization	false
		+-1 Fluid Under-Relaxation Factor Ramp		Ramp Method	No Ramp
		+-2 Solid Under-Relaxation Factor Ramp		Ramp Method	No Ramp
		`-3 AMG Linear Solver		Max Cycles	30
				Verbosity	NONE
				Enable Direct Solver	false
				Maximum Direct Solver Equations	32
				Convergence Tolerance	0.1
				Epsilon	0.0
				Cycle Type	V Cycle
				Group Size Control	Auto
				Group Size	4
				Relaxation Scheme	Gauss-Seidel
				Acceleration Method	None
				Scaling	Disabled
			`-1 V Cycle	Pre-Sweeps	1
				Post-Sweeps	1
				Max Levels	50
	+-5 K-Epsilon Turbulence			Solver Frozen	false
				Reconstruction Frozen	false
				Reconstruction Zeroed	false
				Temporary Storage Retained	false
				Under-Relaxation Factor	0.8
				Boundary Layer Initialization	false
		+-1 Under-Relaxation Factor Ramp		Ramp Method	No Ramp

		`-2 AMG Linear Solver	Max Cycles	30
			Verbosity	NONE
			Enable Direct Solver	false
			Maximum Direct Solver Equations	32
			Convergence Tolerance	0.1
			Epsilon	0.0
			Cycle Type	Flex Cycle
			Group Size Control	Auto
			Group Size	4
			Relaxation Scheme	Gauss-Seidel
			Acceleration Method	None
			Scaling	Disabled
		`-1 Flex Cycle	Restriction Tolerance	0.9
			Prolongation Tolerance	0.5
			Sweeps	1
	+-6 K-Omega Turbulence		Solver Frozen	false
			Reconstruction Frozen	false
			Reconstruction Zeroed	false
			Temporary Storage Retained	false
			Under-Relaxation Factor	0.8
			Boundary Layer Initialization	false
		+-1 Under-Relaxation Factor Ramp	Ramp Method	No Ramp
		`-2 AMG Linear Solver	Max Cycles	30
			Verbosity	NONE
			Enable Direct Solver	false
			Maximum Direct Solver Equations	32
			Convergence Tolerance	0.1
			Epsilon	0.0
			Cycle Type	Flex Cycle
			Group Size Control	Auto
			Group Size	4
			Relaxation Scheme	Gauss-Seidel
			Acceleration Method	None
			Scaling	Disabled
		`-1 Flex Cycle	Restriction Tolerance	0.9
			Prolongation Tolerance	0.5
			Sweeps	1
	+-7 K-Epsilon Turbulent Viscosity		Solver Frozen	false
			Under-Relaxation Factor	1.0
			Maximum Ratio	100000.0
	`-8 K-Omega Turbulent Viscosity		Solver Frozen	false
			Under-Relaxation Factor	1.0
			Maximum Ratio	100000.0
+-32 Stopping Criteria				
	+-1 **Maximum Steps**		Enabled	true
			Maximum Steps	3000
			Logical Rule	Or
			Criterion Satisfied	false
			Tags	[]
	`-2 **Stop File**		Enabled	true
			Stop Inner Iterations	true
			Path	ABORT
			Logical Rule	Or
			Criterion Satisfied	false
			Tags	[]
+-33 Solution Histories				
+-34 Solution Views				
	`-1 **Current Solution**		Iteration	3000
			Time Step	0
			Solution Time	0.0

Tags	[]

Solution

Accumulated CPU Time over all processes (s)	432203.53754800005
Elapsed Time (s)	10867.187659025192
Iterations	3000